

Unambiguous Black Hole Mass from Polarimetry and Application to Hot Jupiters

Dissertation by

Sloane J. Wiktorowicz

In Partial Fulfillment of the Requirements

for the Degree of

Doctor of Philosophy



California Institute of Technology

Pasadena, California

2009

(Defended July 28, 2008)

© 2009

Sloane J. Wiktorowicz

All Rights Reserved

This dissertation is dedicated to my wife Sharon, who has stood by my side and supported me while writing. I also dedicate this work to my family, who have encouraged me to pursue my love of the stars and whose advice and support through the years have been essential.

Acknowledgements

Many thanks go to Keith Matthews, whose help and advice have been essential in construction of my instrument. I would like to thank Michael Ireland and Ian McEwan for valuable discussions on instrumentation, polarimetry, and signal processing. I appreciate the help of the Palomar Observatory staff, especially Bruce Baker, Karl Dunscombe, John Henning, Greg van Idsinga, and Steve Kunsman. Without their help, this instrument would literally not have gotten off the ground. I thank Shri Kulkarni, who inspired me to pursue instrumentation. I acknowledge David Stevenson for a valuable debate regarding condensation in a water-hydrogen mixture and Conner Wiktorowicz for his help in determining uncertainty along the photospheric adiabat. I would like to acknowledge funding from the Moore Foundation. This research has made use of the SIMBAD database, operated at CDS, Strasbourg, France.

Abstract

A novel technique for detecting light scattered by extrasolar planets is presented that has the potential to constrain orbital inclination and planet mass. To develop this technique, I have commissioned a high precision polarimeter on the Hale 5-m telescope at Palomar Observatory. The high mass X-ray binary Cygnus X-1 has been observed, which is a proxy for extrasolar planet studies. The single scattering model of Brown et al. (1978), widely used in the literature, predicts an orbital inclination for Cygnus X-1 that is inconsistent with the lack of observed X-ray eclipses to $4\sigma - 5\sigma$. Previous studies have hinted at this discrepancy, but data quality was such that the confidence in such a discrepancy was not statistically significant. My observations represent the highest precision study of this object, and they illustrate the overwhelming complexity of the supergiant/black hole system. They also call into question the validity of the Brown et al. (1978) formalism, widely used by the community, for inclination estimation in binary systems.

Extrasolar planet host stars have also been observed, and precision of order one part per million has been achieved on bright targets. Precision attained on fainter host stars is of order one part in 10^5 . While scattered light from extrasolar planets has not been conclusively detected, a planetary transit in the HD 189733 system may have been observed in polarized light. Such an event is observed to be 1,000 times weaker in polarized light than in photometry, and it indicates a planetary transit of the Southern Hemisphere of the host star. Such geometric information is difficult to determine by other methods.

The integrated polarization of the debris disk surrounding γ Ophiuchi has been observed to high precision, and the position angle of net polarization is aligned with the disk major axis as seen by the Spitzer Space Telescope. This indicates the disk is primarily composed of forward scattering dust grains larger than the wavelengths of visible light.

Finally, Neptune-mass extrasolar planets orbiting close to their host stars have been modeled to be far too warm for liquid water oceans to exist in their upper atmospheres.

Contents

Acknowledgements	v
Abstract	vii
1 Promises and Pitfalls of Polarimetry	1
1.1 Introduction	1
1.2 Promises of Polarimetry	4
1.2.1 Extrasolar Planets	4
1.2.2 Black Holes and Neutron Stars	10
1.2.3 Circumstellar Disks	10
1.2.4 Evolved Stars	11
1.3 Pitfalls of Polarimetry	13
1.3.1 Telescope Polarization	13
1.3.2 Interstellar Polarization	13
1.3.3 Intrinsic Polarization Variability	20
2 The POLISH Instrument	25
2.1 Introduction	25
2.2 Black Hole Mass from Polarimetry	26
2.3 The Polarimeter	28
2.4 Observing Strategy	34
2.5 Data Reduction	37
2.5.1 Polarization and Noise Calculations	37
2.5.2 PEM Calibration	39
2.5.3 Mean Polarization	42
2.6 Standard Stars with APDs	42
2.6.1 Unpolarized Standard Stars and Systematic Effects	42

2.6.2	Polarized Standard Stars	47
2.7	Standard Stars with PMTs	51
2.8	Comparison to Literature	53
2.8.1	Unpolarized Standard Stars	53
2.8.2	Weakly Polarized Standard Stars	55
2.8.3	Strongly Polarized Standard Stars	61
2.8.4	Absolute Polarization	61
2.8.5	Interstellar Polarization	67
2.9	Discussion	68
2.10	Appendix A: Mueller Matrix for Lab Tests	70
2.11	Appendix B: Mueller Matrix for POLISH	71
2.12	Appendix C: Detector Noise	75
3	Nightly Variability of Polarimetric Standard Stars	81
3.1	Introduction	81
3.2	Observations	82
3.3	Variability	84
3.3.1	Intra-Night Variability and Systematic Effects	84
3.3.2	Night-to-Night Variability	89
3.4	Discussion	99
3.4.1	Standard Stars	99
3.4.2	Extrasolar Planets	104
3.4.3	Debris Disk	113
3.4.4	Cepheid Variables	116
3.5	Conclusion	119
3.6	Appendix D: Single Scattering Geometry	125
4	Cygnus X-1 Inclination from Polarimetry	129
4.1	Introduction	129
4.2	Overview of Cygnus X-1	130
4.2.1	Accretion	130
4.2.2	Periodicities	132
4.2.3	Polarization	134
4.3	Inclination from Polarimetry	136

4.3.1	BME Scattering Model	136
4.3.2	Inclination Bias	138
4.4	Results	140
4.5	Literature Estimates	147
4.5.1	Eclipses	147
4.5.2	Radial Velocity Mass Function	147
4.5.3	Radial Velocity Tomography	151
4.5.4	Ellipsoidal Modulation	152
4.5.5	Polarimetry	153
4.5.6	Disk Precession	158
4.5.7	Quasi-Periodic Oscillation Scaling	159
4.6	Discussion	160
4.7	Conclusion	168
5	Liquid Water Oceans in Ice Giants	181
5.1	Introduction	181
5.2	Photospheric Adiabats	184
5.2.1	Construction	184
5.2.2	Application to Neptune	188
5.3	Phase Transition	190
5.3.1	Cloud Base	190
5.3.2	Supercritical Fluid	192
5.4	Ocean Requirements	193
5.4.1	Deep Interior Mixing Ratio	193
5.4.2	Gravitational Signature	196
5.4.3	Photospheric Temperature	197
5.5	The Water-Hydrogen-Helium System	200
5.6	Extrasolar Hot Neptunes	202
5.7	Future Work	204
5.8	Conclusion	204
5.9	Appendix E: Moist Adiabats	208

List of Figures

1.1	Stokes parameters projected onto the sky	3
1.2	Theoretical orbital modulation of system polarization for a hot Jupiter system	7
1.3	Imaging polarimetry of Uranus	7
1.4	Modeled orbital modulation of polarization of a hot Jupiter	9
1.5	Modeled spectrum of a hot Jupiter in photometry and polarimetry	9
1.6	Modeled scattered flux and polarization of a hot Jupiter through orbit	10
1.7	Imaging polarimetry of R Scl	12
1.8	Correlation of net polarization and mass loss rate for evolved stars	12
1.9	Telescope polarization of the 4.2-m William Herschel Telescope	14
1.10	Interstellar polarization aligned to the galactic magnetic field	14
1.11	Empirical wavelength dependence of interstellar polarization	16
1.12	Theoretical wavelength dependence of interstellar polarization	16
1.13	Observed circular polarization sign change near $\lambda = \lambda_{\max}$	17
1.14	Increase in degree of interstellar polarization up to $d \approx 2$ kpc	17
1.15	Scattering of quasar radio emission by an interstellar dust cloud	19
2.1	Orbital modulation of system polarization for HMXBs	27
2.2	Plan view of the POLISH optical path	28
2.3	Ray trace diagram of the POLISH optical path	29
2.4	Photographs of the POLISH instrument	29
2.5	Typical raw AC and DC data for the unpolarized star HR 5854	36
2.6	Typical raw data for the strongly polarized star HD 204827.	36
2.7	Calibration of the PEM rotation angle	40
2.8	Polarization of HR 5854 after PEM and gain correction	44
2.9	Polarization of HR 8974 after PEM and gain correction.	44
2.10	Run-averaged precision as a function of stellar polarization	54

2.11	Nightly mean polarization of the unpolarized star HR 5854	56
2.12	Intra-night observations of HR 5854 with APD1, UT 2007 Aug 3 and 4	56
2.13	Intra-night observations of HR 5854 with APD1, UT 2007 Aug 5 and 6.	57
2.14	Nightly mean polarization of the unpolarized star HR 8974	57
2.15	Intra-night observations of HR 8974 with APD1, UT 2007 Aug 3, 5, and 6.	58
2.16	Nightly mean polarization of the weakly polarized star HD 9270	58
2.17	Intra-night observations of HD 9270 with APD1, UT 2007 Aug 4, 5, and 6.	59
2.18	Nightly mean polarization of the weakly polarized star γ Oph	59
2.19	Intra-night observations of γ Oph with APD1, UT 2007 Aug 4, 5, and 6.	60
2.20	Nightly mean polarization of the weakly polarized star Algenib	60
2.21	Intra-night observations of Algenib with APD1, UT 2007 Aug 5 and 6.	62
2.22	Nightly mean polarization of the strongly polarized star HD 157999	62
2.23	Intra-night observations of HD 157999 with APD1, UT 2007 Aug 5 and 6.	63
2.24	Nightly mean polarization of the strongly polarized star HD 187929	63
2.25	Intra-night observations of HD 187929 with APD1, UT 2007 Aug 3, 5, and 6.	64
2.26	Nightly mean polarization of the weakly polarized star HD 212311	64
2.27	Intra-night observations of HD 212311 with PMT1, UT 2007 Aug 3 and 4.	65
2.28	Intra-night observations of HD 212311 with PMT1, UT 2007 Aug 5 and 6.	65
2.29	Nightly mean polarization of the strongly polarized star HD 204827	66
2.30	Intra-night observations of HD 204827 with PMT1, UT 2007 Aug 3, 5, and 6.	66
2.31	Precision achieved on standard stars compared to the literature	67
3.1	Quantum efficiency curves for the red enhanced and blue enhanced APDs	82
3.2	Nightly confidence range of normal distribution for all stars	88
3.3	Nightly confidence range of normal distribution for individual stars	88
3.4	CDFs of HR 5854	90
3.5	CDFs of HD 187929	91
3.6	Polarization as a function of stellar distance	97
3.7	Expected and observed ratios of polarization between APDs.	101
3.8	Observed polarization of the HD 175541 exoplanet Jupiter system	106
3.9	Observed polarization of the HD 149026 transiting hot Jupiter system	106
3.10	Polarimetric modulation of the HD 189733 transiting hot Jupiter system	109
3.11	Observed polarization of the HD 189733 transiting hot Jupiter system	109

3.12	HD 189733 transit geometry	110
3.13	Modeled degree of polarization during a transit	110
3.14	Polarimetric observations of a transit of the HD 189733 hot Jupiter	112
3.15	Possible transit of an extrasolar planet seen in polarized light	112
3.16	Debris disk geometry	114
3.17	Position angle of net polarization for γ Oph	115
3.18	Polarization variations in HD 187929 versus Cepheid pulsation phase	119
4.1	Binned observations of Cygnus X-1, August 2007 data	143
4.2	Binned observations of Cygnus X-1, June 2008 data	143
4.3	Examples of synthesized Q and U data sets	146
4.4	Histogram and CDF between BME fits and synthesized data	146
4.5	Confidence intervals for inclination estimates from the BME model	148
4.6	Cygnus X-1 inclination estimates from various methods	148
4.7	Geometry for eclipses and for radial velocity tomography	152
4.8	Polarimetric modulation observed in Aug 2007 and Jun 2008	161
4.9	Summary of Cygnus X-1 polarimetric modulation	162
4.10	U versus Q for the data sets in Figure 4.9.	162
5.1	Temperature-entropy curve for pure water	182
5.2	Photospheric adiabat uncertainty	187
5.3	Photospheric adiabat overlying SF phase boundaries	189
5.4	Pressure-temperature profile along the photospheric adiabat	191
5.5	Critical curve: temperature vs. X	194
5.6	Critical curve: pressure vs. X	194
5.7	Minimum water mixing ratio for an ocean	195
5.8	Density along the photospheric adiabat overlying density models	196
5.9	Ocean probability	199
5.10	P - T profiles along photospheric adiabats with different condensables	201
5.11	Minimum deep interior water mixing ratio necessary for ocean existence	203

List of Tables

2.1	Stokes Parameters Given by Positive AC Phase	33
2.2	Observed Standard Stars	35
2.3	Detector Quantities	39
2.4	Correction Parameters for $\Theta_{\text{PEM}} = \pm 45^\circ$	41
2.5	Raw Polarization of Unpolarized Standard Stars	45
2.6	Telescope Polarization with APDs	46
2.7	Systematic Effects: Unpolarized Standard Stars with APDs	47
2.8	Weakly Polarized Standard Stars with APDs	48
2.9	Strongly Polarized Standard Stars with APDs	50
2.10	Systematic Effects: Polarized Standard Stars with APDs	51
2.11	Weakly Polarized Standard Stars with PMTs	52
2.12	Strongly Polarized Standard Stars with PMTs	52
2.13	Systematic Effects: Standard Stars with PMTs	53
2.14	Corrections for Absolute Polarization	61
3.1	Observed Stars	83
3.2	Confidence of Random Distribution	87
3.3	HR 5854 Variability	92
3.4	HR 8974 Variability	92
3.5	HD 9270 & γ Oph Variability	93
3.6	HD 212311 Variability	93
3.7	Stellar Variability	94
3.8	HD 204827 Variability	95
3.9	Cygnus X-1 Variability	95
3.10	Variability of Interstellar Polarization	100
3.11	Wavelength-Dependent Polarization	100

3.12	Corrections for Absolute Polarization	100
3.13	Variability of Exoplanet Host Stars	105
3.14	HD 187929 Variability	119
4.1	Journal of Observations	141
4.2	BME Fit Parameters	142
4.3	Comparison of Inclination Estimates	149
4.4	Photometric, Precessional Modulation	163
5.1	Deep Interior Mixing Ratios	192
5.2	Cloud Bases	201

Chapter 1

Promises and Pitfalls of Polarimetry

1.1 Introduction

Imagine an observational technique, differential in nature, that takes full advantage of the information content a photon has to offer. Photometric conditions would be unnecessary, allowing ground-based telescopes to outstrip their space-based counterparts for uses where imaging is not required. Indeed, such a technique has been around for decades in the form of polarimetry. Why, then, are the numbers of polarimeters and polarimetrists so few? Does the bright side of polarimetry simply fall on blind eyes?

In 1852, Sir George Gabriel Stokes invented a formalism for decomposing the electric field oscillations of light that is still used today. Consider a right-handed, Cartesian coordinate system with light propagating in the \hat{z} direction. The electric field of this light beam varies in time as

$$\vec{E}(t) = E_x \cos(\omega t - \delta_x) \hat{x} + E_y \cos(\omega t - \delta_y) \hat{y} \quad (1.1)$$

with amplitudes and phases E_i and δ_i . The path of the electric field vector, when projected onto the xy plane, describes an ellipse. Such light is therefore “elliptically polarized”.

The Stokes parameters I, Q, U , and V are defined by the time-averaged quantities

$$I = \langle E_x^2 \rangle + \langle E_y^2 \rangle \quad (1.2a)$$

$$Q = \langle E_x^2 \rangle - \langle E_y^2 \rangle \quad (1.2b)$$

$$U = 2 \langle E_x E_y \cos(\delta_x - \delta_y) \rangle \quad (1.2c)$$

$$V = 2 \langle E_x E_y \sin(\delta_x - \delta_y) \rangle. \quad (1.2d)$$

Thus, the Stokes I parameter describes the total intensity of the beam. Stokes Q and U are measures of the “linear” polarization of the light beam, where Stokes Q represents the net electric field component along the \hat{x} ($+Q$) or \hat{y} ($-Q$) direction and Stokes $\pm U$ describes the net electric field component at $\pm 45^\circ$ from the \hat{x} direction. Stokes V , a measure of the “circular” polarization of the light beam, represents the net electric field component that rotates clockwise ($+V$) or counterclockwise ($-V$) at constant angular frequency.

The orthogonal basis vectors of linear polarization, Q and U , are only separated by 45° in physical space. Rotation of a light beam by $\pm 90^\circ$ reverses the sign of Q and U . Therefore, periodicity in linear polarization occurs by rotation through 180° . When projected onto the sky, Stokes $+Q$ points north/south, $-Q$ east/west, $+U$ northeast/southwest, and $-U$ is northwest/southeast (Figure 1.1). Stokes parameters are usually normalized to the intensity of light, I . The fractional degree and position angle of net polarization are then

$$P \equiv \sqrt{\left(\frac{Q}{I}\right)^2 + \left(\frac{U}{I}\right)^2 + \left(\frac{V}{I}\right)^2} \quad (1.3a)$$

$$\Theta \equiv \frac{1}{2} \arctan \frac{U/I}{Q/I}. \quad (1.3b)$$

Polarimetry is therefore a differential technique, where the *fractional* degree of polarized light and its orientation are the relevant quantities. This is in contrast to absolute techniques such as photometry, which require stringent calibration to determine whether fluctuations in data are intrinsic to the source or are due to systematic effects.

To utilize photometry as a differential technique, one must monitor photometric standard stars

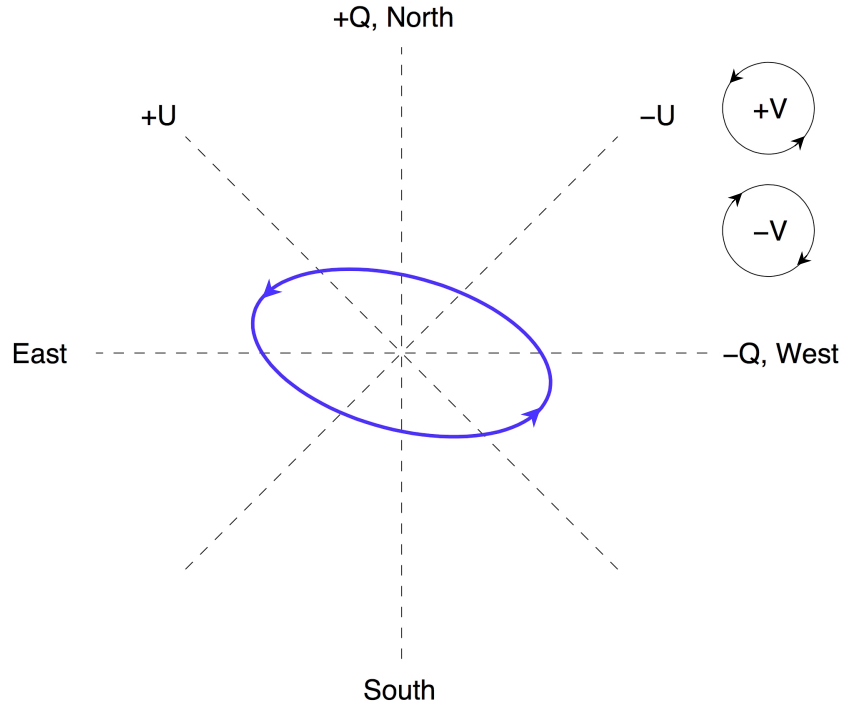


Figure 1.1: Stokes parameters projected onto the sky. The ellipse indicates a general, elliptically polarized light beam with Stokes parameters $-Q$, $+U$, and $+V$, where $Q > U$.

simultaneously with the target. The non-uniformity of the Earth’s atmosphere forces one to choose standard stars at a small angular distance from the target. Thus, if a pocket of turbulence passes through the line of sight of both stars roughly simultaneously, the scintillation event should be subtracted out. Even for high quality calibration, however, photometric precision better than one part in 10^3 is extremely difficult to achieve from the ground. Space-based telescopes overcome scintillation from the atmosphere, but their smaller apertures ensure that even photon shot noise-limited operation rarely produces precision less than one part in 10^4 . However, I will show in subsequent chapters that I have achieved polarimetric precision on bright stars of order one part per million.

Unfortunately, polarimetry still requires calibration. The largest source of uncertainty in polarimetric measurements is usually polarization intrinsic to the telescope and instrument. Polarization of light is sensitive to the geometry of scattering as well as the optical properties of the scatterer. Therefore, asymmetries in mirror coating, as well as asymmetry in the angle of reflection integrated over the mirror surface, will generate intrinsic polarization. Analogous to dark subtraction in photometry, subtraction of this telescope/instrument polarization is required. Generally this progresses by observing “unpolarized” standard stars. Since polarization is sensitive to asymmetry in the

source, nothing in the Universe is truly unpolarized. However, it is possible to measure polarization consistent with zero for some stars. Sky subtraction proceeds identically in polarimetry as it does in photometry, and conventional flat-fielding is required in imaging polarimetry. In addition, polarized standard stars are observed to ensure that the gain of the system is calibrated. This is effectively flat-fielding for single-pixel detectors. Since appropriate calibration can indeed be performed, what are the benefits of observing polarized light from the sky?

1.2 Promises of Polarimetry

1.2.1 Extrasolar Planets

Extrasolar planets are one of the most exciting objects in astronomy to study. Questions such as “How did we get here?” and “Are we alone?” are directly applicable to the study of extrasolar planets. Regarding the former question, planet formation is the result of accretion of material in circumstellar disks. Polarimetry can provide valuable clues to the nuances of this process and will be discussed later. As for the latter question, the existence of planets around other stars has been sought since recorded history. Evidence of Earth-like, or at least life-supporting, planets could have enormous impact on virtually all aspects of society, not the least of which would be the impact on planning and funding future astronomical investigations.

The first extrasolar planets were discovered around a pulsar in 1992 by observing periodic Doppler shifts in its pulses (Wolszczan & Frail 1992). These three nearly Earth-mass planets have masses 0.020 ± 0.002 , 4.3 ± 0.2 , and $3.9 \pm 0.2 M_{\oplus}$ and orbit PSR B1257+12 with periods of ≈ 25 , 67, and 98 days, respectively (Konacki & Wolszczan 2003). Beginning in 1995, hundreds of close-in, Jupiter-mass planets have been detected by periodicities in stellar radial velocity (Mayor & Queloz 1995). Recently, extrasolar planet research has progressed from planet detection to the beginning stages of planet characterization. Infrared planetary emission has been directly detected (Deming et al. 2005), and dayside/nightside contrast in that emission has been observed (Knutson et al. 2007). Moreover, while the initial detected population of extrasolar planets was of order one Jupiter mass, refinement of the radial velocity technique has permitted Neptune-mass planets to be discovered (Lovis et al. 2006).

However, to truly begin to characterize individual planets, their most basic characteristic, mass, must be accurately determined. Since the radial velocity technique is insensitive to stellar reflex motion in the plane of the sky, estimation of precise masses for the large majority of known planets is hampered by the inability to measure orbital inclination, i . Measured mass, m , is only a lower limit to the true mass, M , because $m = M \sin i$. Planets in edge-on orbits transit the disk of their host star every orbit, which causes a periodic dip in the stellar flux as the planet transits the disk of its parent star. The shape of the system lightcurve is indicative of orbital inclination, so inclination estimates from transit observations can be coupled with radial velocity data to derive accurate masses. Indeed, masses of transiting planets can be measured with a precision of less than one Jupiter mass. The transit of HD 209458 was discovered by Charbonneau et al. (2000); since then, dozens of transiting planets have been discovered. However, the probability of transit occurrence in a sample of systems with randomly distributed inclinations scales as R_*/a , where R_* is the stellar radius and a is the planetary semimajor axis. This is because the solid angle subtended by the transit shadow is $2\pi \times 2R_*/a$ out of a total 4π steradians. Thus, transiting planets only comprise $\approx 10\%$ of known extrasolar planets.

Astrometry holds promise for determining masses of planets, because the star's motion in the plane of the sky is observed. The astrometric motion a_* of an extrasolar planet host star is simply the star's lever arm with respect to the center of mass of the system:

$$a_* = a \left(\frac{M_p}{M_*} \right). \quad (1.4)$$

Since typical mass ratios for extrasolar planets/host stars are of order one part in 10^{-3} , the astrometric motion of a star 100 parsecs away with a planet at $a = 0.05$ AU is of order $0.5 \mu\text{as}$. While space-based interferometers have the potential to graze this regime, astrometric mass measurements are more likely for planets at larger semimajor axes. The same selection effect occurs for direct imaging of planetary emission, because a star's diffracted halo decreases in brightness with increase in angular distance. Therefore, orbits of extrasolar planets seen astrometrically or by direct imaging are more likely for planets at large semimajor axes.

This differs from the radial velocity technique, because close-in extrasolar planets are preferentially selected for because of two reasons. First, stellar velocities scale as

$$v = \frac{2\pi a}{T} = \frac{2\pi}{\sqrt{a}} \quad (1.5)$$

for circular orbits, where a is orbital semimajor axis. Second, close-in planets undergo more orbits in a given amount of time than do planets at larger semimajor axes, so confirmation of statistically significant periodicity requires a shorter temporal baseline.

We are developing an observational technique that has the potential to determine system inclination for close-in extrasolar planets (so-called “hot Jupiters”). System inclination, and therefore unambiguous mass, can be found by monitoring the polarization of the system throughout its orbit. Polarization of hot Jupiters arises by scattering of incident starlight by gas molecules, aerosols, and dust grains in the planet’s atmosphere. For a face-on orbit (Figure 1.2a), the planet is always seen at quadrature and will always have half of its disk illuminated. Since the intensity of light scattered by the planet is constant throughout the orbit, the degree of polarization will also be constant.

However, the position angle of polarization will rotate through 360° each orbit. This is because the position angle from single scattering events is perpendicular to the plane containing the light source, the scatterer, and the observer (i.e., the scattering plane). In contrast, an edge-on viewing geometry will generate large, periodic variability in the degree of polarization (Figure 1.2b). For this geometry, the planet will appear to go through the complete cycle of full to new phases, just like the Moon. However, the scattering plane will always lie in the plane of the orbit, so the position angle of net polarization will not vary during the orbit. In general, a hot Jupiter system will exhibit variability in the polarization vector that is indicative of orbital inclination.

Hot Jupiters have orbital periods of a few days, so they intercept about one part in 10^5 of their parent star’s flux. Disk-integrated polarization of Jupiter itself is of order one percent (Hall & Riley 1976), and spatially resolved polarization of comparable magnitude has been observed on Uranus and Neptune (Figure 1.3). Therefore, the precision required to detect hot Jupiters is one part per million to one part in ten million of the star’s total flux. The polarization of the host star itself is at the level of one part in 10^4 or lower and is primarily due to interstellar extinction. Since the planet’s orbital frequency is known to high precision from radial velocity, stellar polarization and its variability can be separated from the planetary signal.

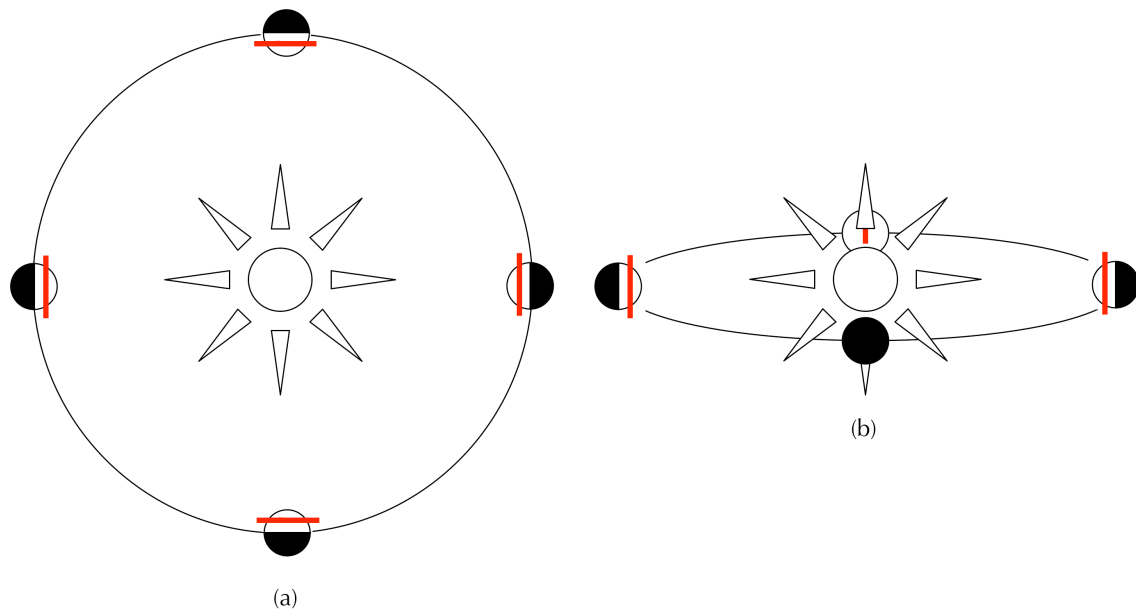


Figure 1.2: Theoretical orbital modulation of system polarization for a hot Jupiter system. The degree of polarization is represented by the white, illuminated portion of the planet. The position angle of net polarization is given by the orientation of the red lines. The face-on case is shown in (a), and the edge-on case is shown in (b).

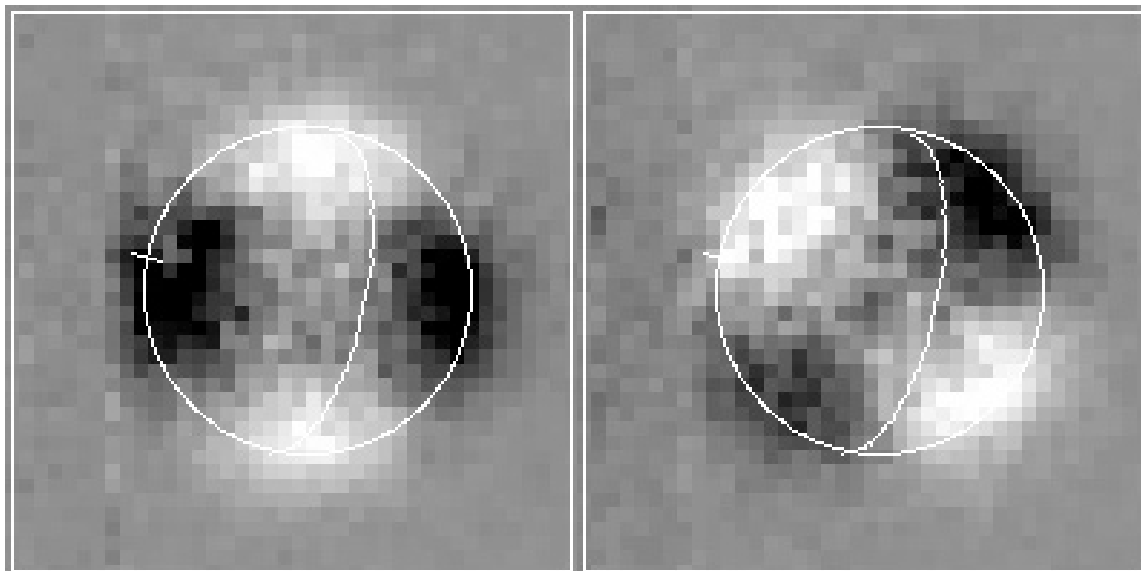


Figure 1.3: Imaging polarimetry of Uranus. This figure is taken from Figure 2 of Schmid et al. (2006). The left image is Stokes Q/I and the right is U/I . Black pixels indicate polarization of -0.5% , and white pixels have polarization of $+0.5\%$. North is up, east is to the left, and the disk of the planet, South Pole, and Equator are outlined in white.

The precision required to observe the modulation in polarization due to the hot Jupiter is one to two orders of magnitude more stringent than the modulation in photometry of the system. However, ground-based photometric observation alone cannot achieve this high precision due to the difficulty in achieving such stringent calibration. Even if the requisite calibration were attained, perhaps from space-based observatories, the low information content from photometry would preclude estimation of system inclination. Polarization is a vector quantity, containing both degree of polarization as well as position angle, while photometry is a scalar quantity. The added information content per photon from polarimetry allows inclinations to be determined. Figure 1.4 (taken from the models of Stam et al. 2004) demonstrates that the amplitude of orbital modulation in polarization of a hot Jupiter is dependent on system inclination. The frequency of polarization modulation is the second harmonic of the orbital frequency because polarization follows a $\cos(2\theta)$ profile through rotation. That is, polarimetric position angles θ and $\theta + 180^\circ$ are identical.

In addition to constraining system inclination (and therefore mass) of extrasolar planets, polarization of these planets can yield information about the atmospheric structure. Calculations of Stam et al. (2004) suggest that both the total reflected flux spectrum and the degree of polarization versus wavelength should be different depending on whether the atmosphere is clear, has cloud layers, or has both cloud and haze layers (Figure 1.5). The maximum polarization of the planet through its orbit will be dependent on the existence or lack of these layers (Figure 1.6b) while the minimum polarization of the planet is dependent on the system inclination (Figure 1.4).

Polarimetry also has the potential to determine the stellar hemisphere transited by an extrasolar planet. This is because the asymmetry in stellar polarization caused by a transiting planet will be reversed between transit ingress and egress. This causes a rotation of the position angle of net polarization of the system throughout the transit, and the sign of rotation on the sky is indicative of the hemisphere that is transited. That is, the position angle of net polarization during a Northern Hemisphere ingress is the same as the position angle during a Southern Hemisphere egress, and vice versa. I will present tentative observations of a transit of the HD 189733 system in Chapter 3.

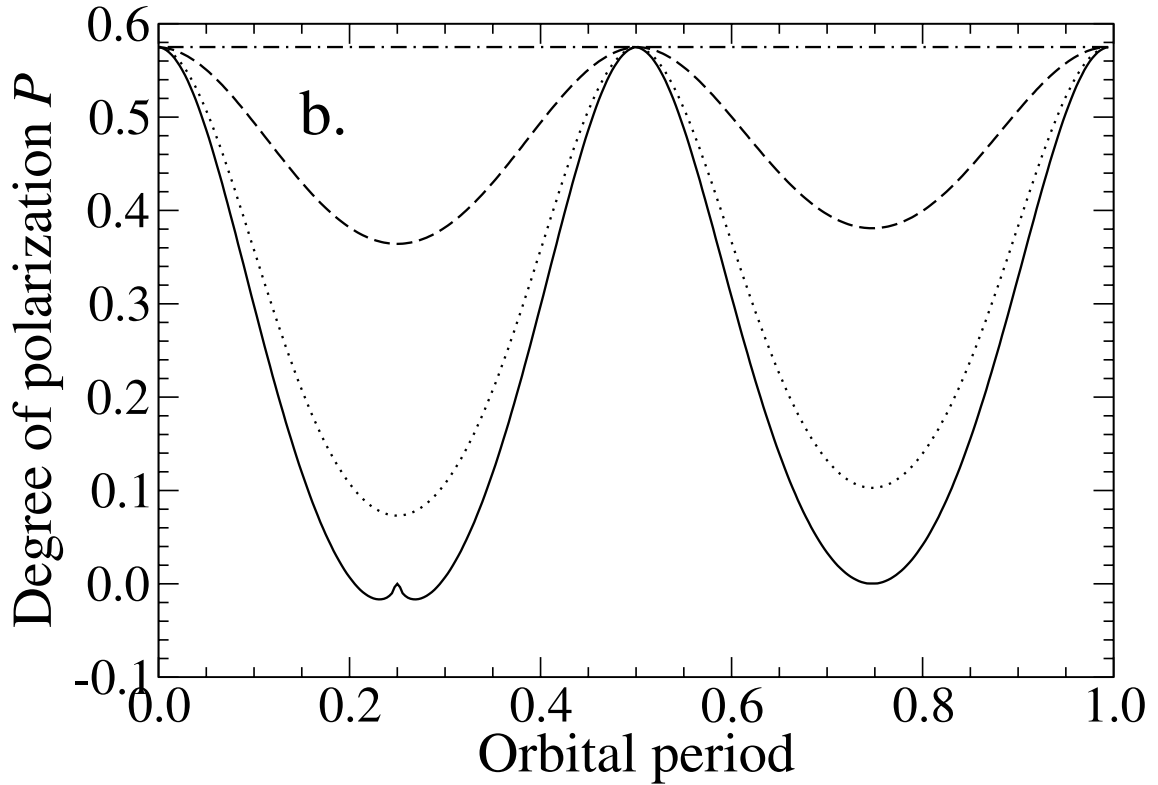


Figure 1.4: Modeled orbital modulation of polarization of a hot Jupiter, given as Figure 7b from Stam et al. (2004). The dot-dashed, dashed, dotted, and solid lines represent inclinations of 0° (face-on), 30° , 60° , and 90° (edge-on), respectively.

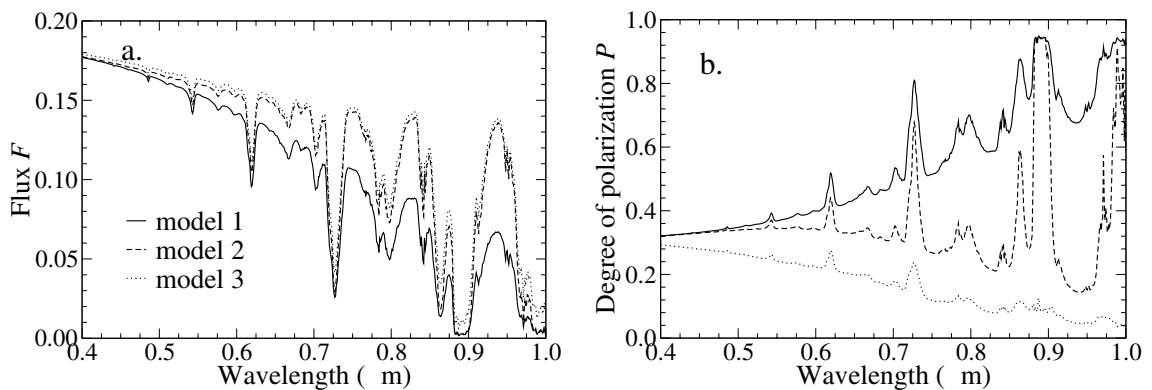


Figure 1.5: (a) Spectrum of scattered flux from a hot Jupiter. (b) Polarized spectrum of a hot Jupiter, taken from Figure 4 of Stam et al. (2004). Models 1, 2, and 3 are for a clear atmosphere, for an atmosphere with a tropospheric cloud layer, and for an atmosphere with both a tropospheric cloud layer and a stratospheric haze layer, respectively. It can be seen that absorption bands are more strongly polarized than the continuum.

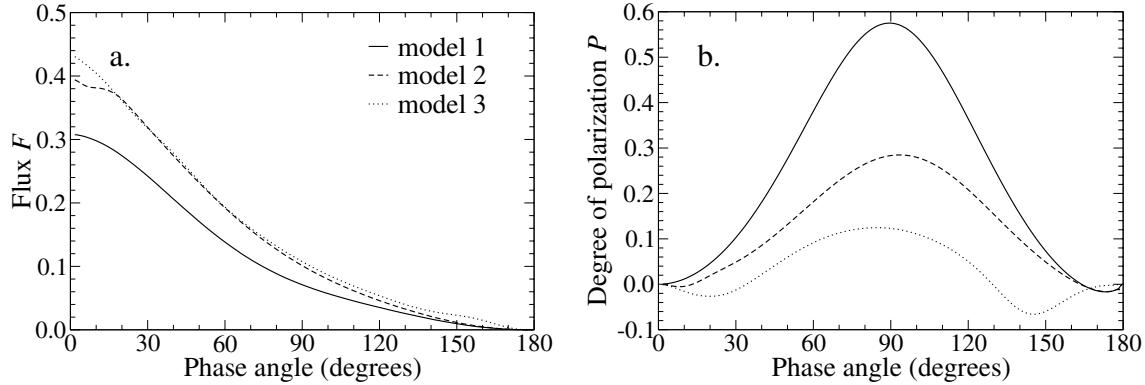


Figure 1.6: (a) Scattered flux and (b) polarization of a hot Jupiter through orbit, taken from Figure 5 of Stam et al. (2004). Existence of clouds and haze can be deduced from the maximum planetary polarization over the orbit.

1.2.2 Black Holes and Neutron Stars

Orbital inclination of high mass X-ray binaries, consisting of an OB supergiant and either a black hole or neutron star, may also be determined from polarimetric monitoring. While the mechanism generating net polarization of the system is different for hot Jupiters and X-ray binaries, phase-locked modulation can give an estimate of inclination. The hot photosphere of the supergiant in such a binary generates significant free electrons which Thomson scatter the stellar flux. Tidal distortion of such a circumbinary envelope, as well as of the supergiant itself, imparts an asymmetry to the system which causes polarimetric modulation. For rigidly rotating, static structure, this modulation occurs at the orbital frequency and first harmonic. Thus, spurious variability at other frequencies can, in principle, be filtered out.

Once the inclination of the system is known, radial velocity data can then provide accurate masses of the compact object, assuming the mass of the supergiant is known. Evolutionary modeling of progenitor stars would greatly benefit from a large sample of known black hole and neutron star masses.

1.2.3 Circumstellar Disks

Vink et al. (2005) observe polarization of seven T Tauri and Herbig Ae/Be objects. They find the position angle of polarization of three objects to be consistent with the position angle of the disk major axis from near-IR interferometric imaging. The remaining four objects have polarimetric position angle $\approx 90^\circ$ from the position angle of the major axis. They interpret these results in terms of

single or multiple scattering by optically thin or thick disks, respectively. They also observe a change in degree of polarization versus wavelength across the $H\alpha$ line. This is interpreted as scattering of starlight by a rotating accretion disk, because the strongest degree of polarization is expected for scattering through 90° . This occurs for material at quadrature phase, which will be moving almost entirely along the line of sight. This material will therefore lie at the Doppler shifted wings of the line.

Nearly edge-on disks of UX Ori objects show increased polarization during times of photometric minima. This is interpreted in terms of dust clumps partially occulting the central star, while light scattered and polarized by the disk is unaffected. Since the amount of polarized light stays roughly constant, while the amount of unpolarized light decreases, the degree of polarization during these occultations increases (Grinin 1994, Grinin et al. 1994, Oudmaijer et al. 2001).

Graham et al. (2007) observe polarization perpendicular to the edge-on disk around AU Mic, which indicates single scattering in an optically thin disk composed of micron sized particles.

1.2.4 Evolved Stars

The process by which nearly spherical stars generate planetary nebulae of strongly asymmetric shape is poorly known. González Delgado et al. (2003) observe a polarized shell of material around the carbon stars R Scl and U Ant (Figure 1.7). Polarimetric modulation of post-AGB stars can be partly explained by non-radial pulsations (Henson et al. 1985, Magalhães et al. 1986, Raveendran & Rao 1989, Yudin & Evans 2002), which may play a role in the production of non-spherical planetary nebulae. Trammell et al. (1994) observed 31 post-AGB stars, and they claim 75% of the sample shows evidence for intrinsic polarization. They take this to be evidence for asphericity in the system. In addition, they observe polarimetric variability which is interpreted as mass loss in the form of clumps. Johnson & Jones (1991) and Biegging et al. (2006) find a positive correlation between evolved star mass loss rate and net polarization (Figure 1.8).

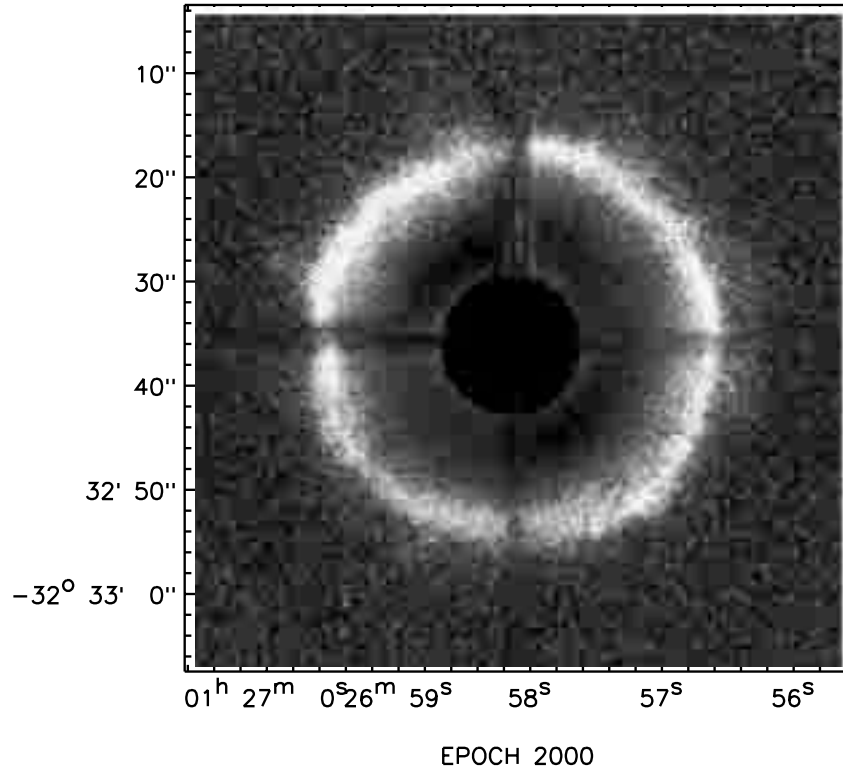


Figure 1.7: Imaging polarimetry of R Scl from Figure 1 of González Delgado et al. (2003).

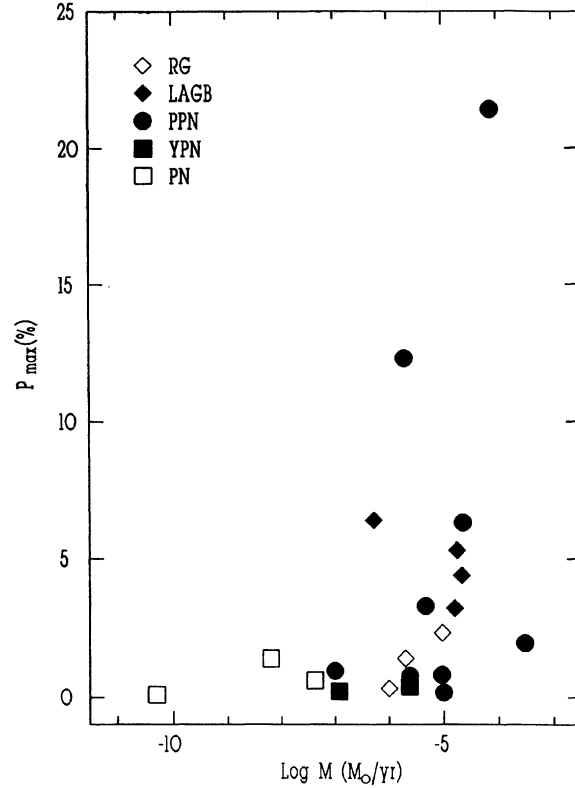


Figure 1.8: Correlation of net polarization and mass loss rate for evolved stars. This figure comes from Figure 3 of Johnson & Jones (1991) and is reproduced by permission of the AAS.

1.3 Pitfalls of Polarimetry

1.3.1 Telescope Polarization

The largest systematic effect in high precision polarimetry is usually telescope and instrument polarization. It is generally present at less than one part in 10^4 , which is below the noise floor for imaging polarimetry. However, observations of polarimetry in integrated light, which are necessary in order to reach precisions required for extrasolar planet and other high precision observations, must calibrate telescope polarization. The procedure generally involves observing with an altitude-azimuth telescope with the field de-rotator disabled. Stars thought to be unpolarized, and consequently non-variable on a night-to-night timescale, are observed through a range of parallactic angles. Such stars are generally nearby, so the effect of interstellar polarization is minimized (section 1.3.2). Since telescope polarization dominates the signal, the modulation of observed polarization as the Earth rotates gives a measure of the telescope polarization (Figure 1.9). However, this process is very time consuming, and it must be performed each night. Indeed, Hough et al. (2006b) estimate 20% of observing time is taken up by telescope polarization calibration.

For equatorial mount telescopes, such as the Hale 5-m, one must observe net polarization of stars that are known to exhibit intrinsic plus interstellar polarization that is consistent with zero. This requires identification of such stars from previous, high precision polarimetric investigations on alt-az telescopes. We therefore consult Hough et al. (2006b) for such zero polarization standard stars observed with the PlanetPol instrument.

1.3.2 Interstellar Polarization

Alignment of interstellar dust grains by the galactic magnetic field causes preferential extinction of the electric field component of background starlight parallel to the long axis of the grains (Davis & Greenstein 1951). This large-scale alignment can be seen in the polarization maps of Mathewson & Ford (1970), shown in Figure 1.10. Serkowski et al. (1975) determine empirically that stars for which interstellar polarization dominates will have a distinctive spectrum of polarization versus wavelength:

$$\frac{P(\lambda)}{P_{\max}} = \exp \left[-1.15 \ln^2 \left(\frac{\lambda_{\max}}{\lambda} \right) \right]. \quad (1.6)$$

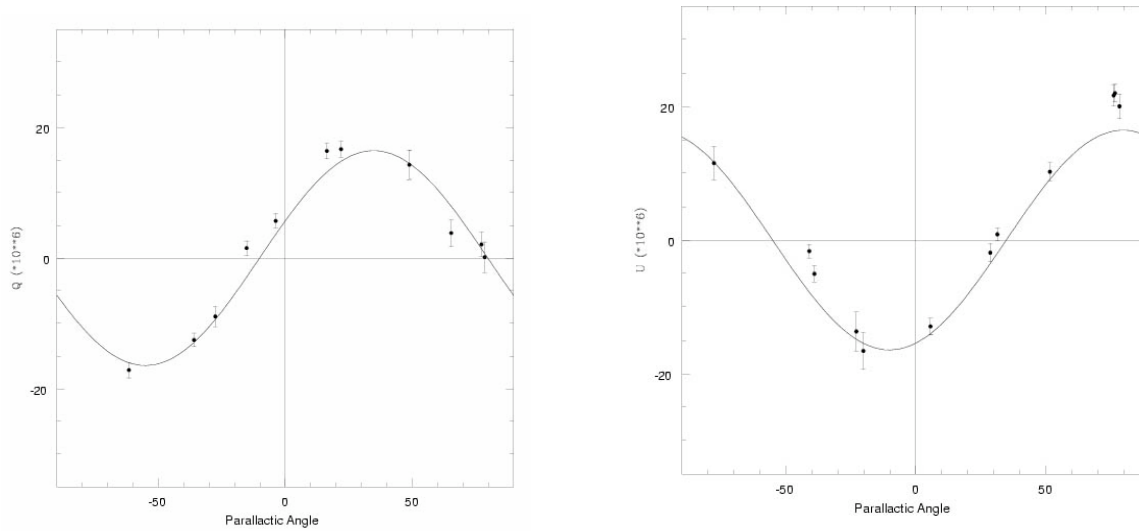


Figure 1.9: Telescope polarization of the 4.2-m William Herschel Telescope in La Palma, Spain, which is found to be $(16.4 \pm 0.4) \times 10^{-6}$. These plots are reproduced from Figure 6 of Hough et al. (2006b) by permission of PASP and the University of Chicago Press.

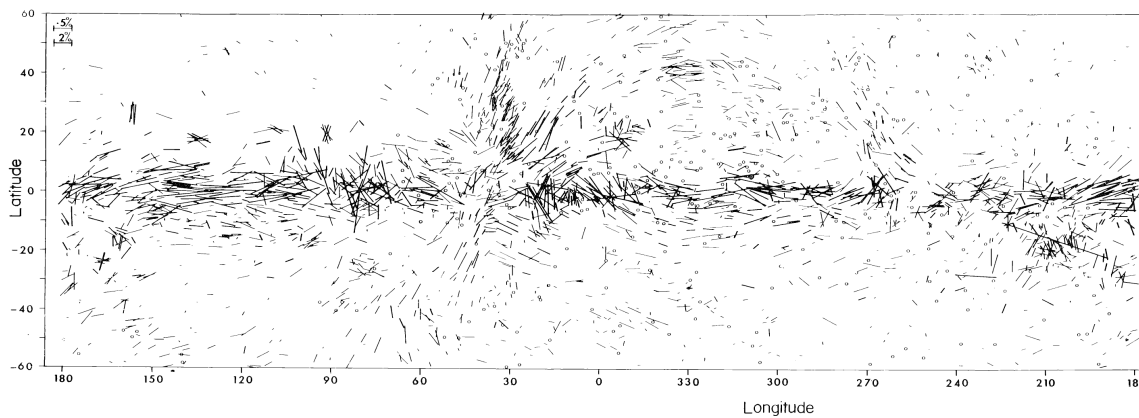


Figure 1.10: Interstellar polarization aligned to the galactic magnetic field, from Figure 1 of Mathewson & Ford (1970).

Here, P_{\max} is the maximum polarization as a function of wavelength and λ_{\max} is the wavelength of maximum polarization (Figure 1.11). Wilking et al. (1980) refined this relation further:

$$\frac{P(\lambda)}{P_{\max}} = \exp \left[-1.7\lambda_{\max} \ln^2 \left(\frac{\lambda_{\max}}{\lambda} \right) \right]. \quad (1.7)$$

The empirical relation of Serkowski et al. (1975) is predicted by the model of interstellar dust proposed by Li & Greenberg (1997). They model dust as cylinders with length to diameter ratio of two, which consist of a silicate core and an organic, refractory mantle. Indeed, Figure 1.12 shows a comparison between polarization predicted by such grains (solid line) and observed interstellar polarization (dotted line). The inset illustrates the prediction of the Li & Greenberg (1997) model of the circular polarization (dotted line) sign change at the wavelength of peak linear polarization (solid line), $\lambda = \lambda_{\max}$. Figure 1.13 shows the first observations of this effect by Kemp & Wolstencroft (1972).

Interstellar polarization represents a significant systematic effect that is difficult to calibrate. This is because observed polarization is the sum of the telescope, instrument, interstellar, and intrinsic polarization vectors. While telescope and instrument polarization may be calibrated, calibration of interstellar polarization is less straightforward. Additionally, the degree of interstellar polarization increases with distance to the target (Figure 1.14) because of the increased number of dust grains in the line of sight column (Mathewson & Ford 1970, Barrett 1996, Fosalba et al. 2002). Therefore, interstellar polarization is significant for almost all targets of interest. For imaging polarimetry, and other relatively low precision polarimetric investigations, one can consult polarization maps to determine the degree and position angle of polarization for stars near the target (Figure 1.10). The mean interstellar polarization in the neighborhood of the target can then be subtracted from the observed polarization of the target.

Four types of observations are generally used to separate the interstellar and intrinsic components of observed polarization: polarization versus wavelength, rotation of position angle with wavelength, circular polarization, and temporal variability. For objects whose polarization spectrum differs from the Serkowski et al. (1975) relation, it is likely that the difference is due to intrinsic polarization of the source. The wavelength of peak polarization λ_{\max} is comparable to the mean grain size along

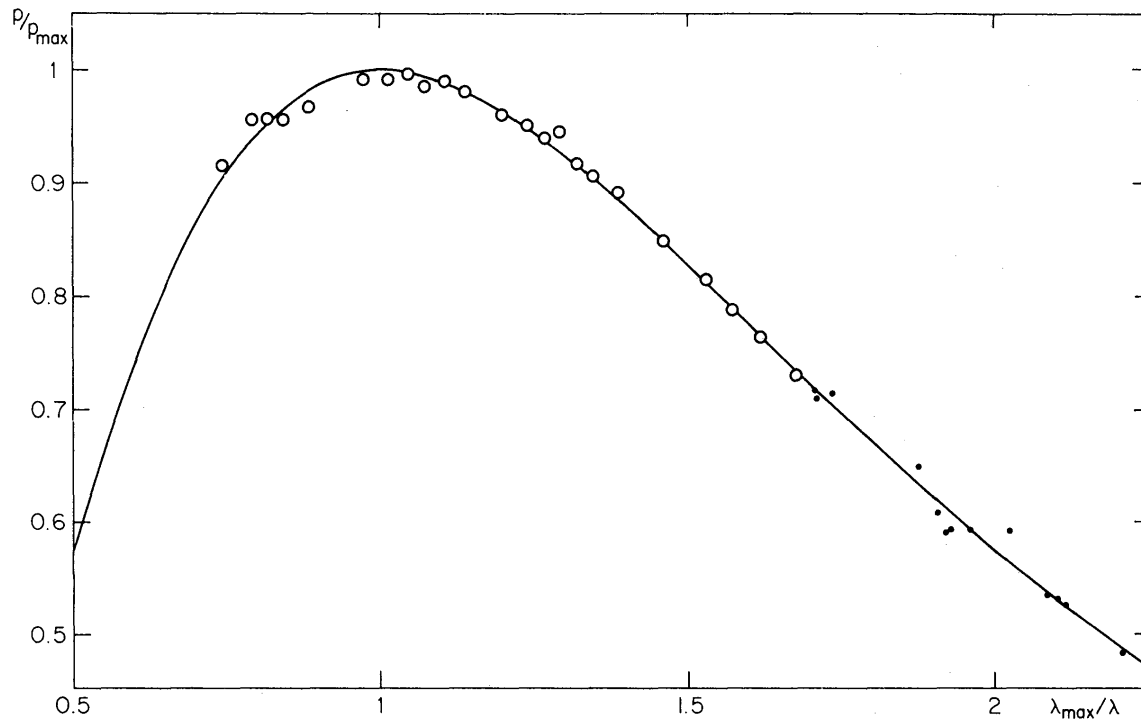


Figure 1.11: Empirical wavelength dependence of interstellar polarization from Equation 1.6. This figure is taken from Figure 3 of Serkowski et al. (1975).

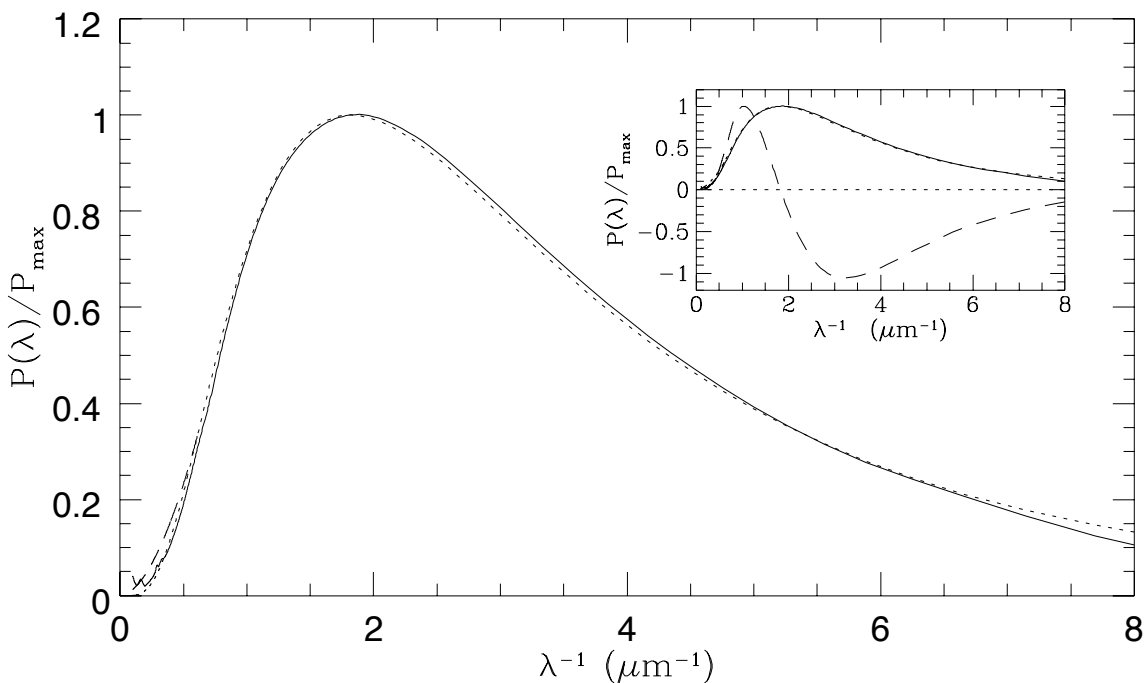


Figure 1.12: Theoretical wavelength dependence of interstellar polarization from Figure 4 of Li & Greenberg (1997). Note the agreement between theory (solid line) and observation (dotted line). The inset shows the reproduction of circular polarization (dashed line) sign change at the wavelength of linear polarization (solid line) maximum, $\lambda = \lambda_{\max}$.

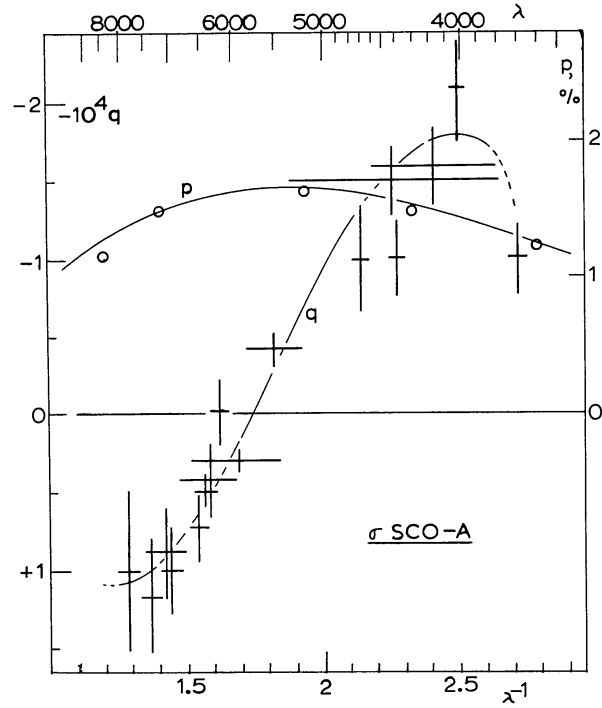


Figure 1.13: Observed circular polarization sign change near $\lambda = \lambda_{\max}$, labeled q , from Figure 1 of Kemp & Wolstencroft (1972). Linear polarization data, labeled p , are from Coyne & Gehrels (1966).

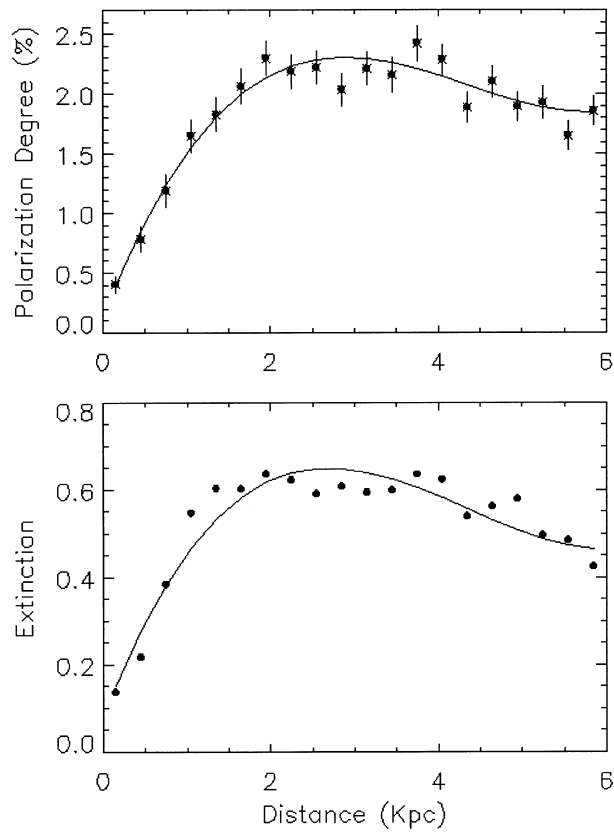


Figure 1.14: Increase in degree of interstellar polarization up to $d \approx 2$ kpc. Note the correlation of polarization with extinction. This figure is from Figure 3 of Fosalba et al. (2002).

the line of sight to the object. Therefore, if both grain size and orientation vary along the line of sight, the position angle of linear polarization will be a function of wavelength (Messinger et al. 1997, Whittet et al. 2001).

While both grain size and orientation must occur for interstellar polarization to generate a rotation of position angle with wavelength, only a change in grain orientation is required to generate circular polarization. This effect was predicted by van de Hulst (1957), and circular polarization of stars dominated by interstellar polarization was observed by Kemp (1972) and Kemp & Wolstencroft (1972). From theoretical modeling of polarization due to grains with varying orientation, Martin (1974) discovered that the handedness of interstellar circular polarization changes sign near the wavelength of peak linear polarization, confirming the observations of Kemp & Wolstencroft (1972).

Polarimetric variability of many stars is observed in high precision campaigns. It is assumed that variability on nightly timescales is indicative of intrinsic polarization, because the interstellar medium is not thought to be variable on those timescales. However, Walker (2007) observe lensing of the quasar Q0954+658 by an AU-sized, interstellar dust cloud $d \approx 500$ pc away from Earth (Figure 1.15). The timescale of this event is ≈ 100 days, with dramatic changes evident on a one week timescale. This shows that ISM variability is probably not important during an individual observing run, but it may be significant from run to run for strongly polarized sources.

Of the combination of the four types of observations listed above, polarimetric variability (linear, circular, or both) phase-locked to orbital or pulsational cycles is the strongest indicator of intrinsic polarization of the source. Additionally, deviation of polarization as a function of wavelength from Equation 1.6 indicates intrinsic polarization. For strongly polarized sources, with $P \approx 1\%$ or larger, rotation of polarimetric position angle with wavelength coupled with a lack of observed circular polarization may also indicate intrinsic polarization. This is because line of sight change in grain orientation is expected to convert linear polarization to circular polarization with $\approx 1\%$ efficiency (Martin 1974, Avery et al. 1975). Thus, intrinsic polarization of order 1% incident on a column of grains with varying orientation along the line of sight should generate detectable circular polarization of order one part in 10^4 .

Lack of circular polarization towards such a target could imply intrinsic Rayleigh scattering.

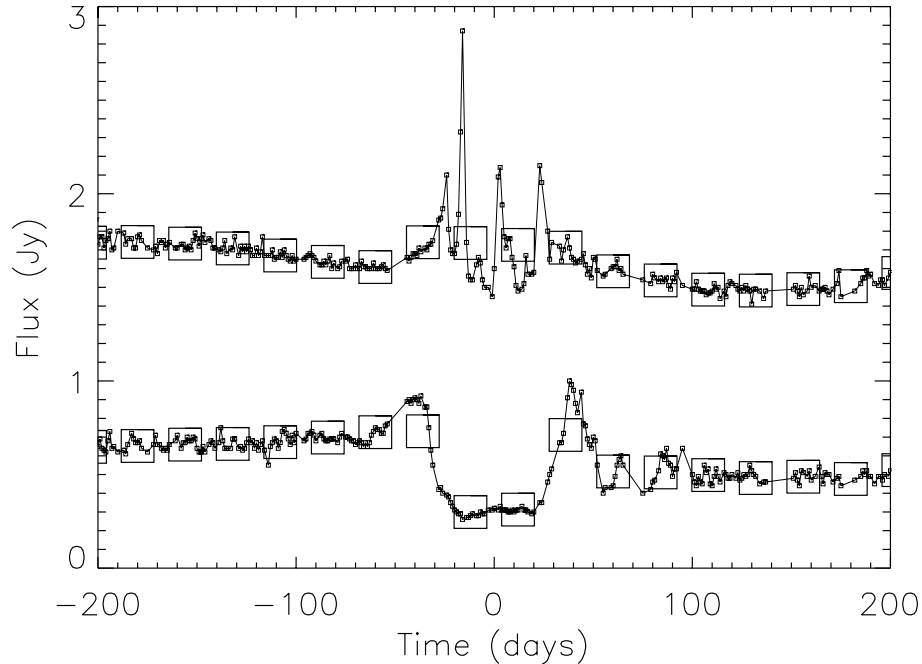


Figure 1.15: Scattering of quasar radio emission by an interstellar dust cloud. Boxes indicate binned observations over 24 day intervals. Top curve represents high frequency (8.1 GHz) observations, to which a 1 mJy vertical offset was applied. Bottom curve shows low frequency (2.7 GHz) monitoring of the event. Reprinted by permission from Walker (2007), Figure 2.

Rayleigh scattering occurs in neutral gas, which may be present in cool stars and accretion streams (Mason et al. 1974, Kallman & White 1982, White et al. 1983, Kitamoto et al. 1984). However, the gas density in the ISM is not significant to provide Rayleigh scattering of background starlight. The position angles of the intrinsic and interstellar polarization components will be different, so the superposition of intrinsic, Rayleigh scattering ($P \propto \lambda^{-4}$) and interstellar polarization (Equations 1.6 and 1.7) will cause a rotation of position angle with wavelength. For comparable degree of polarization between both components, the blue end of the optical spectrum will be dominated by intrinsic polarization while the red end will be dominated by interstellar polarization.

Conversely, the presence of circular polarization with a magnitude much higher than 1% of the degree of linear polarization implies an intrinsic source of circular polarization. Strong magnetic fields are thought to be the cause of such intrinsic circular polarization. This effect has been observed in Cepheid variables (Rudy & Kemp 1978) as well as in the high mass X-ray binary Cygnus X-1 (Michalsky et al. 1975a, b; Severny & Kuvshinov 1975; Michalsky & Swedlund 1977).

It is difficult to determine whether polarization of weakly polarized objects is intrinsic or due

to interstellar polarization, which is one of the major pitfalls of polarimetry. As will be seen later, I determine the position angle of net polarization of the γ Oph debris disk to be aligned with the major axis of the disk as observed by Spitzer. This is clear evidence for intrinsic polarization of the disk. Since geometric information about circumstellar disks is of great importance for star, disk, and planet formation/evolution scenarios, polarimetry is necessary to understand these objects. However, the role of interstellar polarization in the neighborhood of such objects is not always clear, and this can limit the contribution expected of polarimetry.

1.3.3 Intrinsic Polarization Variability

The hot Jupiter parent stars τ Boö (Walker et al. 2008), HD 179949 (Shkolnik et al. 2005, Shkolnik et al. 2007), and HD 189733 (Hébrard & Lecavelier des Etangs 2006, Croll et al. 2007, Winn et al. 2007, Pont et al. 2007, Shkolnik et al. 2007, Moutou et al. 2008) are known to have significant starspot activity, and some spots appear to corotate with the planet. Since starspots are associated with magnetic field activity, it is likely that they induce polarimetric variability at the orbital frequency. This has been observed in τ Boö with PlanetPol, where the planetary signal appears to be swamped by polarized starspots (Hough et al. 2006a). While observations both on and off spectral features may distinguish between starspots and the planet (Figure 1.5), the reduction in throughput will decrease the precision of the measurement. Thus, observations of light scattered by hot Jupiters likely requires 10-m class telescopes or larger.

The lack of true phase-locking observed in Cygnus X-1 (Wolinski et al. 1996) and other OB supergiant/compact object binaries (Dolan & Tapia 1984, 1988) is due to stochastic variability in the system. This may hamper accurate measurement of the orbital inclination with polarimetry. Indeed, it appears that co-adding the modulation from many orbits may not produce the mean state of the system. Thus, single-orbit observations may be necessary, which reduces the polarimetric precision that can be attained. As a proof of concept of the polarimetric technique, I commissioned a polarimeter on the Hale 5-m telescope. The goal of this instrument was to observe and characterize the polarimetric modulation of the Cygnus X-1 high mass X-ray binary. The next chapter describes the engineering and initial results from the instrument.

References

- Avery, R. W., Stokes, R. A., Michalsky, J. J., & Ekstrom, P. A. 1975, *AJ* 80, 1026.
- Barrett, P. 1996, *PASP* 108, 412.
- Biegging, J. H., Schmidt, G. D., Smith, P. S., & Oppenheimer, B. D. 2006, *ApJ* 39, 1053.
- Charbonneau, D., Brown, T. M., Latham, D. W., & Mayor, M. 2000, *ApJ* 529, L45.
- Coyne, G. V. & Gehrels, T. 1966, *AJ* 71, 355.
- Croll, B., Matthews, J. M., Rowe, J. F., Gladman, B., Miller-Ricci, E., Sasselov, D., Walker, G. A. H., Kuschnig, R., Lin, D. N. C., Guenther, D. B., Moffat, A. F. J., Rucinski, S. M., & Weiss, W. W. 2007, *ApJ* 671, 2129.
- Davis, L., Jr. & Greenstein, J. L. 1951, *ApJ* 114, 206.
- Deming, D., Seager, S., Richardson, L. J., & Harrington, J. 2005, *Nature* 434, 740.
- Dolan, J. F. & Tapia, S. 1984, *A&A* 139, 249.
- Dolan, J. F. & Tapia, S. 1988, *A&A* 202, 124.
- Fosalba, P., Lazarian, A., Prunet, S., & Tauber, J. A. 2002, *ApJ* 564, 762.
- González Delgado, D., Olofsson, H., Schwarz, H. E., Eriksson, K., Gustafsson, B., & Gledhill, T. 2003, *A&A* 399, 1021.
- Graham, J. R., Kalas, P. G., & Matthews, B. C. 2007, *ApJ* 654, 595.
- Grinin, V. P. 1994, in *The Nature and Evolutionary Status of Herbig Ae/Be stars*, ed. P. S. Thé, M. R. Pérez, & E. P. J. van den Heuvel, *ASP Conf. Ser.*, 62, 63.
- Grinin, V. P., Thé, P. S., de Winter, D., Giampapa, M., Rostopchina, A. N., Tambovtseva, L. V., van den Ancker, & M. E. 1994, *A&A* 292, 165.
- Hall, J. S. & Riley, L. A. 1976, *Icarus* 29, 231.
- Hébrard, G. & Lecavelier des Etangs, A. 2006, *A&A* 445, 341.
- Henson, G. D., Kemp, J. C., & Kraus, D. J. 1985, *PASP* 97, 1192.
- Hough, J. H., Lucas, P. W., & Bailey, J. A. 2006a, in *IAU Symp. 232, The Scientific Requirements of Extremely Large Telescopes*, ed. P. Whitelock, B. Leibundgut, & M. Dennefeld (Cambridge: Cambridge Univ. Press), 350.

- Hough, J. H., Lucas, P. W., Bailey, J. A., Tamura, M., Hirst, E., Harrison, D., & Bartholomew-Biggs, M. 2006b, *PASP* 118, 1302.
- Johnson, J. J. & Jones, T. J. 1991, *AJ* 101, 1735.
- Kallman, T. R. & White, N. E. 1982, *ApJ* 261, L35.
- Kemp, J. C. 1972, *ApJ* 175, L35.
- Kemp, J. C. & Wolstencroft, R. D. 1972, *ApJ* 176, L115.
- Kitamoto, S. & Miyamoto, S. 1984, *PASJ* 36, 731.
- Konacki, M. & Wolszczan, A. 2003, *ApJ* 589, 495.
- Knutson, H. A., Charbonneau, D., Allen, L. E., Fortney, J. J., Agol, E., Cowan, N. B., Showman, A. P., Cooper, C. S., & Megeath, S. T. 2007, *Nature* 447, 183.
- Li, A. & Greenberg, J. M. 1997, *A&A* 323, L566.
- Lovis, C., Mayor, M., Francesco, P., Yann, A., Benz, W., Bouchy, F., Correia, A. C. M., Laskar, J., Mordasini, C., Queloz, D., Santos, N. C., Udry, S., Bertaux, J.-L., & Sivan, J.-P. 2006, *Nature* 441, 305.
- Magalhães, A. M., Coyne, G. V., Codina-Landaberry, S. J., & Gneiding, C. 1986, *A&A* 154, 1.
- Martin, P. G. 1974, *ApJ* 187, 461.
- Mason, K. O., Hawkins, F. J., Sanford, P. W., Murdin, P., & Savage, A. 1974, *ApJ* 192, L65.
- Mathewson, D. S. & Ford, V. L. 1970, *Mem. RAS* 74, 139.
- Mayor, M. & Queloz, D. 1995, *Nature* 378, 355.
- Messinger, D. W., Whittet, D. C. B., & Roberge, W. G. 1997, *ApJ* 487, 314.
- Michalsky, J. J. & Swedlund, J. B. 1977, *ApJ* 212, 221.
- Michalsky, J. J., Swedlund, J. B., & Avery, R. W. 1975a, *Nature* 254, 39.
- Michalsky, J. J., Swedlund, J. B., & Stokes, R. A. 1975b, *ApJ* 198, L101.
- Moutou, C., Donati, J.-F., Savalle, R., Hussain, G., Alecian, E., Bouchy, F., Catala, C., Collier Cameron, A., Udry, S., & Vidal-Madjar, A. 2008, arXiv:0707.2016.
- Oudmaijer, R. D., Palacios, J., Eiroa, C., Davies, J. K., de Winter, D., Ferlet, R., Garzón, F., Grady, C. A., Cameron, A., Deeg, H. J., Harris, A. W., Horne, K., Merín, B., Miranda, L. F.,

- Montesinos, B., Mora, A., Penny, A., Quirrenbach, A., Rauer, H., Schneider, J., Solano, E., Tsapras, Y., & Wesseliuss, P. R. 2001, *A&A* 379, 564.
- Pont, F., Gilliland, R. L., Moutou, C., Charbonneau, D., Bouchy, F., Brown, T. M., Mayor, M.; Queloz, D., Santos, N., & Udry, S. 2007, *A&A* 476, 1347.
- Raveendran, A. V. & Rao, N. K. 1989, *A&A* 215, 63.
- Rudy, R. J. & Kemp, J. C. 1978, *MNRAS* 183, 595.
- Schmid, H. M., Joos, F., & Tschann, D. 2006, *A&A* 452, 657.
- Serkowski, K., Mathewson, D. S., & Ford, V. L. 1975, *ApJ* 196, 261.
- Severny, A. B. & Kuvshinov, V. M. 1975, *ApJ* 200, L13.
- Shkolnik, E., Walker, G. A. H., Bohlender, D. A., Gu, P.-G., & Kürster, M. 2005, *ApJ* 622, 1075.
- Shkolnik, E., Bohlender, D. A., Walker, G. A. H., & Collier Cameron, A. 2007, arXiv:0712.0004.
- Stam, D. M., Hovenier, J. W., & Waters, L. B. F. M. 2004, *A&A* 428, 663.
- Trammell, S. R., Dinerstein, H. L., & Goodrich, R. W. 1994, *AJ* 108, 984.
- van de Hulst, H. C. 1957, *Light Scattering by Small Particles* (New York: Wiley).
- Vink, J. S., Drew, J. E., Harries, T. J., Oudmaijer, R. D., & Unruh, Y. 2005, *MNRAS* 359, 1049.
- Walker, M. A. 2007, *ASP Conf. Ser.* 365, 299.
- Walker, G. A. H., Croll, B., Matthews, J. M., Kuschnig, R., Huber, D., Weiss, W. W., Shkolnik, E., Rucinski, S. M., Guenther, D. B., Moffat, A. F. J., & Sasselov, D. 2008, *A&A* 482, 691.
- White, N. E., Kallman, T. R., & Swank, J. H. 1983, *ApJ* 269, 264.
- Whittet, D. C. B., Gerakines, P. A., Hough, J. H., & Shenoy, S. S. 2001, *ApJ* 547, 872.
- Wilking, B. A., Lebofsky, M. J., Kemp, J. C., Martin, P. G., & Rieke, G. H. 1980, *ApJ* 235, 905.
- Winn, J. N., Holman, M. J., Henry, G. W., Roussanova, A., Enya, K., Yoshii, Y., Shporer, A., Mazeh, T., Johnson, J. A., Narita, N., & Suto, Y. 2007, *AJ* 133, 1828.
- Wolinski, K. G., Dolan, J. F., Boyd, P. T., Biggs, J. D., Nelson, M. J., Percival, J. W., Taylor, M., & van Citters, G. W. 1996, *ApJ* 457, 859.
- Wolszczan, A. & Frail, D. A. 1992, *Nature* 355, 145.
- Yudin, R. V. & Evans, A. 2002, *A&A* 391, 625.

Chapter 2

The POLISH Instrument

2.1 Introduction

While most astrophysical objects require many parameters in order to be fully described, black holes are unique in that only three parameters suffice: mass, spin, and charge. Mass and spin describe the black hole's gravitational field and event horizon location. Therefore, black holes provide a rare opportunity for theory and observation to jointly pursue two quantities to completely describe one of the most exotic kinds of objects in the Universe.

Though observational and modeling precision is somewhat effective in constraining black hole spin (McClintock et al. 2006), important constraints on black hole mass exist in the case of high mass X-ray binaries (hereafter HMXBs). These binaries consist of an O or B type supergiant and a black hole or neutron star. The most well-studied of these, Cygnus X-1, is thought to consist of a $40 \pm 10 M_{\odot}$, O9.7Iab star and a $13.5 - 29 M_{\odot}$ black hole at a distance of 2.2 ± 0.2 kpc (Ziólkowski 2005). While the constraints on the mass of the compact object are tight enough to declare that it is a black hole, they are insufficient to permit precise modeling of the progenitor star's mass. We have commissioned a polarimeter on the Hale 5-m telescope at Palomar Observatory in California to provide an independent method for determining black hole mass. This polarimeter has the potential to constrain the mass of the Cygnus X-1 black hole to a few solar masses.

¹The following paper is derived from this chapter: Wiktorowicz, S. J. & Matthews, K. 2008, PASP, 120, 1282.

2.2 Black Hole Mass from Polarimetry

A wealth of radial velocity data exists for Cygnus X-1 (Gies et al. 2003) and other HMXBs. However, in the same way that precise masses are elusive for non-transiting extrasolar planets, determination of precise black hole mass is hindered by unknown orbital inclination. This is evidenced by the end product of radial velocity observations, the so-called “mass function”. For Cygnus X-1, Gies et al. (2003) quote the following value:

$$f(M_X) = \frac{M_{\text{opt}} \sin^3 i}{q(1+q)^2} = 0.251 \pm 0.007 M_{\odot}. \quad (2.1)$$

Here, M_X is the mass of the black hole, M_{opt} is the mass of the visible binary component, i is the system inclination, and q is the mass ratio of the visible component to the black hole. Thus, an observational technique to constrain orbital inclination can take advantage of radial velocity data and offer an estimate of black hole mass.

Since system polarization is a geometric effect, the polarization of an HMXB system can be used to determine geometric information about the system, such as orbital inclination. The effective temperature of the supergiant in an HMXB is $T_{\text{eff}} \approx 30,000$ K, which is hot enough to ionize photospheric hydrogen. This causes a high density of free electrons that Thomson-scatter emitted light from the supergiant. While net linear polarization from a spherical cloud of free electrons is zero, asymmetry in the system causes net polarization. The tidal effects of the black hole cause such an asymmetry in the circumbinary envelope, and the orbital modulation of polarization is the key to determining orbital inclination. For instance, consider a face-on HMXB with zero eccentricity and an optically thin circumbinary envelope (Figure 2.1a). The total amount of observed polarized light is independent of orbital phase, and the degree of polarization is therefore constant. However, the angle of net polarization rotates as the binary progresses in its orbit.

In contrast, for a nearly edge-on geometry the degree of polarization varies significantly throughout the orbit, while the angle of net polarization is roughly constant (Figure 2.1b). Therefore, the modulation of the degree and angle of net polarization is a unique measure of orbital inclination for synchronously rotating HMXBs. Combining Equations 1 and 2 from Friend & Cassinelli (1986) and Equation 2 from Brown et al. (2000), the polarization of an axisymmetric envelope due to Thomson scattering is

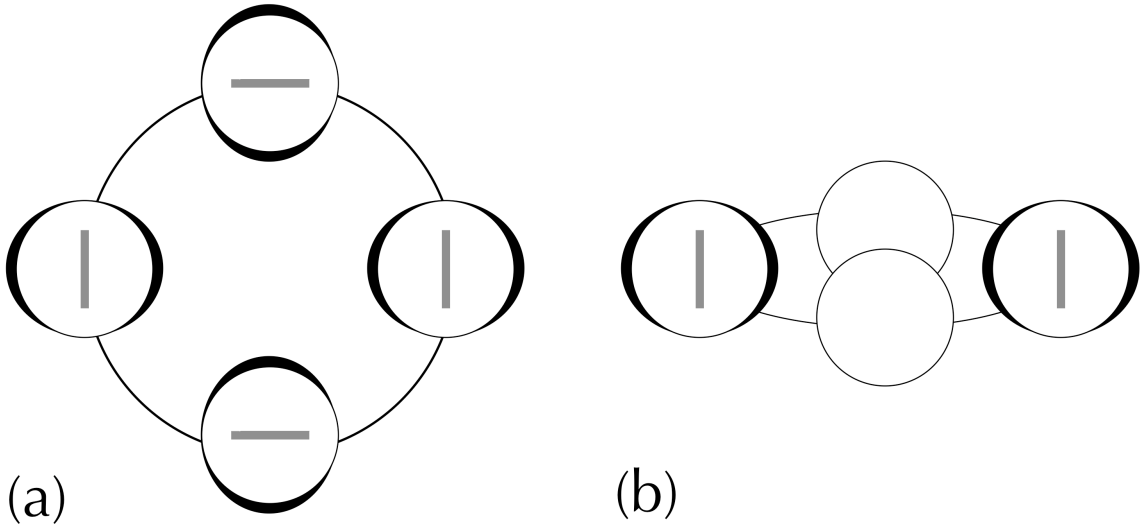


Figure 2.1: Orbital modulation of system polarization for HMXBs. The degree of polarization is represented by the black tidal bulges (the exact cause of polarization is irrelevant to this figure), and position angle of net polarization is given by the orientation of the grey lines. The face-on case is shown in (a), and the edge-on case is shown in (b). The circumbinary envelopes have been drawn displaced from the center of mass for clarity.

$$P = \frac{3}{16} \sigma_T (1 - \cos^2 \phi_{\text{orb}} \sin^2 i) \int_{r_1}^{r_2} \int_{\mu_1}^{\mu_2} n_e(r) \left(1 - \frac{R^2}{r^2}\right)^{\frac{1}{2}} (1 - 3\mu^2) dr d\mu. \quad (2.2)$$

Here, stellar radius is R , the electron number density is $n_e(r) = n_o R^2 / r^2$, system inclination is i , and orbital phase in radians is ϕ_{orb} . Two polarization periods occur per orbital period, because of the $\cos^2 \phi_{\text{orb}}$ term.

This technique has been utilized by a few groups (Kemp et al. 1979, Dolan & Tapia 1989, Wolinski et al. 1996), and Cygnus X-1 has been found to have variable polarization of order $\Delta P \approx 0.1\%$ of its unpolarized flux. However, measurement precision from the above groups is of order one part in 10^4 . The derived inclination estimates were questioned by the community (Milgrom 1979, Aspin et al. 1981) on the grounds that significant underestimation of error occurred because of limited measurement precision. Measuring inclination to 5° requires polarimetric precision of one part in 10^4 to one part in 10^7 (Aspin et al. 1981), depending on system inclination. This requires at least 10^8 to 10^{14} detected photons, which necessitates the use of 4-m class telescopes. Since our system combines a high precision instrument with a 5-m telescope, we aim to measure the polarimetric variability of Cygnus X-1 to better than one part in 10^4 .

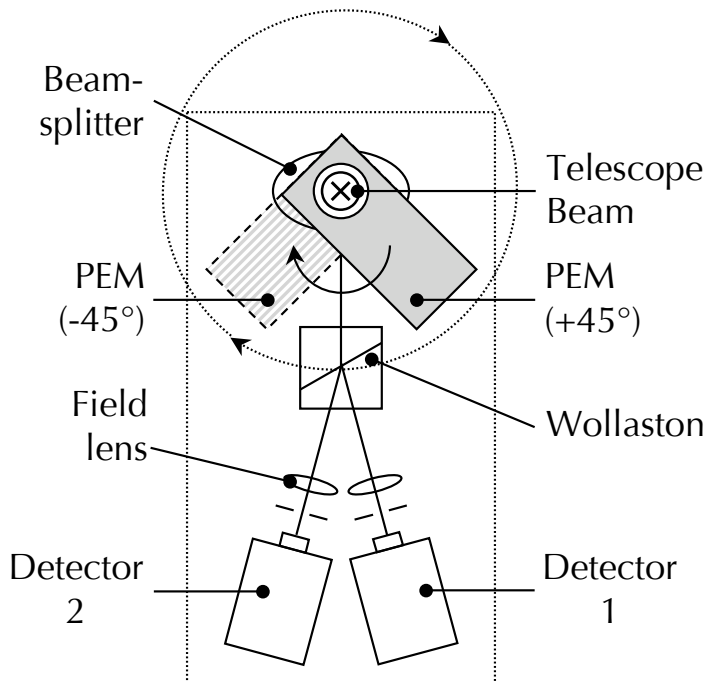


Figure 2.2: Plan view of the POLISH optical path. The telescope beam is directed into the page through the center of the PEM aperture (the “X” in the figure). The PEM is rotated to $\theta_{\text{PEM}} = \pm 45^\circ$ with respect to the centerline, and the instrument itself (dotted box) can be independently rotated on the telescope through $\Delta\phi = 360^\circ$. Field stops are located between the field lenses and detectors.

2.3 The Polarimeter

Polarimeters require the following fundamental components: a polarization modulator, analyzer, detector, and demodulator. The modulator induces a known, periodic characteristic to the unknown polarization of the input beam. The analyzer converts modulation in polarization to modulation in the beam’s intensity, since most detectors are sensitive to intensity and not polarization. Finally, the demodulator extracts the component of the detector’s output that varies at the known frequency of the modulator to reject noise. See Figure 2.2 for a block diagram, Figure 2.3 for a ray trace diagram, and Figure 2.4 for photographs of the instrument.

Traditionally, the modulator is a rotating halfwave plate that rotates the linear polarization of the incident beam. The highest modulation frequency attainable with this component is of order 100 Hz, which is not fast enough to freeze out atmospheric turbulence or to mitigate electronic $1/f$ noise. Additionally, inhomogeneity in both the retardance and cleanliness of the plate can introduce spurious signals, because the beam samples different sections of the halfwave plate at different times. The polarization goal for our instrument, POLISH (POLarimeter for Inclination Studies of

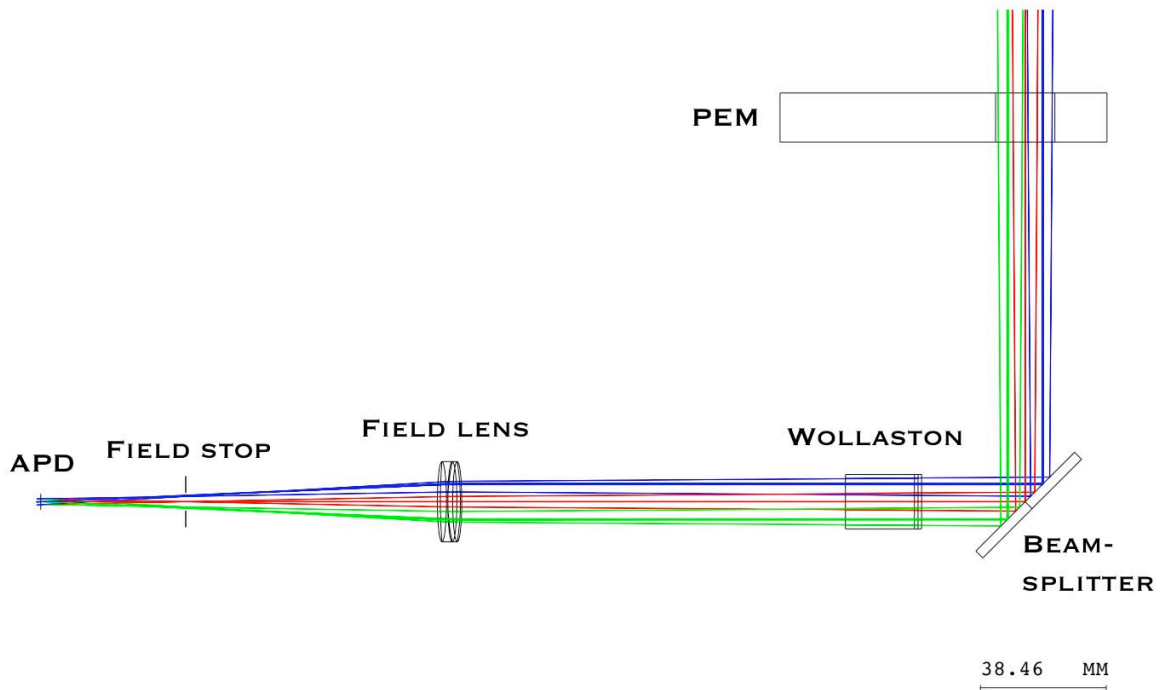


Figure 2.3: Ray trace diagram of the POLISH optical path. The telescope beam enters the instrument from the top right of the figure.

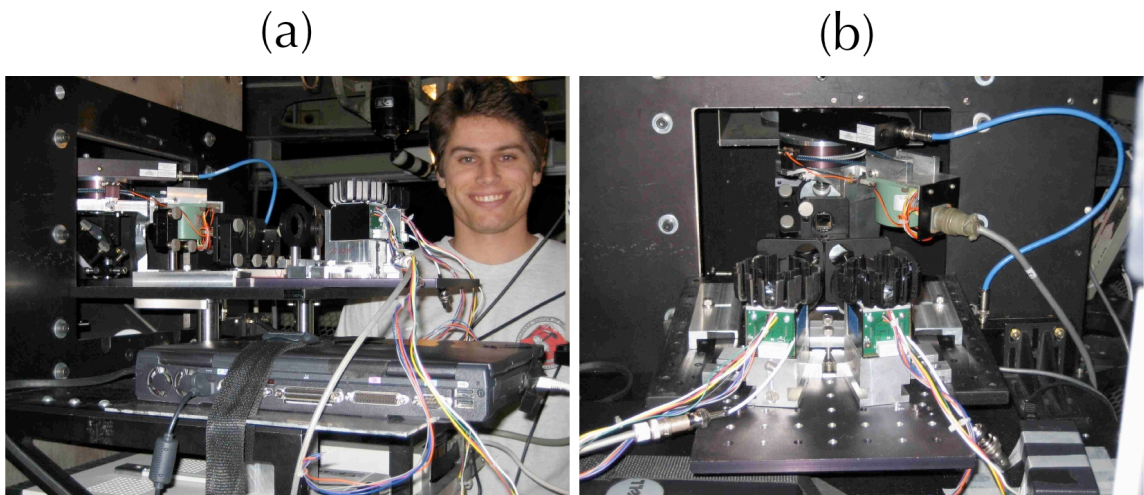


Figure 2.4: Photographs of the POLISH instrument, mounted at Cassegrain focus of the Hale 5-m telescope.

High mass x-ray binaries/Hot Jupiters), is one part per million on bright, unpolarized stars, which necessitates the use of a photoelastic modulator (hereafter PEM; see Kemp 1969).

A PEM is a bar of optical materials (fused silica for use in optical light) in which a resonant acoustic signal at frequencies of tens of kilohertz is induced. The stress-birefringent property of the silica causes time-varying, sinusoidal retardance of the component of polarization oriented at $\pm 45^\circ$ with respect to the compression/extension axis, while the polarization components at 0° and 90° with respect to that axis experiences no retardance. For example, a PEM at $\theta_{\text{PEM}} = \pm 45^\circ$ with respect to the Stokes Q axis will cause retardance to the Q/I Stokes parameter but not to the U/I parameter. Since peak retardance is a function of the amplitude of the acoustic signal, both peak retardance and wavelength of peak retardance can be easily modified. We set the retardance amplitude to $\beta_0 = 0.383$ waves at 500 nm wavelength to give uniform PEM efficiency for both low and high linear polarizations. This also causes linear polarization to be directly proportional to the amplitude of the AC signal divided by the mean DC signal, which is derived in Appendix B.

The high frequency of PEM modulation strongly reduces both atmospheric turbulence and electronic $1/f$ noise. Additionally, the beam always samples the same optical path during the modulation, because the strain on the modulator element is only of order ten parts per million (Kemp 1969). Operationally, a PEM is the opposite of a rotating halfwave plate: while the plate has a constant retardance and time-variable fast axis orientation, a PEM has constant fast axis orientation but time-variable retardance. Since the absolute value of the PEM's retardance determines the polarization of the beam at any instant, compression and extension of the fused silica bar affect the beam identically. Therefore, linear polarization is modulated at twice the frequency of the PEM modulation. We use the I/FS50 PEM and PEM100 controller from Hinds Instruments, Inc. The modulation frequency of this PEM is 50 kHz, and modulation of linearly polarized light occurs at 100 kHz.

Directly downstream from the PEM is a 95R/5T beamsplitter at 45° incidence that allows $\approx 5\%$ of the stellar flux to fall on a Xybion CCD camera for guiding, while the remaining $\approx 95\%$ is reflected into a Wollaston prism toward the detectors. The beamsplitter has a 50-mm diameter, fused silica substrate from Edmund Optics with a custom 400 to 700 nm coating from Opticorp, Inc. The surface accuracy on the substrate is one-tenth of a wavelength.

We utilize a two-wedge, calcite Wollaston prism from Karl Lambert, Inc., as our analyzer. This prism separates each component of a single Stokes parameter into two beams. That is, the $+Q/I$ (or $+U/I$) component is split into one beam, and the $-Q/I$ (or $-U/I$) component is in the other beam. Both beams have equal deviation of 7.5° from the optical axis, which allows the optical layout to be symmetric with respect to the optical axis. A two-wedge prism is used because the larger beam deviation of a three-wedge design would cause the instrument package to be larger than necessary. The surfaces of the Wollaston prism have an antireflection coating in the wavelength range 400 to 700 nm. The transmission in V band is $\approx 97\%$ per surface. By injecting light through a linear polarizer with known fast axis orientation and then through the Wollaston prism, we find that the left beam seen from downstream is vertically polarized ($-Q/I$ when projected onto the sky for a Cassegrain ring angle of 0°). The right beam is horizontally polarized ($+Q/I$ at 0° ring angle).

Each Wollaston beam then impinges on an $f/5.6$, MgF_2 antireflection-coated field lens from Melles Griot. These lenses image the telescope secondary mirror onto the detectors, and they ensure starlight is uniformly spread over the detector active area even in the presence of image wander. Field stops are located in the image plane, after the field lenses, but these are not currently used because contamination of stellar polarization from the sky field is not significant. The beams reach the detectors with a diameter of ≈ 3 mm, which underfills all detectors.

Since Cygnus X-1 has V magnitude ≈ 9 , but the polarization standard stars we observe can be as bright as $V \approx 3$, POLISH has two interchangeable pairs of detectors. Stars fainter than $V \approx 7$ are detected at a higher signal to noise ratio with the pair of Hamamatsu H9307-04 photomultiplier tubes (PMTs), while objects brighter than this will destroy the PMTs. The brighter stars are observed with custom-made Advanced Photonix SD197-70-72-661 (red enhanced) and SD197-70-74-661 (blue enhanced) avalanche photodiode modules (APDs). The high quantum efficiency of APDs is desirable on bright stars to minimize photon shot noise, while the low dark current of PMTs is desirable on fainter stars to minimize detector noise.

Since these detectors are not downstream from spectral filters, they are integrated light detectors in both spatial and spectral senses. Spatial resolution is unnecessary, as the angular size of the Cygnus X-1 system is much smaller than the atmospheric seeing disk. Spectral resolution, while desirable, would seriously degrade the precision attainable with this instrument. Such resolution must be left for future generations of POLISH. The instrumental throughput is calculated to be

74%, 77%, 58%, and 23% in B , V , R , and I bands. The throughput of the telescope/instrument system is calculated to be 60%, 62%, 47%, and 19% in those bands.

The PMTs are identical, side-on modules with active area dimensions 3.7×13.0 mm. Their quantum efficiencies are quoted from the manufacturer to be 18%, 15%, 7%, and 0% in B , V , R , and I bands. The PMT gain can be set by a potentiometer, and we set this gain to $G = 5 \times 10^6$ for all observations. The modules also have a $B = 200$ kHz bandwidth amplifier with transimpedance $T_A = 10^5$ V/A. The quoted output noise voltage resulting from dark current is $\sigma'_V = 10$ (typical) to $100 \mu\text{V}$ (maximum), which implies a noise equivalent power of $\text{NEP} = 0.04$ to 0.13 fW/ $\sqrt{\text{Hz}}$. Dark current is $i'_d = 0.1$ nA.

The APDs are custom-built from Advanced Photonix, Inc., and have 5 mm diameter, circular active areas. Customization of the APDs allowed lower noise at the frequency of linear polarization modulation. The APDs are not identical, as one beam is sampled by the red enhanced module while the other is sampled by the blue enhanced one. The quantum efficiencies for the red enhanced module are quoted as 24%, 62%, 88%, and 75% in B , V , R , and I bands. The blue enhanced module is quoted to have 75%, 82%, 67%, and 35% quantum efficiencies. The blue module operates at a quoted gain of $G = 300$, and the red module operates with an observed gain of $G = 220$. Transimpedance is $T_A = 4 \times 10^6$ V/A for both modules, and amplifier bandwidth is $B = 100$ kHz for the red enhanced and $B = 90$ kHz for the blue enhanced modules. After the APD chip is thermoelectrically cooled to 0° C, dark current is measured to be $i'_d = 4.5$ nA and 3.5 nA at the output of the red and blue modules, respectively. Therefore, the noise equivalent power for each module is $\text{NEP} = 39$ fW/ $\sqrt{\text{Hz}}$ and 9.7 fW/ $\sqrt{\text{Hz}}$, respectively. Each detector is supplied $\pm 12\text{V}$ and $+5\text{V}$, and a 12V case fan blows heat from the APD heat sinks to keep current draw stable.

The demodulator picks out the component of the detected signal that varies at the reference frequency and ideally rejects signals at all other frequencies. The demodulator can either be software or hardware; POLISH makes use of one Stanford Research SR830 digital, dual-phase lock-in amplifier for each detector. The PEM controller sends a square wave reference signal to the lock-in amplifiers at twice the frequency of the PEM modulation, and each lock-in amplifier recovers X (in phase with reference signal) and Y (90° out of phase with the reference signal) components of the detector signal. Together, X and Y determine amplitude R and phase Φ of the detector signal whose modulation frequency is the same as the reference.

Table 2.1: Stokes Parameters Given by Positive AC Phase

Cassegrain angle ($^{\circ}$)	Left Beam (Detector 2)	Right Beam (Detector 1)
0	$-Q/I$	$+Q/I$
45	$-U/I$	$+U/I$
90	$+Q/I$	$-Q/I$
135	$+U/I$	$-U/I$
180	$-Q/I$	$+Q/I$
225	$-U/I$	$+U/I$
270	$+Q/I$	$-Q/I$
315	$+U/I$	$-U/I$

$$R = \sqrt{2(X^2 + Y^2)} \quad (2.3a)$$

$$\Phi = \frac{1}{2} \arctan(Y, X) \quad (2.3b)$$

The lock-in amplifiers record the RMS components of the in-phase and quadrature phase signals, so multiplication by a factor of $\sqrt{2}$ is necessary to determine the amplitude of the AC signal. The notation of the argument of the arctangent is meant to account for signs of X and Y when determining phase.

Signal phase allows direct measurement of the sign of each Stokes parameter ($+Q/I$ versus $-Q/I$, for instance). This is important, because insensitivity to sign would preclude direct measurement of more than 90° of rotation of the Cygnus X-1 system. By placing a linear polarizer with known axis orientation in front of the PEM, we have determined the Stokes parameter sampled by each beam as a function of Cassegrain ring angle. See Table 2.1 for a list of parameters measured for positive AC phase.

Both AC and DC signals from the detector must be recorded to measure polarization (Appendix B). The AC signals are recorded by the lock-in amplifiers, and each detector's DC signal is recorded by a separate HP 34401A digital voltmeter. The time constant and sampling frequency of the lock-in amplifiers, as well as the sampling frequency of the voltmeters, must be chosen with care. To reject 60 Hz noise and its harmonics, each DC reading by the voltmeters consists of an integration over 10 power line cycles. Thus, the voltmeters record data at 6 Hz. The lock-in amplifiers may only

sample the AC signal at powers of two in frequency, so we choose to record the AC data at 8 Hz. The discrepancy in sampling rates between AC and DC data is not important, because AC data should be normalized by *mean* DC data and not in a point-by-point fashion.

In order to Nyquist sample the AC data, we set the lock-in time constants to 30 ms. For the steepest filter rolloff, 24 dB/octave, the effective noise bandwidth is given by $ENBW = 5/(64\tau)$, where τ is the lock-in amplifier’s time constant. For a time constant of 30 ms, $ENBW = 2.6$ Hz. Therefore, we sample the AC data $8/2.6 \approx 3.1$ times per effective time constant, which both satisfies the Nyquist criterion and reduces aliasing. The lock-in amplifiers therefore measure the component of the AC signal that varies in the frequency range $f_0 (1 \pm 1.3 \times 10^{-5})$, where f_0 is the reference frequency. The auxiliary DC output of one lock-in amplifier is connected to a chopping motor on the telescope secondary mirror. This lock-in amplifier sends a voltage signal to the secondary mirror chopping motor, which causes the secondary mirror to chop north to a sky field for sky subtraction of both AC and DC data.

POLISH is located at Cassegrain focus to ensure beam reflections of $\approx 180^\circ$. In addition, the instrument resides at the $f/72$ focus. Both of these steps minimize telescope polarization. To minimize instrument polarization, the first optic the beam encounters after the telescope secondary mirror is the PEM. The lock-in amplifiers and voltmeters are controlled by a laptop, which is mounted to the instrument, via the GPIB interface. Matlab R2006a from The MathWorks, Inc., is used to control the voltmeters and lock-in amplifiers, chop the secondary mirror, and rotate the Cassegrain ring to allow access to both linear Stokes parameters.

2.4 Observing Strategy

A similar, albeit larger, instrument called PlanetPol is mounted on the 4.2-m William Herschel Telescope in La Palma, Spain (Hough et al. 2006, hereafter HLB 06). The goal of this instrument is to detect the modulation of linear polarization caused by stellar flux scattered by hot Jupiters. This observation requires polarimetric precision of one part per million to one part in ten million, which is a precision barely achievable with PlanetPol. We observed many of the polarized and “unpolarized” standard stars from HLB 06 in addition to others from the combined polarimetric catalogs of Heiles (2000). A list of the stars observed is given in Table 2.2, and polarization values in parenthesis rep-

Table 2.2: Observed Standard Stars

Name	Alt. Name	RA	Dec	P	Θ ($^{\circ}$)	Ref ^a	V	Type
Algenib ^b	γ Peg	00 13 14.23	+15 11 00.9	$630(10) \times 10^{-6}$	118.1(5)	1	2.83	B2IV
HD 7927	ϕ Cas	01 20 04.92	+58 13 53.8	3.232(53)%	94.0(5)	1	5.01	F0Ia
HD 9270	η Psc	01 31 29.07	+15 20 44.8	$60(30) \times 10^{-6}$	158(14)	1	3.63	G7IIa
HR 5854	α Ser	15 44 16.07	+06 25 32.3	$4.3(1.0) \times 10^{-6}$	—	2	2.64	K2IIIb
HD 147084	σ Sco	16 20 38.18	-24 10 09.6	3.490(35)%	32.1(3)	1	4.55	A4II/III
HD 154445	SAO 141513	17 05 32.24	-00 53 31.7	3.420(24)%	90.2(2)	1	5.64	B1V
u Her ^c	HD 156633	17 17 19.57	+33 06 00.4	0.0(2)%	—	1	4.80	B1.5Vp+
γ Oph ^d	HD 161868	17 47 53.56	+02 42 26.3	$80(10) \times 10^{-6}$	33.3(3.6)	1	3.75	A0V
HD 157999	σ Oph	17 26 30.98	+04 08 25.1	1.010(35)%	85.9(1.0)	1	4.34	K3Iab
HD 187929 ^e	η Aql	19 52 28.37	+01 00 20.4	1.685(3)%	94.2(1)	2	3.5 - 4.3	(F6.5-G2)1b
HD 204827	SAO 33461	21 28 57.70	+58 44 24.0	5.44(20)%	59.0(1.1)	1	8.00	O9.5V
HD 212311	SAO 34361	22 21 58.55	+56 31 52.8	0.02(5)%	—	1	8.12	A0V
ζ Peg	HD 214923	22 41 27.74	+10 49 52.9	$100(30) \times 10^{-6}$	138.0(8.5)	1	3.40	B8V
HR 8974 ^f	γ Cep	23 39 20.85	+77 37 56.2	$5.2(2.2) \times 10^{-6}$	130(25)	2	3.23	K1IV

^a1—Heiles (2000), 2—HLB 06

^b β Cepheid, pulsator

^c β Lyrid, eclipsing binary

^dDebris disk

^e δ Cepheid, pulsator

^fExtrasolar planet host

resent the 1σ uncertainty in the mean value. V band magnitude and spectral type for the δ Cepheid star HD 187929 (η Aql) are from Bastien et al. (1988) and Oke (1961), respectively. The spectral type of HD 212311 is from Schmidt et al. (1992). All other positional and spectral information is from the SIMBAD database. Observations of Cygnus X-1 itself are detailed in Chapter 4.

After the target star is acquired, a scan of 15 seconds is initiated on both voltmeters simultaneously with a scan of about 30 seconds on both lock-in amplifiers. For the second half of the 30 second lock-in amplifier scans, the voltmeters transmit data to the laptop. For sky subtraction, the telescope secondary mirror chops 25 arcsec north with respect to the target star. Another set of voltmeter and lock-in amplifier scans is then started. After this has completed, the target star is returned to the field of view and another set of scans begins. An integration “triplet” is defined to be an on-source, 30 second AC integration scan and a 15 second DC integration scan both before and after the same scan on a sky field. Sky levels in the optical are expected to be very small compared to target star levels, so sky fields are observed with an asymmetric, 2:1 source to sky chop. See Figure 2.5 for a typical AC and DC measurement of the “unpolarized” HR 5854, and see Figure 2.6 for the strongly polarized HD 204827. The increase in AC level, and therefore in polarization, between HR 5854 and HD 204827 is striking. The LED pulses from the laptop controlling the instrument can be seen to contaminate the DC data for HD 204827, which was observed with the PMTs. Rejection of these pulses is discussed in section 2.5.1.

Since two light beams with perpendicular polarization orientations experience the same retar-

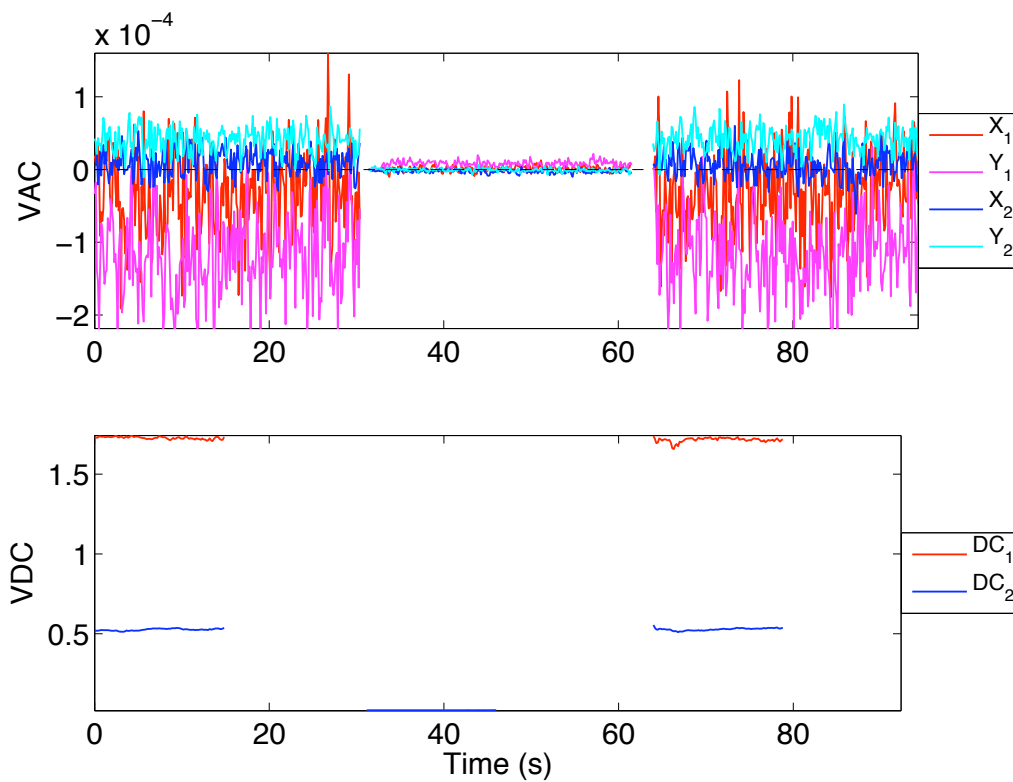


Figure 2.5: Typical raw AC and DC data for the unpolarized star HR 5854. The subscripts on X , Y , and DC indicate data for detectors 1 and 2.

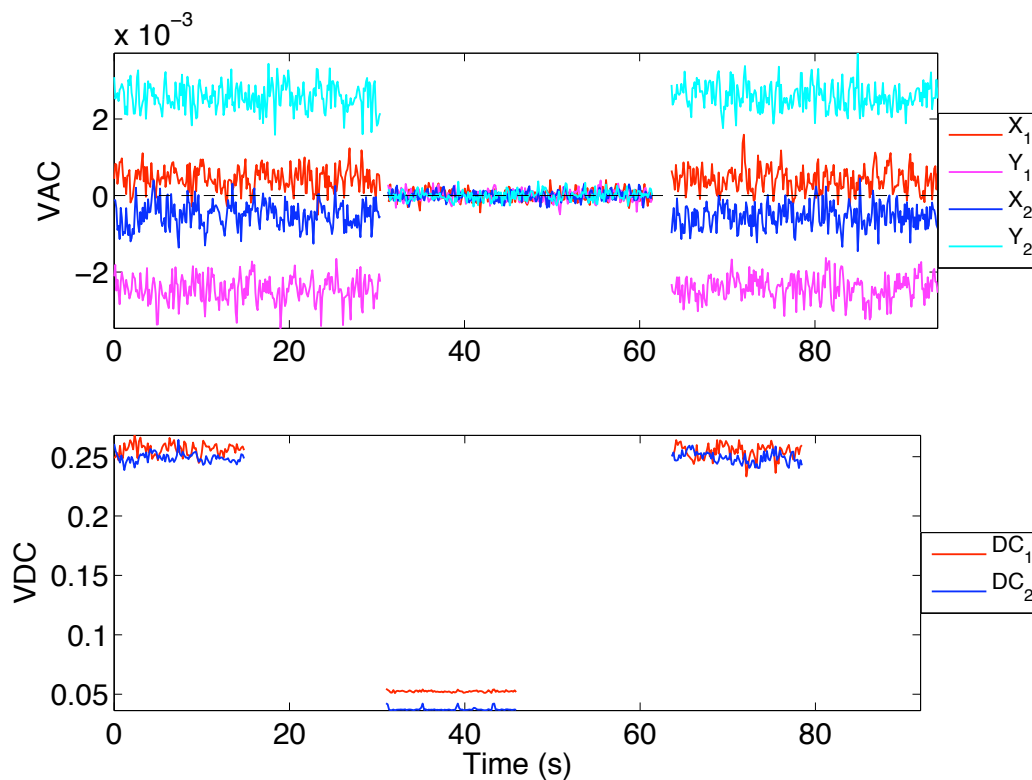


Figure 2.6: Typical raw data for the strongly polarized star HD 204827.

dance when passed through the PEM, the same polarization should be observed for the PEM at $\theta_{\text{PEM}} = \pm 45^\circ$ with respect to the optical axis of the instrument. We rotate the PEM between these two positions to investigate the systematics of the PEM. The PEM is mounted to a gear driven by a stepper motor with an 8:1 step ratio, where the center of the PEM aperture is coincident with the rotation axis of the gear. Each motor step corresponds to a rotation of the PEM by $\Delta\theta_{\text{PEM}} = 0.1125^\circ$. For a Cassegrain ring angle of $\phi = 0^\circ$, the home position of the PEM projects its compression/extension axis northeast onto the sky (the $+U$ direction). This will be referred to as the “PEM $+45^\circ$ ” position. The “PEM -45° ” position causes this projection to be northwest on the sky (the $-U$ direction).

Rotation of a polarized beam follows a $\cos(2\theta)$ profile, so we rotate the Cassegrain ring and instrument through $\Delta\phi = 360^\circ$ to investigate the systematics of the rotation. The precision of the Cassegrain ring angle is 0.1° . A standard observing sequence begins with the Cassegrain ring at $\phi = +180^\circ$ and an integration triplet at the PEM $+45^\circ$ position followed by a triplet at the PEM -45° position. The ring angle is then decremented by $\Delta\phi = 45^\circ$, at which point a PEM -45° triplet and PEM $+45^\circ$ triplet are taken. This process occurs for each target star for Cassegrain ring angles of $+180^\circ > \phi > -180^\circ$ in $\Delta\phi = 45^\circ$ increments to sample all $\pm Q/I$ and $\pm U/I$ Stokes components. The next star will see the ring angles begin at $\phi = -180^\circ$ and end at $\phi = +180^\circ$. The endpoints of $\phi = \pm 180^\circ$ ensure that the ring will not “wind up” and be forced to de-rotate during an observing sequence, wasting observing time. After each triplet, either the PEM or Cassegrain ring is rotated but not both. Each standard star is generally given eight Cassegrain ring rotations ($\Delta\phi = 360^\circ$) at two PEM positions each ($\theta_{\text{PEM}} = \pm 45^\circ$), and two chop integrations are taken at each PEM position. Thus, most standard stars receive about 16 minutes of AC data and about 8 minutes of DC data per night.

2.5 Data Reduction

2.5.1 Polarization and Noise Calculations

Mean X , Y , and DC values for each detector are found for all on-source and sky scans. The mean on-source values are then subtracted by the mean sky values. Assuming Stokes Q/I is observed, the polarization is calculated by the following (Appendix B):

$$\frac{Q_{\text{obs}}}{I_{\text{obs}}} = \frac{\sqrt{2}}{E_{\text{PEM}}} \frac{\sqrt{(X_{\text{src}} - X_{\text{sky}})^2 + (Y_{\text{src}} - Y_{\text{sky}})^2}}{\text{DC}_{\text{src}} - \text{DC}_{\text{sky}}}. \quad (2.4)$$

The efficiency of the PEM, E_{PEM} , is the strength of the AC signal based on the choice of PEM peak retardance, and it is derived in Appendix B. For POLISH, this efficiency is $E_{\text{PEM}} \approx 86\%$. The sign of the final polarization of each on-source scan is multiplied by the sign of the Stokes parameter measured, as given by Table 2.1. That is, the sign of the calculated Stokes parameter is calibrated by the phase from the lock-in amplifiers (Equation 2.3b).

Expected photon shot noise, detector noise, and observed noise are derived in Appendix C as Equations C11 and C12a through C12c:

$$\sigma_{P_{\text{shot}}} = \frac{\gamma_0 \sqrt{2}}{E_{\text{PEM}} \text{DC}} \left\{ \frac{1}{t_{\text{AC}}} \left[B_{\text{AC}} + \frac{1}{2} \min(B_{\text{max}}, B) (E_{\text{PEM}} P)^2 \right] \right\}^{\frac{1}{2}} \quad (2.5a)$$

$$\sigma_{P_{\text{detector}}} = \frac{\gamma \sqrt{2}}{E_{\text{PEM}} \text{DC}} \left\{ \frac{1}{t_{\text{AC}}} \left[B_{\text{AC}} + \frac{1}{2} \min(B_{\text{max}}, B) (E_{\text{PEM}} P)^2 \right] \right\}^{\frac{1}{2}} \quad (2.5b)$$

$$\sigma_{P_{\text{obs}}} = \frac{\sqrt{2}}{E_{\text{PEM}} \text{DC}} \left\{ \frac{1}{t_{\text{AC}}} \left[\frac{X^2 \sigma_X^2 + Y^2 \sigma_Y^2}{X^2 + Y^2} + \frac{1}{2} (E_{\text{PEM}} P \sigma_{\text{DC}})^2 \right] \right\}^{\frac{1}{2}} \quad (2.5c)$$

$$B_{\text{max}} = \left(\frac{\text{DC}}{eGT_A} \right)^{\frac{1}{2}}. \quad (2.5d)$$

Here, $\gamma_0 \equiv 2eGT_A \text{DC}$, $\gamma \equiv 2eG^{1+x} T_A (\text{DC} + i'_d T_A)$, e is the electron charge, $B_{\text{AC}} \approx 2.6$ Hz is the bandwidth of the lock-in amplifiers, and t_{AC} is the integration time of the lock-in amplifiers (Figures 2.5 and 2.6). The values i'_d , x , B , G , and T_A are the detector's output dark current, excess noise factor, bandwidth, gain, and transimpedance, which are listed in Table 2.3. A perfect detector will have noiseless gain, $x = 0$, and dark current $i'_d = 0$. Each of the uncertainties $\sigma_{X,Y,\text{DC}}$ represents the sample standard deviation of X , Y , or DC of the source added in quadrature to that of the sky. The values X , Y , and DC in Equation 2.5c are sky-subtracted.

Short pulses can be seen in the DC data taken with the PMTs (see detector 2 data in Figure 2.6). These pulses have been traced to scattered light from LEDs mounted in the laptop controlling the instrument. They are easily removed by subtracting off any linear trend in a DC scan and then

Table 2.3: Detector Quantities

Detector	G (A/A)	x	T_A (V/A)	B (kHz)	i'_d (nA)
Blue APD	300	0.138	4×10^6	90	3.5
Red APD	220	0.138	4×10^6	100	5.6
PMT	5×10^6	0.013	10^5	200	0.1

rejecting data points that lie more than one RMS from the median DC level. The linear trend is then added back to the DC data before mean and RMS values are computed. The pulses are large enough that few non-pulse data lie above one RMS from the median. Since the spurious LED signals are scattered back into the instrument case, they do not pass through the PEM and therefore have no effect on the AC data.

2.5.2 PEM Calibration

To determine the systematics of the PEM rotation in the lab, we injected pure polarized light into the instrument by placing a linear polarizer between a green LED and the PEM. We aligned the polarizer to the Wollaston axis by rotating it until the maximum DC signal was achieved. This occurs for polarizer angle $\psi = 0^\circ$ with respect to the Wollaston axis, as shown in Equation A5. It might seem that the best way to align the polarizer is by taking the ratio of the AC and DC signal as in Equation 2.4, but it can be seen from Equation B10 that misalignment of the PEM from $\theta_{\text{PEM}} = \pm 45^\circ$ will cause misalignment of the polarizer with this technique. Thus, the PEM was powered down when aligning the polarizer. With the polarizer aligned, $Q_0/I_0 = 99.98\%$ and $U_0/I_0 = 0$.

With the full system turned on, we sampled the polarization as the PEM was swept through the PEM $+45^\circ$ and -45° positions. The results are shown in Figure 2.7. The values of Θ_{PEM} are the expected positions of the rotation motor. For the PEM -45° position, the peak polarization lies almost exactly at $\Theta_{\text{PEM}} = -45^\circ$. Given $U_0/I_0 = 0$ above, Equation B10 implies

$$\frac{Q_{\text{obs}}}{I_{\text{obs}}} = \frac{Q_0}{I_0} \frac{\sin^2 2\theta_{\text{PEM}}}{1 + \frac{Q_0}{I_0} [\cos^2 2\theta_{\text{PEM}} + J_0 (\beta_0) \sin^2 2\theta_{\text{PEM}}]} \quad (2.6)$$

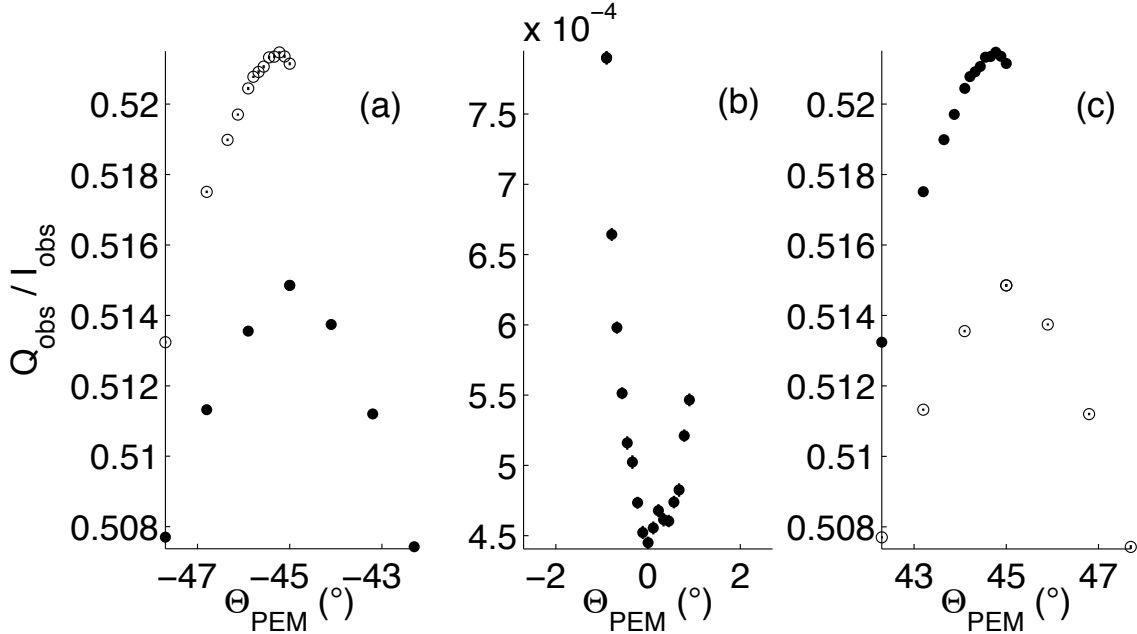


Figure 2.7: Polarization measured near the $\Theta_{\text{PEM}} = -45^\circ$ (a), 0° (b), and $+45^\circ$ (c) positions (solid circles), where the angle is that expected by the rotation motor. Open circles show polarization measured with the PEM rotated by $\Delta\Theta_{\text{PEM}} = \pm 90^\circ$. Polarimetric uncertainty is size of the data points or less.

which has a maximum at $\theta_{\text{PEM}} = \pm 45^\circ$. In Figure 2.7a, since peak polarization is attained at $\Theta_{\text{PEM}} \approx -45^\circ$, it must follow that the PEM position expected by the motor is close to the true $\theta_{\text{PEM}} = -45^\circ$ position. Indeed, we find the $\Theta_{\text{PEM}} = -45^\circ$ motor position lies at $\theta_{\text{PEM}} = -44.98^\circ$.

However, peak polarization is not achieved for $\Theta_{\text{PEM}} = +45^\circ$, but it is achieved at slightly below this value. This can be seen in Figure 2.7c. Since the peak polarization must occur at the true $\theta_{\text{PEM}} = +45^\circ$ position, the $\Theta_{\text{PEM}} = +45^\circ$ motor position must lie at slightly *higher* angle than $\theta_{\text{PEM}} = +45^\circ$. We find the $\Theta_{\text{PEM}} = +45^\circ$ motor position lies at the true $\theta_{\text{PEM}} = +45.20^\circ$ position with respect to the Wollaston axis.

Minimum polarization from Equation 2.6 occurs at $\theta_{\text{PEM}} = 0^\circ$ with respect to the Wollaston axis. From Figure 2.7b, it can be seen that the minimum occurs at a slightly higher angle than $\Theta_{\text{PEM}} = 0^\circ$. Thus, the true position at $\Theta_{\text{PEM}} = 0^\circ$ is $\theta_{\text{PEM}} = -0.19^\circ$. Given that the terms involving θ_{PEM} in Equation 2.6 are of second order, the observed peak polarizations at $\theta_{\text{PEM}} = \pm 45^\circ$ should be identical. Since they are quite clearly different, the effect must be due to the only free parameter in Equation 2.6, the peak retardance β_0 . We feel justified in assuming that $\beta_0 = 2.4048$ radians for $\theta_{\text{PEM}} = -45^\circ$; reasons for this will be provided below. In order for the observed polarization at

Table 2.4: Correction Parameters for $\Theta_{\text{PEM}} = \pm 45^\circ$

$\Theta_{\text{PEM}} (^\circ)$	$\theta_{\text{PEM}} (^\circ)$	β_0 (rad)	G_P
-45	-44.98	2.4048	1.8564(22)
+45	+45.20	2.4506	1.8564(22)

$\theta_{\text{PEM}} = +45^\circ$ to match the value obtained at $\theta_{\text{PEM}} = -45^\circ$, the peak retardance at $\theta_{\text{PEM}} = +45^\circ$ must be $\beta_0 = 2.4506$ radians.

The cause of both the PEM misalignment and change in peak retardance depending on PEM position is due to torque applied to the PEM when it is rotated to the $\Theta_{\text{PEM}} = +45^\circ$ position. At this position, the cable connecting the PEM to the drive circuit pushes up against the case enclosing the optical bench, and the resulting deformation of the cable causes a change in peak retardance. Sections had been cut out of the case to allow motion of the cable when the PEM is rotated, but apparently those sections did not keep the cable from contacting the case. The case was replaced for the next observing run.

The torque applied to the PEM at this position pushes on the gear that holds the PEM. The distance between the motor and the gear is slightly too short, so slack in the belt connecting the two causes the gear to move when torque is applied to the PEM. For the next observing run, the motor was moved slightly away from the gear to tighten the belt. At the $\Theta_{\text{PEM}} = -45^\circ$ position, no torque is applied to the PEM, which is why the peak polarization occurs where expected. Thus, we also assume the peak retardance at this PEM position is the nominal $\beta_0 = 2.4048$ radian value.

The polarized light injected into the system for the lab tests had Stokes parameters of $Q_0/I_0 = 99.98\%$ and $U_0/I_0 = 0$, yet Figure 2.7a shows peak polarization at the $\theta_{\text{PEM}} = -45^\circ$ position to be only $\approx 52\%$. This requires deviation of peak retardance at the $\theta_{\text{PEM}} = -45^\circ$ position from $\beta_0 = 2.4048$ radians, or it requires application of a polarimetric gain factor to all measurements. The peak retardance necessary to explain the low peak polarization at $\theta_{\text{PEM}} = -45^\circ$ is 0.58 radians. Since this value is far too low to be reasonably explained, we adopt the use of a polarimetric gain factor to scale observed polarization to true polarization. By correcting observed polarization according to Equation B11a, we find the polarimetric gain factor to be $G_P = 1.8564(22)$. The correction parameters determined from lab tests are summarized in Table 2.4.

2.5.3 Mean Polarization

After the polarization from each measurement is corrected for PEM position and peak retardance according to Table 2.4, the polarimetric gain factor G_P is applied. Since $P_0 = P_{\text{obs}}G_P$, the polarimetric uncertainty of each measurement is

$$\sigma_{P_0} = \sqrt{(G_P\sigma_{P_{\text{obs}}})^2 + (P_{\text{obs}}\sigma_{G_P})^2}. \quad (2.7)$$

Telescope polarization is then subtracted, which is discussed in detail in the next section. For each measurement, the weighted mean polarization from both detectors 1 and 2 is also taken, and the weight for each detector is the integrated DC level divided by the detector gain. Since the blue enhanced APD has a higher gain than the red enhanced one by a factor of 1.36, the DC signal from the blue enhanced APD is expected to be higher than for the red enhanced one. The polarimetric uncertainty in this combined-detector measurement is taken as the quadrature addition of the polarimetric uncertainties from both detectors.

Nightly mean and run-averaged Q_0/I_0 and U_0/I_0 for each source are determined by taking the weighted mean polarization of all corrected data over the requested timescale. The weighting for each measurement is its sky-subtracted DC level multiplied by integration time. As stated in section 2.5.1, this value is proportional to the total number of detected photons. Weighting by this value ensures all detected photons, rather than all measurements, are weighted equally. This is important for data taken in partly cloudy conditions. The polarimetric uncertainty is the square root of the weighted variance divided by the square root of the number of measurements. It is important to note that this precision is only applicable to stars with no intrinsic polarimetric variability. Analyses of the variability of the observed stars, including Cygnus X-1, are made in Chapter 3.

2.6 Standard Stars with APDs

2.6.1 Unpolarized Standard Stars and Systematic Effects

From Table 2.2, the polarizations of both HR 5854 and HR 8974 are close to zero, which makes them candidates for being truly unpolarized sources. The nightly average polarization of HR 5854

and HR 8974, before subtraction of telescope polarization, are listed in Table 2.5 and plotted in Figures 2.8 and 2.9. For each detector, the weighted mean Stokes parameters for both stars are generally within one sigma of each other. We therefore assume that these stars are indeed unpolarized and that the combination of telescope and instrumental polarization causes the observed net polarization of order one part in 10^4 . Since the light beam from the telescope secondary mirror impinges immediately on the PEM, we assume that instrumental polarization is negligible. Indeed, the very similar setup of PlanetPol has an instrumental polarization of a few parts per million (HLB 06).

The equatorial mount of the Hale 5-m inhibits traditional telescope polarization measurement, which involves allowing the field to rotate and determining the center of the (Q, U) locus. Since HLB 06 performed this analysis and claim part per million polarization of HR 5854 and HR 8974, telescope polarization for the Hale 5-m is thus calculated by the weighted mean polarization from HR 5854 and HR 8974 (Table 2.6). Uncertainty is given as the square root of the weighted variance of the individual scans divided by the square root of the number of scans. The cause of the large telescope polarization of the Hale 5-m is unknown, but it may be due to inhomogeneities in the coating of the primary and/or secondary mirrors.

The PEM is rotated to positions of $\theta_{\text{PEM}} = \pm 45^\circ$ with respect to the Wollaston axis, and the Cassegrain ring is rotated through $\Delta\phi = 360^\circ$. This gives independent measures of the PEM and ring rotation systematics. Note that PlanetPol allows the instrument to be rotated to positions of $\pm 45^\circ$ with respect to their PEM, but this 90° rotation of the instrument also causes the Stokes parameter of opposite sign to be observed. That is, PEM and instrument rotation systematics are coupled for PlanetPol, while they can be independently measured for POLISH. In addition, PlanetPol can measure $\pm Q/I$ and $\pm U/I$, but it can only rotate through 135° . The $\Delta\phi = 360^\circ$ rotation of POLISH enables more thorough measurement of the instrument rotation systematics.

To investigate the PEM systematics, we must subtract the offset due to ring rotation systematics. We first find the weighted mean polarization of each Stokes parameter for each star separately, and at each of the $\theta_{\text{PEM}} = \pm 45^\circ$ positions. We average ring angles $\phi = 0^\circ$ to $\phi = 270^\circ$ in $\Delta\phi = 90^\circ$ increments for the Q/I parameter and $\phi = 45^\circ$ to $\phi = 315^\circ$ in $\Delta\phi = 90^\circ$ increments for the U/I parameter. Therefore, the mean polarization at each PEM position contains the same offset due to ring rotation systematics. The sign of the polarization taken at the $\theta_{\text{PEM}} = -45^\circ$ position is reversed, and the unweighted mean is taken across both Stokes parameters and both PEM posi-

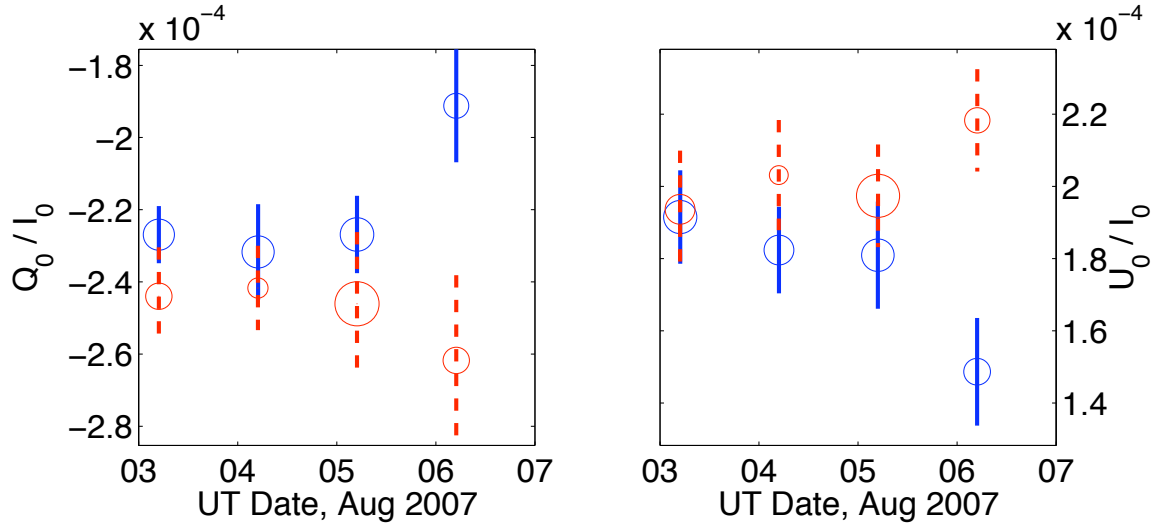


Figure 2.8: Polarization of HR 5854 after PEM and gain correction. These observations are combined with those of HR8974 (Figure 2.9) to determine telescope polarization. Observations with the blue enhanced APD (detector 1) are tinted blue, while observations with the red enhanced APD (detector 2) are tinted red. The area of the data points is proportional to the number of detected photons. Error bars indicate the square root of the weighted variance of the nightly measurements that compose the nightly bins. These conventions are used throughout this chapter.

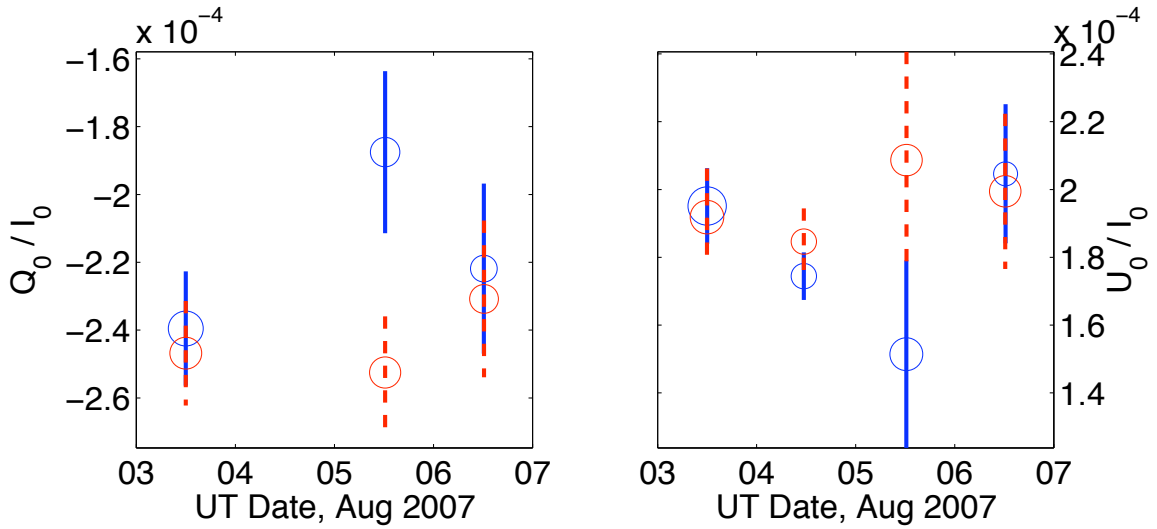


Figure 2.9: Polarization of HR 8974 after PEM and gain correction.

Table 2.5: Raw Polarization of Unpolarized Standard Stars

UT Date	Star	Detector	Q_0/I_0 ($\times 10^{-6}$)	U_0/I_0 ($\times 10^{-6}$)	P ($\times 10^{-6}$)	Θ ($^\circ$)
2007 Aug 3	HR 5854	1	-226.9(2.3)	191.5(3.5)	296.9(2.8)	69.92(29)
2007 Aug 4	-231.7(3.3)	182.4(3.8)	294.9(3.5)	70.90(35)
2007 Aug 5	-226.9(2.7)	181.0(4.3)	290.2(3.4)	70.71(37)
2007 Aug 6	-191.2(4.5)	148.6(4.0)	242.2(4.3)	71.07(50)
Overall	-222.9(2.4)	178.0(2.9)	285.2(2.6)	70.70(27)
2007 Aug 3	...	2	-244.0(3.9)	193.6(4.1)	311.5(4.0)	70.78(37)
2007 Aug 4	-241.7(2.8)	203.1(4.4)	315.7(3.5)	69.98(35)
2007 Aug 5	-246.1(4.7)	197.4(3.8)	315.5(4.4)	70.63(38)
2007 Aug 6	-261.7(5.9)	218.3(4.1)	340.8(5.2)	70.09(41)
Overall	-248.1(2.5)	200.4(2.3)	318.9(2.4)	70.54(22)
2007 Aug 3	...	1,2	-231.6(1.8)	192.2(3.0)	301.0(2.4)	70.16(25)
2007 Aug 4	-233.4(2.7)	186.3(3.5)	298.7(3.0)	70.70(31)
2007 Aug 5	-236.0(3.0)	189.2(3.3)	302.5(3.1)	70.65(30)
2007 Aug 6	-219.9(5.8)	169.6(3.8)	277.7(5.1)	71.17(48)
Overall	-231.9(1.8)	185.8(2.0)	297.1(1.9)	70.64(19)
2007 Aug 3	HR 8974	1	-239.5(3.8)	195.1(3.0)	308.9(3.5)	70.42(31)
2007 Aug 4	-207(25)	174.5(4.0)	271(20)	70.0(1.8)
2007 Aug 5	-187.5(6.0)	151.4(8.0)	241.0(6.8)	70.54(86)
2007 Aug 6	-221.9(7.2)	205(10)	301.8(8.8)	68.66(85)
Overall	-219.6(4.4)	179.9(4.9)	283.8(4.6)	70.34(47)
2007 Aug 3	...	2	-246.8(3.4)	191.9(3.6)	312.6(3.5)	71.07(32)
2007 Aug 4	-199(27)	184.6(4.0)	272(20)	68.6(2.0)
2007 Aug 5	-252.5(4.4)	209(10)	327.6(7.3)	70.22(72)
2007 Aug 6	-230.8(5.6)	199.5(5.7)	305.0(5.7)	69.58(53)
Overall	-243.0(2.9)	197.3(3.4)	313.0(3.1)	70.46(29)
2007 Aug 3	...	1,2	-240.9(3.2)	194.4(2.2)	309.6(2.9)	70.55(25)
2007 Aug 4	-206(37)	177.7(3.4)	272(28)	69.6(2.6)
2007 Aug 5	-201.8(6.9)	166.5(5.9)	261.6(6.5)	70.24(69)
2007 Aug 6	-224.5(5.6)	202.1(5.3)	302.0(5.5)	69.00(52)
Overall	-224.8(3.7)	185.5(2.9)	291.5(3.4)	70.24(32)

tions. The unweighted mean is employed so neither Stokes parameter and neither PEM position dominates. This value is the PEM offset, given by S_{PEM} (Equation 2.8a). The uncertainty in this offset is given as one half the difference between the results for Stokes Q and U (Equation 2.8b). This process is duplicated for each detector and star separately. For the PEM systematic, the index i represents the PEM position, where $i = 0$ indicates $\theta_{\text{PEM}} = +45^\circ$ and $i = 1$ indicates $\theta_{\text{PEM}} = -45^\circ$.

To investigate the systematics when rotating the Cassegrain ring by 90° , i.e. the differences between $\pm Q$ or $\pm U$, we subtract the offset due to PEM systematics. While this value has been calculated above, we prefer to combine the data in such a way as to cause it to cancel. We find the weighted mean value of each Stokes parameter separately using both $\theta_{\text{PEM}} = \pm 45^\circ$ positions. We average ring angles $\phi = 0^\circ$ and $\phi = 180^\circ$ for the $+Q_0/I_0$ parameter, $\phi = 90^\circ$ and $\phi = 270^\circ$

Table 2.6: Telescope Polarization with APDs

UT Date	Detector	Q_0/I_0 ($\times 10^{-6}$)	U_0/I_0 ($\times 10^{-6}$)	P ($\times 10^{-6}$)	Θ ($^\circ$)
2007 Aug 3	1	-233.0(2.6)	192.8(2.4)	302.5(2.5)	70.20(23)
2007 Aug 4	...	-230.9(3.3)	181.2(3.3)	293.5(3.3)	70.93(32)
2007 Aug 5	...	-214.8(4.3)	171.9(4.9)	275.1(4.5)	70.66(48)
2007 Aug 6	...	-203.4(5.1)	157.3(6.1)	257.1(5.5)	71.14(64)
Overall	...	-221.8(2.2)	178.5(2.5)	284.7(2.3)	70.59(24)
2007 Aug 3	2	-245.1(2.5)	193.1(2.8)	312.1(2.6)	70.88(25)
2007 Aug 4	...	-240.0(3.2)	198.1(3.8)	311.2(3.5)	70.23(33)
2007 Aug 5	...	-246.9(3.5)	198.8(3.7)	317.0(3.5)	70.58(32)
2007 Aug 6	...	-252.5(4.8)	211.8(3.7)	329.5(4.4)	70.00(37)
Overall	...	-247.0(1.9)	199.7(1.9)	317.6(1.9)	70.52(17)
2007 Aug 3	1,2	-236.0(2.1)	193.0(2.0)	304.9(2.1)	70.37(19)
2007 Aug 4	...	-232.5(2.8)	184.9(2.8)	297.0(2.8)	70.75(27)
2007 Aug 5	...	-227.5(4.0)	183.6(3.5)	292.3(3.8)	70.55(36)
2007 Aug 6	...	-221.6(4.1)	176.9(3.8)	283.6(4.0)	71.70(40)
Overall	...	-229.8(1.8)	185.7(1.6)	295.5(1.7)	70.53(16)

for $-Q_0/I_0$, $\phi = 45^\circ$ and $\phi = 225^\circ$ for $+U_0/I_0$, and $\phi = 135^\circ$ and $\phi = 315^\circ$ for $-U_0/I_0$. We then reverse the signs of the negative Stokes parameters. Taking the unweighted mean for Q_0/I_0 and U_0/I_0 separately, we find the offsets for both Stokes parameters (Equation 2.8a). The uncertainty is one half the difference between the offsets for the positive and negative Stokes parameters (Equation 2.8b). For the Cassegrain ring systematic, the index i represents the sign of the measured Stokes parameter, where $i = 0$ indicates $+Q, +U$ and $i = 1$ indicates $-Q, -U$.

$$S_{\text{PEM},\phi} = \frac{1}{4} \sum_{i=0}^1 (-1^i) \bar{Q}_i + (-1^i) \bar{U}_i \quad (2.8a)$$

$$\sigma_{\text{PEM},\phi} = \frac{1}{4} \left| \sum_{i=0}^1 (-1^i) \bar{Q}_i - (-1^i) \bar{U}_i \right| \quad (2.8b)$$

In the same way that we found the PEM offset for each Stokes parameter, we now have the Q_0/I_0 and U_0/I_0 offsets for each PEM position. Offsets due to the PEM and ring rotation for HR 5854 and HR 8974 are given in Table 2.7. The ‘‘Detector 1,2’’ value represents systematics obtained when taking the weighted mean polarization from the simultaneous pairs of measurements from detector 1 and 2. The ‘‘Detector Mean’’ value represents the mean systematic across the previous three detector combinations weighted by the inverse square of the uncertainties. This is in contrast

Table 2.7: Systematic Effects: Unpolarized Standard Stars with APDs

Star	Parameter	Detector 1	Detector 2	Detector 1,2	Detector Mean
HR 5854	$S_{\text{PEM}} (\times 10^{-6})$	+3.0(1.2)	+3.22(19)	+2.36(60)	+3.14(24)
...	$S_{\phi} (\times 10^{-6})$	-1.34(13)	+0.78(37)	-0.2(1.2)	-1.11(65)
HR 8974	$S_{\text{PEM}} (\times 10^{-6})$	+4.6(3.2)	+2.8(3.1)	+3.8(1.8)	+3.77(58)
...	$S_{\phi} (\times 10^{-6})$	-4.5(1.6)	-4.9(1.9)	-5.44(99)	-5.12(40)

to our usual use of weighting by DC level in order to benefit those detectors with good measurement of systematic effects.

2.6.2 Polarized Standard Stars

We subtract telescope polarization in two ways. The first is by subtracting the nightly telescope polarization from the nightly stellar polarization, and the second is by subtracting the run-averaged telescope polarization from the nightly stellar polarization. Tables 2.8 and 2.9 list telescope subtracted polarizations for all stars observed with APDs: weakly polarized stars are given in Table 2.8, while strongly polarized stars are listed in Table 2.9. Systematic effects for each star are listed in Table 2.10. Since HR 5854 and HR 8974 are effectively unpolarized, uncertainty in polarimetric position angle Θ is so large as to preclude meaningful estimates on Θ .

Due to poor weather, data at only one Cassegrain ring angle and one PEM position were taken for ζ Peg. The asterisks for this star indicate that, since no measurements for U_0/I_0 or $\theta_{\text{PEM}} = -45^\circ$ exist, the data cannot be calibrated for PEM position and peak retardance. These data have been subtracted by the telescope polarization, but uncertainty in these measurements is surely large. Indeed, there is a large difference between subtraction by the telescope polarization obtained during the single night of ζ Peg observation and by the run-averaged telescope polarization.

Table 2.8: Weakly Polarized Standard Stars with APDs

UT Date	Star	Detector	Q_0/I_0 ($\times 10^{-6}$)	U_0/I_0 ($\times 10^{-6}$)	P ($\times 10^{-6}$)	Θ ($^\circ$)
2007 Aug 3	HR 5854	1	+6.1(3.4)	-1.3(4.2)	6.3(3.5)	-
2007 Aug 4	-0.6(4.7)	+1.9(5.0)	1.9(5.0)	-
2007 Aug 5	-12.6(5.0)	+8.0(6.5)	14.9(5.5)	-
2007 Aug 6	+13.7(6.8)	-9.7(7.3)	16.8(7.0)	-
Overall (Run)	-0.5(3.3)	-0.4(3.9)	0.6(3.5)	-
Overall (Night)	-0.1(4.7)	+0.4(3.0)	0.5(3.1)	-
2007 Aug 3	...	2	+1.1(4.7)	+0.5(4.9)	1.2(4.7)	-
2007 Aug 4	-1.5(4.3)	+5.8(5.8)	6.0(5.8)	-
2007 Aug 5	+0.1(5.8)	-2.7(5.3)	2.7(5.3)	-
2007 Aug 6	-9.3(7.6)	+5.6(5.6)	10.8(7.1)	-
Overall (Run)	-2.2(3.1)	+0.7(3.0)	2.3(3.1)	-
Overall (Night)	-1.6(1.8)	+0.3(1.7)	1.7(1.8)	-
2007 Aug 3	...	1,2	+4.4(2.8)	-0.9(3.6)	4.5(2.8)	-
2007 Aug 4	-0.8(3.9)	+2.3(4.5)	2.4(4.5)	-
2007 Aug 5	-9.1(5.0)	+5.0(4.8)	10.4(4.9)	-
2007 Aug 6	+2.0(7.1)	-8.1(5.4)	8.4(5.5)	-
Overall (Run)	-2.4(2.6)	+0.3(2.6)	2.4(2.6)	-
Overall (Night)	-2.0(2.8)	+0.4(2.3)	2.0(2.8)	-
2007 Aug 3	...	Mean	+4.4(1.7)	-0.70(68)	4.5(1.7)	-
2007 Aug 4	-0.94(38)	+3.0(1.6)	3.2(1.5)	-
2007 Aug 5	-7.9(5.0)	+3.0(4.3)	8.4(5.0)	-
2007 Aug 6	+3.0(9.3)	-3.2(6.9)	4.4(8.1)	-
Overall (Run)	-1.82(80)	+0.30(40)	1.84(79)	-
Overall (Night)	-0.72(62)	-0.10(71)	0.72(63)	-
2007 Aug 3	HR 8974	1	-5.0(4.6)	+2.7(3.8)	5.7(4.4)	-
2007 Aug 4	+23.6(3.3)	-6.8(5.2)	24.5(3.5)	-
2007 Aug 5	+27.2(7.3)	-20.5(9.4)	34.1(8.1)	-
2007 Aug 6	-19.6(8.9)	+47(12)	51(12)	-
Overall (Run)	+2.9(4.9)	+1.9(5.5)	3.4(5.1)	-
Overall (Night)	+3.2(9.3)	+1(11)	3.5(9.5)	-
2007 Aug 3	...	2	-1.8(4.3)	-1.3(4.5)	2.2(4.4)	-
2007 Aug 4	+40.5(3.2)	-13.5(5.5)	42.7(3.5)	-
2007 Aug 5	-5.3(5.6)	+12(11)	13(10)	-
2007 Aug 6	+22.3(7.4)	-12.3(6.8)	25.5(7.2)	-
Overall (Run)	+4.7(3.5)	-1.9(3.8)	5.1(3.5)	-
Overall (Night)	+6.7(7.4)	-2.7(5.1)	7.2(7.1)	-
2007 Aug 3	...	1,2	-3.8(3.9)	+1.6(3.0)	4.1(3.7)	-
2007 Aug 4	+26.8(2.8)	-7.2(4.5)	27.7(3.0)	-
2007 Aug 5	+25.6(7.9)	-17.1(6.8)	30.8(7.6)	-
2007 Aug 6	-3.0(7.0)	+25.6(6.5)	25.8(6.5)	-
Overall (Run)	+5.6(4.1)	-0.1(3.3)	5.6(4.1)	-
Overall (Night)	+7.4(7.1)	-1.4(7.0)	7.6(7.1)	-
2007 Aug 3	...	Mean	-3.5(1.3)	+1.3(1.4)	3.7(1.3)	-
2007 Aug 4	+30.0(7.1)	-8.8(2.9)	31.3(6.8)	-
2007 Aug 5	+11(16)	-12(12)	16(14)	-
2007 Aug 6	+2(16)	+13(22)	13(22)	-
Overall (Run)	+4.6(1.0)	-0.4(1.3)	4.6(1.0)	-
Overall (Night)	-2.4(2.9)	-0.7(2.1)	2.5(2.9)	-
2007 Aug 4	HD 9270	1	-40.2(6.1)	-90.2(4.8)	98.7(5.1)	123.0(1.7)
2007 Aug 5	-40(11)	-101.5(6.1)	109.1(69)	124.3(2.7)
2007 Aug 6	-65(11)	-82.1(8.8)	104.5(9.7)	115.9(2.8)
Overall (Run)	-46.2(4.6)	-92.2(3.8)	103.2(4.0)	121.7(1.2)
Overall (Night)	-45.0(5.7)	-90.0(3.2)	100.6(3.8)	121.7(1.5)
2007 Aug 4	...	2	-	-	-	-
2007 Aug 5	-61.2(7.8)	-81.1(6.7)	101.6(7.1)	116.5(2.1)
2007 Aug 6	-34(13)	-114(16)	120(15)	126.6(3.2)
Overall (Run)	-53.3(7.0)	-91.1(8.1)	105.5(7.9)	119.8(2.0)
Overall (Night)	-49.4(9.4)	-97(12)	109(11)	121.5(2.6)
2007 Aug 4	...	1,2	-40.2(6.1)	-90.2(4.8)	98.7(5.1)	123.0(1.7)
2007 Aug 5	-44.7(8.4)	-97.6(5.0)	107.3(5.7)	122.7(2.1)
2007 Aug 6	-51(10)	-96.9(8.2)	109.3(8.7)	121.2(2.6)
Overall (Run)	-41.5(4.1)	-97.1(3.2)	105.6(3.3)	123.4(1.1)
Overall (Night)	-48.0(2.1)	-97.14(25)	108.33(94)	121.86(49)

Weakly Polarized Standard Stars with APDs (continued)

UT Date	Star	Detector	Q_0/I_0 ($\times 10^{-6}$)	U_0/I_0 ($\times 10^{-6}$)	P ($\times 10^{-6}$)	Θ ($^\circ$)
2007 Aug 4	HD 9270	Mean	-40.2(6.1)	-90.2(4.8)	98.7(5.1)	123.0(1.7)
2007 Aug 5	-50.5(9.2)	-94.6(8.0)	107.2(8.3)	121.0(2.4)
2007 Aug 6	-52(12)	-93(11)	107(11)	120.5(3.0)
Overall (Run)	-45.2(4.2)	-94.8(2.6)	105.0(2.9)	122.3(1.1)
Overall (Night)	-50.94(41)	-94.09(49)	106.99(47)	120.78(12)
2007 Aug 4	γ Oph	1	-106.3(8.0)	+161.2(6.5)	193.1(7.0)	61.7(1.1)
2007 Aug 5	-102.8(7.1)	+159.0(8.0)	189.3(7.8)	61.4(1.1)
2007 Aug 6	-56(12)	+119(12)	132(12)	57.7(2.5)
Overall (Run)	-88.5(6.4)	+142.5(6.3)	167.7(6.3)	60.9(1.1)
Overall (Night)	-92(12)	+149(10)	176(11)	60.9(1.9)
2007 Aug 4	...	2	-87.6(7.5)	+158.9(8.1)	181.5(8.0)	59.4(1.2)
2007 Aug 5	-87.3(6.4)	+164.5(8.3)	186.2(7.9)	59.0(1.1)
2007 Aug 6	-116(11)	+176.0(9.2)	210.8(9.8)	61.7(1.4)
Overall (Run)	-95.3(5.1)	+169.4(5.1)	194.4(5.1)	59.68(75)
Overall (Night)	-95.1(7.4)	+166.8(3.5)	192.0(4.7)	60.55(99)
2007 Aug 4	...	1,2	-102.7(6.7)	+160.2(5.1)	190.3(5.6)	61.33(94)
2007 Aug 5	-97.3(4.7)	+162.5(5.8)	189.4(5.6)	60.45(76)
2007 Aug 6	-78.1(9.1)	+140.7(8.4)	160.9(8.6)	59.5(1.6)
Overall (Run)	-92.1(4.1)	+152.5(4.0)	178.2(4.0)	60.56(65)
Overall (Night)	-94.2(5.6)	+156.1(5.3)	182.3(5.4)	60.55(86)
2007 Aug 4	...	Mean	-98.9(7.9)	+160.26(78)	188.3(4.2)	60.8(1.0)
2007 Aug 5	-95.7(5.7)	+162.1(2.0)	188.2(3.4)	60.28(76)
2007 Aug 6	-83(23)	+148(22)	170(22)	59.7(3.8)
Overall (Run)	-92.4(2.4)	+155.6(9.8)	181.0(8.5)	60.34(86)
Overall (Night)	-96.3(1.7)	+160.49(42)	187.16(96)	60.48(23)
2007 Aug 4	ζ Peg	1	+2(-)*	-	>2(-)*	-
2007 Aug 4	...	2	+15(-)*	-	>15(-)*	-
2007 Aug 4	...	1,2	+5(-)*	-	>5(-)*	-
2007 Aug 4	...	Mean	+7(-)*	-	>7(-)*	-
2007 Aug 5	Algenib	1	-565(19)	-623(19)	841(19)	113.91(64)
2007 Aug 6	-702(11)	-589(11)	917(11)	109.99(34)
Overall (Run)	-646(14)	-613.9(9.0)	891(12)	111.78(37)
Overall (Night)	-658(46)	-600(11)	934(13)	111.17(36)
2007 Aug 5	...	2	-730.0(6.4)	-628.6(7.9)	963.4(7.1)	110.37(22)
2007 Aug 6	-668.3(7.9)	-643.6(7.1)	927.8(7.5)	111.96(23)
Overall (Run)	-698.2(6.3)	-630.2(4.9)	940.6(5.7)	111.03(17)
Overall (Night)	-697(22)	-636.6(5.3)	934(13)	111.17(36)
2007 Aug 5	...	1,2	-625(12)	-627(13)	885(13)	112.54(41)
2007 Aug 6	-687.7(8.7)	-608.7(8.5)	918.4(8.6)	110.76(27)
Overall (Run)	-661.5(8.1)	-619.5(6.9)	906.3(7.6)	111.56(24)
Overall (Night)	-666(21)	-615.0(6.1)	907(16)	111.36(47)
2007 Aug 5	...	Mean	-696(57)	-627.6(1.7)	937(42)	111.0(1.2)
2007 Aug 6	-683(13)	-621(22)	923(18)	111.15(58)
Overall (Run)	-680(20)	-624.5(6.6)	923(16)	111.29(46)
Overall (Night)	-683.3(2.2)	-627.60(36)	927.8(1.6)	111.284(47)
2007 Aug 4	u Her	1	+1547(20)	-440(12)	1609(19)	172.06(22)
2007 Aug 4	...	2	+1585(19)	-497(30)	1661(20)	171.30(50)
2007 Aug 4	...	1,2	+1554(15)	-451.5(9.6)	1618(15)	171.90(18)
2007 Aug 4	...	Mean	+1561(16)	-450(13)	1625(15)	171.97(23)

Table 2.9: Strongly Polarized Standard Stars with APDs

UT Date	Star	Detector	Q_0/I_0 (%)	U_0/I_0 (%)	P (%)	Θ ($^\circ$)
2007 Aug 5	HD 157999	1	-1.0258(10)	+0.1788(25)	1.0413(11)	85.055(68)
2007 Aug 6	-0.9838(14)	+0.1690(28)	0.9982(15)	85.127(79)
Overall (Run)	-1.0026(36)	+0.1728(21)	1.0174(36)	85.109(61)
Overall (Night)	-1.005(15)	+0.1742(3.5)	1.020(15)	85.08(12)
2007 Aug 5	...	2	-1.0672(18)	+0.1867(23)	1.0834(18)	85.038(61)
2007 Aug 6	-1.1216(13)	+0.1961(29)	1.1386(14)	85.042(71)
Overall (Run)	-1.0923(45)	+0.1907(20)	1.1088(45)	85.049(55)
Overall (Night)	-1.089(19)	+0.1902(32)	1.106(19)	85.05(12)
2007 Aug 5	...	1,2	-1.0404(14)	+0.1818(24)	1.0561(14)	85.045(65)
2007 Aug 6	-1.0261(11)	+0.1771(28)	1.0413(12)	85.103(75)
Overall (Run)	-1.0328(15)	+0.1792(19)	1.0482(15)	85.079(51)
Overall (Night)	-1.0336(50)	+0.1797(16)	1.0491(50)	85.068(50)
2007 Aug 5	...	Mean	-1.037(15)	+0.1826(33)	1.053(15)	85.01(11)
2007 Aug 6	-1.044(54)	+0.180(11)	1.059(53)	85.10(39)
Overall (Run)	-1.034(21)	+0.1810(72)	1.049(21)	85.03(22)
Overall (Night)	-1.0377(12)	+0.18246(41)	1.0536(12)	85.014(12)
2007 Aug 3	HD 187929	1	-1.8717(18)	-0.1896(66)	1.8813(19)	92.89(10)
2007 Aug 5	-1.8208(28)	-0.2051(48)	1.8323(29)	93.214(75)
2007 Aug 6	-1.7359(45)	-0.1942(49)	1.7467(45)	93.192(80)
Overall (Run)	-1.8448(68)	-0.1930(42)	1.8548(68)	92.986(65)
Overall (Night)	-1.835(31)	-0.1933(33)	1.845(30)	93.007(71)
2007 Aug 3	...	2	-1.9414(22)	-0.1947(67)	1.9512(22)	92.864(99)
2007 Aug 5	-1.8908(31)	-0.2129(53)	1.9027(32)	93.212(80)
2007 Aug 6	-1.9723(26)	-0.2273(49)	1.9854(27)	93.288(71)
Overall (Run)	-1.9355(36)	-0.2055(45)	1.9464(37)	93.030(67)
Overall (Night)	-1.935(16)	-0.2062(78)	1.946(16)	93.04(12)
2007 Aug 3	...	1,2	-1.8936(12)	-0.1912(66)	1.8813(19)	92.89(10)
2007 Aug 5	-1.8464(32)	-0.2087(49)	1.8323(29)	93.214(75)
2007 Aug 6	-1.8121(32)	-0.2051(48)	1.7467(45)	93.192(80)
Overall (Run)	-1.8741(44)	-0.1970(42)	1.8548(68)	92.986(65)
Overall (Night)	-1.868(19)	-0.1976(44)	1.845(30)	93.007(71)
2007 Aug 3	...	Mean	-1.897(23)	-0.1918(21)	1.906(23)	92.887(47)
2007 Aug 5	-1.850(29)	-0.2086(31)	1.862(29)	93.217(69)
2007 Aug 6	-1.880(96)	-0.209(14)	1.891(96)	93.17(26)
Overall (Run)	-1.907(36)	-0.1981(51)	1.911(36)	92.975(95)
Overall (Night)	-1.879(13)	-0.1974(46)	1.890(13)	92.997(72)
2007 Aug 4	HD 7927	1	-3.6221(57)	-0.296(11)	3.6342(58)	92.336(85)
2007 Aug 4	...	2	-3.718(11)	-0.308(13)	3.731(11)	92.364(97)
2007 Aug 4	...	1,2	-3.6401(47)	-0.298(11)	3.6523(48)	92.342(87)
2007 Aug 4	...	Mean	-3.642(28)	-0.2999(48)	3.654(28)	92.354(41)
2007 Aug 3	HD 147084	1	-	+3.977(15)	-	-
2007 Aug 4	+1.953(16)	+4.0775(37)	4.5210(76)	32.204(90)
Overall (Run)	-	+3.995(15)	-	-
Overall (Night)	-	+4.012(34)	-	-
2007 Aug 3	...	2	-	+4.138(20)	-	-
2007 Aug 4	+2.019(27)	+4.1035(65)	4.573(13)	31.90(15)
Overall (Run)	-	+4.139(16)	-	-
Overall (Night)	-	+4.1312(98)	-	-
2007 Aug 3	...	1,2	-	+4.0335(56)	-	-
2007 Aug 4	+1.968(17)	+4.0827(30)	4.5321(77)	32.134(95)
Overall (Run)	-	+4.0428(66)	-	-
Overall (Night)	-	+4.050(16)	-	-
2007 Aug 3	...	Mean	-	+4.034(33)	-	-
2007 Aug 4	+1.969(22)	+4.0833(77)	4.533(12)	32.13(13)
Overall (Run)	-	+4.048(38)	-	-
Overall (Night)	-	+4.0807(77)	-	-
2007 Aug 4	HD 154445	1	-4.5158(42)	-0.0540(17)	4.5161(42)	90.342(11)
2007 Aug 4	...	2	-4.540(34)	-0.024(13)	4.540(34)	90.150(85)
2007 Aug 4	...	1,2	-4.5208(80)	-0.0481(14)	4.5210(80)	90.3047(86)
2007 Aug 4	...	Mean	-4.5172(32)	-0.0502(35)	4.5175(32)	90.318(22)

Table 2.10: Systematic Effects: Polarized Standard Stars with APDs

Star	Parameter	Detector 1	Detector 2	Detector 1,2	Detector Mean
HD 9270	$S_{\text{PEM}} (\times 10^{-6})$	+0.82(73)	-2.9(3.0)	+0.52(86)	+0.58(66)
...	$S_{\phi} (\times 10^{-6})$	-6.2(1.8)	+28(26)	-6.5(1.3)	-6.3(1.4)
γ Oph	$S_{\text{PEM}} (\times 10^{-6})$	+3.4(2.4)	-0.7(3.8)	+2.03(71)	+2.05(62)
...	$S_{\phi} (\times 10^{-6})$	-7(11)	+4.5(4.3)	-3.2(8.6)	+1.8(4.3)
Algenib	$S_{\text{PEM}} (\times 10^{-6})$	-0.3(6.7)	+0.9(6.5)	+0.1(6.6)	+0.25(48)
...	$S_{\phi} (\times 10^{-6})$	-4(14)	+4.4(1.3)	-1.9(9.4)	+4.2(1.2)
u Her	$S_{\text{PEM}} (\times 10^{-6})$	-23.75(42)	+18(26)	-15.8(5.1)	-23.69(92)
...	$S_{\phi} (\times 10^{-6})$	-	-	-	-
HD 157999	$S_{\text{PEM}} (\times 10^{-6})$	+61(31)	+29(65)	+47(45)	+53(11)
...	$S_{\phi} (\times 10^{-6})$	-12.3(4.2)	+9(10)	-1.8(1.1)	-2.3(2.7)
HD 187929	$S_{\text{PEM}} (\times 10^{-6})$	+20(68)	+23(62)	+20(65)	+20.8(1.3)
...	$S_{\phi} (\times 10^{-6})$	-102(53)	-32(93)	-85(60)	-85(24)
HD 7927	$S_{\text{PEM}} (\times 10^{-6})$	+40(170)	+130(140)	+60(160)	+87(40)
...	$S_{\phi} (\times 10^{-6})$	-277.6(6.1)	+70(340)	-215(57)	-276.8(9.0)
HD 147084	$S_{\text{PEM}} (\times 10^{-6})$	+214(95)	+320(200)	+220(100)	+229(33)
...	$S_{\phi} (\times 10^{-6})$	-	-	-	-

2.7 Standard Stars with PMTs

Even though the bandpasses differ between the APDs and PMTs, we do not determine telescope polarization with the PMTs for many reasons. First, it is difficult to identify “unpolarized” stars with $V > 7$. Second, differences in telescope polarization derived from APD and PMT observations will only be detected after long PMT observations. Third, we aim to detect small scale changes in polarization of target stars, so constant offsets in telescope polarization between APD and PMT observations is not our goal. Therefore, we choose to quickly measure telescope polarization at the part per million level using bright stars and APDs to minimize overhead due to calibration. Table 2.11 shows polarization observations of HD 212311, and observations of HD 204827 are in Table 2.12. Systematic effects for these stars are listed in Table 2.13.

The number of polarized photons from a star is proportional to the polarization, P . Since the photon shot noise on the number of photons scales as $P^{\frac{1}{2}}$, one would expect that the run-averaged precision attainable on stars of similar brightness would also be proportional to $P^{\frac{1}{2}}$. In addition, we expect the instrument to have a noise floor that becomes noticeable for unpolarized stars. As can be seen in Figure 2.10, we find good agreement by fitting the data from the stars observed with APDs to the model

Table 2.11: Weakly Polarized Standard Stars with PMTs

UT Date	Star	Detector	Q_0/I_0 ($\times 10^{-6}$)	U_0/I_0 ($\times 10^{-6}$)	P ($\times 10^{-6}$)	Θ ($^\circ$)
2007 Aug 3	HD 212311	1	+310(190)	+190(160)	360(180)	16(13)
2007 Aug 4	+320(150)	-270(170)	420(160)	160(11)
2007 Aug 5	+300(150)	-70(170)	310(150)	174(16)
2007 Aug 6	+410(140)	-310(220)	510(170)	162(11)
Overall (Run)	+358(79)	-54(79)	362(79)	175.7(6.3)
Overall (Night)	+335(23)	-98(98)	349(35)	171.9(7.7)
2007 Aug 3	...	2	+620(130)	-150(130)	640(130)	173.0(6.0)
2007 Aug 4	+430(140)	+250(140)	500(140)	15.2(8.1)
2007 Aug 5	+560(100)	-110(130)	570(110)	174.5(6.3)
2007 Aug 6	+140(150)	-120(190)	190(170)	160(27)
Overall (Run)	+444(70)	-54(75)	447(70)	176.5(4.8)
Overall (Night)	+451(89)	-33(83)	452(89)	177.9(5.3)
2007 Aug 3	...	1,2	+485(92)	-6(88)	485(92)	179.6(5.2)
2007 Aug 4	+382(71)	+22(88)	383(71)	1.6(6.6)
2007 Aug 5	+440(76)	-90(100)	449(77)	174.5(6.4)
2007 Aug 6	+262(85)	-200(100)	332(96)	161.1(8.9)
Overall (Run)	+401(43)	-49(50)	404(43)	176.5(3.6)
Overall (Night)	+397(42)	-58(40)	401(41)	175.9(2.9)
2007 Aug 3	...	Mean	+497(96)	-10(110)	497(96)	179.4(6.3)
2007 Aug 4	+380(31)	+30(160)	381(33)	2(12)
2007 Aug 5	+454(83)	-90(14)	463(81)	174.4(1.3)
2007 Aug 6	+270(86)	-202(56)	337(77)	161.6(5.8)
Overall (Run)	+403(27)	-51.4(2.5)	407(27)	176.37(30)
Overall (Night)	+386(26)	-94(15)	397(25)	173.1(1.1)

Table 2.12: Strongly Polarized Standard Stars with PMTs

UT Date	Star	Detector	Q_0/I_0 (%)	U_0/I_0 (%)	P (%)	Θ ($^\circ$)
2007 Aug 3	HD 204827	1	-3.838(14)	+6.821(23)	7.826(21)	59.682(62)
2007 Aug 4	-	+6.996(30)	-	-
2007 Aug 5	-3.827(15)	+6.869(22)	7.863(20)	59.560(62)
2007 Aug 6	-3.886(12)	+6.968(22)	7.978(20)	59.572(53)
Overall (Run)	-3.8474(87)	+6.885(15)	7.887(14)	59.598(39)
Overall (Night)	-3.848(14)	+6.904(36)	7.904(32)	59.568(78)
2007 Aug 3	...	2	-3.925(19)	+7.056(15)	8.074(16)	59.544(65)
2007 Aug 4	-	+7.147(14)	-	-
2007 Aug 5	-3.925(25)	+7.049(19)	8.073(20)	59.586(83)
2007 Aug 6	-3.956(23)	+7.110(21)	8.136(21)	59.546(78)
Overall (Run)	-3.937(13)	+7.073(11)	8.095(11)	59.549(44)
Overall (Night)	-3.9371(71)	+7.085(20)	8.105(18)	59.530(41)
2007 Aug 3	...	1,2	-3.878(12)	+6.949(13)	7.958(13)	59.582(46)
2007 Aug 4	-	+7.076(18)	-	-
2007 Aug 5	-3.873(16)	+6.963(15)	7.968(15)	59.542(56)
2007 Aug 6	-3.911(13)	+7.043(14)	8.056(14)	59.521(47)
Overall (Run)	-3.8853(82)	+6.985(10)	7.9929(97)	59.542(31)
Overall (Night)	-3.8857(93)	+7.000(27)	8.006(24)	59.517(54)
2007 Aug 3	...	Mean	-3.873(31)	+6.970(81)	7.974(72)	59.53(17)
2007 Aug 4	-	+7.104(51)	-	-
2007 Aug 5	-3.863(38)	+6.967(64)	7.967(59)	59.50(16)
2007 Aug 6	-3.905(23)	+7.043(48)	8.053(43)	59.50(11)
Overall (Run)	-3.880(31)	+7.001(68)	8.004(61)	59.50(15)
Overall (Night)	-3.888(10)	+7.037(27)	8.040(24)	59.459(57)

Table 2.13: Systematic Effects: Standard Stars with PMTs

Star	Parameter	Detector 1	Detector 2	Detector 1,2	Detector Mean
HD 212311	$S_{\text{PEM}} (\times 10^{-6})$	-95(74)	-32(61)	-58(57)	-58(37)
...	$S_{\phi} (\times 10^{-6})$	-65(59)	+24(30)	-15(45)	0(32)
HD 204827	$S_{\text{PEM}} (\times 10^{-6})$	+540(180)	+550(340)	+487(36)	+490(12)
...	$S_{\phi} (\times 10^{-6})$	-269(28)	+320(210)	+30(110)	-240(100)

$$\hat{\sigma}_P = \left[\left(\frac{P^{\frac{1}{2}}}{a} \right)^2 + \sigma_{P0}^2 \right]^{\frac{1}{2}}. \quad (2.9)$$

Here, a is a scaling factor and σ_{P0} is the noise floor of the instrument, which is added in quadrature to the photon shot noise component. This noise floor appears to be eight parts in ten million. The fitting was performed using a least-squares approach. However, since the data span five orders of magnitude in polarization, the residuals to be minimized are given by

$$\text{SSE} = \sum_i \left(\frac{\sigma_{Pi} - \hat{\sigma}_P}{\sigma_{Pi}} \right)^2. \quad (2.10)$$

The stars observed with APDs are all roughly the same visual magnitude. However, the precision achieved on the weakly polarized HD 212311, observed with PMTs, is worse than for the stars observed with APDs. HD 212311 is roughly 5 magnitudes fainter than its bright counterparts (Table 2.2), so the precision is expected to be $(10^{0.4 \times 5})^{\frac{1}{2}} = 10$ times worse, as observed. Thus, the scaling factor determined for the APD stars, a , will be an order of magnitude different from the scaling factor for the PMT stars. This is why the PMT stars were excluded from the above fit. However, precision on the strongly polarized HD 204827 is surprisingly consistent with the slope for the bright stars. This is most likely due to the larger dataset obtained on HD 204827.

2.8 Comparison to Literature

2.8.1 Unpolarized Standard Stars

Individual measurements and nightly mean polarization for most stars are shown in Figures 2.11 to 2.30. Those that are not displayed generally have only one night of observations. We compare

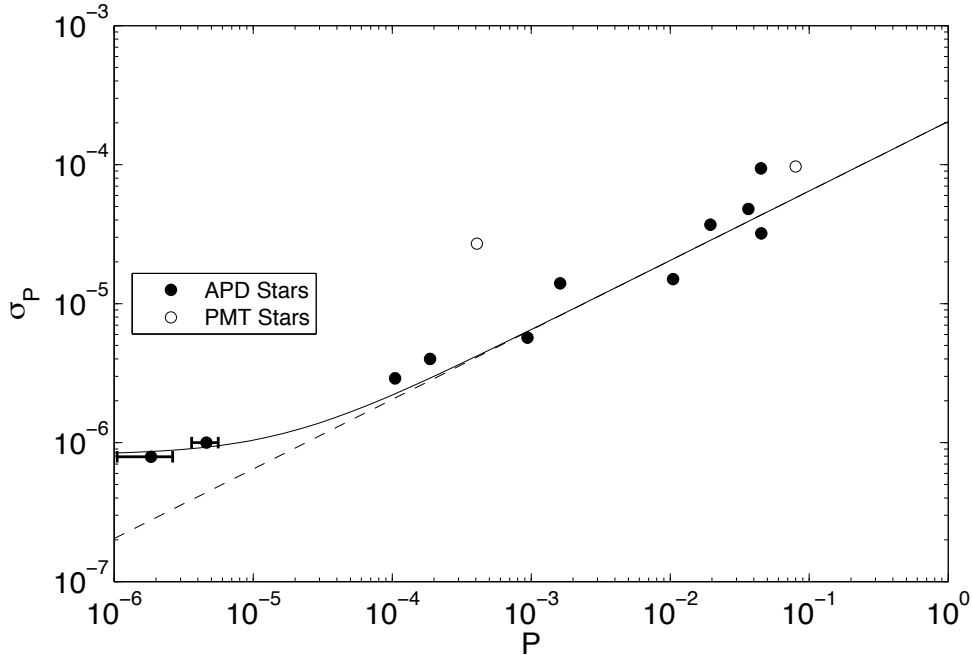


Figure 2.10: Run-averaged precision as a function of stellar polarization. Photon shot noise considerations predict precision proportional to the square root of polarization, which is observed. The solid line is a fit to the data with power law slope $1/2$ plus the quadrature addition of an instrumental noise floor, while the dashed line is the $P^{1/2}$ term.

our results to the polarization catalog of Heiles (2000) and to HLB 06 in Figure 2.31. To determine polarization for each star, Heiles (2000) take the weighted mean polarization from different authors. The weights are the inverse square of the uncertainties from each author. Uncertainty in stellar polarization in Heiles (2000) is the square root of the sum of squares of residuals between each author’s polarization and the Heiles (2000) mean polarization.

Uncertainty in degree of polarization is listed nightly for strongly polarized stars in Table 3 of HLB 06 (HD 7927, HD 147084, HD 154445, and HD 187929). To determine run-averaged uncertainty for these stars, we first convert their degree, position angle, and uncertainties to Q/I , U/I , and associated uncertainties. We then perform a weighted mean for each Stokes parameter separately, where the weights are the inverse square of the nightly uncertainties in those parameters. Since degree of polarization is defined to be a positive quantity, taking the mean degree of polarization from the ensemble of nights would be incorrect.

The degree of polarization measured by POLISH is plotted as open stars, and stellar polarization increases toward the bottom of the plot. Our precision in the degree of polarization is plotted as

filled black circles, precision values computed from HLB 06 are light grey diamonds, and Heiles (2000) precision values are dark grey squares. The horizontal line before the second star from the bottom in Figure 2.31 separates those stars observed with APDs (at the top) from those observed with PMTs (at the bottom).

The rightmost column of the figure shows the position angle of net polarization, where north is at the top and east is at the left of the plots. Black lines indicate position angle measured with POLISH, HLB 06 position angles are light grey lines, and Heiles (2000) position angles are dark grey lines. Agreement between the data sets for stars with low polarization is of course poor, because position angle of net polarization is meaningless for these stars. As stellar polarization increases, agreement in position angle also increases. Since agreement between our measurements and the literature regarding degree of polarization is not our primary objective, accuracy in our observations is assessed by agreement in position angle of polarization.

The unpolarized standard stars observed in order to determine telescope polarization, HR 5854 (α Ser, HD 140573) and HR 8974 (γ Cep, HD 222404), have run-averaged polarimetric precision of one part per million or better. This was our precision goal for bright, unpolarized stars. The precision achieved by PlanetPol on these stars is comparable to our results. However, we have improved the precision on these stars by three orders of magnitude with respect to the Heiles (2000) catalog. HR 8974 is known to harbor an extrasolar planet with a minimum mass of 1.60 ± 0.13 Jupiter masses, a period of 902.9 ± 3.5 days, and a semimajor axis of 2.044 ± 0.057 AU (Neuhäuser et al. 2006). We expect the amplitude of the planetary polarimetric signal to be of order 10^{-8} or less and consequently undetectable.

2.8.2 Weakly Polarized Standard Stars

We have improved the polarimetric precision achieved on HD 9270 (η Psc) by an order of magnitude with respect to Heiles (2000). Precision on γ Oph (HD 161868) and Algenib (γ Peg, HD 886), however, is only slightly better than tabulated in Heiles (2000). It is expected that longer integration on these stars will improve this precision. Finally, the precision achieved on u Her (SAO 65913) has been improved by two orders of magnitude from Heiles (2000). There is an order of magnitude improvement in precision on HD 212311 with respect to Heiles (2000).

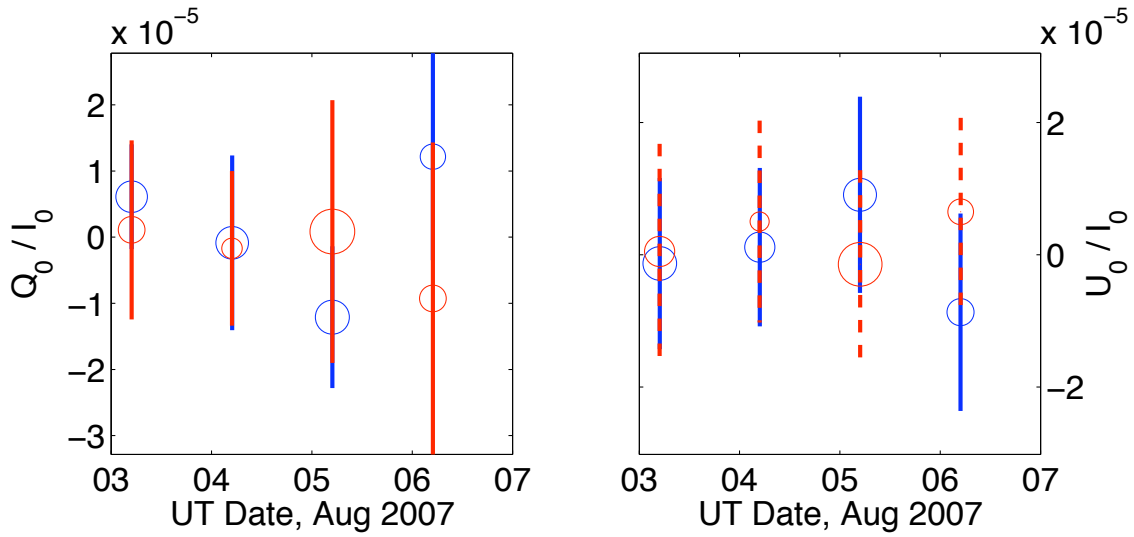


Figure 2.11: Nightly mean polarization of the unpolarized star HR 5854. This star was observed with APDs, and the data are plotted after calibration of the PEM position, peak retardance, gain, and telescope polarization. Solid blue lines indicate observations by the blue enhanced APD1, while dotted red lines are observed with the red enhanced APD2.

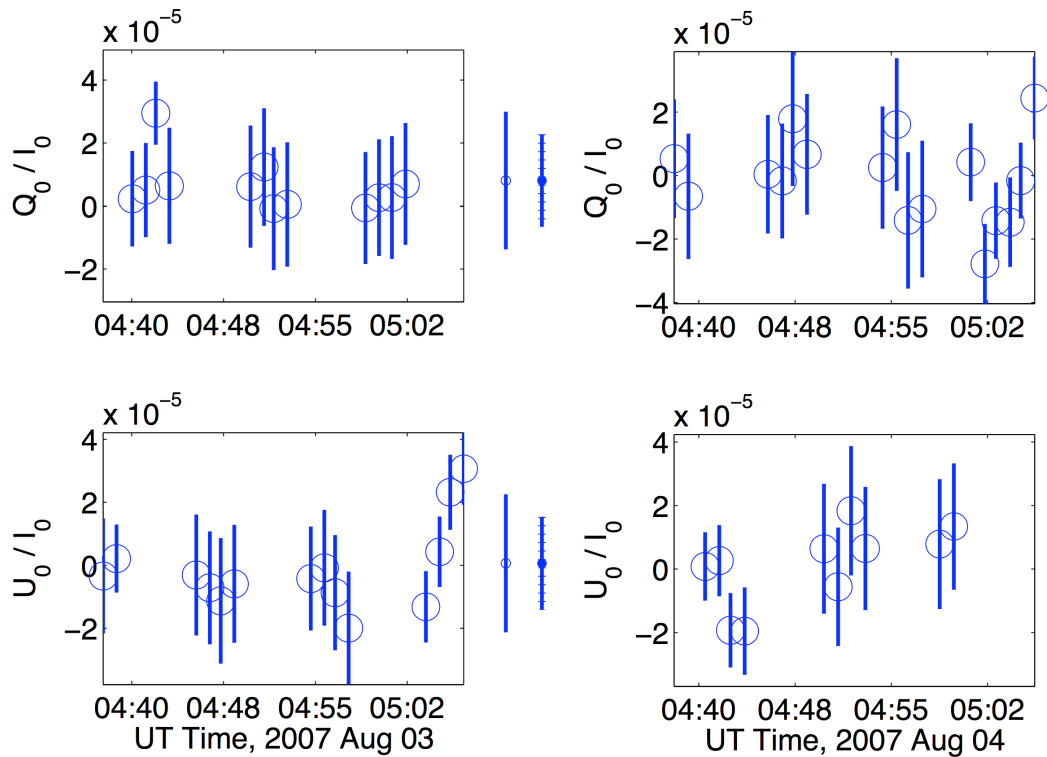


Figure 2.12: Intra-night observations of HR 5854 with APD1, UT 2007 Aug 3 and 4. Observed noise calculated from fluctuations in AC and DC levels is given by error bars on individual data points (Figure 2.5 and Equation 2.5c). Area of data points is proportional to the number of detected photons. Theoretical detector noise (Equation C11) is given as vertical lines outside the plot boxes, while theoretical photon shot noise (Equation 2.5a) is represented by dashed vertical lines outside the plot boxes. These conventions are used throughout this chapter.

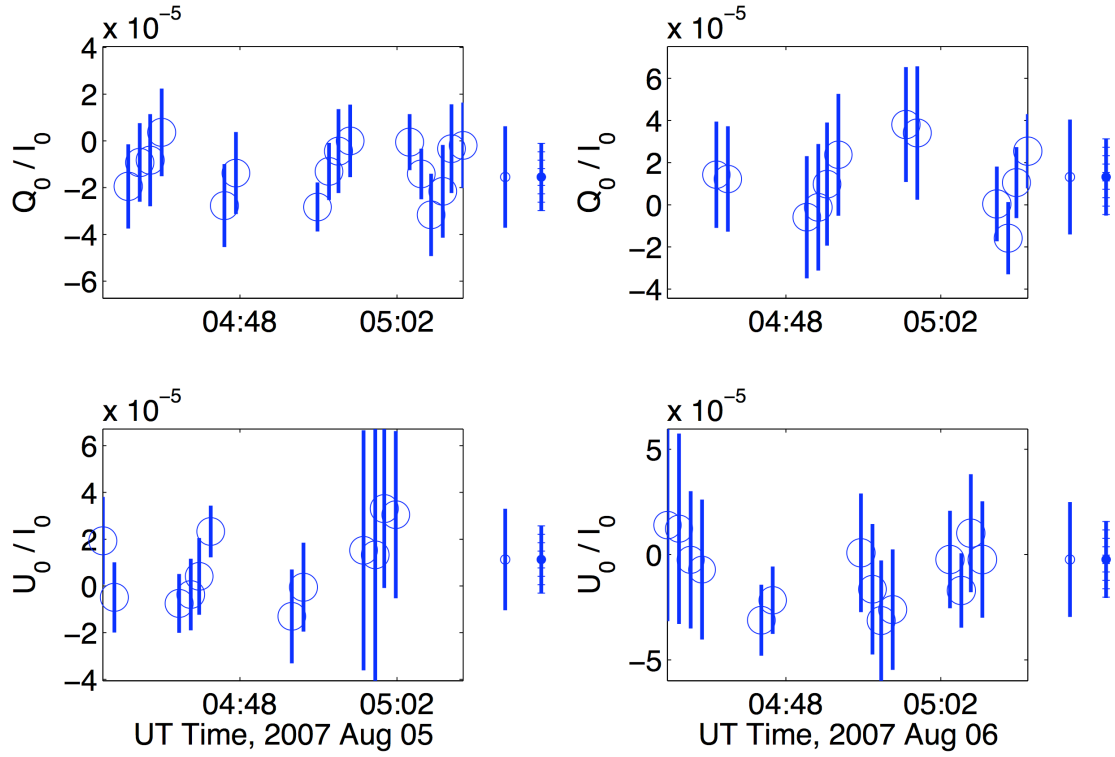


Figure 2.13: Intra-night observations of HR 5854 with APD1, UT 2007 Aug 5 and 6.

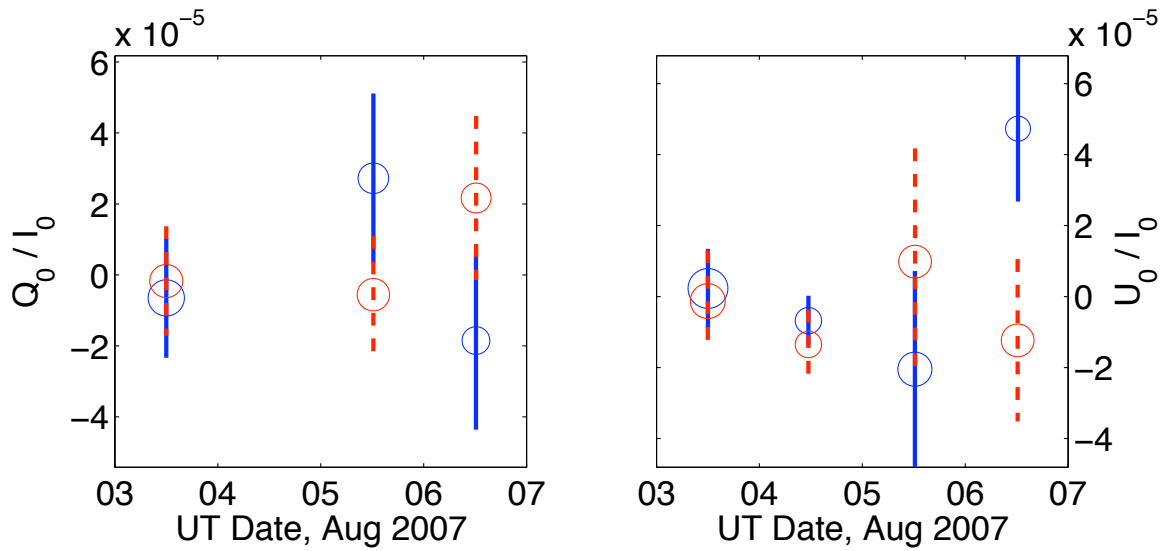


Figure 2.14: Nightly mean polarization of the unpolarized star HR 8974 after calibration of the PEM position, peak retardance, gain, and telescope polarization.

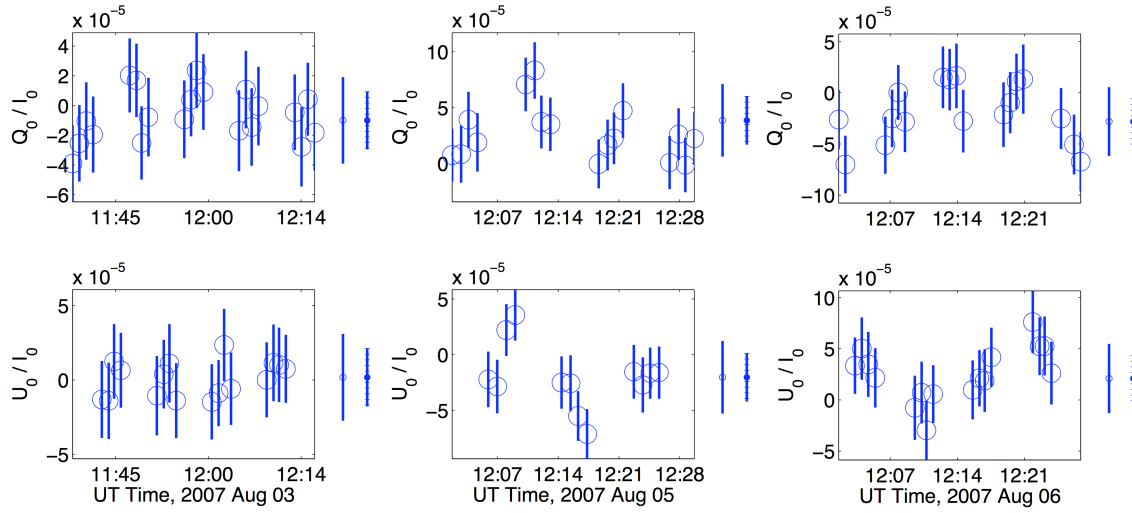


Figure 2.15: Intra-night observations of HR 8974 with APD1, UT 2007 Aug 3, 5, and 6.

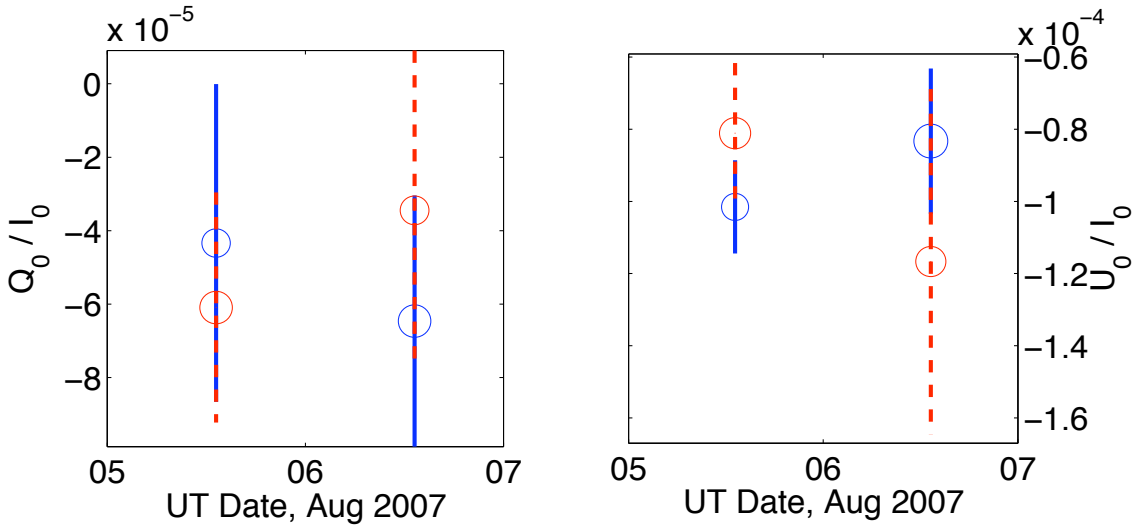


Figure 2.16: Nightly mean polarization of the weakly polarized star HD 9270 after calibration of the PEM position, peak retardance, gain, and telescope polarization.

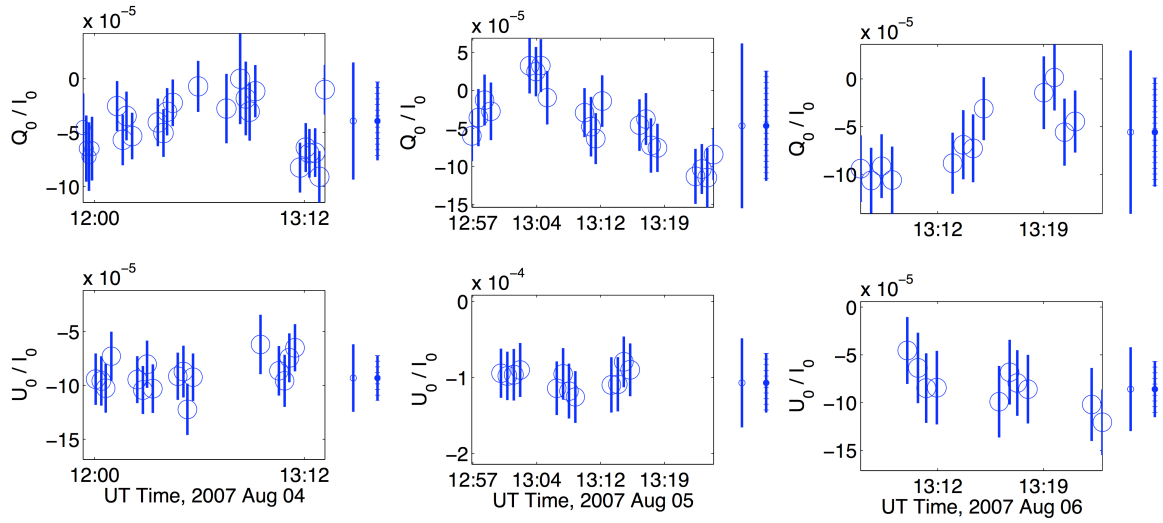


Figure 2.17: Intra-night observations of HD 9270 with APD1, UT 2007 Aug 4, 5, and 6.

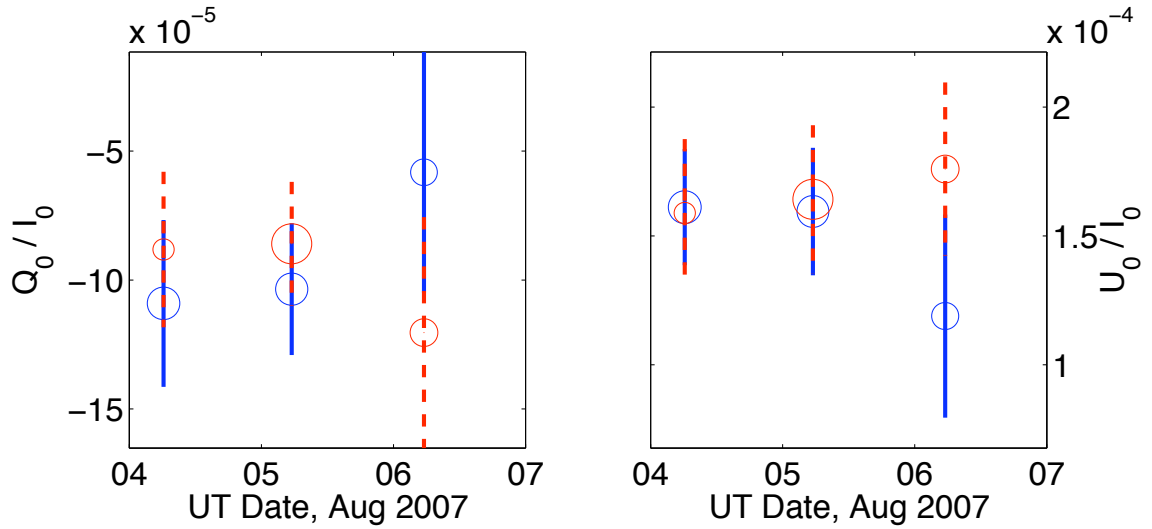


Figure 2.18: Nightly mean polarization of the weakly polarized star γ Oph after calibration of the PEM position, peak retardance, gain, and telescope polarization.

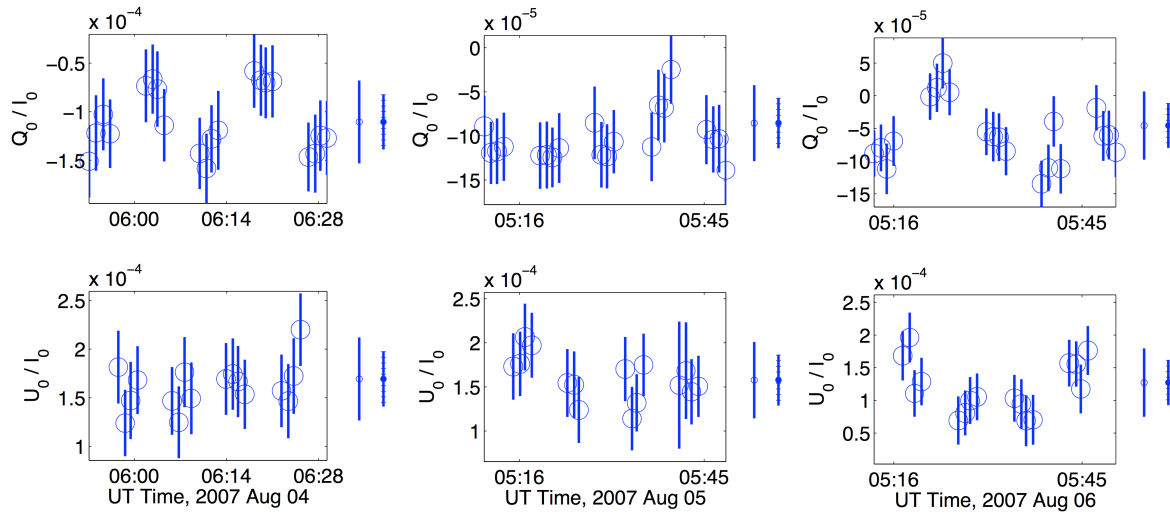


Figure 2.19: Intra-night observations of γ Oph with APD1, UT 2007 Aug 4, 5, and 6.

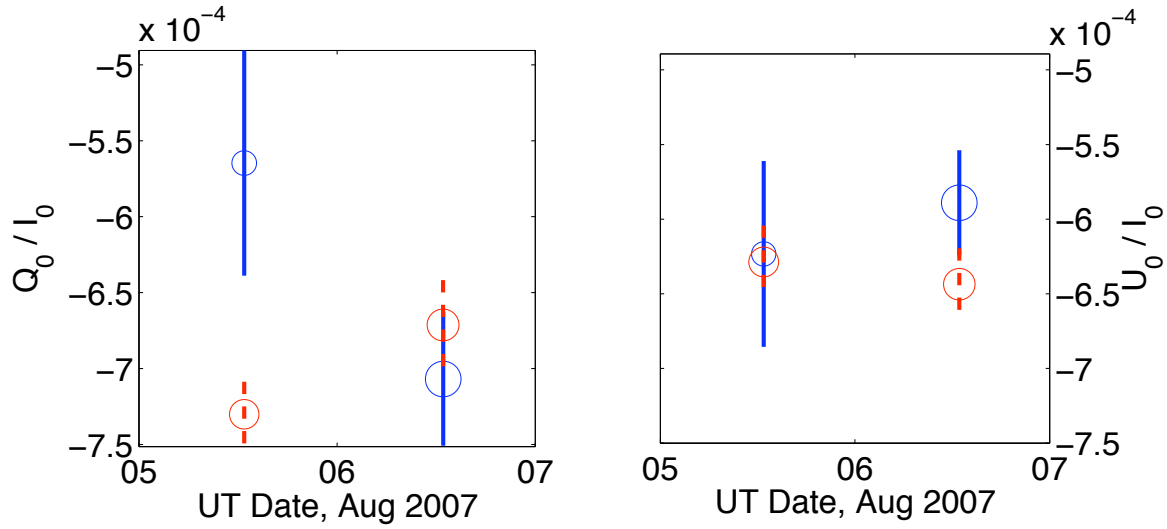


Figure 2.20: Nightly mean polarization of the weakly polarized star Algenib after calibration of the PEM position, peak retardance, gain, and telescope polarization.

Table 2.14: Corrections for Absolute Polarization

Parameter	APD 1	APD 2	Mean	PMT 1	PMT 2	Mean
$P_{\text{POLISH}} - P_{\text{Heiles}} (\times 10^{-4})$	1.8(3.6)	1.8(3.8)	1.8438(21)	8(35)	9(37)	8.84(53)
$P_{\text{POLISH}}/P_{\text{Heiles}}$	0.843(87)	0.842(62)	0.84224(69)	0.690(20)	0.672(22)	0.6811(89)

2.8.3 Strongly Polarized Standard Stars

Precision on HD 157999 (σ Oph) has been improved by an order of magnitude, while precision on HD 187929 (η Aql) is comparable between our measurements, those from PlanetPol, and those from Heiles (2000). Our precision on HD 7927 (ϕ Cas) is comparable to that from PlanetPol, and we improve the precision with respect to Heiles (2000) by an order of magnitude. We assume that the discrepancy between the HLB 06 position angle ($42.18 \pm 0.01^\circ$) and our measurements for HD 7927 is simply a typographical error in their paper. We expect that their intended value is 92.18° , which is close to our value.

While precision on HD 147084 (o Sco) from PlanetPol is a full order of magnitude better than from our measurements, this is likely a result of our lower integration time. Precision between Heiles (2000) and our measurements is comparable. Precision on HD 154445 between our measurements, PlanetPol, and Heiles (2000) lie within an order of magnitude of each other, which may suggest intrinsic variability of the source. We only have one night of data on this star, so this possibility will not be investigated in our forthcoming paper. Finally, we improve the precision on HD 204827 by an order of magnitude with respect to Heiles (2000).

2.8.4 Absolute Polarization

To find the difference in absolute polarization between our measurements from each detector and Heiles (2000), we take the mean weighted difference for each Stokes parameter. The weight used is the inverse square of the Heiles (2000) uncertainty. The results are shown in Table 2.14. The individual offset for each detector is consistent with zero, but the mean value for each detector type is significant. To determine the consistency of our polarimetric gain factor G_P with the Heiles (2000) polarizations for each detector, we take the mean weighted ratio of the Heiles (2000) Stokes parameters with respect to our measured Stokes parameters. We find a different gain factor for each detector type is necessary to make absolute polarization consistent. However, multiplying our measurements by this gain factor would increase uncertainty unnecessarily. Since we are interested in relative polarization variability over time, we do not apply this gain factor.

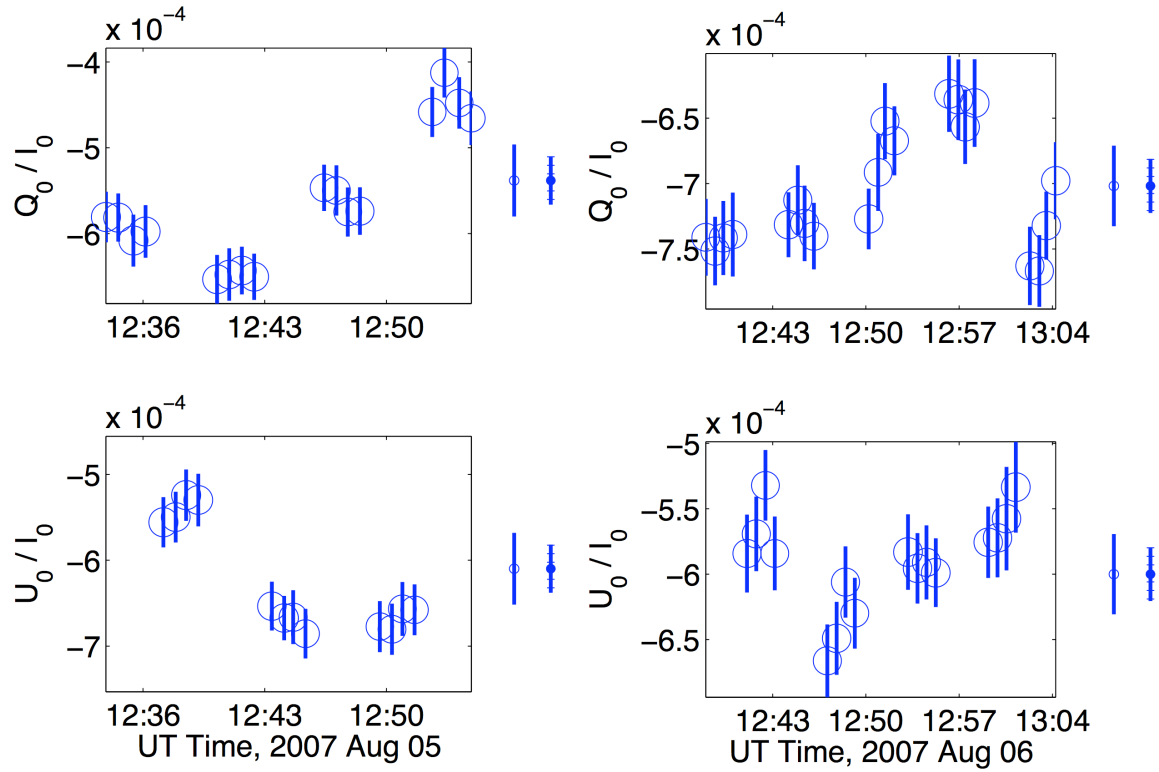


Figure 2.21: Intra-night observations of Algib with APD1, UT 2007 Aug 5 and 6.

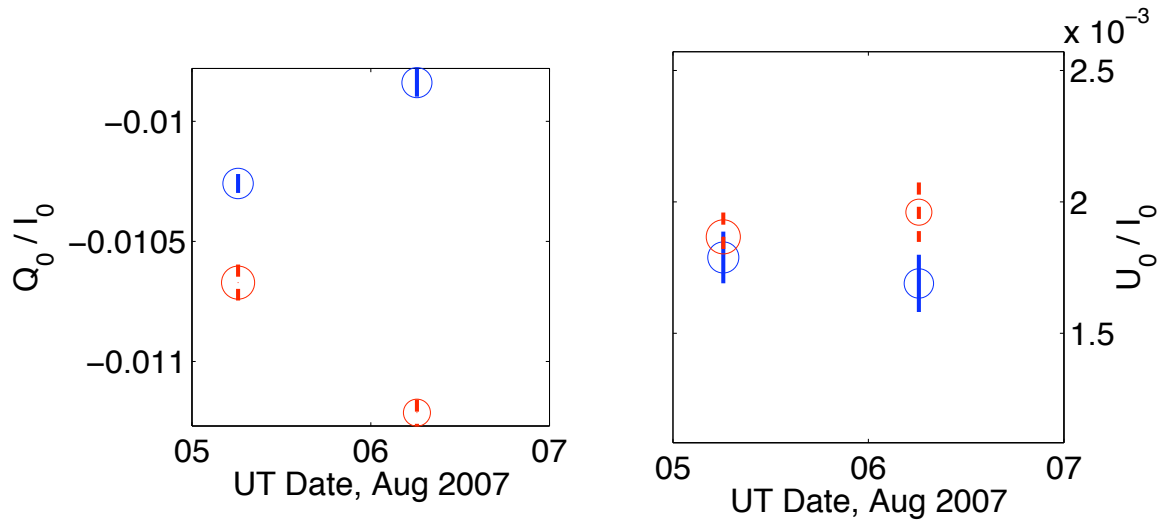


Figure 2.22: Nightly mean polarization of the strongly polarized star HD 157999 after calibration of the PEM position, peak retardance, gain, and telescope polarization.

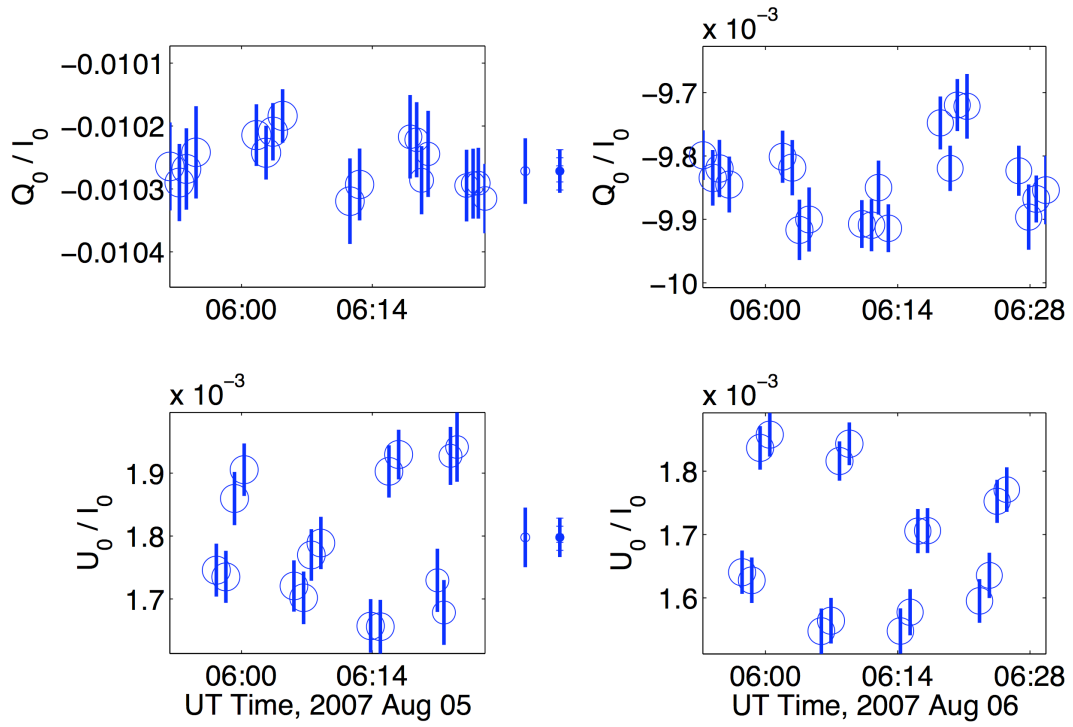


Figure 2.23: Intra-night observations of HD 157999 with APD1, UT 2007 Aug 5 and 6.

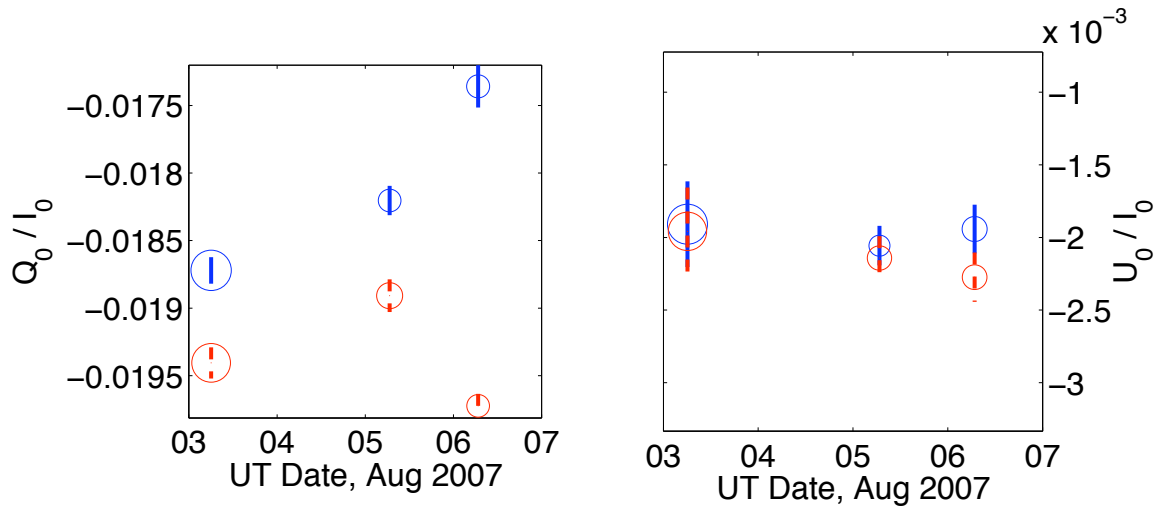


Figure 2.24: Nightly mean polarization of the strongly polarized star HD 187929 after calibration of the PEM position, peak retardance, gain, and telescope polarization.

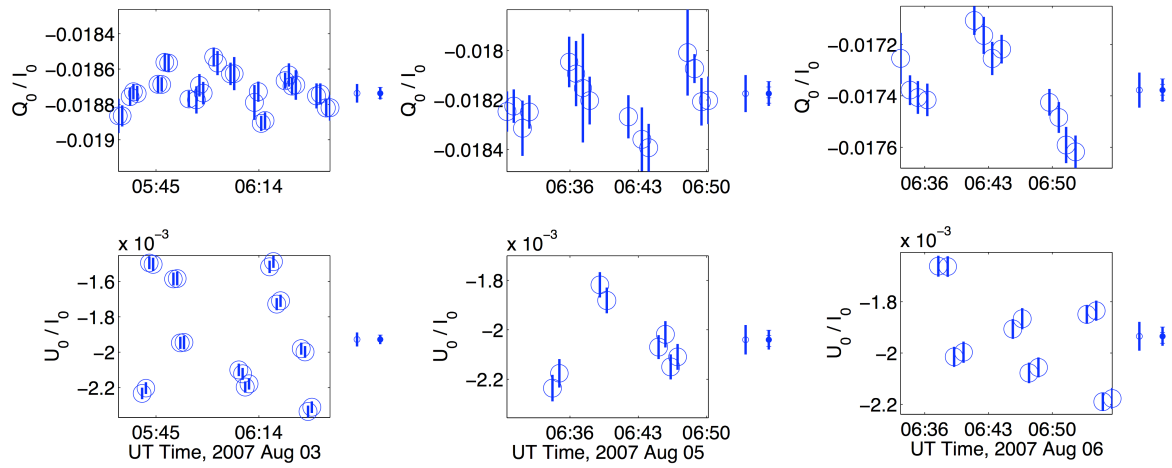


Figure 2.25: Intra-night observations of HD 187929 with APD1, UT 2007 Aug 3, 5, and 6.

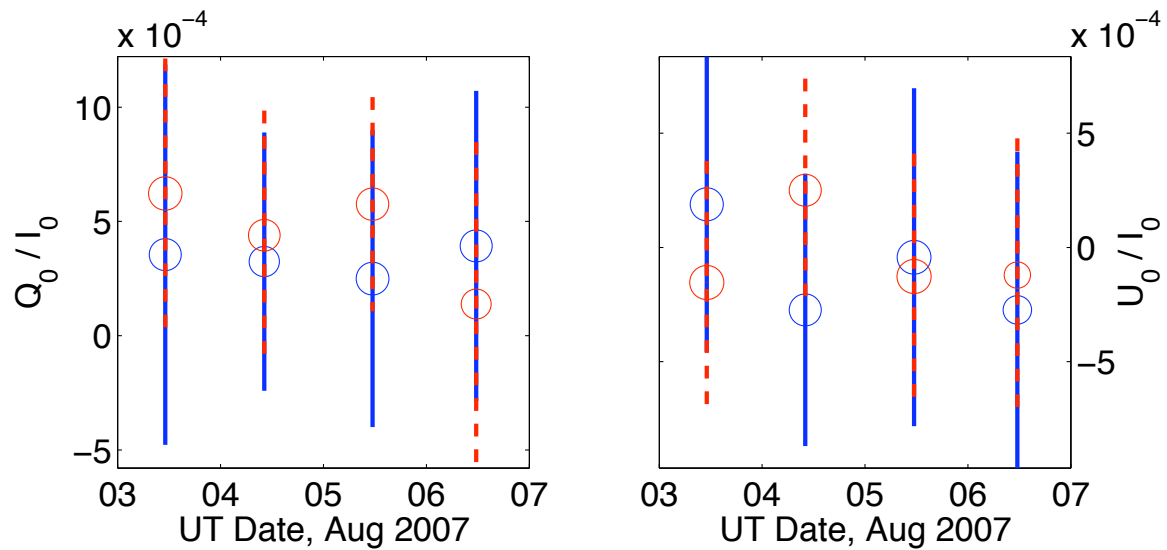


Figure 2.26: Nightly mean polarization of the weakly polarized star HD 212311 after calibration of the PEM position, peak retardance, gain, and telescope polarization.

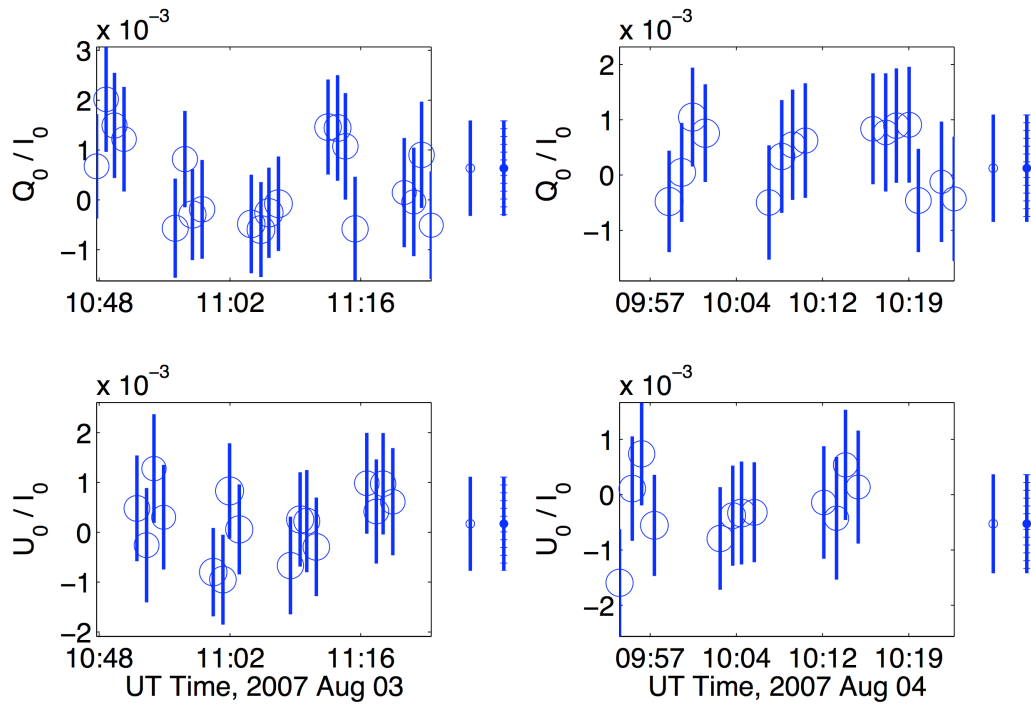


Figure 2.27: Intra-night observations of HD 212311 with PMT1, UT 2007 Aug 3 and 4.

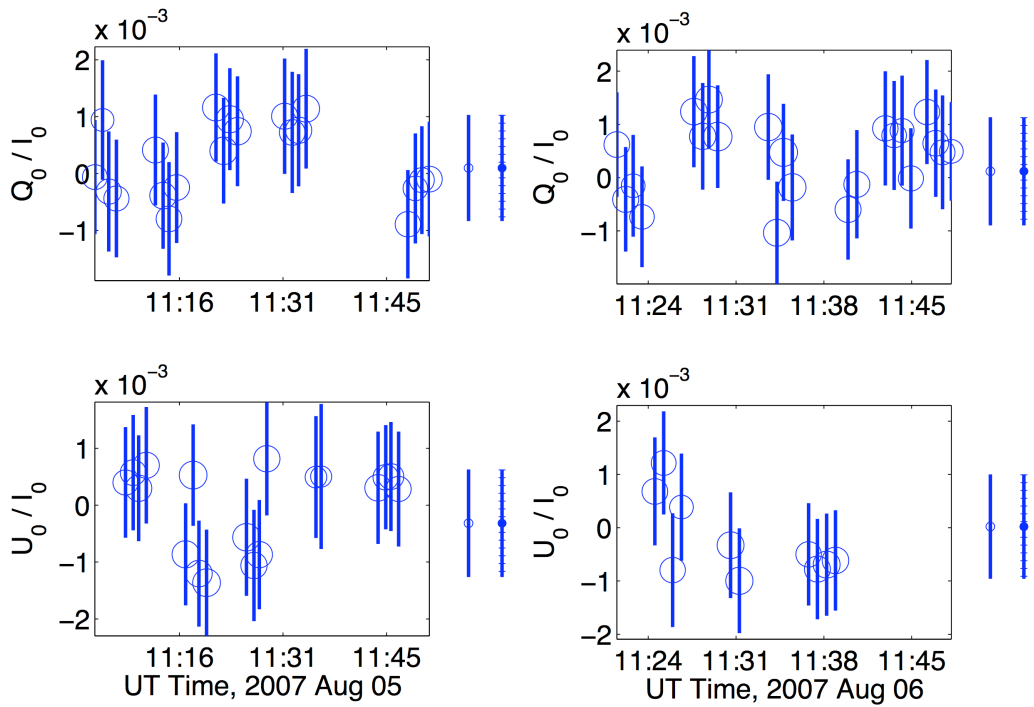


Figure 2.28: Intra-night observations of HD 212311 with PMT1, UT 2007 Aug 5 and 6.

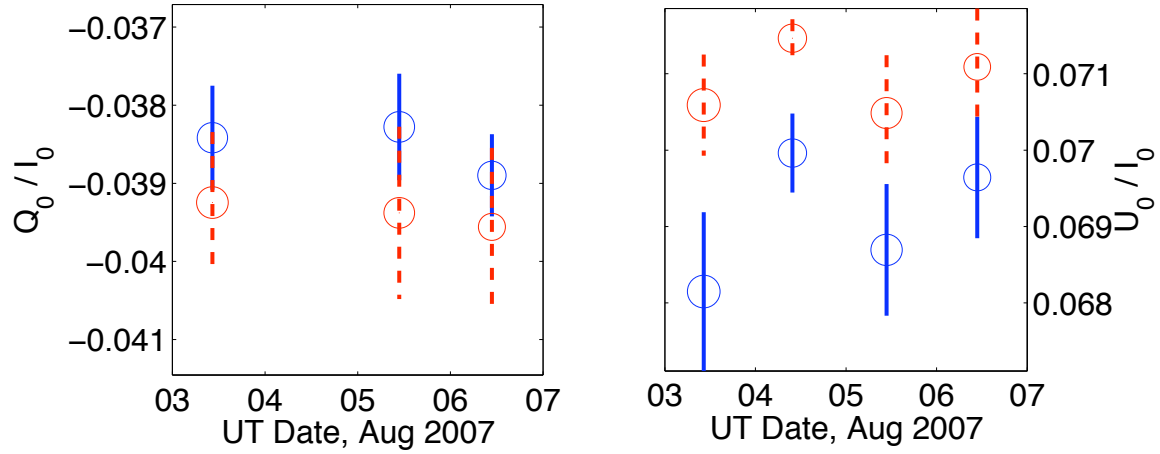


Figure 2.29: Nightly mean polarization of the strongly polarized star HD 204827 after calibration of the PEM position, peak retardance, gain, and telescope polarization.

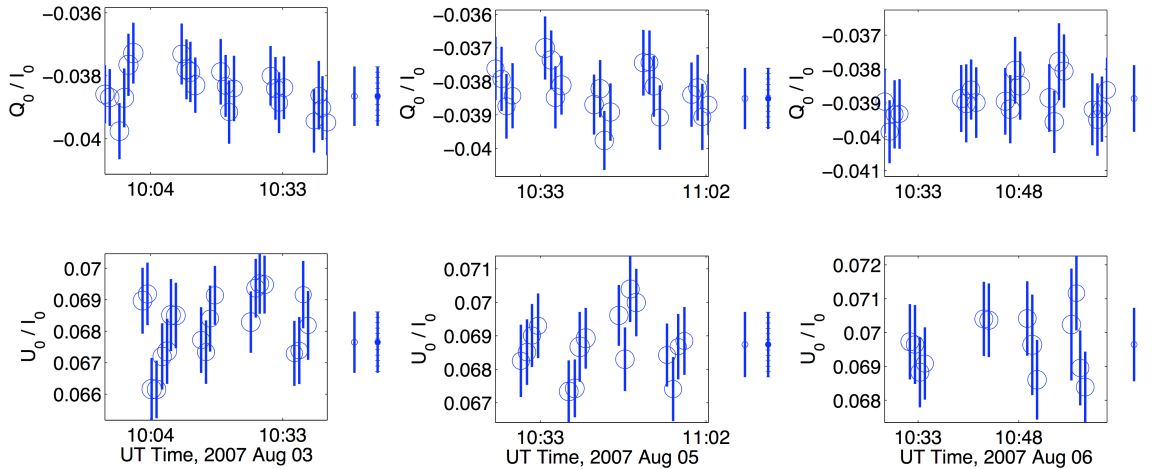


Figure 2.30: Intra-night observations of HD 204827 with PMT1, UT 2007 Aug 3, 5, and 6.

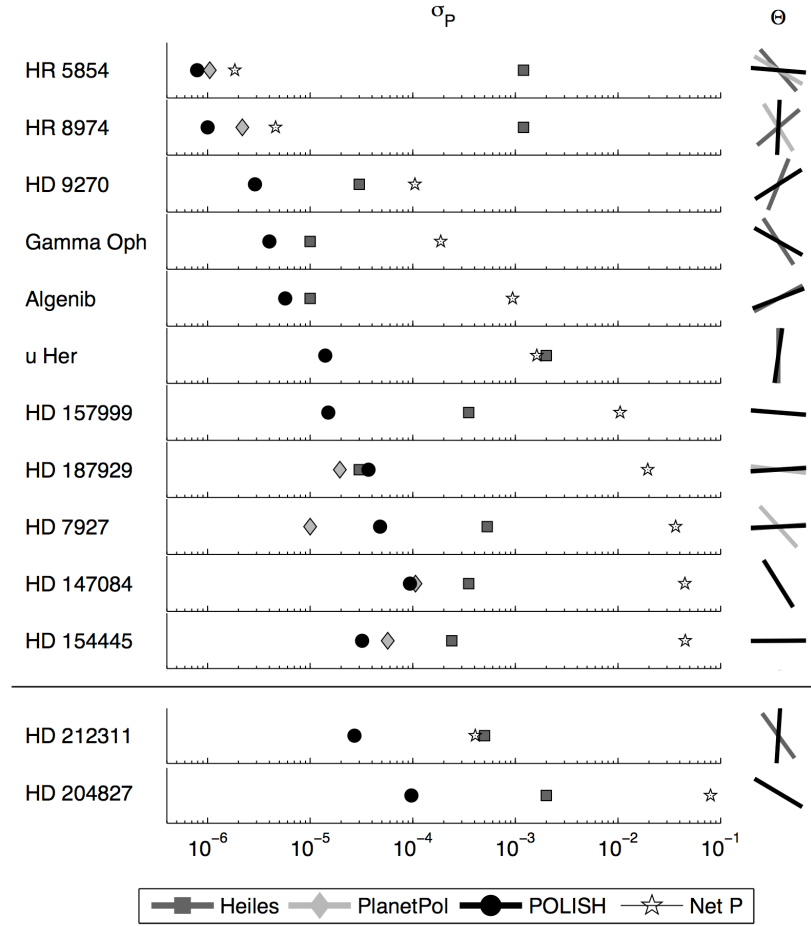


Figure 2.31: Precision achieved on standard stars compared with HLB 06 and Heiles (2000). Stars above the horizontal line across the figure have been observed with APDs, and the two stars below this line have been observed with PMTs. For each detector, stars are listed from top to bottom in order of increasing net polarization according to our measurements.

2.8.5 Interstellar Polarization

Serkowski et al. (1975) determined empirically that stars for which interstellar polarization dominates will have a distinctive spectrum of polarization versus wavelength:

$$\frac{P(\lambda)}{P_{\max}} = \exp \left[-1.15 \ln^2 \left(\frac{\lambda_{\max}}{\lambda} \right) \right]. \quad (2.11)$$

Here, P_{\max} is the maximum polarization as a function of wavelength and λ_{\max} is the wavelength of maximum polarization. Interstellar polarization is thought to be caused by preferential extinction of starlight by aligned, non-spherical dust grains. The component of starlight with electric field vector parallel to the long axis of aligned dust grains will suffer greater extinction than the component of

the electric field perpendicular to the long axis of the grains (Davis & Greenstein 1951). The exact cause of grain alignment is debated, but presence of magnetic fields is a significant component.

Of the stars observed in Table 2.2, the following have been investigated by Serkowski et al. (1975): HD 7927, HD 147084, HD 154445, HD 157999, HD 187929, and HD 204827. All of these have wavelength dependence of polarization indicative of interstellar polarization, which implies that intrinsic polarization does not dominate for these stars. Indeed, Schmidt et al. (1992) find good fits of their data to interstellar polarization curves for HD 7927, HD 154445, and HD 204827.

2.9 Discussion

We have commissioned a high precision, integrated light polarimeter in order to detect variability in the optical, linear polarization of high mass X-ray binaries. This variability should be indicative of system inclination, and high precision monitoring is hoped to constrain the black hole mass in these systems. While results from observations of Cygnus X-1 will be in Chapter 4, we report on the high precision attained on standard stars.

Noise on individual measurements of most stars is comparable to photon shot noise (Figures 2.11 to 2.30). When combining measurements, we obtained precision on most stars that is comparable to PlanetPol, a similar instrument mounted on the William Herschel Telescope (HLB 06). Precision achieved on unpolarized stars is up to three orders of magnitude better than listed in the combined polarimetric catalogs of Heiles (2000), and precision on strongly polarized stars is improved by up to an order of magnitude. The large improvement in polarimetric precision arises from the combination of large telescope aperture, a high-quality polarization modulator, and high frequency modulation.

We find night-to-night precision of three to ten parts per million on bright, weakly polarized standard stars ($10^{-4} < P < 10^{-3}$). This precision increases as $\sigma_P \propto P^{\frac{1}{2}}$, where it reaches about one part in 10^4 for stars with P between one and ten percent. Thus, night-to-night precision scales as expected from photon shot noise statistics. Consultation of Tables 2.10 and 2.13 shows that systematic effects reveal themselves at the level of $\approx 1\%$ of the measured polarization. The night-to-night noise floor of the instrument appears to be eight parts in ten million even in the presence of telescope polarization on the order of one part in 10^4 . High precision monitoring of stellar variability is discussed in the next chapter.

References

- Aspin, C., Simmons, J. F. L., & Brown, J. C. 1981, MNRAS 194, 283.
- Bastien, P., Drissen, L., Menard, F., Moffat, A. F. J., Robert, C. & St-Louis, N. 1988, AJ 95, 900.
- Brown, J. C., Ignace, R., & Cassinelli, J. P. 2000, A&A 356, 619.
- Davis, L., Jr. & Greenstein, J. L. 1951, ApJ 114, 206.
- Dolan, J. F. & Tapia, S. 1989, ApJ 344, 830.
- Friend, D. B. & Cassinelli, J. P. 1986, ApJ 303, 292.
- Gies, D. R., and 10 coauthors. 2003, ApJ 583, 424.
- Hamamatsu Photonics K.K. 1999, "Photomultiplier Tubes: Basics and Applications", 2nd Ed.
- Heiles, C. 2000, AJ 119, 923.
- Hough, J. H., Lucas, P. W., Bailey, J. A., Tamura, M., Hirst, E., Harrison, D., & Bartholomew-Biggs, M. 2006, PASP 118, 1302.
- Hsu, J.-C. & Breger, M. 1982, ApJ 262, 732.
- Kemp, J. C. 1969, J. Opt. Soc. Am. 59, 950.
- Kemp, J. C., Barbour, M. S., Parker, T. E., & Herman, L. C. 1979, ApJ 228, L23.
- McClintock, J. E., Shafee, R., Narayan, R., Remillard, R. A., Davis, S. W., & Li, L.-X. 2006, ApJ 652, 518.
- Milgrom, M. 1979, A&A 76, 338.
- Oke, J. B. 1961, ApJ 133, 90.
- Schmidt, G. D., Elston, R., & Lupie, O. 1992, AJ 104, 1563.
- Serkowski, K., Mathewson, D. S., & Ford, V. L. 1975, ApJ 196, 261.
- Wolinski, K. G., Dolan, J. F., Boyd, P. T., Biggs, J. D., Nelson, M. J., Percival, J. W., Taylor, M., & van Citters, G. W. 1996, ApJ 457, 859.
- Ziólkowski, J. 2005, MNRAS 358, 851.

2.10 Appendix A: Mueller Matrix for Lab Tests

Mueller matrices describe how the polarization state of incident light is modified by optical components. For the lab tests in section 2.5.2, the polarizing components employed are a linear polarizer and Wollaston prism, so the Mueller matrix of the system is

$$M = M_W \times T_{-\psi} \times M_{\text{pol}} \times T_{\psi} \quad (\text{A1})$$

Starting from the left hand side of Equation A1, the matrices represent the Wollaston, the rotation matrix for the linear polarizer at angle ψ with respect to the Wollaston axis, and the Mueller matrix for the polarizer. Incident light is first affected by the Mueller matrix at the end of the equation, and the incident polarization state is successively modified by the matrices to the left. That is,

$$\begin{pmatrix} I_{\text{obs}} \\ Q_{\text{obs}} \\ U_{\text{obs}} \\ V_{\text{obs}} \end{pmatrix} = M \begin{pmatrix} I_0 \\ Q_0 \\ U_0 \\ V_0 \end{pmatrix} \quad (\text{A2})$$

where I_0 , Q_0 , U_0 , and V_0 are the Stokes parameters of the incident light and I_{obs} , Q_{obs} , U_{obs} , and V_{obs} are the observed Stokes parameters. For this system,

$$\begin{aligned} \begin{pmatrix} I_{\text{obs}} \\ Q_{\text{obs}} \\ U_{\text{obs}} \\ V_{\text{obs}} \end{pmatrix} &= \frac{T}{2} \begin{pmatrix} 1 & \pm 1 & 0 & 0 \\ \pm 1 & 1 & 0 & 0 \\ 0 & 0 & 0 & 0 \\ 0 & 0 & 0 & 0 \end{pmatrix} \times \begin{pmatrix} 1 & 0 & 0 & 0 \\ 0 & \cos 2\psi & -\sin 2\psi & 0 \\ 0 & \sin 2\psi & \cos 2\psi & 0 \\ 0 & 0 & 0 & 1 \end{pmatrix} \\ &\times \begin{pmatrix} 1 & 1 & 0 & 0 \\ 1 & 1 & 0 & 0 \\ 0 & 0 & 0 & 0 \\ 0 & 0 & 0 & 0 \end{pmatrix} \times \begin{pmatrix} 1 & 0 & 0 & 0 \\ 0 & \cos 2\psi & \sin 2\psi & 0 \\ 0 & -\sin 2\psi & \cos 2\psi & 0 \\ 0 & 0 & 0 & 1 \end{pmatrix} \times \begin{pmatrix} I_0 \\ Q_0 \\ U_0 \\ V_0 \end{pmatrix} \quad (\text{A3}) \end{aligned}$$

where $T = 25 \pm 2\%$ is the transmission of the polarizer. A perfect polarizer is assumed, which passes no light with polarization perpendicular to its axis. The PEM was disabled for this test, and only

the DC reading from the voltmeters was used. Thus, the average intensity is

$$I_{\text{obs}} = \frac{T}{2} [I_0 (1 + \cos 2\psi) + Q_0 \cos 2\psi (1 + \cos 2\psi) + U_0 \sin 2\psi (1 + \cos 2\psi)] \quad (\text{A4})$$

The LED is essentially unpolarized, so $Q_0 \approx U_0 \approx 0$ and Equation A4 reduces to

$$I \approx TI_0 (1 + \cos 2\psi) \quad (\text{A5})$$

2.11 Appendix B: Mueller Matrix for POLISH

In general, the Mueller matrix of POLISH is given by

$$M_{\text{POLISH}} = T_{-\phi} \times M_{\text{D}} \times M_{\text{L}} \times M_{\text{W}} \times M_{\text{B}} \times T_{-\theta_{\text{PEM}}} \times M_{\text{PEM}} \times T_{\theta_{\text{PEM}}} \times T_{\phi} \times M_{\text{T}} \quad (\text{B1})$$

Starting from the left hand side of Equation B1, the matrices are the rotation matrix for Cassegrain ring angle ϕ , the Mueller matrices for the detector window, field lenses, Wollaston prism, and beamsplitter, the rotation matrix for PEM angle $\theta \equiv \theta_{\text{PEM}}$, the Mueller matrix for the PEM, and the Mueller matrix for the telescope. Subtraction of telescope polarization is necessary to calibrate for M_{T} .

Since the PEM and Wollaston prism convert the polarization of the incident light into intensity modulation, the polarization state of light past the Wollaston is not our concern. The reflection of light off the beamsplitter is at nearly 90° and is stable during observations, so any polarization imparted to the light by the beamsplitter is just a constant offset to the polarization. Therefore, we only consider the throughput of the detector window, field lenses, and beamsplitter. We denote the throughput of the instrument as E , and it is given in section 2.3. The POLISH Mueller matrix becomes

$$\begin{aligned}
M_{\text{POLISH}} = E & \begin{pmatrix} 1 & 0 & 0 & 0 \\ 0 & \cos 2\phi & -\sin 2\phi & 0 \\ 0 & \sin 2\phi & \cos 2\phi & 0 \\ 0 & 0 & 0 & 1 \end{pmatrix} \times \begin{pmatrix} 0.5 & \pm 0.5 & 0 & 0 \\ \pm 0.5 & 0.5 & 0 & 0 \\ 0 & 0 & 0 & 0 \\ 0 & 0 & 0 & 0 \end{pmatrix} \times \begin{pmatrix} 1 & 0 & 0 & 0 \\ 0 & \cos 2\theta & -\sin 2\theta & 0 \\ 0 & \sin 2\theta & \cos 2\theta & 0 \\ 0 & 0 & 0 & 1 \end{pmatrix} \\
& \times \begin{pmatrix} 1 & 0 & 0 & 0 \\ 0 & 1 & 0 & 0 \\ 0 & 0 & \cos \beta & \sin \beta \\ 0 & 0 & -\sin \beta & \cos \beta \end{pmatrix} \times \begin{pmatrix} 1 & 0 & 0 & 0 \\ 0 & \cos 2\theta & \sin 2\theta & 0 \\ 0 & -\sin 2\theta & \cos 2\theta & 0 \\ 0 & 0 & 0 & 1 \end{pmatrix} \times \begin{pmatrix} 1 & 0 & 0 & 0 \\ 0 & \cos 2\phi & \sin 2\phi & 0 \\ 0 & -\sin 2\phi & \cos 2\phi & 0 \\ 0 & 0 & 0 & 1 \end{pmatrix} \\
& \tag{B2}
\end{aligned}$$

The instantaneous retardance of the PEM is given by $\beta = \alpha + \beta_0 \sin \omega t$. The retardance offset of the PEM, α , is assumed to be negligible from calibration by Hinds Instruments, Inc. Note that $\omega = 2\pi \times 50.12$ kHz. The top sign in the Wollaston matrix (+) indicates the left beam which reaches detector 2, and the bottom sign (-) represents the right beam which reaches detector 1. The instrumental Mueller matrix, listed by columns one through four, now becomes

$$M_{\text{POLISH}}(:, 1) = E/2 \begin{pmatrix} 1 \\ \pm \cos 2\phi \\ \pm \sin 2\phi \\ 0 \end{pmatrix} \tag{B3a}$$

$$M_{\text{POLISH}}(:, 2) = E/2 \begin{pmatrix} \pm [(\cos^2 2\theta + \sin^2 2\theta \cos \beta) \cos 2\phi - 1/2 \sin 4\theta (1 - \cos \beta) \sin 2\phi] \\ (\cos^2 2\theta + \sin^2 2\theta \cos \beta) \cos^2 2\phi - 1/4 \sin 4\theta (1 - \cos \beta) \sin 4\phi \\ 1/2 [(\cos^2 2\theta + \sin^2 2\theta \cos \beta) \sin 4\phi - \sin 4\theta (1 - \cos \beta) \sin^2 2\phi] \\ 0 \end{pmatrix} \tag{B3b}$$

$$M_{\text{POLISH}}(:, 3) = E/2 \begin{pmatrix} \pm [(\cos^2 2\theta + \sin^2 2\theta \cos \beta) \sin 2\phi + 1/2 \sin 4\theta (1 - \cos \beta) \cos 2\phi] \\ 1/2 [(\cos^2 2\theta + \sin^2 2\theta \cos \beta) \sin 4\phi + \sin 4\theta (1 - \cos \beta) \cos^2 2\phi] \\ (\cos^2 2\theta + \sin^2 2\theta \cos \beta) \sin^2 2\phi + 1/4 \sin 4\theta (1 - \cos \beta) \sin 4\phi \\ 0 \end{pmatrix} \tag{B3c}$$

$$M_{\text{POLISH}}(:, 4) = E/2 \begin{pmatrix} \mp \sin 2\theta \sin \beta \\ -\sin 2\theta \sin \beta \cos 2\phi \\ -\sin 2\theta \sin \beta \sin 2\phi \\ 0 \end{pmatrix} \tag{B3d}$$

The functions of θ multiplying $\cos \beta$ are zero for integer multiples of 90° and one for odd integer multiples of 45° . Thus, the full amplitude of the intensity modulation occurs for the PEM oriented $\theta = \pm 45^\circ$ with respect to the PEM compression/extension axis. Given $\beta = \beta_0 \sin \omega t$ from above, we expand the retardance in terms of Bessel functions:

$$\sin(\beta_0 \sin \omega t) = 2 \sum_{n=0}^{\infty} J_{2n+1}(\beta_0) \sin[(2n+1)\omega t] \quad (\text{B4a})$$

$$\cos(\beta_0 \sin \omega t) = J_0(\beta_0) + 2 \sum_{n=1}^{\infty} J_{2n}(\beta_0) \cos 2n\omega t \quad (\text{B4b})$$

The $\sin \beta$ expansion in Equation B4a generates odd harmonics of the PEM reference frequency, while the $\cos \beta$ expansion in Equation B4b generates even harmonics. In Equations B3a through B3d, the second and third columns of M_{POLISH} have factors of $\cos \beta$, while the fourth column has factors of $\sin \beta$. When multiplying these columns with incident light as per Equation A2, the Q_0 and U_0 Stokes parameters will be modulated at even PEM harmonics, while the V_0 parameter will be modulated at odd harmonics. Thus, we choose to set our lock-in amplifiers to record the second harmonic of modulated intensity. By setting $n = 2$ in Equation B4b, we can see that the modulated signal will have amplitude $2J_2(\beta_0)$, but it will also have an offset of $J_0(\beta_0)$. Therefore, we see a hint that choice of peak retardance β_0 will affect both AC and DC components of the detected intensity. This will be proven below.

Plugging Equations B3a through B3d into Equation A2 and rearranging terms, we find the detected intensity modulation to be

$$\begin{aligned} \frac{2}{E} I = I_0 \pm & \left[\cos^2 2\theta \cos 2\phi \mp \frac{1}{2} \sin 4\theta \sin 2\phi + \left(\sin^2 2\theta \cos 2\phi + \frac{1}{2} \sin 4\theta \sin 2\phi \right) J_0(\beta_0) \right] Q_0 \\ & \pm \left[\sin^2 2\theta \cos 2\phi + \frac{1}{2} \sin 4\theta \sin 2\phi \right] [2J_2(\beta_0) \cos 2\omega t] Q_0 \\ & \pm \left[\cos^2 2\theta \sin 2\phi + \frac{1}{2} \sin 4\theta \cos 2\phi + \left(\sin^2 2\theta \sin 2\phi \mp \frac{1}{2} \sin 4\theta \cos 2\phi \right) J_0(\beta_0) \right] U_0 \\ & \pm \left[\sin^2 2\theta \sin 2\phi \mp \frac{1}{2} \sin 4\theta \cos 2\phi \right] [2J_2(\beta_0) \cos 2\omega t] U_0 \end{aligned} \quad (\text{B5})$$

The lock-in amplifiers output the RMS value of the AC component of the intensity, given by R . The amplitude of the AC signal is therefore

$$R\sqrt{2} = E/2 \left\{ \pm 2J_2(\beta_0) \left[\left(\sin^2 2\theta \cos 2\phi + \frac{1}{2} \sin 4\theta \sin 2\phi \right) Q_0 + \left(\sin^2 2\theta \sin 2\phi \mp \frac{1}{2} \sin 4\theta \cos 2\phi \right) U_0 \right] \right\} \quad (\text{B6})$$

The mean intensity, or DC level, is given by

$$\begin{aligned} \frac{2}{E} \text{DC} = I_0 \pm & \left[\cos^2 2\theta \cos 2\phi \mp \frac{1}{2} \sin 4\theta \sin 2\phi + J_0(\beta_0) \left(\sin^2 2\theta \cos 2\phi + \frac{1}{2} \sin 4\theta \sin 2\phi \right) \right] Q_0 \\ & \pm \left[\cos^2 2\theta \sin 2\phi + \frac{1}{2} \sin 4\theta \cos 2\phi + J_0(\beta_0) \left(\sin^2 2\theta \sin 2\phi \mp \frac{1}{2} \sin 4\theta \cos 2\phi \right) \right] U_0 \end{aligned} \quad (\text{B7})$$

For $\theta = \pm 45^\circ$ and $\beta_0 = 2.4048$ radians, the first zero of $J_0(\beta)$, Equations B6 and B7 reduce to

$$R\sqrt{2} = \pm \frac{E}{2} [2J_2(\beta_0) (Q_0 \cos 2\phi + U_0 \sin 2\phi)] \quad (\text{B8a})$$

$$\text{DC} = \frac{EI_0}{2} \quad (\text{B8b})$$

Two integrations with the Cassegrain ring rotated $\Delta\phi = 45^\circ$ apart are therefore required to determine both linear Stokes parameters Q_0/I_0 and U_0/I_0 .

For Cassegrain ring angle $\phi = 0^\circ$, the normalized polarization in terms of the observables R and DC is given by

$$\frac{Q_{\text{obs}}}{I_{\text{obs}}} \equiv \frac{\sqrt{2}}{2J_2(\beta_0)} \frac{R}{\text{DC}} = \frac{Q_0}{I_0} \quad (\text{B9})$$

In terms of the PEM position θ and peak retardance β_0 , Equation B9 can be written as

$$\frac{Q_{\text{obs}}}{I_{\text{obs}}} = \frac{\frac{Q_0}{I_0} \sin^2 2\theta \mp \frac{1}{2} \frac{U_0}{I_0} \sin 4\theta}{1 \pm \frac{Q_0}{I_0} [\cos^2 2\theta + J_0(\beta_0) \sin^2 2\theta] \pm \frac{1}{2} \frac{U_0}{I_0} \sin 4\theta [1 \mp J_0(\beta_0)]} \quad (\text{B10})$$

The ratio of R and DC in Equation B9 is therefore defined to be the observed polarization. When

defining the PEM efficiency as $E_{\text{PEM}} = 2J_2(\beta_0)$, and noting the definition of R from Equation 2.3a, Equation B9 reduces to Equation 2.4. The PEM efficiency is the strength of the intensity modulation for a given polarization. Maximum efficiency of $E_{\text{PEM}} = 97.1\%$ is achieved for retardance of π radians (halfwave retardance), while our choice of $\beta_0 = 2.4048$ radians results in $E_{\text{PEM}} = 86.4\%$.

For $\theta \neq \pm 45^\circ$ and/or $\beta_0 \neq 2.4048$ radians, the observed polarization $Q_{\text{obs}}/U_{\text{obs}}$ can still be used to determine the true polarization Q_0/U_0 . In general,

$$\frac{Q_0}{I_0} = \frac{\frac{Q_{\text{obs}}}{I_{\text{obs}}} \left\{ 1 \pm \frac{1}{2} \frac{U_0}{I_0} \sin 4\theta [1 \mp J_0(\beta_0)] \right\} \pm \frac{1}{2} \frac{U_0}{I_0} \sin 4\theta}{\sin^2 2\theta \mp \frac{Q_{\text{obs}}}{I_{\text{obs}}} [\cos^2 2\theta + J_0(\beta_0) \sin^2 2\theta]} \quad (\text{B11a})$$

$$\frac{U_0}{I_0} = \frac{\frac{U_{\text{obs}}}{I_{\text{obs}}} \left\{ 1 \pm \frac{1}{2} \frac{Q_0}{I_0} \sin 4\theta [\mp 1 + J_0(\beta_0)] \right\} - \frac{1}{2} \frac{Q_0}{I_0} \sin 4\theta}{\sin^2 2\theta \mp \frac{U_{\text{obs}}}{I_{\text{obs}}} [\cos^2 2\theta + J_0(\beta_0) \sin^2 2\theta]} \quad (\text{B11b})$$

The decreased efficiency by using $\beta_0 = 2.4048$ instead of π radians decreases the AC signal from polarized stars by a factor of $J_2(\pi)/J_2(2.4048) = 1.12$, and it will slightly decrease the signal to noise ratio of polarimetric measurements using POLISH. However, the choice of $\beta_0 = \pi$ radians coupled with PEM misalignment ($\theta \neq \pm 45^\circ$) magnifies the amount of U_0/I_0 that leaks into measurements of $Q_{\text{obs}}/I_{\text{obs}}$, and vice versa, by a factor of

$$\frac{1 - J_0(\pi)}{1 - J_0(2.4048)} = 1.30 \quad (\text{B12})$$

We therefore use a peak retardance of $\beta_0 = 2.4048$ radians in our measurements.

2.12 Appendix C: Detector Noise

Given pre-gain signal current i_0 and pre-gain dark current i_d , the number of pre-gain photoelectrons during an integration of duration t_{AC} , and the shot noise on this quantity, will be given by

$$n = \frac{(i_0 + i_d) t_{\text{AC}}}{e} \quad (\text{C1a})$$

$$\sigma_n = \left[\frac{(i_0 + i_d) t_{\text{AC}}}{e} \right]^{\frac{1}{2}} \quad (\text{C1b})$$

The pre-gain shot noise current is essentially the pre-gain shot noise in electrons times e/t_{AC} , because current has units of coulombs per second. This value is

$$\sigma_i = \left[\frac{2eB(i_0 + i_d)}{t_{AC}} \right]^{\frac{1}{2}} \quad (C2)$$

where B is the system bandwidth in Hz and will be discussed later. The factor of $\sqrt{2}$ comes about when converting between photocurrent and photoelectrons. The post-gain shot noise current is

$$\sigma'_i = G \left[\frac{2eBF(i_0 + i_d)}{t_{AC}} \right]^{\frac{1}{2}} \quad (C3)$$

where G is detector gain and

$$F \approx G^x \quad (C4)$$

is the gain noise factor (post-gain quantities are primed). This factor arises because the gain process itself has statistical fluctuations. The excess noise factor, x , is a constant. Thus, we find the post-gain shot noise current to be

$$\sigma'_i = \left[\frac{2eBG^{2+x}(i_0 + i_d)}{t_{AC}} \right]^{\frac{1}{2}} \quad (C5)$$

Since voltage is measured at the output of the detectors, we convert signal and dark current to signal and dark voltage. The pre-gain signal and dark current are therefore

$$i_0 = \frac{DC}{GT_A} \quad (C6a)$$

$$i_d = \frac{i'_d}{G} \quad (C6b)$$

where T_A is the amplifier transimpedance in V/A and the post-gain dark current is i'_d . Output noise voltage is related to noise current by $\sigma'_v = T_A \sigma'_i$, so we plug Equations C6a and C6b into Equation C5 and multiply by the transimpedance to find

$$\sigma'_v = \left[\frac{2eBG^{1+x}T_A(\text{DC} + i'_d T_A)}{t_{\text{AC}}} \right]^{\frac{1}{2}} \quad (\text{C7})$$

This is the expected voltage noise on the output of the detectors. We now relate this quantity to fluctuations in the observables X , Y , and DC.

In general, error propagation on a function $g(x_1, x_2, \dots, x_j)$ is given by

$$\sigma_g = \left[\sum_j \left(\frac{\partial g}{\partial x_j} \sigma_{x_j} \right)^2 \right]^{\frac{1}{2}} \quad (\text{C8})$$

By propagating error through Equation 2.4, we find polarimetric uncertainty of a measurement to be related to uncertainty in X , Y , and DC according to

$$\sigma_P = \frac{\sqrt{2}}{2J_2(\beta_0)\text{DC}} \left(\frac{X^2\sigma_X^2 + Y^2\sigma_Y^2}{X^2 + Y^2} + \frac{X^2 + Y^2}{\text{DC}^2} \sigma_{\text{DC}}^2 \right)^{\frac{1}{2}} \quad (\text{C9})$$

Rearranging terms, and absorbing the $t_{\text{AC}}^{-1/2}$ factor from Equation C7, we find

$$\sigma_P = \frac{\sqrt{2}}{E_{\text{PEM}}\text{DC}} \left\{ \frac{1}{t_{\text{AC}}} \left[\frac{X^2\sigma_X^2 + Y^2\sigma_Y^2}{X^2 + Y^2} + \frac{1}{2} (E_{\text{PEM}}P\sigma_{\text{DC}})^2 \right] \right\}^{\frac{1}{2}} \quad (\text{C10})$$

For an imperfect detector, expected voltage noise is given by Equation C7. However, we must determine the bandwidth B with care. Photon shot noise is white noise, which means that it occurs at all frequencies. However, it clearly cannot continue up to infinite frequency, because integrated power would also be infinite. The maximum frequency at which photon shot noise can occur will be the count rate of noise photons. Thus, we determine maximum bandwidth by the square root of the number of detected photons,

$$B_{\text{max}} = \left(\frac{\text{DC}}{eGT_A} \right)^{\frac{1}{2}} \quad (\text{C11})$$

The detectors have bandwidth ranging from about 100 kHz to 200 kHz. However, the lock-in am-

plifiers only admit noise in a bandwidth of $B_{AC} \approx 2.6$ Hz, while the voltmeters have bandwidth of $B_{DC} \approx 1$ MHz. Thus, the bandwidth for shot noise on X and Y will be $\min(B_{\max}, B_{\text{detector}}, B_{AC}) = B_{AC}$ for all stars. The bandwidth for shot noise on DC will be $\min(B_{\max}, B_{\text{detector}}, B_{DC})$, which will depend on stellar intensity.

Using Equation C7, we can determine photon shot noise ($x = 0$ and $i'_d = 0$) and detector noise ($x \neq 0$ and $i'_d \neq 0$) on X , Y , and DC. We can also compare these values to the observed fluctuations during each measurement.

$$\begin{bmatrix} \sigma_X \\ \sigma_Y \\ \sigma_{DC} \end{bmatrix}_{\text{shot}} = \gamma_0 \begin{bmatrix} B_{AC} \\ B_{AC} \\ \min(B_{\max}, B_{\text{detector}}) \end{bmatrix}^{\frac{1}{2}} \quad (\text{C12a})$$

$$\begin{bmatrix} \sigma_X \\ \sigma_Y \\ \sigma_{DC} \end{bmatrix}_{\text{detector}} = \gamma \begin{bmatrix} B_{AC} \\ B_{AC} \\ \min(B_{\max}, B_{\text{detector}}) \end{bmatrix}^{\frac{1}{2}} \quad (\text{C12b})$$

$$\begin{bmatrix} \sigma_X \\ \sigma_Y \\ \sigma_{DC} \end{bmatrix}_{\text{obs}} = \begin{bmatrix} \text{std}(X_{\text{src}})^2 + \text{std}(X_{\text{sky}})^2 \\ \text{std}(Y_{\text{src}})^2 + \text{std}(Y_{\text{sky}})^2 \\ \text{std}(DC_{\text{src}})^2 + \text{std}(DC_{\text{sky}})^2 \end{bmatrix}^{\frac{1}{2}} \quad (\text{C12c})$$

Here, $\gamma_0 \equiv 2eGT_A DC$, $\gamma \equiv 2eG^{1+x}T_A(DC + i'_d T_A)$, and “std” indicates the sample standard deviation. Finally, inserting Equations C12a through C12c into Equation C10 yields the uncertainty in polarization from photon shot noise, detector noise, and observed fluctuations.

For the APDs, the gain noise factor is quoted as $F = 2.2$ at gain $G = 300$. From Equation C4, we find $x_{\text{APD}} = 0.138$. For the PMTs, the gain noise factor is as follows (Hamamatsu Photonics 1999):

$$F = \frac{1}{\epsilon} \left(1 + \sum_{k=1}^K \frac{1}{\delta_k} \right) \quad (\text{C13})$$

where ϵ is the PMT collection efficiency, δ_k is the secondary electron emission ratio at each dynode k , and K is the number of dynodes (the multiplicative regions of the PMT). The PMT collection

efficiency ϵ is the fraction of photoelectrons emitted by the photocathode that reach the first dynode. Assuming $\epsilon = 1$ and $\delta_k = \delta$ (all dynodes have the same gain),

$$F = \frac{\delta}{\delta - 1} \tag{C14}$$

and gain is simply $G = \delta^K$. Since the PMT gain over its nine dynodes is 5×10^6 from Table 2.3, $\delta = 0.55$, $F = 1.2$, and $x = 0.013$. That is, gain from the PMTs is an order of magnitude less noisy than from the APDs, which is why PMTs are preferred over APDs for faint objects.

Chapter 3

Nightly Variability of Polarimetric Standard Stars

3.1 Introduction

Nightly, high precision monitoring of polarization standard stars is necessary for calibration of polarized sources. The POLISH instrument on the Hale 5-m telescope is designed to observe polarimetric variability in Cygnus X-1, the most well-studied high mass X-ray binary. This binary is thought to consist of a $40 \pm 10 M_{\odot}$, O9.7Iab supergiant and a $13.5 - 29 M_{\odot}$ black hole at a distance of 2.2 ± 0.2 kpc (Ziółkowski 2005). It has a polarimetric period of 2.8 days, which is half the orbital period of 5.6 days (Gies et al. 2003). The amplitude of variability is of order 0.1% in both Stokes Q and U (Kemp et al. 1979, Dolan & Tapia 1989, Wolinski et al. 1996). The spectrum of the strong, linear polarization of order 5% is consistent with interstellar origin (Gehrels 1972, Wolinski et al. 1996), and other members of the Cygnus OB association also share polarization at this level. The intrinsic polarization of the source is due to Thomson scattering by the abundant free electrons from the supergiant as well as Rayleigh scattering from the circumbinary envelope. However, the geometry of the scatterers is poorly understood.

The goal of this observing program is to constrain the orbital inclination of the HDE 226868/Cygnus X-1 supergiant/black hole system and provide a mass estimate for the black hole. In order to constrain the inclination to 5° , however, polarimetric monitoring of Cygnus X-1 must be performed with precision of one part in 10^4 to one part in ten million (Aspin et al. 1981). Systematic effects, especially those that vary on nightly timescales, must be calibrated to this level. Thus, both polarized and unpolarized standard stars must be observed to high precision.

¹The following paper is derived from observations in this chapter: Wiktorowicz, S. J. 2009, ApJ, in press.

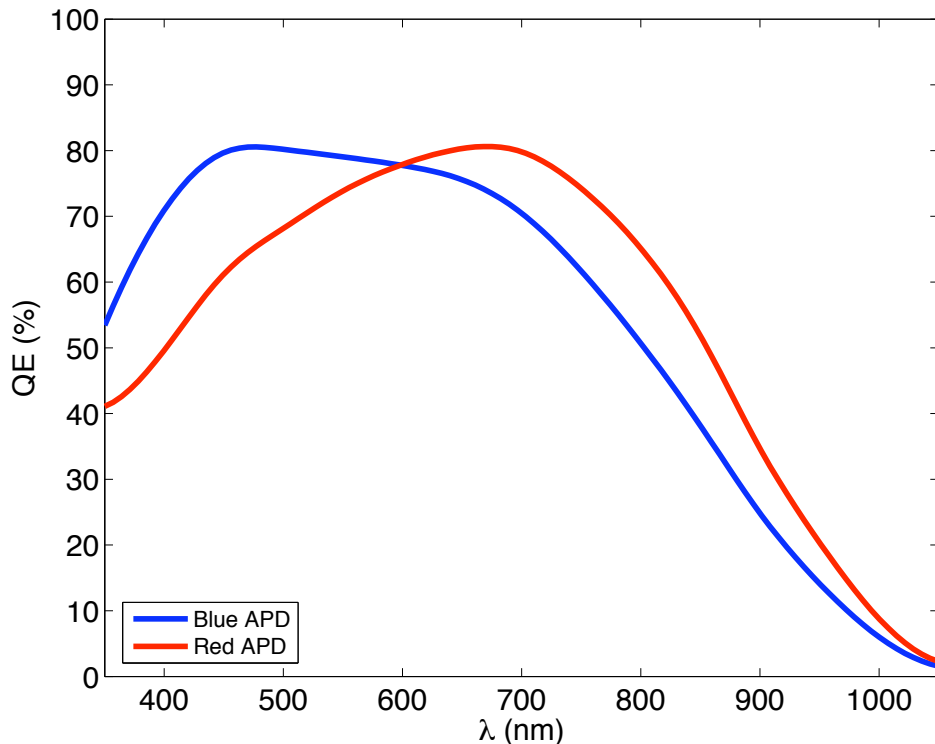


Figure 3.1: Quantum efficiency curves for the red enhanced and blue enhanced APDs (detector 2 and 1, respectively).

3.2 Observations

The POLISH instrument (POLarimeter for Inclination Studies of High mass x-ray binaries/Hot Jupiters) is a visible light polarimeter commissioned at the Cassegrain focus of the Hale 5-m telescope at Palomar Observatory, California. This instrument utilizes a photoelastic modulator (PEM) and lock-in amplifiers to modulate and detect incident, polarized light at 100 kHz. These components contribute to the high signal-to-noise observations by the instrument. A Wollaston prism feeds a pair of avalanche photodiodes (APDs) or photomultiplier tubes (PMTs), depending on stellar intensity. Stars with $V < 7$ mag are observed with avalanche photodiodes (see Figure 3.1 for quantum efficiency versus wavelength), while stars fainter than this are observed with photomultiplier tubes. The bandpass of the instrument is limited by the detectors; the lack of spectral filters increases throughput of the instrument and allows for high precision observations. On-source guiding is accomplished by use of a beamsplitter, which allows $\approx 5\%$ of the flux to be sent to a Xybion CCD camera.

Table 3.1: Observed Stars

Name	Alt. Name	RA	Dec	P	Θ ($^\circ$)	V	Type
Algenib ^a	γ Peg	00 13 14.23	+15 11 00.9	$940.6(5.7) \times 10^{-6}$	111.03(17)	2.83	B2IV
HD 7927	ϕ Cas	01 20 04.92	+58 13 53.8	3.6523(48)%	92.342(87)	5.01	F0Ia
HD 9270	η Psc	01 31 29.07	+15 20 44.8	$105.0(2.9) \times 10^{-6}$	122.3(1.1)	3.63	G7IIa
HR 5854	α Ser	15 44 16.07	+06 25 32.3	$1.84(79) \times 10^{-6}$	—	2.64	K2IIIb
HD 147084	o Sco	16 20 38.18	-24 10 09.6	4.4961(94)%	32.025(97)	4.55	A4II/III
HD 149026 ^b	SAO 65349	16 30 29.62	+38 20 50.3	$568.9(7.3) \times 10^{-6}$	80.83(51)	8.16	G0IV
HD 154445	SAO 141513	17 05 32.24	-00 53 31.7	4.5175(32)%	90.318(22)	5.64	B1V
u Her ^c	HD 156633	17 17 19.57	+33 06 00.4	0.1618(15)%	171.90(18)	4.80	B1.5Vp+
γ Oph ^d	HD 161868	17 47 53.56	+02 42 26.3	$178.2(4.0) \times 10^{-6}$	60.56(65)	3.75	A0V
HD 157999	σ Oph	17 26 30.98	+04 08 25.1	1.0482(15)%	85.079(51)	4.34	K3Iab
HD 175541 ^b	GJ 736	18 55 40.88	+04 15 55.2	$1117.8(8.3) \times 10^{-6}$	76.96(21)	8.03	G8V
HD 187929 ^e	η Aql	19 52 28.37	+01 00 20.4	1.9464(37)%	93.030(67)	3.5 - 4.3	(F6.5-G2)Ib
Cygnus X-1 ^f	SAO 69181	19 58 21.68	+35 12 05.8	6.9733(94)%	138.729(33)	8.95	O9.7Iab
HD 189733 ^b	V452 Vul	20 00 43.71	+22 42 39.1	$450.7(5.1) \times 10^{-6}$	73.30(34)	7.68	K1.5V
HD 204827	SAO 33461	21 28 57.70	+58 44 24.0	7.9929(97)%	59.542(31)	8.00	O9.5V
HD 212311	SAO 34361	22 21 58.55	+56 31 52.8	$407(27) \times 10^{-6}$	176.37(30)	8.12	A0V
HR 8974	γ Cep	23 39 20.85	+77 37 56.2	$4.6(1.0) \times 10^{-6}$	—	3.23	K1IV

^a β Cepheid, pulsator

^bExtrasolar planet host

^c β Lyrid, eclipsing binary

^dDebris disk

^e δ Cepheid, pulsator

^fHigh mass X-ray binary

Each on-source measurement consists of one ≈ 30 second integration. Data are sky subtracted by chopping the secondary mirror 25 arcsec due north of the source position. Polarization values are corrected for PEM systematics and then telescope polarization is subtracted. Polarization uncertainty in each measurement is generally two to three times the photon shot noise limit, and night-to-night polarization uncertainty scales according to shot noise statistics. That is, $\sigma_P \propto P^{\frac{1}{2}}$, where σ_P is the polarization uncertainty and P is the stellar polarization. The polarization noise floor of the instrument is about eight parts in ten million for night-to-night observations.

The stars observed are listed in Table 3.1. V band magnitude and spectral type for HD 187929, a δ Cepheid variable, are from Bastien et al. (1988) and Oke (1961) respectively. Spectral type for HD 212311 is from Schmidt et al. (1992). All other non-polarimetric data are from the SIMBAD database. The polarization and position angle values in parentheses represent the standard error of the mean. This is not a measure of source variability; rather, these uncertainties are the square root of the weighted variance of measurements divided by the square root of the number of measurements. Weighting is proportional to number of detected photons to ensure that each detected photon, as opposed to each measurement, is treated equally. This is particularly important when cirrus clouds are present, because observed stellar intensity may vary throughout the night.

The absolute polarization value for each star is related to instrumental gain factors and is not our primary concern. Indeed, we find a correction factor of 0.836 ± 0.064 must be multiplied to polarization measurements from POLISH to make absolute polarization consistent with the Heiles (2000) polarization catalogs. However, this correction factor would increase uncertainty in our measurements unnecessarily. Instead, we aim to discern *relative* changes in polarization with high precision, so this correction factor is not applied to our data.

Cygnus X-1 is known to be variable of order $\Delta P \approx 0.1\%$, and it is included in this paper as a variable control source. This system illustrates the dangers of using the standard error of the mean to determine polarimetric precision of the measurements. That is, Cygnus X-1 is listed in Table 3.1 with a standard error of $\sigma_P \approx 10^{-4}$, which is an order of magnitude lower than the known $\Delta P \approx 0.1\%$ variability. Normalizing the standard deviation of the measurements by the square root of the number of measurements is only valid for normally distributed, i.e., non-variable, data.

3.3 Variability

3.3.1 Intra-Night Variability and Systematic Effects

To determine whether the data from a single night are normally distributed, we use the Kolmogorov-Smirnov (K-S) test. We compare the cumulative distribution function (CDF) of measurements from that night to the CDF for a normal distribution. This test is useful because it makes no assumptions about how the data are distributed, and it is also applicable to data sets of differing size. The benefit of the latter property of the K-S test will become apparent in the next section. The null hypothesis, which posits that the CDF for a given night is randomly distributed, can be rejected if the confidence level α is less than a predetermined value. In this section, rejection of the null hypothesis indicates one, or both, of the following: (1) the star is non-variable on timescales less than one night, and/or (2) systematic effects with timescales less than one night are significant.

In order to generate the CDF for a normal distribution, we first note the definition of the CDF:

$$\text{CDF}(Q) \equiv \frac{\int_{-\infty}^Q F(Q') dQ'}{\int_{-\infty}^{\infty} F(Q') dQ'}. \quad (3.1)$$

The probability density function for normally distributed data is

$$F(Q') = \frac{1}{\sigma\sqrt{2\pi}} \exp\left[-\frac{(Q' - \bar{Q}')^2}{2\sigma^2}\right]. \quad (3.2)$$

The normalization in Equation 3.2 ensures that the denominator in Equation 3.1 is equal to unity. In Equation 3.2, σ is the standard deviation of the data set, Q' , and the mean value of the data set is given by \bar{Q}' . Inserting $F(Q')$ from Equation 3.2 into Equation 3.1, we find the cumulative distribution function for normally distributed data to be

$$\text{CDF}(Q) = \frac{1}{2} \left[1 + \text{erf}\left(\frac{Q - \bar{Q}}{\sigma\sqrt{2}}\right) \right]. \quad (3.3)$$

Here, $\text{erf}(x)$ is the error function and is defined as

$$\text{erf}(x) \equiv \frac{2}{\sqrt{\pi}} \int_0^x e^{-t^2} dt. \quad (3.4)$$

To calculate α , we find whether

$$D > \frac{K_\alpha}{\sqrt{n}} \quad (3.5a)$$

$$D > K_\alpha \sqrt{\frac{n_1 + n_2}{n_1 n_2}}. \quad (3.5b)$$

Here, D is the Kolmogorov-Smirnov statistic, which represents the maximum deviation between the CDF from a given night and the CDF expected from the normal distribution. When comparing one data set to a theoretical distribution, Equation 3.5a is used, and Equation 3.5b is used when comparing two data sets. The number of measurements in each data set is given by n , n_1 , or n_2 . The relationship between K_α and α is

$$\frac{\sqrt{2\pi}}{K_\alpha} \sum_{i=1}^{\infty} \exp\left[-\frac{(2i-1)^2 \pi^2}{8K_\alpha^2}\right] = 1 - \alpha. \quad (3.6)$$

Measurement of D allows one to solve for K_α in Equation 3.5b, and the confidence level α of non-variability can then be found from Equation 3.6.

Confidence levels of normally distributed, nightly data are listed in Table 3.2. It is convenient to convert α to units of the standard deviation, σ , which is given by $\sqrt{2} \operatorname{erf}^{-1}(\alpha)$. Here, $\operatorname{erf}^{-1}(x)$ is the inverse of the error function. Even though only two detectors are used at one time, combining the simultaneous polarization measurement from both detectors is useful. To do this, the weighted mean polarization is taken for each simultaneous pair of measurements. Again, the weighting is proportional to number of photons detected, which is proportional to the signal divided by the detector gain. Combination of measurements from both detectors is referred to as “Detector 1,2”.

The range of confidence values across all detectors from Table 3.2, for each star and for each night, are plotted in Figure 3.2. We require normal distribution confidence level to be $< 1\sigma$ to claim variability or significant systematic effects during a single night. However, all nights have roughly the same range of confidence levels, and the upper levels are $> 3\sigma$. Thus, variability and systematic effects on timescales less than one night do not appear to be significant. Figure 3.3 shows each star’s confidence levels from Table 3.2 separately. The horizontal, dashed line indicates the 1σ confidence level of normal distribution for a particular star’s measurements on a particular night. There appear to be no systematic trends in confidence level seen in all stars during the run, reiterating the conclusion from Figure 3.2 that intra-night systematic effects are not significant.

No stars appear to be significantly variable during a single night. The low confidence levels in both Stokes Q and U for HR 8974 on UT August 5 are inconsistent with the high confidence levels on UT August 3 and 6. Reasons for this are unknown, but it is still likely that polarization from this source is not variable at a detectable level on timescales less than one night. Stokes Q data for HD 147084 do not exist. As stated in section 1, polarization from Cygnus X-1 is known to be variable on the order of $\Delta Q, U \approx 0.1\%$ with a 2.8 day period. Cygnus X-1 observations lasted about three hours per night, so variations of $\Delta Q, U \approx 10^{-5}$ to 10^{-4} are therefore to be expected during each night. However, this variability does not appear to be detected with much confidence, as measurements are distributed randomly to $\approx 2\sigma$ in general.

Table 3.2: Confidence of Random Distribution

UT Date	Star	Q_1 Conf.	Q_2 Conf.	$Q_{1,2}$ Conf.	U_1 Conf.	U_2 Conf.	$U_{1,2}$ Conf.
2007 Aug 3	HR 5854	0.3σ	2.6σ	0.7σ	0.9σ	1.5σ	0.4σ
2007 Aug 4	...	2.8σ	1.7σ	2.8σ	2.4σ	2.0σ	3.2σ
2007 Aug 5	...	2.6σ	2.2σ	4.0σ	2.0σ	1.8σ	3.6σ
2007 Aug 6	...	3.0σ	0.7σ	1.8σ	2.5σ	1.8σ	1.7σ
2007 Aug 3	HR 8974	3.6σ	2.9σ	3.7σ	2.5σ	1.7σ	4.9σ
2007 Aug 4	...	—	—	—	3.2σ	4.6σ	2.3σ
2007 Aug 5	...	1.7σ	1.5σ	0.6σ	0.5σ	1.7σ	1.8σ
2007 Aug 6	...	2.5σ	3.1σ	3.5σ	4.0σ	0.9σ	2.5σ
2007 Aug 4	HD 9270	1.5σ	—	—	1.7σ	—	—
2007 Aug 5	...	3.7σ	2.4σ	1.8σ	2.8σ	1.2σ	4.4σ
2007 Aug 6	...	1.7σ	1.7σ	2.1σ	2.9σ	1.4σ	3.9σ
2007 Aug 4	γ Oph	0.9σ	1.9σ	2.0σ	1.9σ	2.5σ	4.3σ
2007 Aug 5	...	0.5σ	2.4σ	2.2σ	2.3σ	3.4σ	2.5σ
2007 Aug 6	...	0.8σ	3.4σ	0.7σ	1.6σ	1.8σ	1.7σ
2007 Aug 3	HD 212311	0.6σ	1.7σ	0.9σ	3.2σ	1.5σ	1.6σ
2007 Aug 4	...	1.3σ	1.3σ	3.2σ	2.6σ	2.1σ	2.0σ
2007 Aug 5	...	0.8σ	1.0σ	1.7σ	0.2σ	1.2σ	1.6σ
2007 Aug 6	...	1.2σ	1.8σ	1.2σ	0.8σ	1.5σ	2.6σ
2007 Aug 5	Algenib	0.9σ	2.0σ	1.9σ	0.2σ	2.7σ	0.6σ
2007 Aug 6	...	0.4σ	2.9σ	0.4σ	2.8σ	1.5σ	1.5σ
2007 Aug 5	HD 157999	0.8σ	2.4σ	0.7σ	1.2σ	1.6σ	0.9σ
2007 Aug 6	...	1.6σ	0.3σ	1.7σ	1.2σ	2.2σ	1.5σ
2007 Aug 3	HD 187929	2.3σ	1.5σ	2.2σ	1.2σ	0.6σ	0.9σ
2007 Aug 5	...	1.4σ	2.7σ	2.1σ	2.5σ	2.5σ	1.5σ
2007 Aug 6	...	2.6σ	1.6σ	3.9σ	2.7σ	2.2σ	1.8σ
2007 Aug 3	HD 147084	—	—	—	1.3σ	0.4σ	0.8σ
2007 Aug 4	...	—	—	—	1.1σ	3.4σ	1.4σ
2007 Aug 3	HD 204827	2.6σ	2.9σ	3.7σ	1.8σ	2.6σ	2.7σ
2007 Aug 4	...	—	—	—	4.2σ	2.4σ	1.4σ
2007 Aug 5	...	2.4σ	1.5σ	0.6σ	2.5σ	2.8σ	2.1σ
2007 Aug 6	...	1.1σ	1.2σ	1.2σ	2.2σ	3.1σ	1.2σ
2007 Aug 3	Cygnus X-1	2.4σ	1.6σ	1.9σ	1.1σ	2.7σ	2.4σ
2007 Aug 4	...	1.0σ	1.2σ	2.4σ	0.3σ	1.8σ	0.8σ
2007 Aug 5	...	1.5σ	1.1σ	1.7σ	1.0σ	2.6σ	1.2σ
2007 Aug 6	...	0.8σ	0.7σ	0.7σ	0.9σ	1.5σ	2.1σ

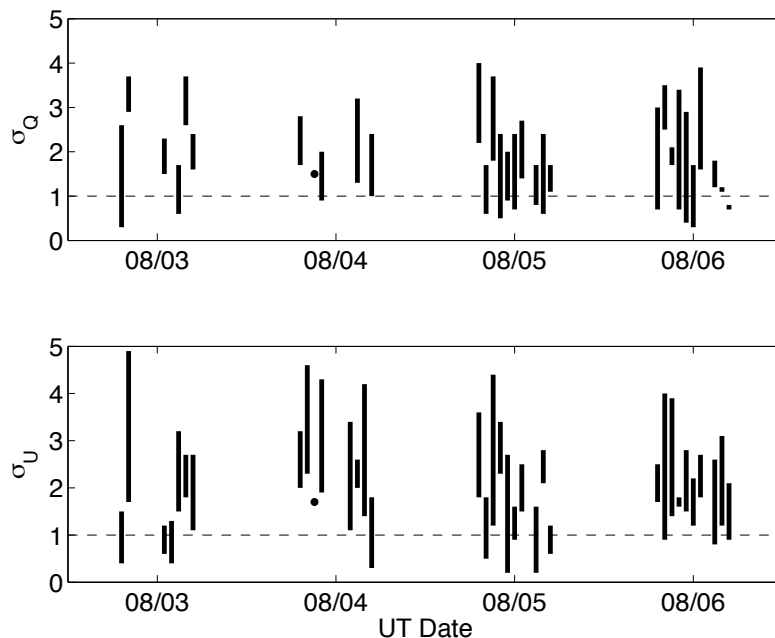


Figure 3.2: Nightly confidence range of normal distribution for all stars. Each vertical line represents the range in confidence level for each star across all detector combinations. Ranges for each star have been displaced from their neighbors in the x-direction for clarity. The points on 2007 Aug 4 are for HD 9270, which only has data from one detector (this can also be seen in Figure 3.3).

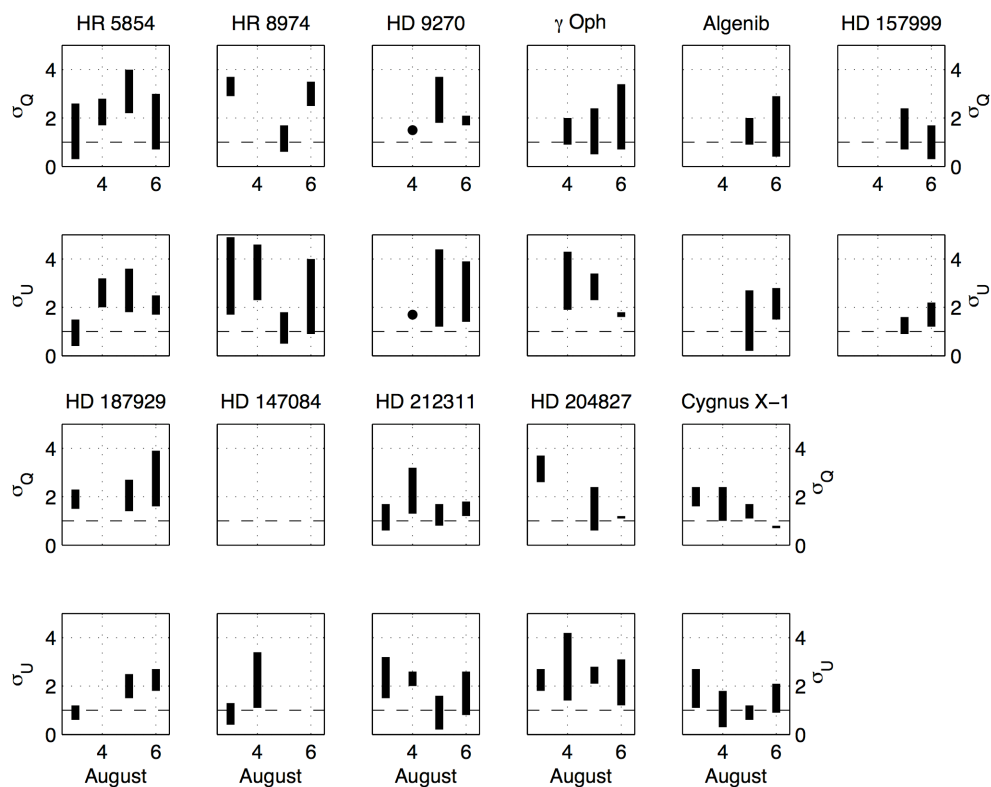


Figure 3.3: Nightly confidence range of normal distribution for individual stars. UT date ranges between 2007 Aug 3 and 2007 Aug 6. Lower values of $\sigma_{Q,U}$ indicate non-random distribution of nightly data.

A hint of intra-night variability in Cygnus X-1 exists for the UT 2007 Aug 6 Stokes Q data, where the confidence of normal distribution ranges from 0.7σ to 0.8σ . Both detector 1 and detector 2 (blue and red enhanced APDs, respectively) agree on this confidence level. However, we do not claim to have detected variability in Cygnus X-1 during this night because (1) the Stokes U confidence ranges for this object do not lie entirely below the 1σ threshold, and (2) the Stokes Q confidence ranges for HD 204827 for that night are also low and tight at 1.1σ to 1.2σ . It appears that some systematic effect caused non-random distribution of data for both of these objects, during this particular night, and only for the Stokes Q data. We currently have no explanation for this.

3.3.2 Night-to-Night Variability

To test for stellar variability over timescales of one night or longer, we compare the CDF of measurements between a pair of nights according to the Kolmogorov-Smirnov (K-S) test. We require $\alpha < 0.01$ in order to reject the null hypothesis and claim stellar variability. Plotted in Figures 3.4 and 3.5 are CDFs measured with each detector, or with the combination of detectors, for the pair of nights listed in the captions. The heavy, solid line is the CDF for the earlier night of the pair, and the thin, solid line is the CDF for the later night. The vertical, dotted line is the D statistic for each pair of CDFs.

To determine extent of polarimetric variability, we find the difference between each weighted mean Stokes parameter for the pair of nights tested. The uncertainty in this variability estimate is the quadrature addition of uncertainties from each night. The uncertainty from each night is taken to be the square root of the weighted variance divided by the square root of the number of measurements. We list α values and polarimetric variability in Tables 3.3 to 3.9. Absolute variability is defined by $\Delta Q, U \equiv Q, U_{\text{night2}} - Q, U_{\text{night1}}$, while relative variability is defined as $\delta Q, U \equiv (Q, U_{\text{night2}} - Q, U_{\text{night1}}) / |Q, U_{\text{night1}}|$. Weighted mean polarimetric variability $\Delta Q, U_{\text{mean}}$ and $\delta Q, U_{\text{mean}}$ are taken across detector 1, detector 2, and the detector 1,2 combination to determine the likelihood of variability. Here, the weighting is the inverse square of the uncertainty in each detector's estimate of variability. Significant variability is claimed if the following three conditions are met: (1) $\alpha > 0.01$ for both detectors and their combination, (2) ΔQ_{mean} or $\Delta U_{\text{mean}} > 3$ times their uncertainty, and (3) δQ_{mean} or $\delta U_{\text{mean}} > 3$ times their uncertainty.

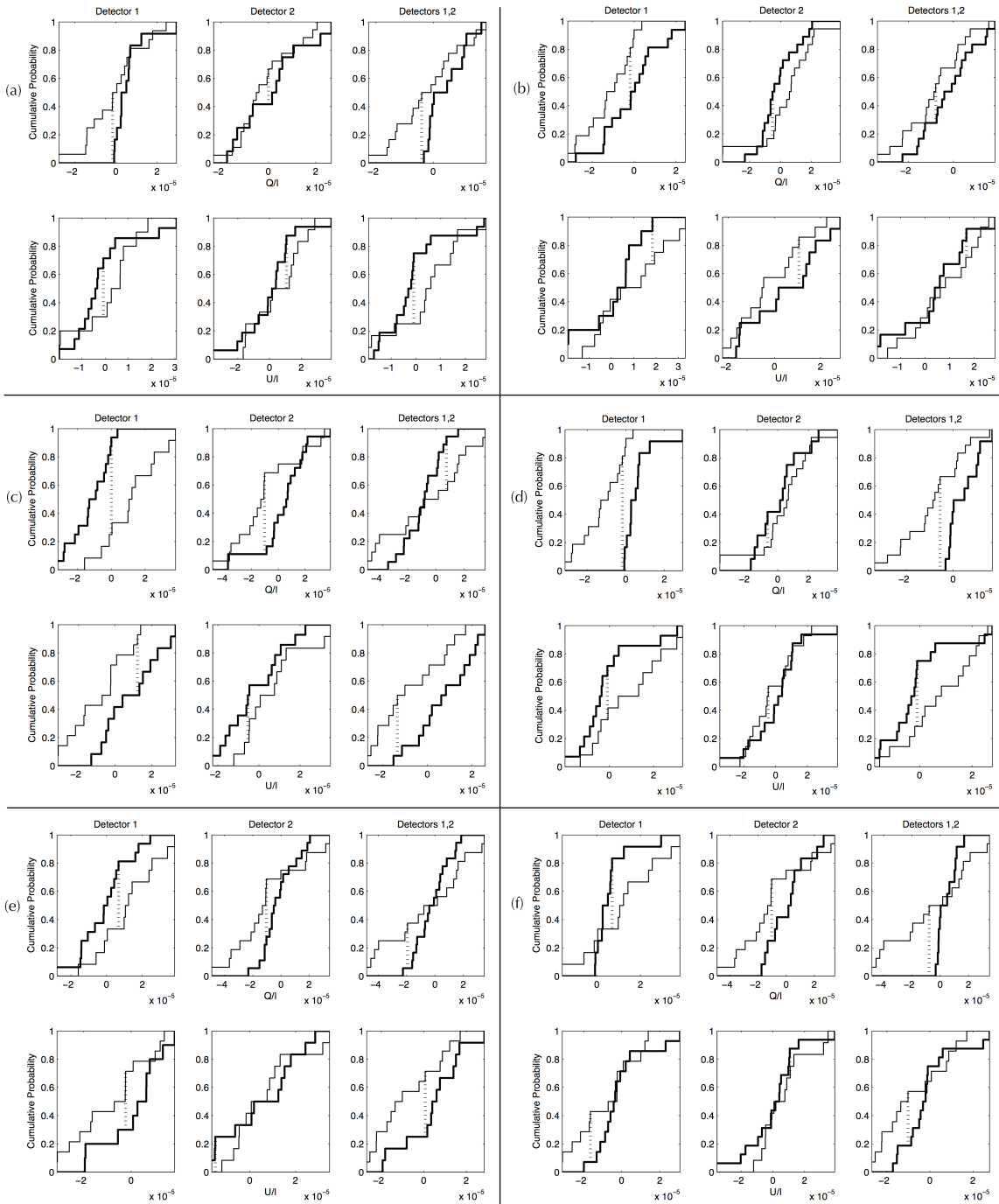


Figure 3.4: CDFs of HR 5854 for 2007 Aug 3 and 4 (a), Aug 4 and 5 (b), Aug 5 and 6 (c), Aug 3 and 5 (d), Aug 4 and 6 (e), Aug 3 and 6 (f).

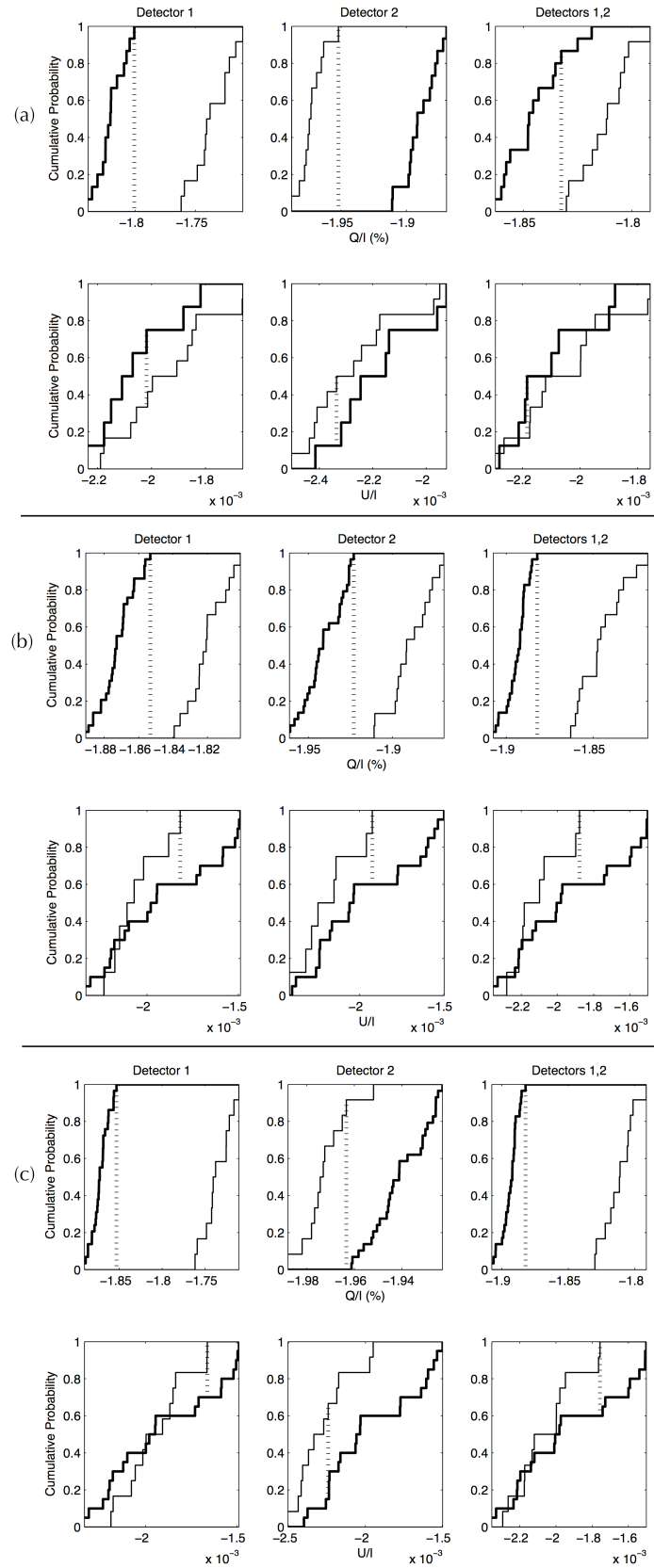


Figure 3.5: CDFs of HD 187929 for 2007 Aug 5 and 6 (a), Aug 3 and 5 (b), and Aug 3 and 6 (c).

Table 3.3: HR 5854 Variability

UT Date Δ Nights	2007 Aug 3 1	2007 Aug 4 1	2007 Aug 5 1	2007 Aug 3 2	2007 Aug 4 2	2007 Aug 3 3
α_{Q1}	0.065	0.094	0.003	2×10^{-4}	0.086	0.100
α_{Q2}	0.759	0.270	0.007	0.759	0.051	0.145
$\alpha_{Q1,2}$	0.055	0.491	0.169	0.003	0.353	0.065
α_{U1}	0.269	0.579	0.186	0.305	0.269	0.334
α_{U2}	0.290	0.382	0.469	0.699	0.847	0.927
$\alpha_{U1,2}$	0.065	0.954	0.153	0.080	0.123	0.221
$\Delta Q_1 (\times 10^{-6})$	-6.7(5.8)	-12.0(6.9)	26.3(8.5)	-18.7(6.1)	14.3(8.3)	7.6(7.6)
$\Delta Q_2 (\times 10^{-6})$	-2.6(6.3)	1.5(7.2)	-9.3(9.6)	-1.0(7.5)	-7.8(8.7)	-10.4(8.9)
$\Delta Q_{1,2} (\times 10^{-6})$	-5.2(4.8)	-8.3(6.3)	11.1(8.6)	-13.5(5.7)	2.8(8.1)	-2.4(7.6)
$\Delta Q_{\text{Mean}} (\times 10^{-6})$	-5.0(1.5)	-6.6(5.5)	11(14)	-12.4(6.7)	3.4(8.9)	-0.9(7.2)
$\Delta U_1 (\times 10^{-6})$	3.1(6.5)	6.1(8.2)	-17.6(9.7)	9.3(7.7)	-11.5(8.8)	-8.4(8.4)
$\Delta U_2 (\times 10^{-6})$	5.3(7.6)	-8.5(7.9)	8.2(7.7)	-3.2(7.2)	-0.2(8.1)	5.1(7.4)
$\Delta U_{1,2} (\times 10^{-6})$	3.2(5.8)	2.7(6.6)	-13.1(7.2)	5.9(6.0)	-10.4(7.1)	-7.2(6.5)
$\Delta U_{\text{Mean}} (\times 10^{-6})$	3.69(91)	0.3(5.9)	-6(11)	4.1(4.9)	-7.5(5.0)	-3.5(6)
δQ_1	-1.09(77)	-20(190)	2.09(70)	-3.1(1.4)	30(210)	1.2(1.7)
δQ_2	-2.3(6.8)	1.0(4.0)	-	-0.9(5.3)	-5(19)	-9(36)
$\delta Q_{1,2}$	-1.17(88)	-11(61)	1.23(79)	-3.0(1.7)	4(17)	-0.5(1.6)
δQ_{Mean}	-1.13(11)	0.98(91)	1.71(43)	-2.96(42)	-0.1(4.7)	0.31(94)
δU_1	2.5(6.2)	3(12)	-2.2(1.3)	7(21)	-6(14)	-7(25)
δU_2	10(120)	-1.5(1.0)	3.1(4.6)	-6(56)	-0.0(1.4)	10(110)
$\delta U_{1,2}$	4(11)	1.2(4.7)	-2.6(1.9)	7(23)	-4.5(7.3)	-8(36)
δU_{Mean}	2.73(59)	-1.31(66)	-2.1(1.2)	6.0(3.4)	-0.24(97)	-6.5(3.1)

Table 3.4: HR 8974 Variability

UT Date Δ Nights	2007 Aug 3 1	2007 Aug 4 1	2007 Aug 5 1	2007 Aug 3 2	2007 Aug 4 2	2007 Aug 3 3
α_{Q1}	-	-	0.003	0.003	-	0.220
α_{Q2}	-	-	0.005	0.648	-	0.001
$\alpha_{Q1,2}$	-	-	0.020	0.001	-	0.404
α_{U1}	0.259	0.236	0.031	3×10^{-4}	0.065	0.009
α_{U2}	0.225	0.134	0.189	0.092	0.788	0.094
$\alpha_{U1,2}$	0.948	0.270	0.002	0.048	0.032	0.004
$\Delta Q_1 (\times 10^{-6})$	-	-	-47(12)	32.3(8.6)	-	-15(10)
$\Delta Q_2 (\times 10^{-6})$	-	-	27.6(9.3)	-3.5(7.1)	-	24.1(8.5)
$\Delta Q_{1,2} (\times 10^{-6})$	-	-	-29(11)	29.4(8.8)	-	0.7(8.0)
$\Delta Q_{\text{Mean}} (\times 10^{-6})$	-	-	-10(33)	16(17)	-	5(15)
$\Delta U_1 (\times 10^{-6})$	-9.5(6.4)	-14(11)	68(15)	-23(10)	54(13)	45(13)
$\Delta U_2 (\times 10^{-6})$	-12.2(7.2)	26(12)	-25(13)	14(12)	1.2(8.8)	-11.0(8.2)
$\Delta U_{1,2} (\times 10^{-6})$	-8.8(5.4)	-9.9(8.1)	42.7(9.4)	-18.6(7.4)	32.9(7.9)	24.1(7.2)
$\Delta U_{\text{Mean}} (\times 10^{-6})$	-9.8(1.4)	-3(15)	29(35)	-13(14)	25(20)	14(21)
δQ_1	-	-	-1.72(38)	6.4(5.1)	-	-2.9(4.0)
δQ_2	-	-	5.2(4.6)	-1.9(7.5)	-	13(29)
$\delta Q_{1,2}$	-	-	-1.12(27)	7.8(7.3)	-	0.2(2.0)
δQ_{Mean}	-	-	-1.31(42)	4.8(3.8)	-	-0.4(1.5)
δU_1	-3.5(4.0)	-2.0(2.7)	3.3(1.2)	-9(11)	8.0(5.6)	17(25)
δU_2	-10(38)	1.91(88)	-2.0(1.0)	11(35)	0.09(63)	-9(34)
$\delta U_{1,2}$	-5.6(9.3)	-1.4(1.7)	2.50(71)	-12(21)	4.6(2.4)	15(32)
δU_{Mean}	-3.90(95)	1.0(1.5)	1.5(2.1)	-7.8(5.4)	0.5(1.4)	10(11)

Table 3.5: HD 9270 & γ Oph Variability

Star	HD 9270	HD 9270	HD 9270	γ Oph	γ Oph	γ Oph
UT Date	2007 Aug 4	2007 Aug 5	2007 Aug 4	2007 Aug 4	2007 Aug 5	2007 Aug 4
Δ Nights	1	1	2	1	1	2
α_{Q1}	0.685	0.584	0.124	0.172	0.001	0.005
α_{Q2}	–	0.016	–	0.329	0.013	0.172
$\alpha_{Q1,2}$	–	0.873	–	0.035	0.172	0.172
α_{U1}	0.329	0.032	0.251	0.998	0.015	0.004
α_{U2}	–	0.039	–	0.811	0.249	0.094
$\alpha_{U1,2}$	–	0.998	–	0.860	0.109	0.094
$\Delta Q_1 (\times 10^{-6})$	0(12)	–25(15)	–24(13)	4(11)	46(14)	50(14)
$\Delta Q_2 (\times 10^{-6})$	–	27(16)	–	0.4(9.8)	–29(13)	–28(13)
$\Delta Q_{1,2} (\times 10^{-6})$	–	–6(13)	–	5.4(8.2)	19(10)	25(11)
$\Delta Q_{\text{Mean}} (\times 10^{-6})$	–	–2(20)	–	3.4(2.2)	12(28)	15(31)
$\Delta U_1 (\times 10^{-6})$	–11.4(7.8)	19(11)	8(10)	–2(10)	–40(14)	–42(13)
$\Delta U_2 (\times 10^{-6})$	–	–33(17)	–	6(12)	11(12)	17(12)
$\Delta U_{1,2} (\times 10^{-6})$	–	0.7(9.6)	–	2.2(7.7)	–22(10)	–19.5(9.8)
$\Delta U_{\text{Mean}} (\times 10^{-6})$	–	3(17)	–	1.8(2.8)	–16(20)	–15(22)
δQ_1 (%)	1(30)	–62(51)	–61(37)	3.3(9.9)	45(12)	47(12)
δQ_2 (%)	–	44(23)	–	0(11)	–33(16)	–32(17)
$\delta Q_{1,2}$ (%)	–	–13(32)	–	5.3(7.7)	20(10)	24(10)
δQ_{Mean} (%)	–	14(38)	–	3.6(1.9)	18(27)	23(27)
δU_1 (%)	–12.6(9.1)	19.1(10.0)	9(11)	–1.4(6.4)	–25.2(8.2)	–26.2(7.8)
δU_2 (%)	–	–41(22)	–	3.5(7.4)	6.9(7.8)	10.7(8.1)
$\delta U_{1,2}$ (%)	–	0.7(9.9)	–	1.4(4.9)	–13.4(6.0)	–12.2(5.9)
δU_{Mean} (%)	–	5(17)	–	1.1(1.7)	–11(12)	–10(14)

Table 3.6: HD 212311 Variability

HD 212311	2007 Aug 3	2007 Aug 4	2007 Aug 5	2007 Aug 3	2007 Aug 4	2007 Aug 3
Δ Nights	1	1	1	2	2	3
α_{Q1}	0.423	0.936	0.602	0.560	0.975	0.701
α_{Q2}	0.576	0.883	0.037	0.560	0.478	0.034
$\alpha_{Q1,2}$	0.576	0.739	0.164	0.978	0.070	0.070
α_{U1}	0.112	0.055	0.353	0.665	0.516	0.079
α_{U2}	0.356	0.305	0.959	0.982	0.300	0.966
$\alpha_{U1,2}$	0.969	0.869	0.875	0.665	0.579	0.485
ΔQ_1 (%)	0.001(24)	–0.002(21)	0.011(21)	–0.001(24)	0.009(21)	0.010(24)
ΔQ_2 (%)	–0.019(19)	0.013(18)	–0.042(18)	–0.006(17)	–0.029(21)	–0.048(0)
$\Delta Q_{1,2}$ (%)	–0.010(12)	0.006(10)	–0.018(11)	–0.005(12)	–0.012(11)	–0.022(13)
ΔQ_{Mean} (%)	–0.0105(61)	0.0062(46)	–0.018(17)	–0.0043(17)	–0.011(11)	–0.023(18)
ΔU_1 (%)	–0.046(24)	0.021(24)	–0.024(28)	–0.026(24)	–0.003(28)	–0.049(27)
ΔU_2 (%)	0.040(19)	–0.036(19)	–0.001(23)	0.005(18)	–0.037(24)	0.003(23)
$\Delta U_{1,2}$ (%)	0.003(12)	–0.010(13)	–0.012(15)	–0.008(13)	–0.023(14)	–0.020(14)
ΔU_{Mean} (%)	0.004(27)	–0.012(18)	–0.0112(71)	–0.007(10)	–0.023(10)	–0.019(16)
δQ_1	0.05(79)	–0.06(62)	0.36(81)	–0.02(76)	0.28(74)	0.34(94)
δQ_2	–0.31(27)	0.31(50)	–0.75(27)	–0.09(26)	–0.67(37)	–0.77(25)
$\delta Q_{1,2}$	–0.21(21)	0.15(29)	–0.41(22)	–0.09(23)	–0.32(26)	–0.46(20)
δQ_{Mean}	–0.236(74)	0.16(11)	–0.50(24)	–0.090(16)	–0.38(25)	–0.56(21)
δU_1	–2.4(1.5)	0.75(66)	–4(12)	–1.36(97)	–0.1(1.1)	–2.6(1.8)
δU_2	2.6(1.7)	–1.43(56)	–0.1(2.2)	0.3(1.0)	–1.49(80)	0.2(1.4)
$\delta U_{1,2}$	5(52)	–5(17)	–1.4(3.1)	–10(200)	–10(38)	–30(470)
δU_{Mean}	–0.1(2.5)	–0.5(1.1)	–0.61(73)	–0.57(83)	–0.99(68)	–0.9(1.4)

Table 3.7: Stellar Variability

Star	Algenib	HD 157999	HD 187929	HD 187929	HD 187929	HD 147084
UT Date	2007 Aug 5	2007 Aug 5	2007 Aug 5	2007 Aug 3	2007 Aug 3	2007 Aug 3
Δ Nights	1	1	1	2	3	1
α_{Q1}	2×10^{-5}	1×10^{-8}	3×10^{-6}	5×10^{-9}	8×10^{-8}	–
α_{Q2}	1×10^{-5}	1×10^{-8}	3×10^{-6}	5×10^{-9}	1×10^{-6}	–
$\alpha_{Q1,2}$	4×10^{-4}	3×10^{-6}	9×10^{-5}	5×10^{-9}	8×10^{-8}	–
α_{U1}	0.013	0.037	0.375	0.320	0.509	0.005
α_{U2}	0.431	0.211	0.509	0.320	0.036	0.441
$\alpha_{U1,2}$	0.086	0.211	0.660	0.320	0.181	0.005
$\Delta Q_1 (\times 10^{-6})$	-138(22)	420(17)	849(53)	509(34)	1358(49)	–
$\Delta Q_2 (\times 10^{-6})$	62(10)	-544(22)	-816(41)	506(38)	-309(34)	–
$\Delta Q_{1,2} (\times 10^{-6})$	-62(15)	143(18)	343(46)	472(34)	815(34)	–
$\Delta Q_{\text{Mean}} (\times 10^{-6})$	3(76)	90(370)	-20(700)	495(17)	460(670)	–
$\Delta U_1 (\times 10^{-6})$	34(21)	-99(38)	109(69)	-155(82)	-46(82)	1000(150)
$\Delta U_2 (\times 10^{-6})$	-15(11)	94(37)	-144(73)	-182(86)	-326(83)	-350(210)
$\Delta U_{1,2} (\times 10^{-6})$	18(16)	-46(37)	36(68)	-175(82)	-139(82)	492(63)
$\Delta U_{\text{Mean}} (\times 10^{-6})$	1(20)	-16(81)	10(100)	-170(11)	-170(120)	497(29)
δQ_1 (%)	-24.4(4.6)	4.09(17)	4.66(29)	2.72(18)	7.25(26)	–
δQ_2 (%)	8.5(1.3)	-5.10(22)	-4.31(22)	2.61(19)	-1.59(18)	–
$\delta Q_{1,2}$ (%)	-10.0(2.6)	1.37(17)	1.86(25)	2.49(18)	4.30(18)	–
δQ_{Mean} (%)	3(10)	0.9(3.5)	-0.0(3.8)	2.608(95)	2.4(3.5)	–
δU_1 (%)	5.5(3.3)	-5.5(2.0)	5.3(3.3)	-8.2(4.5)	-2.4(4.4)	2.51(40)
δU_2 (%)	-2.4(1.7)	5.0(2.0)	-6.8(3.5)	-9.3(4.7)	-16.8(4.8)	-0.84(50)
$\delta U_{1,2}$ (%)	2.9(2.5)	-2.5(2.0)	1.7(3.3)	-9.1(4.6)	-7.3(4.5)	1.22(16)
δU_{Mean} (%)	0.3(3.2)	-1.0(4.4)	0.4(4.9)	-8.88(50)	-8.4(5.8)	1.22(74)

Table 3.8: HD 204827 Variability

HD 204827 Δ Nights	2007 Aug 3 1	2007 Aug 4 1	2007 Aug 5 1	2007 Aug 3 2	2007 Aug 4 2	2007 Aug 3 3
α_{Q1}	—	—	0.013	0.879	—	0.019
α_{Q2}	—	—	0.560	0.602	—	0.483
$\alpha_{Q1,2}$	—	—	0.172	0.725	—	0.212
α_{U1}	0.029	0.071	0.064	0.455	0.864	0.005
α_{U2}	0.106	0.183	0.182	0.759	0.677	0.097
$\alpha_{U1,2}$	0.011	0.024	0.025	0.635	0.677	0.003
ΔQ_1 (%)	—	—	-0.059(19)	0.011(21)	—	-0.048(18)
ΔQ_2 (%)	—	—	-0.021(33)	-0.009(31)	—	-0.030(30)
$\Delta Q_{1,2}$ (%)	—	—	-0.037(20)	0.004(20)	—	-0.033(18)
ΔQ_{Mean} (%)	—	—	-0.045(14)	0.0046(71)	—	-0.0387(77)
ΔU_1 (%)	0.175(38)	-0.127(37)	0.099(31)	0.048(32)	-0.028(37)	0.147(32)
ΔU_2 (%)	0.091(21)	-0.098(24)	0.061(28)	-0.007(24)	-0.037(25)	0.054(26)
$\Delta U_{1,2}$ (%)	0.127(22)	-0.113(23)	0.080(20)	0.015(20)	-0.033(23)	0.094(20)
ΔU_{Mean} (%)	0.117(29)	-0.109(10)	0.079(13)	0.014(19)	-0.0335(32)	0.092(32)
δQ_1 (%)	—	—	-1.54(51)	0.29(54)	—	-1.25(48)
δQ_2 (%)	—	—	-0.54(85)	-0.24(80)	—	-0.78(76)
$\delta Q_{1,2}$ (%)	—	—	-0.97(53)	0.11(52)	—	-0.85(46)
δQ_{Mean} (%)	—	—	-1.15(37)	0.12(18)	—	-1.00(21)
δU_1 (%)	2.57(56)	-1.81(52)	1.44(45)	0.71(47)	-0.40(53)	2.16(48)
δU_2 (%)	1.28(29)	-1.37(33)	0.86(40)	-0.10(34)	-0.52(36)	0.76(37)
$\delta U_{1,2}$ (%)	1.83(32)	-1.59(32)	1.14(29)	0.21(29)	-0.46(32)	1.36(28)
δU_{Mean} (%)	1.67(43)	-1.54(16)	1.13(20)	0.19(28)	-0.473(41)	1.32(47)

Table 3.9: Cygnus X-1 Variability

Cygnus X-1 Δ Nights	2007 Aug 3 1	2007 Aug 4 1	2007 Aug 5 1	2007 Aug 3 2	2007 Aug 4 2	2007 Aug 3 3
α_{Q1}	4×10^{-17}	1×10^{-7}	1×10^{-16}	2×10^{-17}	2×10^{-7}	4×10^{-6}
α_{Q2}	3×10^{-16}	2×10^{-5}	6×10^{-13}	6×10^{-17}	2×10^{-5}	6×10^{-5}
$\alpha_{Q1,2}$	2×10^{-16}	7×10^{-8}	6×10^{-17}	7×10^{-17}	4×10^{-7}	8×10^{-8}
α_{U1}	3×10^{-10}	4×10^{-11}	7×10^{-14}	0.056	0.007	2×10^{-8}
α_{U2}	1×10^{-17}	1×10^{-16}	1×10^{-18}	3×10^{-4}	8×10^{-6}	4×10^{-14}
$\alpha_{U1,2}$	3×10^{-17}	2×10^{-16}	3×10^{-17}	0.016	4×10^{-6}	1×10^{-16}
ΔQ_1 (%)	-0.210(15)	-0.100(15)	0.222(14)	-0.310(13)	0.121(15)	-0.089(13)
ΔQ_2 (%)	-0.216(18)	-0.115(19)	0.218(19)	-0.331(18)	0.103(18)	-0.113(18)
$\Delta Q_{1,2}$ (%)	-0.216(12)	-0.107(13)	0.218(13)	-0.323(12)	0.111(13)	-0.105(12)
ΔQ_{Mean} (%)	-0.2139(28)	-0.1067(55)	0.2193(18)	-0.3199(80)	0.1124(70)	-0.1006(97)
ΔU_1 (%)	-0.207(24)	0.233(24)	-0.197(18)	0.026(21)	0.036(22)	-0.171(19)
ΔU_2 (%)	-0.183(12)	0.240(11)	-0.175(10)	0.057(12)	0.065(11)	-0.118(12)
$\Delta U_{1,2}$ (%)	-0.188(11)	0.235(12)	-0.1817(98)	0.047(10)	0.053(11)	-0.1352(87)
ΔU_{Mean} (%)	-0.1881(68)	0.2370(26)	-0.1809(69)	0.0479(92)	0.0563(90)	-0.134(15)
δQ_1 (%)	-20.2(1.3)	-12.1(1.7)	30.4(2.3)	-29.8(1.1)	14.6(2.0)	-8.5(1.2)
δQ_2 (%)	-19.3(1.4)	-12.8(2.0)	27.8(2.8)	-29.7(1.4)	11.4(2.2)	-10.1(1.5)
$\delta Q_{1,2}$ (%)	-20.2(1.1)	-12.6(1.5)	29.2(2.1)	-30.2(1.0)	12.9(1.7)	-9.8(1.1)
δQ_{Mean} (%)	-19.97(36)	-12.46(28)	29.26(97)	-29.95(23)	13.1(1.2)	-9.44(69)
δU_1 (%)	-3.04(36)	3.32(33)	-2.90(27)	0.38(30)	0.51(31)	-2.51(28)
δU_2 (%)	-2.64(18)	3.36(15)	-2.54(15)	0.81(17)	0.91(15)	-1.71(17)
$\delta U_{1,2}$ (%)	-2.74(16)	3.32(16)	-2.66(15)	0.68(14)	0.75(15)	-1.96(13)
δU_{Mean} (%)	-2.73(11)	3.343(21)	-2.64(11)	0.70(13)	0.80(12)	-1.95(24)

Most stars are intrinsically unpolarized. For instance, the Sun itself is polarized at the level of less than one part in ten million (Kemp et al. 1987). Polarization of starlight is thought to be caused by interstellar dust clouds along the line of sight. Davis & Greenstein (1951) proposed that elongated dust grains, aligned with their spin axes parallel to the galactic magnetic field, cause preferential extinction of starlight with electric field parallel to the long axis of the grains. Serkowski et al. (1975) discovered an empirical relation to determine whether the polarization of starlight is consistent with origin from interstellar dust. By comparing the wavelength of peak polarization for 364 stars, they find

$$\frac{P(\lambda)}{P_{\max}} = \exp \left[-1.15 \ln^2 \left(\frac{\lambda_{\max}}{\lambda} \right) \right]. \quad (3.7)$$

Here, P_{\max} is the maximum polarization as a function of wavelength and λ_{\max} is the wavelength of maximum polarization. This wavelength is taken to be the mean grain size along the line of sight to the star. Stars with wavelength dependence of polarization lying along this curve are thought to be dominated by interstellar polarization. According to Serkowski et al. (1975), the following stars in our sample are dominated by interstellar polarization: HD 147084, HD 157999, HD 187929, and HD 204827. Additionally, Schmidt et al. (1992) find good fits of their data to interstellar polarization curves for HD 204827. Even Cygnus X-1 appears to owe $\approx 98\%$ of its polarization to interstellar dust grains (Gehrels 1972, Wolinski et al. 1996).

If grain orientation varies along the line of sight, circular polarization will be produced (Serkowski 1962). Additionally, if grain size also varies along the line of sight, position angle of polarization will be wavelength-dependent (Martin 1974). Therefore, the combination of circular polarization and wavelength-dependent linear polarization measurements can constrain grain properties along the line of sight.

Mean polarization versus distance is shown in Figure 3.6. More distant stars tend to have stronger polarization, which is expected if the origin is interstellar. Indeed, all stars in this figure with polarization $P > 1\%$ are dominated by interstellar polarization (cf. Serkowski et al. 1975). Stars with polarization less than this have not been investigated by Serkowski et al. (1975), because they had probably been assumed to be unpolarized. Thus, it is probable that polarization from all stars contains a contribution from the interstellar medium.

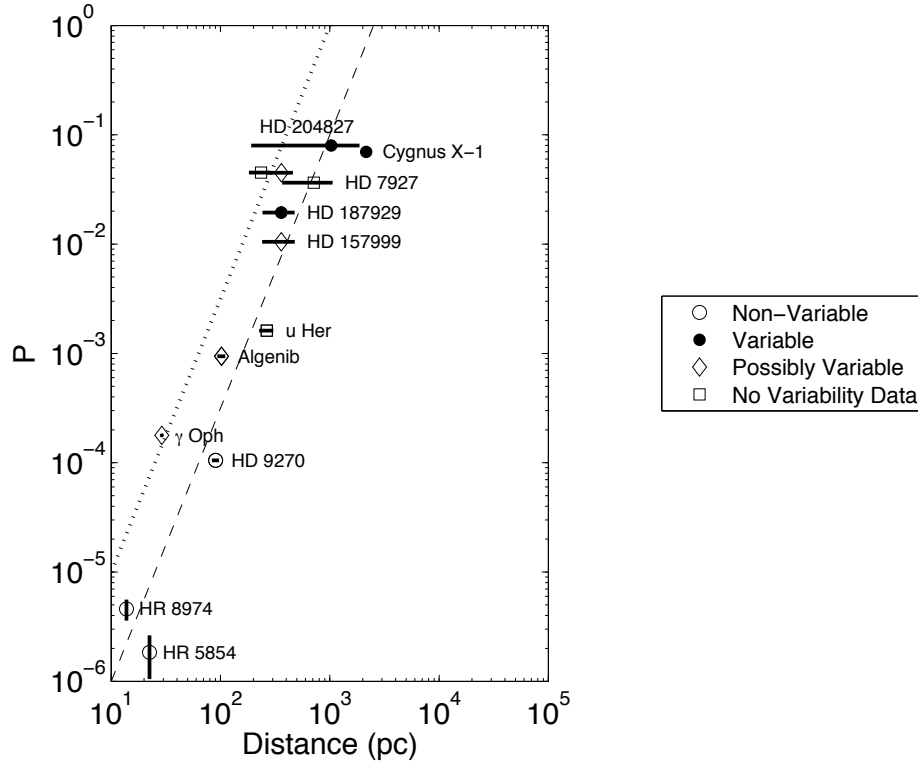


Figure 3.6: Polarization as a function of stellar distance. Stars with only one night of observations have also been included. The dashed and dotted lines are guides for the eye.

It is interesting that γ Oph has about an order of magnitude stronger polarization than the dashed trend in Figure 3.6 might indicate. This excess polarization may be due to the debris disk around γ Oph. However, the three stars lying near the dotted trend (γ Oph, HD 154445, and HD 147084) are all close to each other in the sky toward the Galactic Center. This region of enhanced extinction should also have strong interstellar polarization, which should be manifested as a vertical offset to the dashed line.

Similar polarimetric position angle between these three stars would imply that polarization of γ Oph is not due to its debris disk. However, position angles of net polarization are $60.56 \pm 0.65^\circ$, $90.318 \pm 0.022^\circ$, and $32.025 \pm 0.097^\circ$ for γ Oph, HD 154445, and HD 147084, respectively. Thus, there is no common orientation of interstellar dust grains in the lines of sight for these three stars. Indeed, the polarization maps of Mathewson & Ford (1970) show large differences in polarimetric position angle between these stellar locations. The star with no variability data with $P \approx 1\%$ is HD 154445, and the possibly variable star of similar polarization is HD 147084.

However, some stars are intrinsically polarized, evidenced by presence of wavelength-dependent position angle and absence of circular polarization. Intrinsic polarization may be due to circumstellar material or to tidal distortion from binary companions. Polarimetric variability may therefore be caused by intrinsic processes in the stellar atmosphere or surroundings, or it may be caused by changes in the line of sight interstellar medium. A first-order approach to determine the likelihood of ISM variability is to calculate the time taken for a star to traverse its own disk from proper motion, t_{var} . Table 3.10 lists proper motions and parallaxes from the SIMBAD database as well as stellar radii R from the Catalog of Apparent Diameters and Absolute Radii of Stars (CADARS: Pasinetti-Fracassini et al. 2001), 3rd Edition. A distance estimate was not found in the literature for HD 212311, so we approximate this by scaling its V band magnitude (from Table 3.1) to the magnitude and distance of γ Oph. This star has a similar spectral type to HD 212311. HD 7927, HD 149026, HD 175541, HD 189733, HD 204827, and HD 212311 are assumed to have radii $R \approx R_{\odot}$.

Parallax for Cygnus X-1 from SIMBAD is 0.56 ± 1.01 mas, while Ziółkowski (2005) presents a distance of 2.15 ± 0.2 kpc (3σ) for their evolutionary models of this object based on spectroscopy and photometry from Massey et al. (1995). The two values are consistent, but the Massey et al. (1995) value is more precise. We therefore convert the Massey et al. (1995) distance into expected parallax and include in Table 3.10. Stellar radii, R , are from the Catalog of Apparent Diameters and Absolute Radii of Stars (CADARS: Pasinetti-Fracassini et al. 2001), 3rd Edition, for all but HDE 226868 (Cygnus X-1 companion), HD 204827, and HD 212311. The CADARS catalog is obtained through the VizieR Service (Ochsenbein et al. 2000). Radius of HDE 226868 is $22.77 \pm 2.3 R_{\odot}$ from Ziółkowski (2005).

Since the bandpasses differ slightly between the red and blue enhanced APDs (Figure 3.1), we attempt to measure change in polarization and position angle for stars observed with APDs. Differences in run-averaged values between detectors are listed in Table 3.11. Difference in P between APDs 2 and 1 is the quadrature addition of the differences in the Stokes parameters. Again, values in bold are significant at the level of three or more times the uncertainty. It can be seen that we detect significant differences in polarization between the APDs for three out of the five stars for which interstellar polarization has been seen. The other two out of five (HD 147084 and HD 154445) show differences in polarization between detector that are significant at 2.4 and 1.6 times the uncertainty, respectively.

We investigate whether differences in polarization from each APD are due to their bandpasses resolving the shape of the interstellar polarization spectrum. Table 3.12 shows that the gain factor necessary to convert our measured Stokes parameters to absolute polarization does not vary between APDs 1 and 2. Therefore, dividing the degree of polarization measured by each APD cancels out any absolute polarization gain factor and takes advantage of our high precision data. We numerically integrate the product of the Serkowski et al. (1975) polarization spectrum from Equation 3.7 with the quantum efficiency of each APD.

The ratio of the integrals from both APDs gives the expected effect of the interstellar polarization spectrum, $(P_2/P_1)_{\text{exp}}$. Values of λ_{max} represent the mean value from the compilation of Serkowski et al. (1975) weighted by the inverse square of the uncertainty. The observed ratios of polarization from both APDs, $(P_2/P_1)_{\text{obs}}$, are also listed. Bold values indicate significant departures from a ratio of unity. We plot the expected and observed ratios of P_2/P_1 in Figure 3.7. The large difference between expected and observed ratios of polarization between the APDs suggests that the differing bandpasses between the APDs may not be significant. The observed ratios seem to be correlated with the expected ratios from the interstellar polarization spectrum, but we currently do not understand the cause of this. Stability of APD1 is known to be far superior to that of APD2, so the anomalously high polarizations detected by APD2 may be a systematic effect.

3.4 Discussion

3.4.1 Standard Stars

HR 5854 (α Ser, HD 140573). No variability estimates were found in the literature for this unpolarized star. While some α , $\Delta Q, U$, and $\delta Q, U$ values in Table 3.3 indicate variability, the large majority indicate this star is non-variable on timescales of one to three nights. This is consistent with the essentially unpolarized nature of this star as well as the minimum ≈ 1 month timescale for significant change in the line of sight ISM column. We find no significant difference in polarization between detectors.

HD 9270 (η Psc, HR 437). The interstellar polarization maps of Mathewson & Ford (1970) show weak polarization in this region of the sky. No variability estimates were found in the literature

Table 3.10: Variability of Interstellar Polarization

Name	P	Θ ($^\circ$)	PM_{RA} (mas/yr)	PM_{Dec} (mas/yr)	π (mas)	R (mas)	t_{var} (days)
HR 5854	$1.84(79) \times 10^{-6}$	—	+134.66	+44.14	44.54(71)	4.8	25
HR 8974	$4.6(1.0) \times 10^{-6}$	—	-48.85	+127.19	72.50(52)	3.9	21
HD 9270	$105.0(2.9) \times 10^{-6}$	+122.3(1.1)	+25.73	-3.29	11.09(82)	3.8	107
γ Oph	$178.2(4.0) \times 10^{-6}$	60.56(65)	-23.15	-75.12	34.42(99)	0.61	5.7
HD 212311	$407(27) \times 10^{-6}$	176.37(30)	+21.00	+1.40	≈ 5	≈ 0.02	≈ 0.4
HD 189733	$450.7(5.1) \times 10^{-6}$	73.30(34)	-2.49	-250.81	51.94(87)	≈ 0.2	≈ 0.4
HD 149026	$568.9(7.3) \times 10^{-6}$	80.83(51)	-77.12	+53.34	12.68(79)	≈ 0.06	≈ 0.2
Algenib	$940.6(5.7) \times 10^{-6}$	111.03(17)	+4.7	-8.24	9.79(81)	0.43	33
HD 175541	$1117.8(8.3) \times 10^{-6}$	76.96(21)	-7.84	-89.86	7.8(1.1)	0.027	≈ 0.1
u Her	0.1618(15)%	171.90(18)	-3.68	-5.74	3.77(56)	0.2	21
HD 157999	1.0482(15)%	85.079(51)	+1.25	+7.09	2.78(92)	5.2	530
HD 187929	1.9464(37)%	93.030(67)	+6.94	-7.30	2.78(91)	1.8	130
HD 7927	3.6523(48)%	92.342(87)	-1.31	-2.19	1.40(68)	≈ 0.007	≈ 0.9
HD 147084	4.4961(94)%	32.025(97)	-4.23	-14.71	2.77(76)	1.3	62
HD 154445	4.5175(32)%	90.318(22)	+4.34	-1.91	4.26(96)	0.16	25
Cygnus X-1	6.9733(94)%	138.729(33)	-3.82	-7.62	0.465(43)	0.049	4.2
HD 204827	7.9929(97)%	59.542(31)	-1.21	-2.92	0.97(79)	≈ 0.005	≈ 0.5

Table 3.11: Wavelength-Dependent Polarization

Name	$Q_2 - Q_1$ ($\times 10^{-6}$)	$U_2 - U_1$ ($\times 10^{-6}$)	$P_2 - P_1$ ($\times 10^{-6}$)	$\Theta_2 - \Theta_1$ ($^\circ$)	λ_{max} (nm)	$(P_2/P_1)_{exp}$	$(P_2/P_1)_{obs}$
HR 5854	-1.7(4.5)	1.1(4.9)	2.0(4.6)	—	—	—	4(21)
HR 8974	1.8(6.0)	-3.8(6.7)	4.2(6.6)	—	—	—	1.5(2.4)
HD 9270	-7.1(8.4)	1.1(8.9)	7.2(8.4)	1.9(2.3)	—	—	1.023(86)
γ Oph	-6.8(8.2)	26.9(8.1)	27.7(8.1)	1.2(1.3)	—	—	1.159(53)
Algenib ^a	-52(15)	-16(10)	55(15)	0.75(41)	—	—	1.055(15)
u Her	38(28)	-57(32)	69(31)	0.76(55)	—	—	1.033(18)
HD 157999 ^b	-897(58)	179(29)	915(57)	0.060(82)	580(30)	1.0094(62)	1.0899(58)
HD 187929 ^{b,c}	-907(77)	-125(62)	916(77)	0.044(93)	546(15)	1.0021(33)	1.0493(43)
HD 7927 ^{b,c}	-960(120)	-120(170)	970(120)	0.03(13)	511.9(3.9)	0.99445(91)	1.0266(34)
HD 147084 ^{a,b}	660(310)	260(75)	710(290)	0.30(17)	664.0(8.0)	1.0256(14)	1.0115(34)
HD 154445 ^b	-240(340)	300(130)	390(240)	0.192(86)	573(49)	1.008(10)	1.0053(76)

^aCircular polarization detected^bInterstellar P versus λ ^cRotation of θ versus λ

Table 3.12: Corrections for Absolute Polarization

Parameter	APD1	APD2	Mean	PMT1	PMT2	Mean
$P_{POLISH} - P_{Heiles}$ ($\times 10^{-4}$)	1.8(3.6)	1.8(3.8)	1.8438(21)	8(35)	9(37)	8.84(53)
P_{POLISH}/P_{Heiles}	0.843(87)	0.842(62)	0.84224(69)	0.690(20)	0.672(22)	0.6811(89)

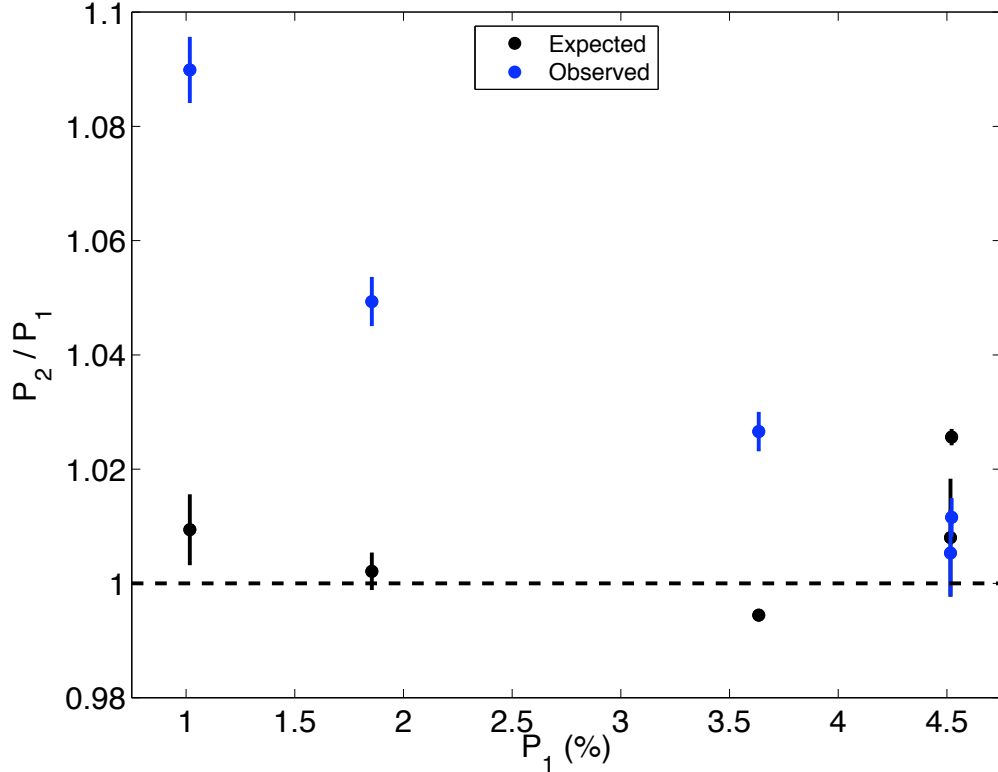


Figure 3.7: Expected and observed ratios of polarization between APDs.

for this weakly polarized star. HD 9270 is not significantly variable on one to two night timescales according to Table 3.5, and lack of detected variability is expected due to its weak polarization. The minimum ≈ 3.5 month timescale for significant ISM change in the line of sight to HD 9270 is expected to inhibit variability for the duration of our observations. We find no significant difference in polarization or position angle between detectors.

HD 212311. This weakly polarized star is classified as an unpolarized standard according to Schmidt et al. (1992), who report B and V band polarizations of $(2.8 \pm 2.5) \times 10^{-4}$ and $(3.4 \pm 2.1) \times 10^{-4}$, respectively. We also detect linear polarization of order one part in 10^4 , but it is detected at the 15σ confidence level. We therefore caution against the use of HD 212311 as an unpolarized standard. Because of its weak polarization, we do not expect significant changes in polarization to be detected. Indeed, Schmidt et al. (1992) claim it is non-variable, and we confirm non-variability up to our detection limit on one to three night timescales, as seen in Table 3.6.

u Her (HD 156633). Rudy & Kemp (1977) find phase-locked polarization modulation of amplitude 0.03% in this partially eclipsing binary with two day period (Kukarkin et al. 1958). Orbital

inclination is 76° (Batten 1967) to 77° (Merril 1963), and the secondary appears to fill its Roche lobe (Merril 1963, Kovachev & Reinhardt 1975). By assuming intrinsic polarization to be zero at conjunctions, Rudy & Kemp (1977) assert the interstellar polarization to be 0.02% to 0.03%. The minimum timescale for significant ISM variability is ≈ 1 month, which proves that variability in u Her is intrinsic. Unfortunately, our observations only span one night, so we are unable to comment on variability.

HD 157999 (σ Oph, HR 6498). Serkowski et al. (1975) find wavelength dependence of polarization consistent with interstellar origin. No variability estimates were found in the literature for this polarized star. HD 157999 appears to be significantly variable in Stokes Q on a one night timescale (Table 3.7), but the signs of variability ΔQ and δQ vary between detector. This star may be variable from night to night, but we do not have enough data to state this with much confidence. The minimum timescale for ISM column variability of ≈ 1.5 years requires that polarimetric variability, if subsequently confirmed, must be intrinsic to the star.

Variability estimates for HD 157999 are preferentially stronger in Stokes Q than in Stokes U . Since the highest signal to noise ratio is achieved on the Stokes parameter with highest polarization, variability in this Stokes parameter will be most easily detected. HD 157999 has polarimetric position angle $\Theta \approx 90^\circ$, so Stokes Q is an order of magnitude stronger than Stokes U . This is most likely the reason for strong Stokes Q variability and weaker Stokes U variability.

HD 7927 (ϕ Cas, HR 382). Serkowski et al. (1975) find significant interstellar polarization in the line of sight to this star based on the wavelength dependence of polarization. Many authors (Gehrels & Silvester 1965, Coyne & Gehrels 1966, Hsu & Breger 1982, Dolan & Tapia 1986, Bastien et al. 1988, Wolff et al. 1996) find significant wavelength dependence of position angle. Dolan & Tapia (1986) and Bastien et al. (1988) claim nightly variability of this star and interpret it to be intrinsic in origin. However, Clarke & Naghizadeh-Khouei (1994) reject the variability claim of Bastien et al. (1988) on the grounds that their statistical analyses lacked rigor. They perform a K-S test on the cumulative distribution function of position angle to claim non-variability of this star. Bastien et al. (2007) re-analyze the Bastien et al. (1988) data and assert that variability exists. Unfortunately, our observations only span one night; therefore, we cannot comment on variability of HD 7927.

HD 147084 (*o Sco*, **HR 6081**). Both Martin (1974) and Serkowski et al. (1975) find wavelength-dependent linear polarization consistent with interstellar origin. Dolan & Tapia (1986) observe low significance changes in polarimetric position angle Θ with wavelength: their probability of constant Θ versus wavelength is 0.35 according to the χ^2 test. While their uncertainty in position angle for this star is substantially larger than other stars in their program, the lack of wavelength dependence on position angle is supported by many authors (Serkowski 1968, Serkowski et al. 1975, Hsu & Breger 1982, Bailey & Hough 1982, Clarke 1986).

However, Kemp (1972) and Kemp & Wolstencroft (1972) detect significant wavelength-dependent circular polarization in the line of sight to this star. Martin (1974) further finds the wavelength dependence of circular polarization to be consistent with significant change in grain orientation along the line of sight. Reconciliation of the lack of wavelength dependence on position angle as well as the presence of significant circular polarization can occur by two effects. Either grain orientation but not size varies along the line of sight, the star possesses intrinsic polarization, or both.

Dolan & Tapia (1986) posit that the star is intrinsically polarized, and they hypothesize that this intrinsic polarization has wavelength dependence on position angle opposite that due to the line of sight dust grains. This hypothesis may be supported by the timescale of variability seen by Bastien et al. (1988) as well as by the reanalysis by Bastien et al. (2007). In Figure 2 of Bastien et al. (1988), variability in degree of polarization as well as position angle seems to occur over the first nine-night interval. Consultation of Table 3.10 shows that ISM variability requires at least two months to be detected, implying that the source of variability may be intrinsic. On the other hand, the remaining ≈ 31 nights in Figure 2 of Bastien et al. (1988) do not show much variability. Additionally, Clarke & Naghizadeh-Khouei (1994) criticize the Bastien et al. (1988) assertion of variability. A simpler explanation of the lack of wavelength-dependent position angle is that grain size may not change in the line of sight. Unfortunately, we have no Stokes Q measurements, and the variability in Stokes U changes sign between our detectors (Table 3.7). Therefore, our data are not sufficient to confirm variability of Bastien et al. (1988) or to otherwise shed light on this subject.

HD 204827. Serkowski et al. (1975) find polarization of this star to be caused by the ISM. Hsu & Breger (1982) see significant change in position angle with wavelength. Dolan & Tapia (1986) also observe changes in polarimetric position angle Θ with wavelength: their probability of constant Θ versus wavelength according to the χ^2 test varies from $\alpha = 0.09$ to $\alpha < 10^{-5}$ over a two month

interval. However, Schulz & Lenzen (1983) claim that no significant rotation of position angle occurs with wavelength. A χ^2 analysis of their *UBVRI* band data gives the probability of constant position angle to be $\alpha = 0.07$. Clayton et al. (1995) also claim that no substantial change in position angle occurs with wavelength, but their Figure 1 clearly shows the trend of increasing position angle with increasing wavelength seen by Hsu & Breger (1982) and Dolan & Tapia (1986). Indeed, they perform no statistical tests to verify their claim. No circular polarization measurements were found in the literature.

Three authors classify this strongly polarized star as variable on a ≈ 4 night timescale (Dolan & Tapia 1986, Bastien et al. 1988, reanalysis by Bastien et al. 2007), but Schmidt et al. (1992) claim it is not. Additionally, Clarke & Naghizadeh-Khouei (1994) criticize the variability claim of Bastien et al. (1988). We observe significant changes in Stokes U (ΔU_{mean} and δU_{mean} in Table 3.8) on timescales of one to three nights. However, the cumulative distribution functions do not significantly vary on one and two night timescales ($\alpha_U > 0.01$), but they do significantly vary on a three night timescale. The few nights for which Stokes Q data exist show significant variability in ΔQ_{mean} and δQ_{mean} as well, but again the CDFs do not significantly vary. Therefore, we confirm variability of this star on a three night timescale and suspect it to be present on shorter timescales, but further data are required for confirmation. The minimum timescale for ISM variability is of order one day from Table 3.10, which raises the possibility of polarimetric variability due to the ISM.

3.4.2 Extrasolar Planets

HR 8974 (γ Cep, HD 222404). No variability estimates were found in the literature for this unpolarized star. The primary component of the binary system with period 67.5 ± 1.4 years (Neuhäuser et al. 2007) harbors an extrasolar planet. Hatzes et al. (2003) discovered a planetary companion to the primary star, and the minimum 1.60 ± 0.13 Jupiter mass planet has a period of $T \approx 903$ days and semimajor axis $a \approx 2.04$ AU (Neuhäuser et al. 2007). Therefore, we expect the amplitude of the planetary polarimetric signal to be of order 10^{-8} or less and consequently undetectable. This star does not appear to be significantly variable on one to three night timescales, as seen in Table 3.4. This is consistent with the essentially unpolarized nature of this star as well as the minimum ≈ 1 month timescale for significant change in the line of sight ISM column. We find no significant difference in polarization between detectors.

Table 3.13: Variability of Exoplanet Host Stars

Name	System Properties				Stokes	χ^2/n	α	$\frac{1}{2}\Delta(Q, U)$ (10^{-5})
	M (M_J)	T (days)	a (AU)	i ($^\circ$)				
HD 189733 ^a	1.150(46)	2.2185733(20)	0.0312(4)	85.76(29)	Q/I	6.7/6	0.353	4.7(3.2)
...	U/I	6.9/6	0.329	4.8(2.7)
HD 149026 ^a	0.36(3)	2.8758887(35)	0.0432(6)	$85.4_{-0.8}^{+0.9}$	Q/I	2.3/7	0.942	3.2(2.3)
...	U/I	5.8/7	0.560	7.6(4.1)
HD 175541	$0.61 \sin i$	297.3(6.0)	1.03	?	Q/I	5.4/6	0.492	5.4(2.7)
...	U/I	9.1/6	0.168	6.2(2.4)
HR 8974	$(1.60 \pm 0.13) \sin i$	902.9(3.5)	2.044(57)	?	Q/I	2.9/3	0.401	1.47(86)
...	U/I	0.6/4	0.965	0.26(41)

^aTransiting planet

HD 175541. No variability estimates were found in the literature for this weakly polarized star. It harbors a planet with minimum mass 0.61 Jupiter masses, a period of $T \approx 297$ days, and semimajor axis 1.03 AU (Johnson et al. 2007). Since the fraction of starlight intercepted by the planet is less than one part in 10^7 , any observed polarimetric variability from the system cannot be due to the planet. Constant polarization of this system over six nights can only be rejected at the $\alpha = 17\%$ level of significance according to the χ^2 test (Table 3.13 and Figure 3.8). We require $\alpha < 1\%$ in order to confirm variability of the star. Therefore, we cannot claim variability of HD 175541 with confidence; however, Figure 3.8 shows qualitative evidence of a long-period trend in the polarization of this star. This may be due to variability in the ISM, because the minimum timescale for this process is less than one day.

HD 149026. No variability estimates were found in the literature for this weakly polarized star. A short-period, transiting planet exists around this star with $M = 0.36 \pm 0.03 M_J$ (Winn et al. 2008), $T \approx 2.9$ day period, semimajor axis $a \approx 0.04$ AU, and $i = 85.4_{-0.8}^{+0.9}$ (Nutzman et al. 2008). Constant polarization of this system can only be rejected at the $\alpha = 56\%$ level of significance; therefore, we do not observe significant variability (Table 3.13 and Figure 3.9). It is interesting to note that the Stokes U observations near phase 0.8, where phase 0 is set to be mid-transit, are somewhat different from each other. Therefore, there does not appear to be strong phase-locking of the polarization of the system to the orbital period of the planet. This is expected from a system where the planet only intercepts of order one part in 10^5 of the stellar flux; consequently, the polarimetric amplitude of the system from the transiting planet is expected to be one part per million to one part in ten million.

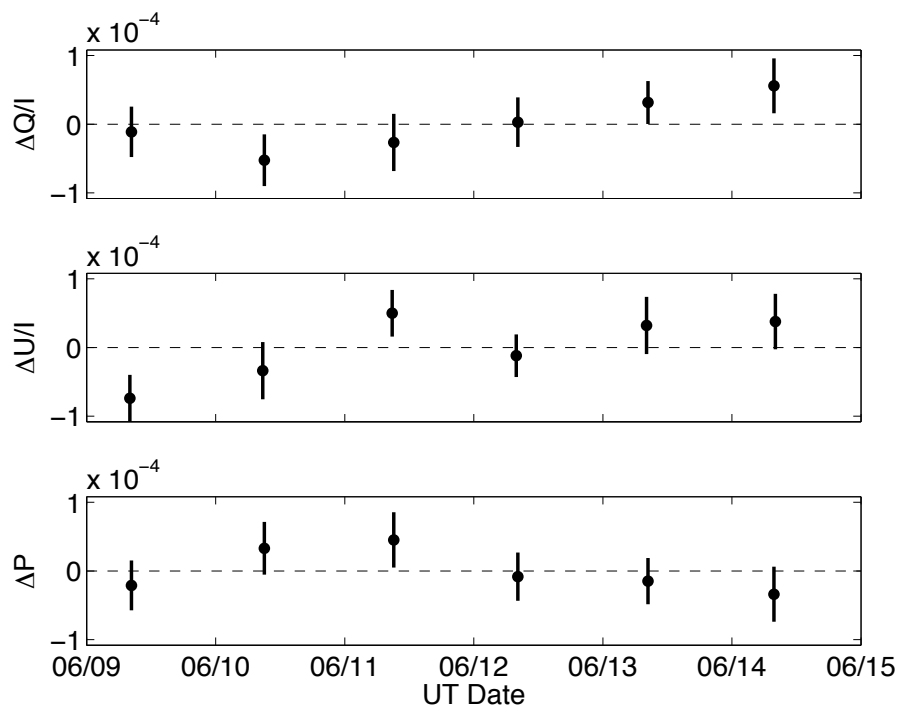


Figure 3.8: Observed polarization of the HD 175541 exoplanet system. Mean polarization of order one part in 10^4 has been subtracted.

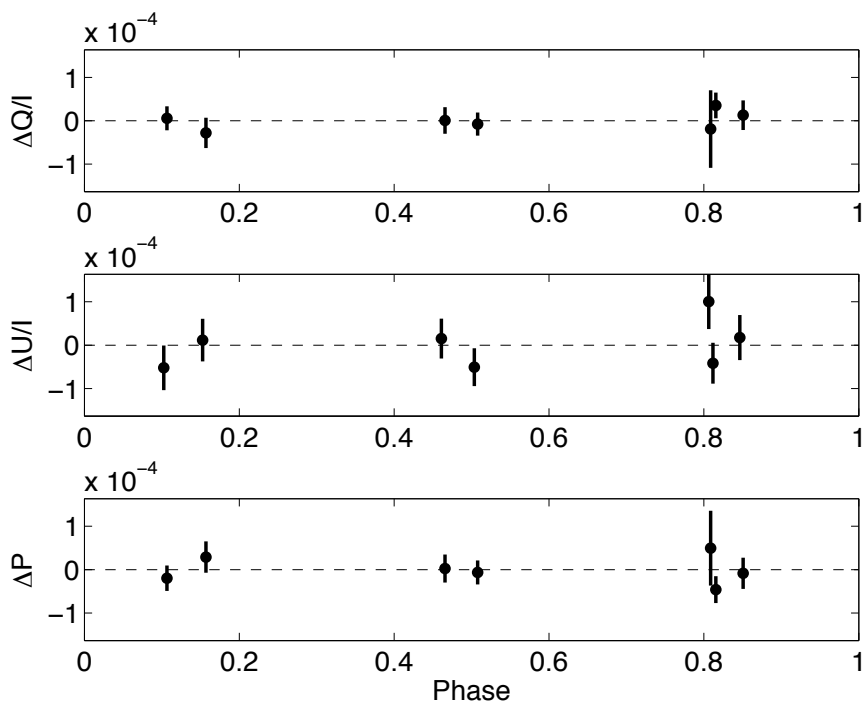


Figure 3.9: Observed polarization of the HD 149026 transiting hot Jupiter system. Mean polarization of order one part in 10^4 has been subtracted. Phase 0 represents mid-transit (0.5 phase difference between transit and radial velocity ephemerides).

HD 189733 (V452 Vul). Berdyugina et al. (2008, hereafter B08) observe marginal variability of this system, which harbors a transiting hot Jupiter with $M = 1.150 \pm 0.046 M_J$, $T \approx 2.2$ days, $a \approx 0.03$ AU, and $i = 85.76 \pm 0.29^\circ$ (Winn et al. 2007). They attribute this modulation to stellar flux scattered by the hot Jupiter. However, planetary polarization is expected to be only of order one part per million or less, especially when multiple scattering in the planetary atmosphere is taken into account (cf. Seager et al. 2000). The polarimetric modulation of HD 189733 appears to be two orders of magnitude larger than expected from a planetary origin, where B08 observe $\Delta P \approx 2 \times 10^{-4}$. Indeed, in order to explain this large of a modulation from scattering by a planetary atmosphere, B08 invoke a Lambertian sphere, with geometric albedo of 2/3. Even with this unrealistically large albedo, B08 require a planetary radius 30% larger than the radius measured by transits. The ratio of planetary to stellar radii is accurately obtained from transit observations, and near-IR interferometry has accurately determined the stellar radius (Baines et al. 2007). Planetary radius estimates from transit and interferometric observations are more reliable than the polarimetric estimate by B08. Therefore, the polarimetric modulation observed by B08 cannot be due to the planet.

A potential cause of polarimetric variability in hot Jupiter host stars is starspot activity. Photometric observations by the MOST satellite suggest the existence of starspots on the short period τ Boö that follow the rotation period of the star (Walker et al. 2008). There is also some evidence that Ca II H and K emission from the short period HD 179949 may follow the stellar rotation period (Shkolnik et al. 2005, 2008). HD 187933 is known to be active, with up to 1% of its surface covered in spots at any time (Hébrard & Lecavelier des Etangs 2006, Croll et al. 2007, Pont et al. 2007, Winn et al. 2007, Moutou et al. 2008). These spots appear to rotate with the roughly 11.8 day stellar rotation period (Henry & Winn 2008, Croll et al. 2008). Unfortunately, B08 do not discuss the probability of starspots causing their observed modulation.

Plotted in Figure 3.10 are the phase-binned observations of B08. They observe polarization peaks at quadrature phases and vanishing polarization at conjunctions. B08 take these observations to be evidence of a planetary origin of the polarimetric signature of the system. That is, a planet at quadrature ensures a 90° scattering angle, which maximizes the degree of polarization from the planet. At conjunctions, however, a planet is at near-full or near-new phase, which generates zero net polarization. However, the Lambertian planetary model of B08 fails to accurately describe the Stokes U variability near phase 0.2 (Figure 3.10). This may be evidence of the more complex polarization modulation due to a corotating, polarized starspot. While the ISM may be variable on

a timescale less than the orbital period of the planet, the consistent but weak variability observed by B08 and POLISH at these phases suggests that ISM variability is not the cause of observed modulation in HD 189733.

In Figure 3.11, we show nightly mean polarization of HD 189733 observed with POLISH. There appears to be qualitative variability in our polarimetric observations, which is similar to that observed by B08. However, since constant polarization can only be rejected at a χ^2 significance of $\alpha = 33\%$, variability cannot be confirmed. Like B08, we observe increases in both Stokes Q and U during this phase. When plotting $\Delta P = \sqrt{(\Delta Q/I)^2 + (\Delta U/I)^2}$, which is the degree of “excess” polarization after mean polarization in each Stokes parameter is removed, we find weak evidence for an increase in degree of polarization near quadrature. We also find weak evidence for a low degree of polarization near phase 0.5, which is defined to be inferior conjunction of the star. At this phase, a corotating starspot will lie behind the stellar limb, so a decrease in polarization near phase 0.5 does not prove a planetary origin for the polarimetric modulation. Longer phase coverage of the polarimetric modulation of the system is required to determine the existence of a polarized starspot.

Because of the high degree of polarization of flux scattered through 90° , a stellar limb is expected to be polarized. The position angle of limb polarization is expected to be tangent to the limb, because the scattering plane is in the radial direction. Outside of a transit, the symmetry of main sequence stellar disks ensures low net intrinsic stellar polarization. However, as a planet contacts the limb of a star to mark the beginning of a transit, the partial occultation of the star’s limb generates net polarization. The partial loss of polarization tangent to the stellar limb causes net polarization of the starlight parallel to the line connecting the centers of the planet and star (Figure 3.12). During mid-transit, the polarization vector is perpendicular to the orbital plane, but the degree of polarization is low. This is because stellar polarization is concentrated in the limb. For $83^\circ < i < 90^\circ$, the planet will transit at mid-latitudes on the star, so the North/South Polar limb will not be occulted. Thus, the maximum change in polarization during the transit will take place at ingress and egress, as opposed to mid-transit.

The strength of the polarimetric modulation during the transit has been modeled by Carciofi & Magalhães (2005), which is presented as our Figure 3.13. The amplitude varies over two orders of magnitude, from one part per million to one part in 10^4 , depending on the strength of the stellar limb polarization, its radial dependence, and the wavelength observed. The strongest signal appears

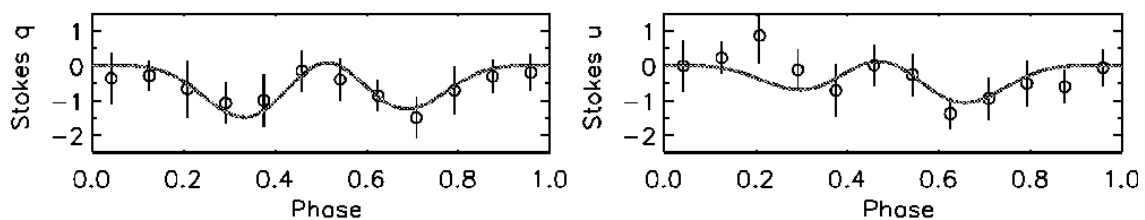


Figure 3.10: Polarimetric modulation of the HD 189733 transiting hot Jupiter system from Figure 1 of Berdyugina et al. (2008). Mean polarization of order one part in 10^4 has been subtracted.

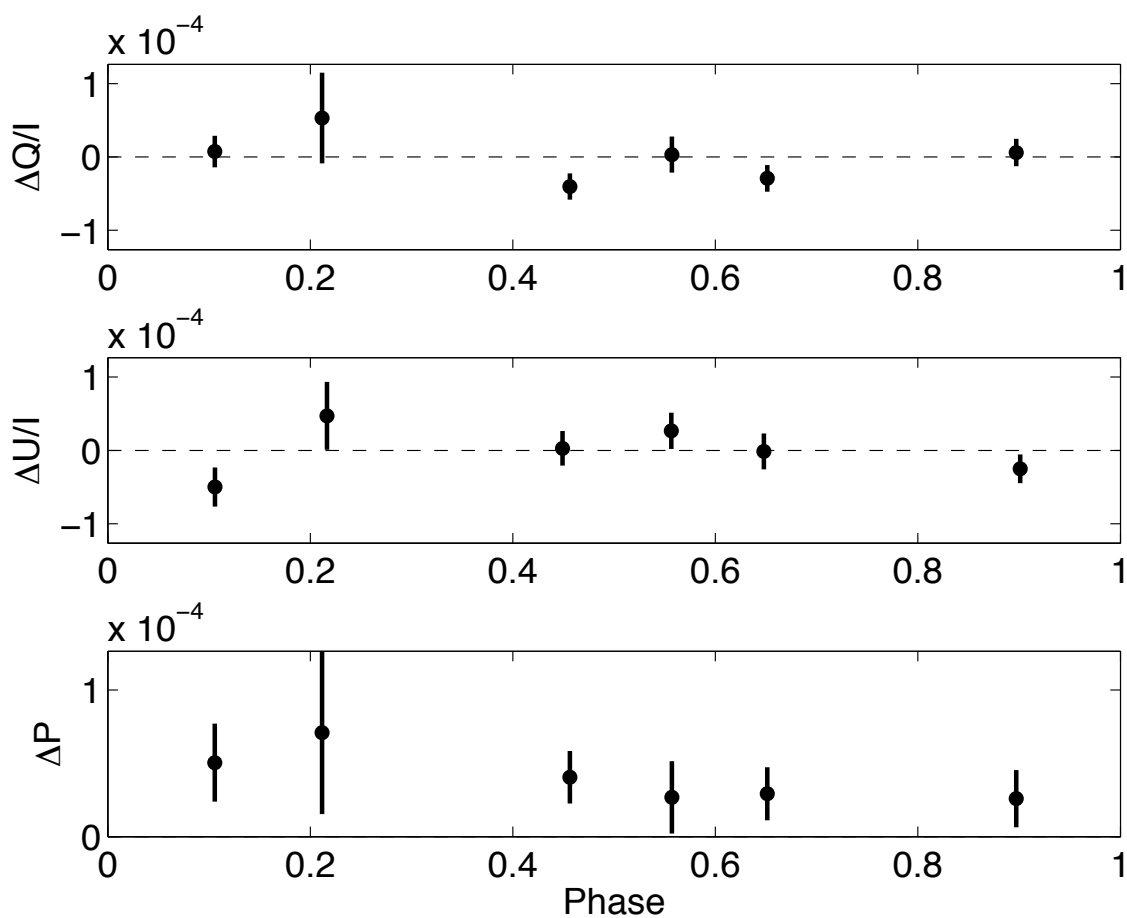


Figure 3.11: Observed polarization of the HD 189733 transiting hot Jupiter system. Mean polarization of order one part in 10^4 has been subtracted. Phase 0 represents mid-transit (0.5 phase difference between transit and radial velocity ephemerides).

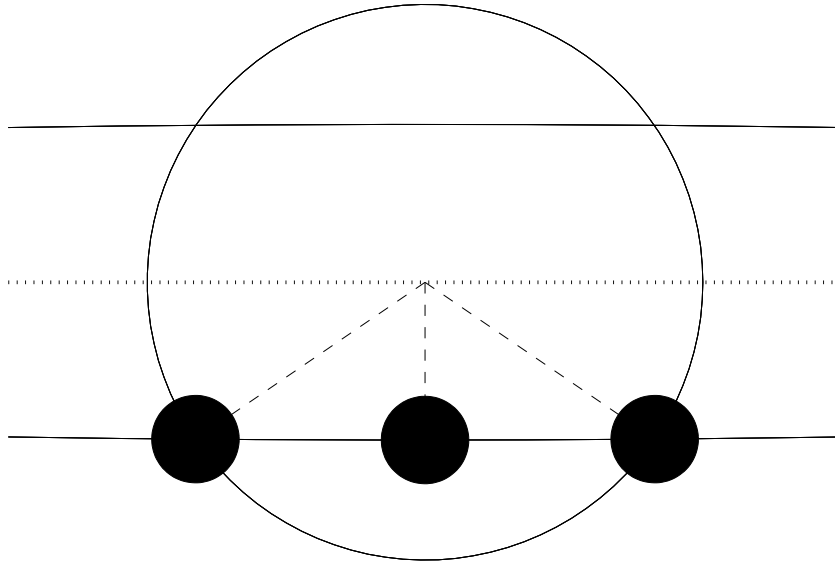


Figure 3.12: HD 189733 transit geometry, planet and star are to scale. Dashed lines indicate position angle of net polarization at transit ingress, mid-transit, and egress. A degeneracy exists in photometry between a Northern and Southern Hemisphere transit, where the dotted line indicates the equatorial plane of the star. Polarimetry appears to have resolved this degeneracy: a Southern Hemisphere transit (pictured) is consistent with the observations.

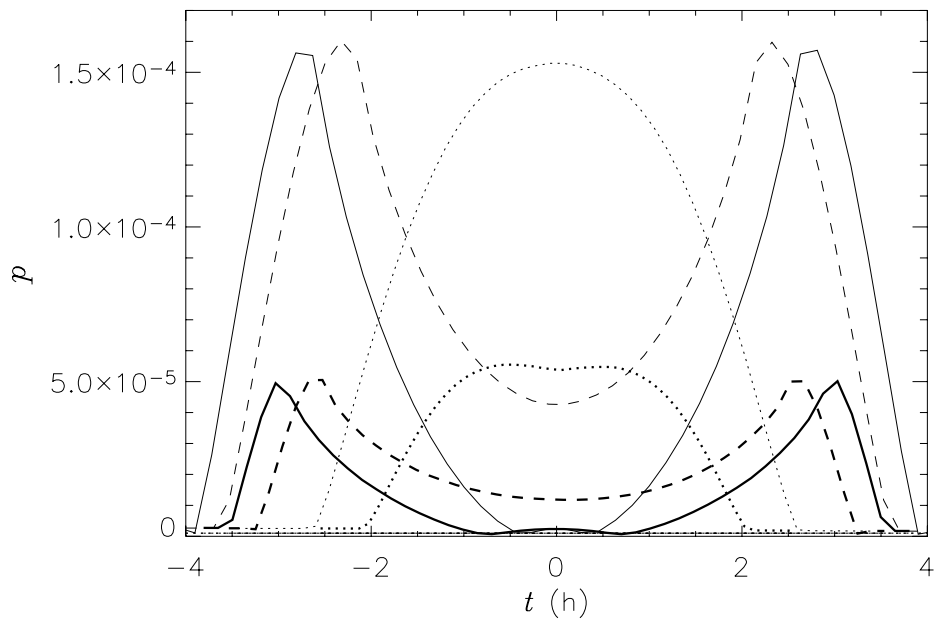


Figure 3.13: Modeled degree of polarization during a transit. Vertical scale is highly model-dependent. This figure is taken from Figure 5 of Carcofi & Magalhães (2005).

to exist at the Ca I $\lambda 4227$ resonant line, and the $P(\lambda) \propto \lambda^{-4}$ dependence of Rayleigh scattering in the stellar photosphere is also present. Thus, our $\approx B$ band instrument is well suited for the detection of a polarized transit. We observed HD 189733 for ≈ 3 hours at Cassegrain ring angle $\phi = 60^\circ$, with ≈ 30 minutes both before and after the transit as well as ≈ 2 hours during the transit. This ring angle was chosen to maximize the polarimetric signal, based on the estimation by B08 of a $\Omega = 16^\circ$ longitude of ascending node. Since the equatorial plane is therefore estimated to have a position angle of $\Theta = 16^\circ$ on the sky, the net polarization of the system (due to the planet outside of transit) is expected to lie at $\Theta = 90^\circ + 16^\circ = 106^\circ$.

During transit ingress and egress, however, position angle of net polarization of the system lies at 45° or 135° with respect to the orbital plane (Figure 3.12). To maximize the sensitivity of POLISH to the transit, we chose to set the Cassegrain ring to $\phi = 45^\circ + 16^\circ \approx 60^\circ$. Note that the use of the Wollaston prism provides equal sensitivity to Stokes components 90° apart. Thus, only the sign of the observed polarization changes whether the transit induces $\Theta = 45^\circ$ or $\Theta = 135^\circ$ polarization with respect to the orbital plane. Subtracting the polarization from each detector enhances the signature of the transit, because the slope of the modulation is opposite for each detector. That is, for system polarization at 45° with respect to the orbital plane, detector 1 will record positive polarization while detector 2 will measure negative polarization. For system polarization at 135° with respect to the orbital plane, the magnitude of the polarization will be the same as for 45° , but the signs will be reversed.

Raw data are shown in Figure 3.14, while Figure 3.15 represents the results after applying a weighted, moving average with a bin size of 79 points. The subscript on the polarization indicates the detector. The dotted boxes in Figure 3.15 represent the uncertainty in polarization as well as the size of the moving average bin. The bin size is chosen to maximize sensitivity to variability at the transit timescale. Since detector 1 observes positive polarization at ingress and negative at egress, while detector 2 observes the opposite, it appears that the planet transits the Southern Hemisphere of the star. This transit appears to have an amplitude of $\Delta P \approx 3 \times 10^{-5}$, which is 1,000 times weaker than the amplitude in photometry.

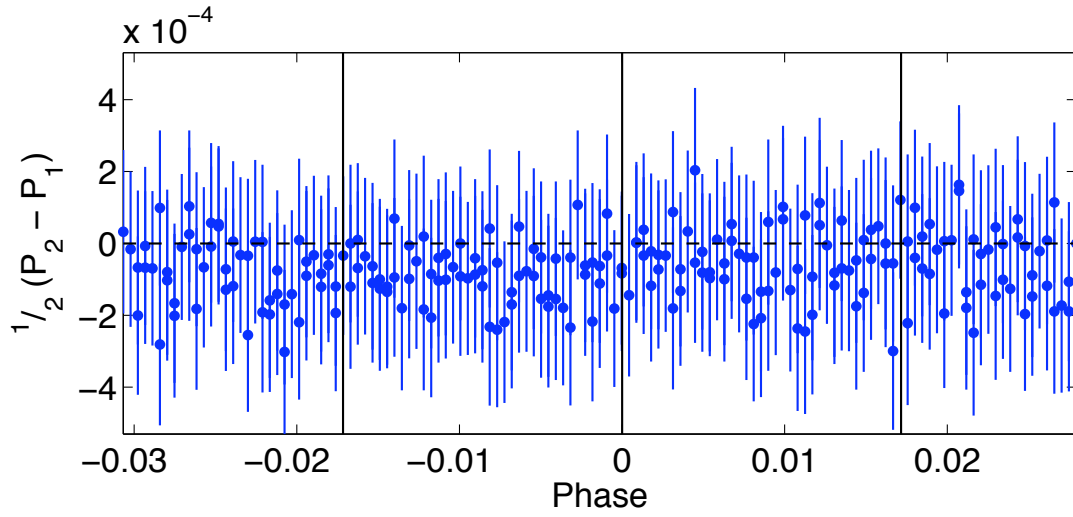


Figure 3.14: Sky-subtracted, polarimetric observations of a transit of the HD 189733 hot Jupiter. The duration of the time series is ≈ 3 hours. Vertical black lines mark transit ingress, mid-transit, and egress.

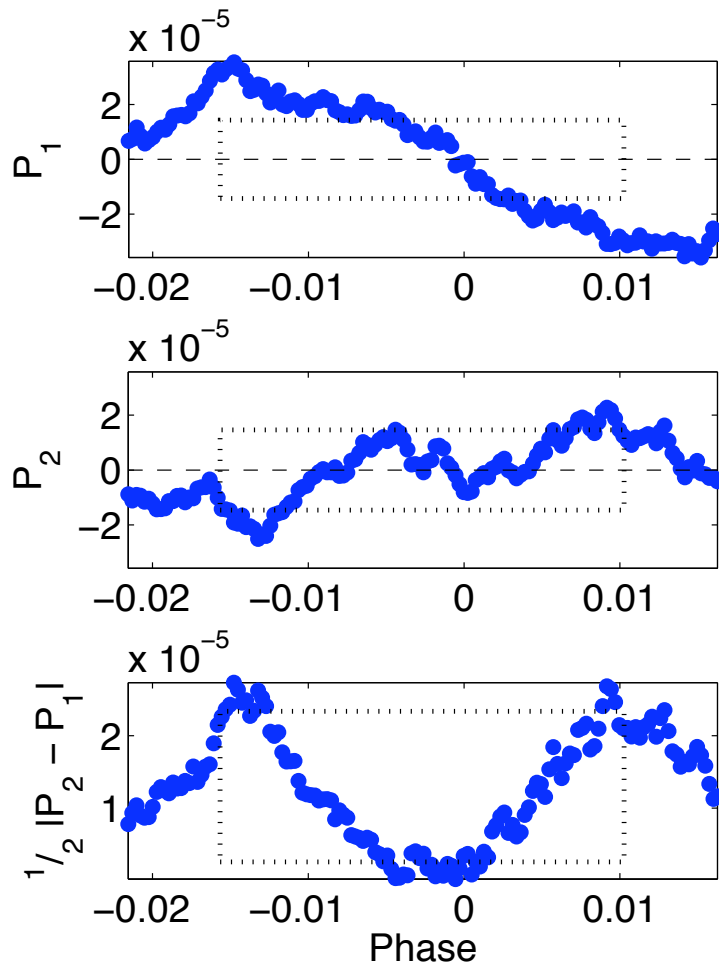


Figure 3.15: Possible transit of an extrasolar planet seen in polarized light. Phase 0 corresponds to mid-transit, and the transit duration is 1.827 hours (Winn et al. 2007).

3.4.3 Debris Disk

γ Oph (HD 161868, HR 6629). No variability estimates were found in the literature for this weakly polarized star. It is not significantly variable on one to two night timescales according to Table 3.5. Lack of detected variability is expected due to weak polarization. The minimum ≈ 1 week timescale for ISM variability in the line of sight to γ Oph is approaching the timescale of our observations. Interestingly, marginally significant variability on both a one and two night timescale is observed with detector 1. However, since this is not seen in detector 2, we cannot confirm variability.

γ Oph harbors a debris disk imaged by the Spitzer Space Telescope with inner and outer radii of ≈ 13 and ≈ 520 AU, respectively. This disk, containing $0.010 M_{\oplus}$ of dust, is inclined at $50 \pm 5^{\circ}$ with its major axis at a position angle of $55 \pm 2^{\circ}$ (Su et al. 2008). Multiplying the degree of polarization from Table 3.1 by the 0.836 ± 0.064 correction factor described in section 2, we find absolute polarization of this source to be $P = (1.49 \pm 0.12) \times 10^{-4}$.

To model the expected polarization of the disk, we assume single scattering of the parent star's flux by an optically thin disk composed of small (comparable to the wavelengths of visible light) dust grains. We set γ Oph at the origin O of a right-handed coordinate system. The disk lies on the xy plane, and the observer is along the direction $\theta = i$ (Figure 3.16). Following the derivation in the Appendix (Equations D11a and D11b), the Stokes parameters of the light scattered off the disk are

$$\left(\frac{Q}{I}\right)_{\text{disk}} = \frac{\sin^2 i}{2 + \sin^2 i} \quad (3.8a)$$

$$\left(\frac{U}{I}\right)_{\text{disk}} = 0 \quad (3.8b)$$

which are identical to the expressions of Shakhovskoi (1965). The $+Q$ direction is perpendicular to the disk's major axis for nonzero inclination, and the $-Q$ direction is parallel to the major axis. These Stokes parameters are rotated with respect to celestial north by the position angle of the disk's major axis.

As expected, $(Q/I)_{\text{disk}} = (U/I)_{\text{disk}} = 0$ for $i = 0$. That is, polarization from a face-on disk is zero because of symmetry. For an edge-on disk with $i = \frac{\pi}{2}$, $(Q/I)_{\text{disk}} = \frac{1}{3}$ and $(U/I)_{\text{disk}} = 0$.

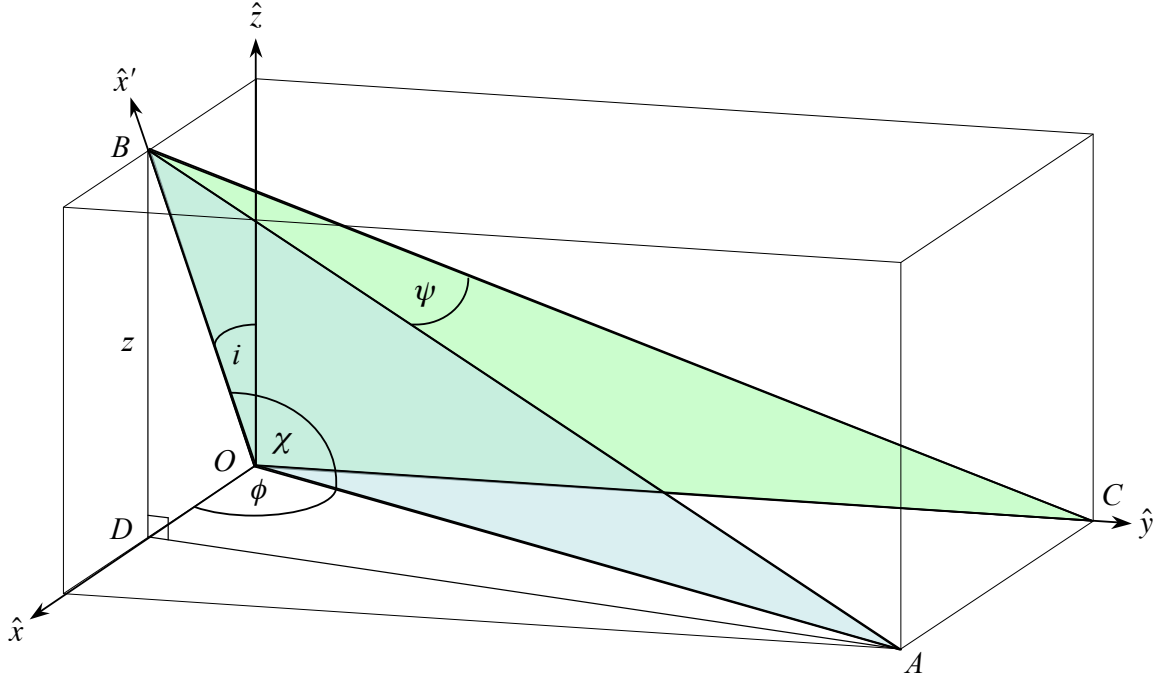


Figure 3.16: Debris disk geometry. The disk is in the xy plane, the blue plane \overline{OAB} is the scattering plane, and the green plane OBC is the observer plane.

These results indicate polarization perpendicular to the disk's major axis for all inclination angles, which is predicted by Sunyaev & Titarchuk (1985). Given $i = 50^\circ$ for the γ Oph disk from Su et al. (2008), we find $(Q/I)_{\text{disk}} = 0.23$ and $(U/I)_{\text{disk}} = 0$ before adding in the star's unpolarized light. Since $(Q/I)_{\text{disk}}$ is positive, polarization is expected to be perpendicular to the disk's major axis from single scattering by small particles. However, Table 3.1 shows the position angle of polarization to be $\Theta = 60.56 \pm 0.65^\circ$, while the position angle of the disk's major axis is $\Theta_{\text{disk}} = 55 \pm 2^\circ$ (Figure 3.17). Thus, the alignment of the disk polarization with the major axis indicates that either multiple scattering dominates or grain size is large enough for forward-scattering to be dominant.

The latter hypothesis is corroborated by Su et al. (2008), who assume grain sizes ranging from $5 \mu\text{m}$ to $63 \mu\text{m}$ based on the spectral energy distribution of the disk. They adopt a constant surface density model for the disk, and the size distribution of the grains is in collisional equilibrium. That is, size distribution is modeled as $n(a) \propto a^{-\frac{7}{2}}$ for grain diameter a . Therefore, the number density of grains as a function of radius in the disk is $n(r) = n_0 \int_{a_{\text{min}}}^{a_{\text{max}}} a^{-\frac{7}{2}} da$, where n_0 is a constant. Assuming grain volume $V(a) = \frac{4}{3}\pi a^3$, their grain density of $\rho = 2.5 \text{ g/cm}^3$, and disk mass $0.010 M_\oplus$, we find $n_0 = 2.6 \times 10^{-7}$ from Equation D12. Assuming grain cross-section $\sigma(a) = \pi a^2$, we use Equation D13 to find the fraction of the stellar flux scattered off the disk to be

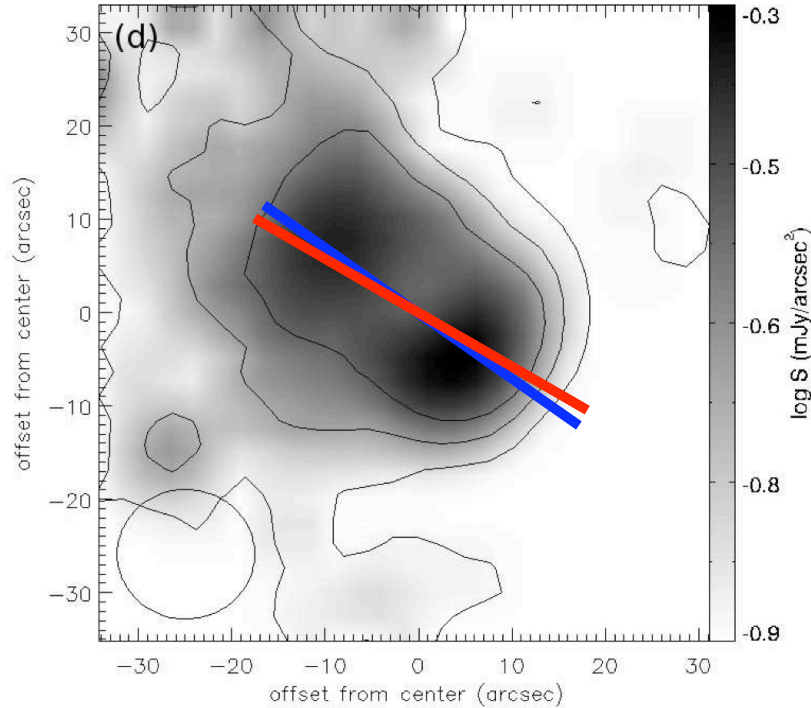


Figure 3.17: Position angle of net polarization, $\Theta = 60.56 \pm 0.65^\circ$ (red line) overlain on a Spitzer image of the γ Oph debris disk (Figure 1d from Su et al. 2008). Position angle of the disk major axis when projected on the sky, $\Theta_{\text{disk}} = 55 \pm 2^\circ$, is shown as the blue line.

$$I_{\text{disk}} = 2\pi^2 n_0 \left(\frac{1}{\sqrt{a_{\text{min}}}} - \frac{1}{\sqrt{a_{\text{max}}}} \right) \ln \left(\frac{r_{\text{max}}}{r_{\text{min}}} \right) (2 + \sin^2 i). \quad (3.9)$$

Here, the inner disk radius is r_{in} , and the outer radius is r_{out} . Given grain sizes from $5 \mu\text{m}$ to $63 \mu\text{m}$, disk extent 13 to 520 AU, and $i = 50^\circ$ from Su et al. (2008), we find $I_{\text{disk}} = 1.6 \times 10^{-3}$. Multiplying this by the expected disk polarization $P_{\text{disk}} = \sqrt{(Q/I)_{\text{disk}}^2 + (U/I)_{\text{disk}}^2} = 0.23$ found above, the polarization of the γ Oph system is expected to be $P_{\text{exp}} = 4 \times 10^{-4}$. This is the same order of magnitude as the observed polarization $P_{\text{obs}} = (1.49 \pm 0.12) \times 10^{-4}$.

Multiple scattering is expected to rotate the polarization position angle by 90° with respect to the single scattering case. This will cause polarization to be parallel to the major axis of the disk (Angel 1969, Sunyaev & Titarchuk 1985, Phillips & Mészáros 1986, Kartje & Königl 1991), as observed. However, multiple scattering tends to decrease the degree of polarization. Since the expected polarization from single scattering is of the same order of magnitude as the observed polarization, multiple scattering cannot be dominant. Thus, the most likely explanation for the alignment of polarimetric position angle and disk major axis is that the grains are predominantly forward-scattering.

Assuming the expected polarization from the single scattering model in Figure 3.16 correctly predicts the system polarization, the slight discrepancies between observed and expected polarization as well as position angle may be due to interstellar polarization. Solving for the interstellar polarization vector necessary to decrease degree of polarization as well as rotate it by 5° , we find $Q_{\text{IP}} = (4.6 \pm 2.5) \times 10^{-5}$, $U_{\text{IP}} = (-2.11 \pm 0.13) \times 10^{-4}$, $P_{\text{IP}} = (2.16 \pm 0.14) \times 10^{-4}$, and $\Theta_{\text{IP}} = 141.2 \pm 3.2^\circ$. Uncertainties in interstellar polarization are the minimum possible assuming no uncertainty in expected degree of disk polarization. The probability of random interstellar polarization lying within 86° of the disk's random major axis orientation is 23%, which is not significantly low. Therefore, we posit that the line of sight to γ Oph contains interstellar polarization of degree $P_{\text{IP}} \approx 2.2 \times 10^{-4}$ and lying at position angle $\Theta_{\text{IP}} \approx 141^\circ$. This degree of interstellar polarization appears to be high when compared with stars at similar distances (Figure 3.6), but γ Oph lies toward the Galactic Center, along with HD 147084 and HD 154445. These stars appear to have enhanced polarization with respect to stars at comparable distances, which is explainable by enhanced dust cloud density along this galactic longitude.

3.4.4 Cepheid Variables

Algenib (γ Peg, HD 886, HR 39). Rudy & Kemp (1978) find circular polarization present and assert a nonzero magnetic field with a null result probability of $\alpha = 0.004$ under the χ^2 test. While no mention is made as to whether this circular polarization could be interstellar in origin, the proximity of this star strongly implies that interstellar polarization, both linear and circular, should be negligible. Thus, the observed circular polarization must be intrinsic to Algenib. No variability estimates were found in the literature for this polarized β Cepheid star.

As with HD 157999, this star appears to be significantly variable in Stokes Q on a one night timescale (Table 3.7), but the signs of variability ΔQ and δQ vary between detectors. Indeed, weighted mean variabilities between detectors, ΔQ_{mean} and δQ_{mean} , are not significant. While both APDs have slightly different bandpasses (Figure 3.1), we find no significant difference in position angle between these detectors over the entire run on this star. Thus, it appears that this star may be variable from night to night, but we do not have enough data to state this with much confidence.

The minimum ≈ 1 month timescale for ISM column variability requires that polarimetric vari-

ability, if subsequently confirmed, must be intrinsic to the star. The intrinsic circular polarization of the star points to an intrinsic origin for the linear polarization. Indeed, Figure 3.6 implies that the linear polarization in the line of sight to Algenib is an order of magnitude larger than for HD 9270, which is at a similar distance. The polarization maps of Mathewson & Ford (1970) show that HD 9270 and Algenib are both located in the same region of weak polarization in the sky. Therefore, we assert that the linear polarization seen in Algenib is intrinsic to the star.

The position angle of net polarization for Algenib is $\Theta = 111^\circ$ from Table 3.1, so its $P \approx 1\%$ polarization is split fairly evenly between Stokes Q and U . This is because Stokes $+Q$ is projected north/south on the sky ($\Theta = 0^\circ/180^\circ$), Stokes $-Q$ is east/west ($\Theta = 90^\circ/270^\circ$), Stokes $+U$ is northeast/southwest ($\Theta = 45^\circ/225^\circ$), and Stokes $-U$ is northwest/southeast ($\Theta = 315^\circ/135^\circ$). One might therefore expect that variability in Algenib would occur with equal amplitude in both Stokes Q and U . Reasons for stronger variability in Stokes Q as opposed to U are unknown.

HD 187929 (η Aql, HR 7570). Serkowski et al. (1975) find polarization as a function of wavelength of this δ Cepheid variable to be consistent with interstellar origin. Dolan & Tapia (1986) and Clarke (1986) independently discovered changes in polarimetric position angle with wavelength, and this result has been confirmed by Wolff et al. (1996). The probability of constant position angle versus wavelength is $\alpha < 10^{-5}$ according to the χ^2 test (Dolan & Tapia 1986). However, Stokes et al. (1974) and Wade et al. (2002) do not detect significant circular polarization of this star. Therefore, some linear polarization must be intrinsic to the star, because rotation of position angle with respect to wavelength cannot be due to dust grain rotation along the line of sight. Polarimetric variability is inconclusive according to Dolan & Tapia (1986), “suspected” by Bastien et al. (1988), and rejected by both Clarke & Naghizadeh-Khouei (1994) and the Bastien et al. (2007) reanalysis of Bastien et al. (1988) data.

However, we detect strong variability in both Stokes parameters on a two night timescale, as $\Delta Q, U_{\text{mean}}$ and $\delta Q, U_{\text{mean}}$ are much larger than three times their respective uncertainties. The sign of variability on a one night timescale varies between detector, so it is difficult to claim variability on this timescale with confidence. While the variability in Stokes Q on a three night timescale has different sign between detector 1 and detector 2, variability in Stokes U on this timescale has the same sign. As with variability of this star on a one night timescale, variability on a three night timescale is difficult to claim without more data.

It is possible that changes in variability occur with wavelength, since changes in position angle are known to occur with wavelength. While both APDs have slightly different bandpasses (Figure 3.1), we find no significant difference in position angle between these detectors over the entire run on this star. According to Table 3.10, the minimum timescale for ISM variability along the line of sight to this star is ≈ 4 months. In addition, the observed variability in Stokes Q is only ≈ 3 times larger than that in Stokes U , even though run-averaged Stokes Q is ≈ 10 times larger than Stokes U . One would expect that a random orientation of the system in the plane of the sky would cause intrinsic polarization variability to occur with roughly equal amplitude in each Stokes parameter. However, variability in interstellar polarization would be expected to be stronger in the dominant Stokes parameter. Thus, the variability of this star must be caused by changes in its intrinsic polarization.

The period of this Cepheid variable is $T \approx 7.2$ days (Gray & Stevenson 2007). Even though Cepheids are radial pulsators, there must be some asymmetry in the distribution of scatterers in the star's envelope to introduce time-variable, intrinsic polarization. Indeed, polarimetric monitoring of post-AGB stars has shown pulsation phase-locked variability that is generally explained by non-radial pulsations (Henson et al. 1985, Magalhães et al. 1986, Raveendran & Rao 1989, Yudin & Evans 2002). Trammell et al. (1994), on the other hand, suggest polarimetric variability to be caused by clumpy mass loss. From ephemerides in Table 2 of Gray & Stevenson (2007), our observations on UT 2007 Aug 3, 5, and 6 were taken at phases 0.013 to 0.018, 0.296 to 0.298, and 0.436 to 0.438, respectively. Maximum negative radial velocity is achieved at phase ≈ 0.05 , zero radial velocity at phase 0.5, and maximum positive radial velocity occurs at phase ≈ 0.8 . Thus, our observations almost completely bracket the ranges of increasing radial velocity from maximum negative radial velocity to its first zero crossing.

Variations in polarization are plotted against pulsation phase in Figure 3.18. While the data for UT 2007 Aug 6 (phase 0.44) are inconsistent from detector to detector, the positive increase in polarization between UT 2007 Aug 3 and 5 (phases 0.02 and 0.30) is clear. Net polarization, $P = \sqrt{Q^2 + U^2}/I$, decreases between these two nights when the star's change in size is at a maximum.

From Sudzius (1969) and Depenchuk (1980), the star dims by $\Delta V \approx 0.34$ mag, or 27%, between these phases. From Table 3.14, we see a strong, *relative* decrease in polarization of $\delta P =$

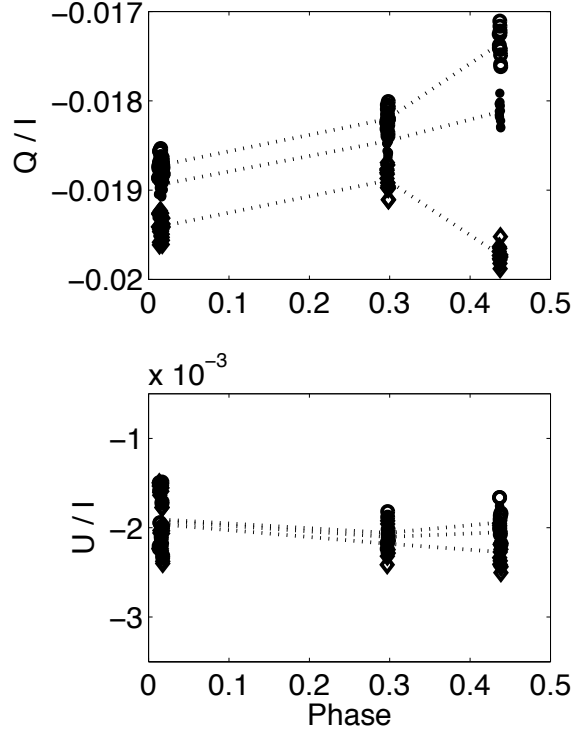


Figure 3.18: Polarization variations in HD 187929 versus Cepheid pulsation phase. Open circles are data from detector 1, open diamonds are from detector 2, and filled circles are weighted mean measurements from both detectors (“detector 1,2”). Dotted lines are guides for the eye.

Table 3.14: HD 187929 Variability

Detector	ΔP ($\times 10^{-6}$)	δP (%)	$\Delta\Theta$ ($^\circ$)
1	-490(35)	-2.60(18)	0.32(13)
2	-485(39)	-2.49(20)	0.35(13)
Mean	-487.8(2.5)	-2.550(59)	0.336(12)

$2.550 \pm 0.059\%$ and a weak, *absolute* increase in position angle $\Delta\Theta = 0.336 \pm 0.012^\circ$ in this time interval. Thus, it appears that the radial increase in size of the star dampens the intrinsic polarization, because a change in stellar intensity should have no effect on polarization. This is because the Stokes parameters Q and U are normalized by the Stokes I intensity parameter.

3.5 Conclusion

We have observed no conclusive polarimetric variability with timescales less than four nights on stars with polarization $P < 2\%$. No star, even the famously variable Cygnus X-1, exhibits detectable po-

larimetric variability during a single night. We have observed no significant variability of the long period extrasolar planet host star HR 8974, which has a period $T \approx 2.5$ years. However, there is weak, qualitative evidence for long period variability in HD 175541, which harbors a long period extrasolar planet with $T \approx 10$ months. The polarization expected from the planets in these systems is less than one part in 10^7 , so observed variability must be due to stochastic variability in the host star itself. No phase-locked behavior is observed for the transiting extrasolar planet system HD 149026, and we do not detect significant variability of the HD 189733 transiting system. Marginal variability in this system is claimed by Berdyugina et al. (2008).

We present tentative evidence for a transit of HD 189733 in polarized light, which is the first reported observation of this effect. The characteristic double-peaked profile predicted by Carciofi & Magalhães (2005), due to occultation of stellar limb polarized, is observed. The transit depth appears to be $\Delta P \approx 3 \times 10^{-5}$, which is three orders of magnitude weaker than seen in photometry (Winn et al. 2007). Polarimetry provides additional geometric information that is difficult to determine from photometric transits. For instance, our observations imply a Southern Hemisphere transit by the planet due to the observed sign of rotation of the polarization vector.

The polarized light scattered by the γ Oph debris disk has been detected, and its position angle is closely aligned to the disk's major axis when projected on the sky. This is evidence for an optically thin disk composed of predominantly forward-scattering dust grains, which must therefore be larger than the wavelengths of visible light. In addition, we find evidence that the line of sight to this nearby star contains interstellar polarization of an order of magnitude larger than do stars at similar distances and along other sightlines. This is consistent with galactic longitude of this star near the Galactic Center.

Polarimetric variability of the β Cepheid pulsator Algenib is observed at low significance. There exists significant circular polarization intrinsic to this star (Rudy & Kemp 1978), which suggests that linear polarimetric variability should also be present. A longer temporal baseline of polarimetric observations is therefore desired. We have confirmed the suspected polarimetric variability of the δ Cepheid star HD 187929 on a two night timescale, which represents $\approx 30\%$ of the pulsation phase. Indeed, this star is known to harbor significant intrinsic linear polarization (Dolan & Tapia 1986, Clarke 1986). While Cepheid variables are radial pulsators, temporal variability of intrinsic linear polarization indicates time-variable asymmetry in the system. Degree of polarization of this star

decreases as stellar radius increases, which is likely due to an increase in symmetry of the system. We confirm polarimetric variability of HD 204827, for which the community position is inconclusive. Nightly variability in the control system, Cygnus X-1, is confirmed to high significance. The next chapter will describe in detail observations of Cygnus X-1.

References

- Angel, J. R. P. 1969, *ApJ* 158, 219.
- Aspin, C., Simmons, J. F. L., & Brown, J. C. 1981, *MNRAS* 194, 283.
- Bailey, J. & Hough, J. H. 1982, *PASP* 94, 618.
- Baines, E. K., van Belle, G. T., ten Brummelaar, T. A., McAlister, H. A., Swain, M., Turner, N. H., Sturmman, L., & Sturmman, J. 2007, *ApJ* 661, L195.
- Bastien, P., Drissen, L., Menard, F., Moffat, A. F. J., Robert, C. & St-Louis, N. 1988, *AJ* 95, 900.
- Bastien, P., Vernet, E., Drissen, L., Ménard, F., Moffat, A. F. J., Robert, C., & St-Louis, N. 2007, *ASP Conf. Ser.* 364, 529.
- Batten, A. H. 1967, *Pub. Dom. Ap. Obs.* 13, 162.
- Berdyugina, S. V., Berdugin, A. V., Fluri, D. M., & Piirola, V. 2008, *ApJ* 673, L83.
- Carciofi, A. C. & Magalhães, A. M. 2005, *ApJ* 635, 570.
- Clarke, D. 1986, *A&A* 156, 213.
- Clarke, D. & Naghizadeh-Khouei, J. 1994, *AJ* 108, 687.
- Clayton, G. C., Wolff, M. J., Allen, R. G. & Lupie, O. L. 1995, *ApJ* 445, 947.
- Coyne, G. V. & Gehrels, T. 1966, *AJ* 71, 355.
- Croll, B., Matthews, J. M., Rowe, J. F., Gladman, B., Miller-Ricci, E., Sasselov, D., Walker, G. A. H., Kuschnig, R., Lin, D. N. C., Guenther, D. B., Moffat, A. F. J., Rucinski, S. M., & Weiss, W. W. 2007, *ApJ* 671, 2129.
- Croll, B., Matthews, J. M., Walker, G. A. H., Rowe, J. F., Miller-Ricci, E., Kuschnig, R., Sasselov, D., Rucinski, S., Walker, A., Guenther, D. B., Moffat, A. F. J., & Weiss, W. W. 2008, *ApJ*, submitted.

- Davis, L., Jr. & Greenstein, J. L. 1951, ApJ 114, 206.
- Depenchuk, E. A. 1980, IAU 1819, 1.
- Dolan, J. F. & Tapia, S. 1986, PASP 98, 792.
- Dolan, J. F. & Tapia, S. 1989, ApJ 344, 830.
- Gehrels, T. 1972. ApJ 173, L23.
- Gehrels, T. & Silvester, A. B. 1965. AJ 70, 579.
- Gies, D. R., Bolton, C. T., Thomson, J. R., Huang, W., McSwain, M. V., Riddle, R. L., Wang, Z., Wiita, P. J., Wingert, D. W., Csák, B., & Kiss, L. L. 2003, ApJ 583, 424.
- Gray, D. F. & Stevenson, K. B. 2007, PASP 119, 398.
- Hatzes, A. P., Cochran, W. D., Endl, M., McArthur, B., Paulson, D. B., Walker, G. A. H., Campbell, B., & Yang, S. 2003, ApJ 599, 1383.
- Hébrard, G. & Lecavelier des Etangs, A. 2006, A&A 445, 341.
- Heiles, C. 2000, AJ 119, 923.
- Henry, G. W. & Winn, J. N. 2008, AJ 135, 68.
- Henson, G. D., Kemp, J. C., & Kraus, D. J. 1985, PASP 97, 1192.
- Hsu, J.-C. & Breger, M. 1982, ApJ 262, 732.
- Johnson, J. A., Fischer, D. A., Marcy, G. W., Wright, J. T., Driscoll, P., Butler, R. P., Hekker, S., Reffert, S., & Vogt, S. S. 2007, ApJ 665, 785.
- Kartje, J. F. & Königl, A. 1991, ApJ 375, 69.
- Kemp, J. C. 1972, ApJ 175, L35.
- Kemp, J. C. & Wolstencroft, R. D. 1972, ApJ 176, L115.
- Kemp, J. C., Barbour, M. S., Parker, T. E., & Herman, L. C. 1979, ApJ 228, 23.
- Kemp, J. C., Henson, G. D., Steiner, C. T., Powell, E. R. 1987, Nature 326, 270.
- Kovachev, B. J. & Reinhardt, M. 1975, Acta Astr. 25, 133.
- Kukarkin, B. V. Parenago, P. P., Efremov, Y. I., & Kholopov, P. N. 1958, in *General catalogue of Variable Stars*. Academy of Science USSR, Moscow.

- Leigh, C., Cameron, Andrew C., Horne, K., Penny, A., & James, D. 2003, MNRAS 344, 1271.
- Magalhães, A. M., Coyne, G. V., Codina-Landaberry, S. J., & Gneiding, C. 1986, A&A 154, 1.
- Martin, P. G. 1974, ApJ 187, 461.
- Massey, P., Johnson, K. E., & DeGioia-Eastwood, K. 1995, ApJ 454, 151.
- Mathewson, D. S., & Ford, V. L. 1970, Mem. RAS 74, 139.
- Merril, J. E. 1963, in *Photoelectric Astronomy for Amateurs*, ed. F. B. Wood. Macmillan, New York, p. 176.
- Moutou, C., Donati, J.-F., Savalle, R., Hussain, G., Alecian, E., Bouchy, F., Catala, C., Collier Cameron, A., Udry, S., & Vidal-Madjar, A. 2008, A&A 473, 651.
- Neuhäuser, R., Mugrauer, M., Fukugawa, M., Torres, G., & Schmidt, T. 2007, A&A 462, 777.
- Nutzman, P., Charbonneau, D., Winn, J. N., Knutson, H. A., Fortney, J. J., Holman, M. J., Agol, E. 2008, arXiv:0805.0777.
- Ochsenbein, F., Bauer, P., & Marcout, J. 2000, A& AS 143, 221.
- Oke, J. B. 1961, ApJ 133, 90.
- Pasinetti-Fracassini, L. E., Pastori, L., Covino, S., & Pozzi A. 2001, A&A 367, 521.
- Phillips, K. C. & Mészáros, P. 1986, ApJ 310, 284.
- Pont, F., Gilliland, R. L., Moutou, C., Charbonneau, D., Bouchy, F., Brown, T. M., Mayor, M., Queloz, D., Santos, N., & Udry, S. 2007, A&A 476, 1347.
- Raveendran, A. V. & Rao, N. K. 1989, A&A 215, 63.
- Rudy, R. J. & Kemp, J. C. 1977, ApJ 216, 767.
- Rudy, R. J. & Kemp, J. C. 1978, MNRAS 183, 595.
- Schmidt, G. D., Elston, R., Lupie, O. L. 1992, AJ 104, 1563.
- Schulz, A. & Lenzen, R. 1983, A&A 121, 158.
- Seager, S., Whitney, B. A., & Sasselov, D. D. 2000, ApJ 540, 504.
- Serkowski, K. 1962, Adv. Astr. & Ap. 1, 289.
- Serkowski, K. 1968, ApJ 154, 115.

- Serkowski, K., Mathewson, D. S., & Ford, V. L. 1975, *ApJ* 196, 261.
- Shakhovskoi, N. M. 1965, *SvA* 8, 833.
- Shkolnik, E., Walker, G. A. H., Bohlender, D. A., Gu, P.-G., & Kürster, M. 2005, *ApJ* 622, 1075.
- Shkolnik, E., Bohlender, D. A., Walker, G. A. H., & Collier Cameron, A. 2008, *ApJ* 676, 628.
- Stokes, R. A., Swedlund, J. B., Avery, R. W., & Michalsky, J. J. 1974, *AJ* 79, 6.
- Sudzius, J. 1969, *Viln. Astron. Obs. Biul.* 26, 23.
- Su, K. Y. L., Rieke, G. H., Stapelfeldt, K. R., Smith, P. S., Bryden, G., Chen, C. H., & Trilling, D. E. 2008, *ApJ* 679, L125.
- Sunyaev, R. A. & Titarchuk, L. G. 1985, *A&A* 143, 374.
- Trammell, S. R., Dinerstein, H. L., & Goodrich, R. W. 1994, *AJ* 108, 984.
- Wade, G. A., Chadid, M., Shorlin, S. L. S., Bagnulo, S., & Weiss, W. W. 2002, *A&A* 392, L17.
- Walker, G. A. H., Croll, B., Matthews, J. M., Kuschnig, R., Huber, D., Weiss, W. W., Shkolnik, E., Rucinski, S. M., Guenther, D. B., Moffat, A. F. J., & Sasselov, D. 2008, *A&A* 482, 691.
- Winn, J. N., Holman, M. J., Henry, G. W., Roussanova, A., Enya, K., Yoshii, Y., Shporer, A., Mazeh, T., Johnson, J. A., Narita, N., & Suto, Y. 2007, *AJ* 133, 1828.
- Winn, J. N., Henry, G. W., Torres, G., & Holman, M. J. 2008, *ApJ* 675, 1531.
- Wolff, M. J., Nordsieck, K. H., & Nook, M. A. 1996, *AJ* 111, 856.
- Wolinski, K. G., Dolan, J. F., Boyd, P. T., Biggs, J. D., Nelson, M. J., Percival, J. W., Taylor, M., & van Citters, G. W. 1996, *ApJ* 457, 859.
- Yudin, R. V. & Evans, A. 2002, *A&A* 391, 625.
- Ziólkowski, J. 2005, *MNRAS* 358, 851.

3.6 Appendix D: Single Scattering Geometry

Consider a right handed coordinate system (x, y, z) with the observer along the x' axis, which is inclined at an angle i with respect to the x axis (Figure 3.16). An infinitesimally thin debris disk lies along the xy plane, and the central star illuminates the disk from the origin. For a dust grain located at point A , photons will be scattered through an angle χ (the angle between the radius vector and the x' axis). The scattering plane contains the star, dust grain, and the observer. The electric field of scattered light will be perpendicular to this plane for particles smaller than the wavelengths of incident light. The $x'y$ plane and the scattering plane intersect along the x' axis, and the angle between them is ψ . The Stokes parameters of photons scattered off the grain are given by

$$\begin{pmatrix} I_{\text{grain}} \\ Q_{\text{grain}} \\ U_{\text{grain}} \end{pmatrix} = \sigma \begin{pmatrix} 1 + \cos^2 \chi \\ \sin^2 \chi \cos 2\psi \\ \sin^2 \chi \sin 2\psi \end{pmatrix} \quad (\text{D1})$$

where σ is the scattering cross section of the grain.

To find angle χ in terms of ϕ and i , we note

$$\overline{AB}^2 = z^2 + \overline{AD}^2 = z^2 + A_x'^2 + r^2 - 2rA_x' \cos \phi \quad (\text{D2a})$$

$$\overline{AB}^2 = r^2 + \overline{OB}^2 - 2r\overline{OB} \cos \chi. \quad (\text{D2b})$$

Equating Equations D2a and D2b and noting $z^2 + A_x'^2 = \overline{OB}^2$,

$$A_x' \cos \phi = \overline{OB} \cos \chi. \quad (\text{D3})$$

Since

$$\tan i = \frac{A_x'}{z} \quad (\text{D4a})$$

$$\sec i = \frac{\overline{OB}}{z} \quad (\text{D4b})$$

we arrive at

$$\cos \chi = \cos \phi \sin i. \quad (\text{D5})$$

To find angle ψ we first find the vectors normal to both the scattering and $x'y$ planes. The scattering plane contains vectors $\overrightarrow{OB} = (A'_x, 0, z)$ and $\overrightarrow{OA} = (A_x, A_y, 0)$, while the $x'y$ plane contains vectors \overrightarrow{OB} and $\overrightarrow{OC} = (0, A_y, 0)$. Therefore, vectors normal to the scattering plane, \vec{n}_s , and to the $x'y$ axis, \vec{n}_x , are

$$\vec{n}_s = \overrightarrow{OB} \times \overrightarrow{OA} = (-A_y z, A_x z, A'_x A_y) \quad (\text{D6a})$$

$$\vec{n}_x = \overrightarrow{OB} \times \overrightarrow{OC} = (-A_y z, 0, A'_x A_y). \quad (\text{D6b})$$

Finally, the angle between these vectors is given by

$$\cos \psi = \frac{\vec{n}_s \cdot \vec{n}_x}{|\vec{n}_s| |\vec{n}_x|} = \left\{ \frac{z^2 + A_x'^2}{z^2 \left[1 + \left(\frac{A_x}{A_y} \right)^2 \right] + A_x'^2} \right\}^{\frac{1}{2}} \quad (\text{D7a})$$

$$\cos \psi = (\cot^2 \phi \cos^2 i + 1)^{-\frac{1}{2}}. \quad (\text{D7b})$$

For an ensemble of grains located at $\theta = \frac{\pi}{2}$, Equation D1 becomes

$$\begin{pmatrix} I_{\text{disk}} \\ Q_{\text{disk}} \\ U_{\text{disk}} \end{pmatrix} = \sigma \int_0^{2\pi} \int_{r_{\text{in}}}^{r_{\text{out}}} \frac{n(r)}{r^2} \begin{pmatrix} 1 + \cos^2 \chi \\ \sin^2 \chi \cos 2\psi \\ \sin^2 \chi \sin 2\psi \end{pmatrix} r dr d\phi. \quad (\text{D8})$$

We are interested in the normalized Stokes parameters $(Q/I)_{\text{disk}}$ and $(U/I)_{\text{disk}}$. Since neither χ nor ψ depends on the radius r , we have

$$I_{\text{disk}} = R_0 \int_0^{2\pi} 1 + \cos^2 \chi d\phi \quad (\text{D9a})$$

$$Q_{\text{disk}} = R_0 \int_0^{2\pi} \sin^2 \chi \cos 2\psi d\phi \quad (\text{D9b})$$

$$U_{\text{disk}} = R_0 \int_0^{2\pi} \sin^2 \chi \sin 2\psi d\phi \quad (\text{D9c})$$

$$R_0 = \sigma \int_{r_{\text{in}}}^{r_{\text{out}}} \frac{n(r)}{r} dr. \quad (\text{D9d})$$

Given χ and ψ from Equations D5 and D7b,

$$I_{\text{disk}} = R_0 \int_0^{2\pi} 1 + \cos^2 \phi \sin^2 i \, d\phi = \pi R_0 (2 + \sin^2 i) \quad (\text{D10a})$$

$$Q_{\text{disk}} = R_0 \int_0^{2\pi} \sin^2 \phi - \cos^2 \phi \cos^2 i \, d\phi = \pi R_0 \sin^2 i \quad (\text{D10b})$$

$$U_{\text{disk}} = R_0 \int_0^{2\pi} \sin 2\phi \cos i \, d\phi = 0. \quad (\text{D10c})$$

Thus, we derive the relations of Shakhovskoi (1965) describing the single-scattering polarization of a disk illuminated centrally:

$$\left(\frac{Q}{I}\right)_{\text{disk}} = \frac{\sin^2 i}{2 + \sin^2 i} \quad (\text{D11a})$$

$$\left(\frac{U}{I}\right)_{\text{disk}} = 0. \quad (\text{D11b})$$

Because the inclination terms in Equation D11a are squared, polarimetry is unable to distinguish between inclinations $\pm i$.

To estimate the single-scattering polarization when unpolarized light from the central star is added to the polarized light from the disk, we need the number density of dust grains $n(r, a)$. The disk mass is

$$M = \int_{r_{\text{in}}}^{r_{\text{out}}} \int_{a_{\text{min}}}^{a_{\text{max}}} 2\pi r \, n(r, a) \, V(a) \, \rho \, da \, dr \quad (\text{D12})$$

for grain volume and density $V(a)$ and ρ . We assume $n(r, a) = n_0 n(r) n(a)$, where a is grain diameter and n_0 is a constant. From Equations D10a and D9d, the fraction of the stellar flux reflected by the disk is

$$I = n_0 \int_0^{2\pi} \int_{r_{\text{in}}}^{r_{\text{out}}} \int_{a_{\text{min}}}^{a_{\text{max}}} \frac{\sigma(a) \, n(r) \, n(a)}{r} (1 + \cos^2 \phi \sin^2 i) \, da \, dr \, d\phi. \quad (\text{D13})$$

Chapter 4

Cygnus X-1 Inclination from Polarimetry

4.1 Introduction

Masses are difficult to measure accurately, because most methods are only generally applicable to binary systems. Astrometric motion of binaries can be fit to Kepler's laws to determine component masses. However, many systems orbit too closely, or are too distant from Earth, for their astrometric motion to be resolved. The radial velocity technique is used to determine line of sight motion of luminous sources, and orbital parameters such as period and eccentricity can be determined to exquisite precision. However, since this technique is blind to motion in the plane of the sky, and hence to orbital inclination, masses determined from this technique are only lower limits. Statistical analyses can be applied to large samples of objects, such as extrasolar planets, to estimate the true distribution of masses. But masses of individual objects obtained by the radial velocity technique can be very imprecise.

Since polarization is a geometry-dependent effect, one might expect that it can be used to constrain orbital inclination of binary systems. In particular, polarimetry holds promise for determining masses in high mass X-ray binaries. These systems consist of an OB supergiant and black hole, the prototype of which is Cygnus X-1. The $40 \pm 10 M_{\odot}$ (Ziółkowski 2005), O9.7Iab supergiant in this system (Walborn 1973) nearly fills its Roche lobe, and the $13.5 - 29 M_{\odot}$ black hole (Ziółkowski 2005) accretes matter partly from a focused stellar wind (Gies & Bolton 1986b) as well as occasional Roche lobe overflow. Tighter constraints on the mass of the Cygnus X-1 black hole are necessary to test stellar evolution models and study general relativity on finer scales.

4.2 Overview of Cygnus X-1

4.2.1 Accretion

Cygnus X-1 harbors an accretion disk, which is evident by its X-ray luminosity of $(2 - 5.5) \times 10^{37}$ erg/s (Syunyaev & Trümper 1979, Dolan et al. 1979, Balucinska-Church et al. 2000) and significant emission of gamma rays (Albert et al. 2007). Its X-ray spectrum is composed of blackbody and power law components. The blackbody component of the spectrum comes from the accretion disk, where $kT \approx 0.1$ keV and the disk luminosity is 4.7×10^{36} erg/s (Balucinska-Church et al. 1995). The power law component, with flux $F(E) \propto E^{-\Gamma}$, is generated by Compton scattering of disk emission by either a hot corona of electrons (Shapiro et al. 1976) or at the base of a jet (Brocksopp et al. 1999a).

Stirling et al. (2001) observed a highly collimated (opening angle of < 2 degree), relativistic ($v/c \geq 0.6$) jet of ≈ 30 AU in length with the VLBA. Such a jet has been confirmed by Gallo et al. (2005) and Fender et al. (2006), and it points toward a nebula that Gallo et al. (2005) discovered in both the radio and the optical. Since the proper motion of Cygnus X-1 is perpendicular to the jet, the binary has never been at the center of the nebula. Therefore, the nebula is not a supernova remnant from the formation of the black hole; rather, it is interpreted as a bow shock between the remnants of the jet and the ISM. The kinetic energy of the jet and assumed counterjet represents 30% to 100% of the bolometric X-ray luminosity of Cygnus X-1 (Gallo et al. 2005, Russell et al. 2007). Thus, it appears that the energy of accretion is partitioned roughly equally between the jet and radiation.

The X-ray luminosity occasionally transitions from the fiducial, “low/hard” state to the “high/soft state”. The low/hard state dominates the duty cycle: Cygnus X-1 is in this state about 90% of the time (Gallo et al. 2005). In the low/hard state, the relatively low accretion rate generates relatively low X-ray luminosity. The accretion rate is of order

$$\dot{m} \approx 0.1 \dot{M}_{\text{Edd}} \quad (4.1a)$$

$$\dot{M}_{\text{Edd}} = \frac{L_{\text{Edd}}}{0.1c^2} \quad (4.1b)$$

$$L_{\text{Edd}} \equiv \frac{4\pi GMm_p c}{\sigma_T} \quad (4.1c)$$

where \dot{M}_{Edd} is the Eddington accretion rate for 10% efficiency and L_{Edd} is the Eddington luminosity. The black hole mass is M , m_p is the mass of a proton, and σ_T is the Thomson scattering cross section for the electron. The low accretion rate in the low/hard state allows the optically thick, but geometrically thin, disk to be evaporated more efficiently. This causes the disk inner radius to retreat to $r_{\text{in}} > 100R_s$, where $R_s \equiv 2GM/c^2$ is the Schwarzschild radius. An optically thin, hot corona of electrons flows from the disk inner radius to the event horizon. This corona generates the Comptonized power law, of photon index $\Gamma \approx 1.5$, that dominates the low/hard spectrum (Esin et al. 1998).

Occasionally, the mass accretion rate slightly increases, by only $\approx 15\%$ (Esin et al. 1998), which causes an increase in X-ray luminosity of about 10% to 20% (Brocksopp et al. 1999a). Evaporation of the disk proceeds less efficiently in the high/soft state, and the disk inner radius advances to the last stable orbit of the black hole, $r_{\text{in}} = 3R_s$. This causes the disk blackbody emission to dominate over the power law from the corona (Esin et al. 1998). Exactly how disk accretion rate is tied to supergiant mass loss is debated, however.

The characteristic P Cygni profile observed in H α from the supergiant indicates mass loss in the form of a stellar wind (Ninkov et al. 1987b). Since stellar wind from an OB supergiant issues roughly isotropically, atoms flowing towards the observer will have blueshifted absorption. Conversely, atoms flowing away from the observer will emit redshifted radiation. In the presence of the black hole, however, the distorted equipotential surface of the system will focus the stellar wind through the L1 point (Friend & Castor 1982, Gies & Bolton 1986b). Indeed, Miller et al. (2005) see evidence for such a wind from Chandra X-ray spectroscopy. The wind forms an accretion disk around the black hole. Intuitively, one would expect that increased mass loss from the supergiant would lead to increased accretion onto the black hole. However, the interaction of the radiatively-driven stellar wind and the X-ray luminosity of the accretion disk complicates matters.

Line radiation from the supergiant imparts momentum to absorbing atoms in the photosphere, which can accelerate the atoms past the supergiant's escape velocity to form a radiatively-driven wind (Castor et al. 1975). X-ray photoionization of atoms in this wind by the accretion disk will dramatically slow the wind, because the loss of electrons decreases the total force that stellar radiation can impart to the wind atoms. Increased stellar mass loss will form a denser wind, which will not be photoionized as completely. Thus, the mean wind speed will be increased. Since accretion rate

is given by $\dot{m} \propto \dot{M}v^{-4}$, where \dot{M} is mass loss and v is flow velocity (Bondi & Hoyle 1944), a faster wind causes a lower accretion rate, even in the presence of increased stellar mass loss (Ho & Arons 1987, Stevens 1991). In contrast, wind density will be lower for decreased supergiant mass loss. X-ray ionization of the wind will be more complete, so there will exist fewer available lines for wind atoms to absorb. The slower wind will be accreted more readily than the faster wind. Therefore, decreased mass loss by the supergiant actually translates to a higher accretion rate by the black hole.

Gies et al. (2003, hereafter G03) observe a decrease in H α equivalent width, and therefore strength of mass loss, during an X-ray flare. The time lag between these two events is small compared to the ten hour timescale for the wind to traverse the region between binary components, which indicates any lag is related to light travel time. They argue that the ionization of the supergiant's photosphere inhibits generation of a stellar wind, because wind velocity is lower than the escape velocity. This results in weak mass loss. However, they observe departures from such a simple model where mass loss is anticorrelated with X-ray flux.

Large changes in H α emission have been observed by G03 while X-ray flux is constant. They also observe large variations in redshifted H α emission even during inferior conjunction of the black hole (phase 0.5). At this phase, the H α observed flows away from the black hole and is shadowed from X-rays by the primary. This gas does indeed lie in the X-ray shadow because similar H α strength is observed during both low/hard and high/soft states, where X-ray luminosity changes. G03 calculate supergiant mass loss to be $(2.57 \pm 0.05) \times 10^{-6} M_{\odot}/\text{yr}$ during the low/hard state, where X-ray flux is decreased. Mass loss in the presence of increased X-ray emission during the high/soft state appears to be only $(2.00 \pm 0.03) \times 10^{-6} M_{\odot}/\text{yr}$, which supports the hypothesis that increased accretion onto the black hole is actually produced by decreased mass loss by the supergiant.

4.2.2 Periodicities

The 5.6 day orbital period of Cygnus X-1 (Webster & Murdin 1972, Bolton 1972) is mirrored by ellipsoidal light modulation, where the tidally distorted, $V \approx 9$ supergiant fluctuates with amplitude $\Delta V \approx 0.04$ mag at twice the orbital frequency due to its time-variable cross-sectional area (Walker 1972; Lyutyj et al. 1973; Lester et al. 1973; Bochkarev et al. 1975; Bruevich et al. 1978; Balog et al. 1981; Gies & Bolton 1982; Khaliullina & Khaliullin 1981; Kemp et al. 1987; Ninkov et al. 1987a,

b; Voloshina et al. 1997; Brocksopp et al. 1999b). In addition to photometric observations in the optical, such second harmonic modulation has been observed in X-rays (Holt et al. 1976, Holt et al. 1979, Friedhorsky et al. 1995, Zhang et al. 1996, Paciesas et al. 1997, Pooley et al. 1999, Brocksopp et al. 1999a, Wen et al. 1999, Kitamoto et al. 2000, Manchanda 2001, Özdemiř & Demircan 2001, Lachowicz et al. 2006, Poutanen et al. 2008), ultraviolet (Wolinski et al. 1996, Brocksopp et al. 1999a), near-IR (Leahy & Ananth 1992, Nadzhip et al. 1996, Brocksopp et al. 1999a), and radio (Pooley et al. 1999, Brocksopp et al. 1999a, Lachowicz et al. 2006).

There is also weak evidence for 39- and 78-day periods of unknown origin in ultraviolet and X-ray photometry (Kemp et al. 1978b), optical photometry (Karitskaya 1979, Lyutyi 1985, Kemp et al. 1987), and optical polarimetry (Kemp et al. 1978b). Kemp et al. (1978b) do not observe optical variability with these periods, and Dolan et al. (1979) do not observe X-ray variability. Therefore, it is unclear whether these periods are actually present.

Finally, there appears to be a longer period in the system, which is thought to originate from an oblique accretion disk that precesses due to gravitational torques from the supergiant. Previous observations imply a 294 day period from X-ray data (Metzger & Dolan 1968, Friedhorsky & Terrell 1982, Manchanda 1983, Friedhorsky et al. 1983), optical measurements (Karitskaya 1979, Kemp 1983, Kemp et al. 1983, Kemp et al. 1987), and ultraviolet/optical polarimetry (Kemp et al. 1983). However, more recent research suggests a 150 day period from X-ray (Pooley et al. 1999, Brocksopp et al. 1999a, Kitamoto et al. 2000, Özdemiř & Demircan 2001, Lachowicz et al. 2006, Ibragimov et al. 2007, Poutanen et al. 2008), ultraviolet (Brocksopp et al. 1999a), optical (Brocksopp et al. 1999a, G03) and radio observations (Pooley et al. 1999, Brocksopp et al. 1999a, Lachowicz et al. 2006, Ibragimov et al. 2007, Poutanen et al. 2008). It has been suggested that the 294 day period is just aliasing of the “true” 150 day period, and that it is therefore not a real effect (Özdemiř & Demircan 2001).

However, Kemp et al. (1983) saw a weaker 147 day period in addition to their 294 day period, and the 294 day period was observed through ≈ 15 cycles. Lachowicz et al. (2006, hereafter L06) see weak evidence for a current 293 day period in radio data, and they find a weak 150 day period to be present in the old data of Friedhorsky et al. (1983). L06 have studied archival data from the X-ray satellite Ariel 5 between 1976 and 2003, and they see a consistent, 150 day period throughout this time span. They further observe that the phase of precession has stayed roughly constant over

those ≈ 65 precessional periods. Additionally, using archival data from the Vela 5B satellite from 1969 to 1979, L06 see the existence of the 294 day period but not the 150 day period. Therefore, L06 suggest that the dominant period of disk precession physically evolved from the 294 day period to its second harmonic around 1980.

4.2.3 Polarization

The Cygnus X-1 system exhibits strong linear polarization in the optical with mean polarization $P_{\text{lin}} \approx 5\%$. The optical (Gehrels 1972, Wolinski et al. 1996) and near-IR spectrum of polarization (Wilking et al. 1980) is consistent with the empirical interstellar polarization relation of Serkowski et al. (1975) as modified by Wilking et al. (1980). Since Cygnus X-1 is 2.2 ± 0.2 kpc distant (Ziólkowski 2005) and in the plane of the galaxy, such strong interstellar polarization is almost unavoidable (Mathewson & Ford 1970, Barrett 1996, Fosalba et al. 2002). The position angle of net polarization changes by $\Delta\Theta(\lambda) = 0.8^\circ$ between U and V bands, which is significant at the 3σ level (Kemp et al. 1976).

Dolan & Tapia (1989) reject the hypothesis of constant position angle with wavelength at the 1% level of significance, and Wolinski et al. (1996) also observe the change in position angle. In addition, they observe wavelength-dependent Rayleigh scattering in the system as well as polarization in the ultraviolet larger than expected from interstellar polarization (section 4.5.5). Finally, the linear polarization of Cygnus X-1 is partly phase-locked to the first and second harmonic of the orbital frequency with amplitude $\Delta P_{\text{lin}} \approx 0.2\%$ (Nolt et al. 1975; Kemp et al. 1978a, 1979; Kemp 1980a, Dolan & Tapia 1989; Wolinski et al. 1996; Nagae et al. 2008). These results imply that the linear polarization of Cygnus X-1 consists of interstellar and intrinsic components.

In addition to possessing strong linear polarization, Cygnus X-1 also harbors nonzero circular polarization of $P_{\text{circ}} \approx 0.05\%$ (Michalsky et al. 1975a, b; Severny & Kuvshinov 1975; Michalsky & Swedlund 1977). The sense of circular polarization changes sign near the wavelength of peak linear polarization, which is consistent with interstellar origin (Martin 1974). Indeed, comparable circular polarization is observed in HD 204827, which is near Cygnus X-1 in the plane of the sky (Serkowski et al. 1975). Additionally, rotation of interstellar grain alignment along the line of sight to the system converts linear polarization to circular polarization with $\approx 1\%$ efficiency (Martin 1974,

Avery et al. 1975), which can account for the mean circular polarization of Cygnus X-1. Indeed, a change in grain size in addition to orientation along the line of sight produces a change in position angle with wavelength, which has been observed above.

However, in addition to variable linear polarization, circular polarization from Cygnus X-1 has also been observed to be variable (Michalsky et al. 1975b, Michalsky & Swedlund 1977). The B band amplitude of $\Delta P_{\text{circ}} \approx 0.05\%$, were it caused by interstellar conversion of the variable linear polarization, would require the linear polarization to be variable at the $\Delta P_{\text{lin}} \approx 5\%$ level. Since this is an order of magnitude larger than the observed $\Delta P_{\text{lin}} \approx 0.2\%$, the circular polarization of Cygnus X-1 must consist of interstellar and intrinsic components. The dominant period of circular polarization has been observed to change from 2.8 days to 5.6 days over the course of eleven months (Michalsky & Swedlund 1977).

Gnedin et al. (2003, hereafter Gn03) suggest that a magnetic field origin for the intrinsic circular polarization of Cygnus X-1 implies a magnetic field at the last stable orbit of the black hole ($r_0 \equiv 3R_s$) of $B(r_0) = 10^7 - 10^8$ G. Long et al. (1980) observe linear polarization of X-rays to be $2.4 \pm 1.1\%$ at 2.6 keV and $5.3 \pm 2.5\%$ at 5.2 keV. Gn03 admit that the statistical significance of these detections is low, but they suggest that the decrease in X-ray polarization at lower energies may be due to Faraday depolarization. Faraday depolarization is the decrease in net polarization due to volume-integrated Faraday rotation (rotation of the plane of polarization due to a magnetic field). From Gnedin & Silant'ev (1980), the angle of Faraday rotation, χ_F , is

$$\chi_F \approx 0.6\tau_T \left(\frac{B}{10^6 \text{ G}} \right) \left(\frac{1 \text{ keV}}{E} \right)^2 \cos \theta. \quad (4.2)$$

Here, θ is the angle between the local magnetic field and radiation propagation, and τ_T is the optical depth to Thomson scattering of the region. Assuming the difference in polarization between 2.6 keV and 5.3 keV is real, Gn03 calculate a magnetic field of $B(r_0) \geq 3 \times 10^7$ G. Furthermore, Gn03 suggest that Faraday depolarization of optical polarization implies $B(r_0) \approx 10^7$ G for a dipolar magnetic field. Thus, estimates of the strength of the magnetic field in the vicinity of the black hole, due to optical circular polarization as well as Faraday depolarization in the optical and in X-rays, imply a magnetic field of order $B(r_0) = 10^7 - 10^8$ G.

4.3 Inclination from Polarimetry

4.3.1 BME Scattering Model

The standard technique for inclination inversion from polarimetric observations comes from the theory of Brown et al. (1978, hereafter BME). An optically thin envelope of arbitrary distribution around one, or both, components in a binary with zero eccentricity is assumed. As long as the envelope is corotating and phase locked to the binary, polarimetric modulation of Thomson or Rayleigh scattered flux will be dependent on orbital inclination. For an envelope symmetric with respect to the orbital plane, BME note that polarimetric modulation will occur at the second harmonic of the orbital frequency. Asymmetry in the envelope will generate a first harmonic component.

From Aspin et al. (1981),

$$Q(\lambda) = \tau_0 [\gamma_1 \sin 2i \cos \lambda - \gamma_2 \sin 2i \sin \lambda - (1 + \cos^2 i) \gamma_3 \cos 2\lambda + (1 + \cos^2 i) \gamma_4 \sin 2\lambda] \quad (4.3a)$$

$$U(\lambda) = 2\tau_0 [\gamma_1 \sin i \sin \lambda + \gamma_2 \sin i \cos \lambda - \gamma_3 \cos i \sin 2\lambda - \gamma_4 \cos i \cos 2\lambda] \quad (4.3b)$$

$$\tau_0 \equiv \frac{\sigma_0}{2} \sum_{j=1}^2 \iiint n(r, \theta, \phi) \sin \theta_j dr_j d\theta_j d\phi_j \quad (4.3c)$$

$$\tau_0 \gamma_1 \equiv \frac{\sigma_0}{2} \sum_{j=1}^2 f_j \iiint n(r, \theta, \phi) \sin 2\theta_j \cos \phi_j dr_j d\theta_j d\phi_j \quad (4.3d)$$

$$\tau_0 \gamma_2 \equiv \frac{\sigma_0}{2} \sum_{j=1}^2 f_j \iiint n(r, \theta, \phi) \sin 2\theta_j \sin \phi_j dr_j d\theta_j d\phi_j \quad (4.3e)$$

$$\tau_0 \gamma_3 \equiv \frac{\sigma_0}{2} \sum_{j=1}^2 f_j \iiint n(r, \theta, \phi) \sin^2 \theta_j \cos 2\phi_j dr_j d\theta_j d\phi_j \quad (4.3f)$$

$$\tau_0 \gamma_4 \equiv \frac{\sigma_0}{2} \sum_{j=1}^2 f_j \iiint n(r, \theta, \phi) \sin^2 \theta_j \sin 2\phi_j dr_j d\theta_j d\phi_j. \quad (4.3g)$$

Here, $\lambda = 2\pi\phi$ is the orbital longitude for zero eccentricity, ϕ is orbital phase, and $\sigma_0 \equiv 3\sigma_T/(16\pi)$. Spherical coordinates are in the reference frame of the binary, where $\theta = 0$ is perpendicular to the orbital plane. Summation progresses over stars $j = 1, 2$ in the binary, and f_j is the fractional luminosity of star j with respect to the system's flux. Regardless of the distribution of scatterers $n(r, \theta, \phi)$ and the intensity of each star, polarimetric modulation will occur at the fundamental and second harmonics of the orbital frequency.

Observed modulations in normalized Stokes parameters Q and U are decomposed into Fourier components according to

$$Q(\lambda) = q_0 + q_1 \cos \lambda + q_2 \sin \lambda + q_3 \cos 2\lambda + q_4 \sin 2\lambda \quad (4.4a)$$

$$U(\lambda) = u_0 + u_1 \cos \lambda + u_2 \sin \lambda + u_3 \cos 2\lambda + u_4 \sin 2\lambda. \quad (4.4b)$$

Note that observed Stokes parameters Q and U are normalized by stellar intensity. Terms of third order in orbital frequency are expected for non-zero eccentricity. It is generally accepted that the eccentricity of Cygnus X-1 is zero (Gies & Bolton 1982; Ninkov et al. 1987a, b; Brocksopp et al. 1999b), though there is some evidence to the contrary (Hutchings 1974, Bolton 1975, Hutchings 1978, Guinan et al. 1979). Therefore, Fourier components higher than second order in orbital frequency are generally ignored.

Orbital inclination i is related to the Fourier amplitudes in Equations 4.4a and 4.4b by

$$\left(\frac{1 - \cos i}{1 + \cos i} \right)^2 = \frac{(q_2 + u_1)^2 + (q_1 - u_2)^2}{(q_1 + u_2)^2 + (q_2 - u_1)^2} \quad (4.5a)$$

$$\left(\frac{1 - \cos i}{1 + \cos i} \right)^4 = \frac{(q_4 + u_3)^2 + (q_3 - u_4)^2}{(q_3 + u_4)^2 + (q_4 - u_3)^2} \quad (4.5b)$$

and the position angle of the line of quadratures (Dolan & Tapia 1989) is given by

$$\Theta_{\text{quad}} = \frac{\Omega}{2} + 90^\circ \quad (4.6a)$$

$$\tan \Omega_a = \frac{D - T}{B - C} \quad (4.6b)$$

$$\tan \Omega_b = \frac{B + C}{D + T} \quad (4.6c)$$

$$B = \frac{u_4 - q_3}{(1 - \cos i)^2} \quad (4.6d)$$

$$C = \frac{u_4 + q_3}{(1 + \cos i)^2} \quad (4.6e)$$

$$D = \frac{q_4 - u_3}{(1 + \cos i)^2} \quad (4.6f)$$

$$T = \frac{u_3 + q_4}{(1 - \cos i)^2} \quad (4.6g)$$

according to Drissen et al. (1986a). Inclinations from Equations 4.5a and 4.5b, and values of Ω from Equations 4.6b and 4.6c, should be equal and provide a consistency check of the model. Because terms in i are raised to the even powers (Equations 4.5b and 4.5a), degeneracies exist between i and $i \pm 180^\circ$ as well as between Ω and $\Omega \pm 180^\circ$.

4.3.2 Inclination Bias

Inclination estimates from polarimetry are known to be biased toward high (edge-on) inclination, where the strength of the bias is inversely related to the signal to noise ratio of the data. For an edge-on geometry and a phase-locked, optically thin distribution of scatterers, symmetry dictates that the observed polarization will be either parallel or perpendicular to the orbital plane throughout the orbit. Therefore, the polarization components parallel and perpendicular to the orbital plane will be modulated sinusoidally, while the polarization components at $\pm 45^\circ$ with respect to the orbital plane will be zero during the orbit. Observed U versus Q will trace a line over the course of the orbit, where the position angle of that line in (Q, U) space will be related to the position angle of the line of quadratures in the plane of the sky.

Conversely, polarization observed from a face-on system will trace a circle in (Q, U) space due to symmetry. This is because a face-on system will have constant degree of polarization, $P(\lambda) = \sqrt{Q(\lambda)^2 + U(\lambda)^2}$, throughout the orbit. Since $P(\lambda)$ will be constant, $U(\lambda) = \pm \sqrt{P(\lambda)^2 - Q(\lambda)^2}$ is the equation of a circle in (Q, U) space. Given noisy data obtained on a system with arbitrary inclination, a linear fit to observed $U(\lambda)$ versus $Q(\lambda)$ will begin to have higher confidence. Consequently, low quality data will bias inverted inclination towards high values. For arbitrary inclination, truly phase-locked systems will trace out an ellipse in (Q, U) space, where BME and Rudy & Kemp (1978) independently discovered the eccentricity of the ellipse to be

$$e = \frac{\sin^2 i}{1 + \cos^2 i}. \quad (4.7)$$

Because of the polarimetric bias inherent to the BME technique, many authors (Milgrom 1978, Simmons et al. 1980, Aspin et al. 1981, Simmons et al. 1982, Wolinski & Dolan 1994) have criticized the use of formal error propagation when determining uncertainty in inclination. Uncertainty derived from error propagation, where inclination uncertainty is related to uncertainties in the Fourier

components of Equations 4.5a and 4.5b, dramatically overestimates the confidence in an inclination estimate. The standard mechanism for estimating the confidence interval on polarimetrically-derived inclination was developed by Aspin et al. (1981) and Simmons et al. (1982), and it was extended by Wolinski & Dolan (1994).

Consider a time series of $N = N_Q + N_U$ observations in Stokes Q and U wrapped to the binary’s orbital phase. Let uncertainty in each observation be σ . The maximum and minimum values of the *fits* to $Q(\lambda)$ and $U(\lambda)$, as opposed to the maximum *observed* $Q(\lambda)$ and $U(\lambda)$, are denoted q_{\max} , u_{\max} , q_{\min} , and u_{\min} . The relevant quantity in determining data quality is the so-called “figure of merit” γ , which is effectively the square of the signal to noise ratio of each $Q(\lambda)$ and $U(\lambda)$ fit. The amplitude of polarimetric variability A and the figure of merit γ are given by

$$A = \frac{|q_{\max} - q_{\min}| + |u_{\max} - u_{\min}|}{4} \quad (4.8a)$$

$$\gamma = \left(\frac{A}{\sigma}\right)^2 \frac{N}{2} \quad (4.8b)$$

from Aspin et al. (1981) and Simmons et al. (1982), respectively.

Using the regularized Monte Carlo approach of Dolan (1984), Wolinski & Dolan (1994, hereafter WD94) generate $Q(\lambda, i)$ and $U(\lambda, i)$ curves expected from single scattering in a close binary. They calculate these curves for inclinations ranging from 0° to 90° in 5° increments. The primary is constructed from 5,000 elements that illuminate the scattering region. These authors take into account limb and gravity darkening of the primary as well as the change in projected area of the illuminating element as seen by the scatterer. WD94 add noise with zero mean and variance σ^2 to $Q(\lambda, i)$ and $U(\lambda, i)$, where 1,000 curves are generated for each inclination step. Based on the figures of merit of the synthesized data sets, they find confidence intervals on inclination derived from Equation 4.5b. WD94 recommend calculating i and γ from Equations 4.5b and 4.8b and determining the confidence interval on derived inclination from their Figure 4.

4.4 Results

For each night, the weighted mean polarization is taken for each Cassegrain ring angle, where the weight is proportional to number of detected photons. Uncertainty in each of these bins is the square root of the weighted variance of the measurements in the bin. These data are listed in Table 4.1, where n_{phot} is the number of detected photons, and n_{msmts} is the number of 30 second measurements, in each bin. Fitting Equations 4.4a and 4.4b to the binned data in Table 4.1, we obtain the Fourier coefficients listed in Table 4.2. Data from this work are listed as W07 and W08 for August 2007 and June 2008 observations, respectively. Kemp (1980b) data are denoted K80, and Dolan & Tapia (1989) data are DT89. These will be explained later.

The standard fit involves the zeroth, first, and second harmonics of the orbital frequency (listed in bold in Table 4.2). However, we have included additional fits, using only the zeroth and second harmonics as well as using the zeroth through third harmonics. The strength of the first harmonic is sensitive to the distribution of scatterers about the orbital plane, and the strength of the third harmonic is sensitive to orbital eccentricity. Binned data from August 2007 and June 2008 are plotted in Figures 4.1 and 4.2, respectively. The area of each open circle is proportional to the total number of detected photons in each bin.

The “max – min” values in Table 4.2 are the peak to peak differences in the fits for $Q(\lambda)$ and $U(\lambda)$. Fit χ^2 , number of observations, and the significance level for fit rejection, α , are listed. The amplitudes of the first, second, and third harmonic components are given by

$$\begin{pmatrix} q_{\text{I}} \\ q_{\text{II}} \\ q_{\text{III}} \end{pmatrix} = \begin{pmatrix} q_1^2 + q_2^2 \\ q_3^2 + q_4^2 \\ q_5^2 + q_6^2 \end{pmatrix}^{\frac{1}{2}} \quad (4.9a)$$

$$\begin{pmatrix} u_{\text{I}} \\ u_{\text{II}} \\ u_{\text{III}} \end{pmatrix} = \begin{pmatrix} u_1^2 + u_2^2 \\ u_3^2 + u_4^2 \\ u_5^2 + u_6^2 \end{pmatrix}^{\frac{1}{2}} \quad (4.9b)$$

$$\begin{pmatrix} p_{\text{I}} \\ p_{\text{II}} \\ p_{\text{III}} \end{pmatrix} = \begin{pmatrix} q_{\text{I}}^2 + u_{\text{I}}^2 \\ q_{\text{II}}^2 + u_{\text{II}}^2 \\ q_{\text{III}}^2 + u_{\text{III}}^2 \end{pmatrix}^{\frac{1}{2}}. \quad (4.9c)$$

Table 4.1: Journal of Observations

Data Set UT Date	MJD	Phase	Q (%)	U (%)	n_{phot} ($\times 10^7$)	θ_{Cass} ($^\circ$)	n_{msmts}	
W07 2007 Aug 2	54314.477	0.5369	—	-4.355(42)	2.4	45	3	
	54314.480	0.5375	0.632(49)	—	5.0	270	11	
	54314.486	0.5385	—	-4.397(43)	5.2	225	12	
	54314.487	0.5387	0.662(68)	—	5.0	180	12	
	54314.501	0.5411	—	-4.474(61)	4.3	315	10	
	54314.504	0.5418	—	-4.531(60)	4.1	135	11	
2007 Aug 3	54314.511	0.5431	0.622(43)	—	3.8	0	9	
	54315.332	0.6896	0.726(41)	—	4.5	90	4	
	54315.344	0.6918	—	-4.658(45)	7.4	135	10	
	54315.348	0.6924	—	-4.681(37)	16.1	45	52	
	54315.349	0.6927	0.710(51)	—	16.8	0	56	
	54315.351	0.6930	0.724(42)	—	8.0	180	12	
	54315.357	0.6940	—	-4.684(22)	6.4	225	8	
	54315.357	0.6941	0.698(31)	—	6.3	270	8	
2007 Aug 4	54315.357	0.6941	—	-4.657(26)	6.3	315	8	
	54316.325	0.8670	—	-4.821(22)	20.5	45	29	
	54316.326	0.8672	0.589(61)	—	5.1	90	6	
	54316.330	0.8678	—	-4.743(20)	4.5	135	4	
	54316.336	0.8689	0.565(43)	—	23.0	0	36	
	54316.341	0.8699	—	-4.776(31)	4.1	315	4	
	54316.345	0.8705	0.578(50)	—	8.4	180	14	
	54316.352	0.8717	—	-4.804(60)	6.6	225	10	
2007 Aug 5	54316.352	0.8718	0.533(65)	—	6.0	270	8	
	54317.300	0.0411	—	-4.597(23)	8.6	135	4	
	54317.305	0.0419	0.482(67)	—	8.5	90	4	
	54317.348	0.0497	0.504(43)	—	13.8	180	12	
	54317.368	0.0532	—	-4.660(35)	23.6	45	36	
	54317.368	0.0533	0.489(50)	—	23.7	0	36	
	54317.375	0.0544	—	-4.649(31)	11.1	225	8	
	54317.375	0.0544	—	-4.632(45)	11.0	315	8	
2007 Aug 6	54317.375	0.0544	0.498(47)	—	10.8	270	8	
	54318.351	0.2288	0.649(39)	—	17.7	180	12	
	54318.352	0.2290	—	-4.773(23)	17.5	225	12	
	54318.354	0.2293	0.640(38)	—	17.3	270	12	
	54318.356	0.2296	—	-4.736(21)	17.3	315	12	
	54318.373	0.2328	0.639(54)	—	28.2	0	32	
W08 2007 Jun 8	54318.377	0.2334	—	-4.782(23)	25.9	45	28	
	54625.951	0.0698	—	-4.805(30)	7.8	135	6	
	54625.958	0.0709	0.571(20)	—	7.7	90	6	
	54625.976	0.0742	0.575(24)	—	11.5	0	14	
	54625.977	0.0743	—	-4.819(14)	11.9	45	14	
	2007 Jun 9	54626.873	0.2344	0.759(20)	—	13.5	0	20
		54626.885	0.2366	—	-5.006(29)	13.7	45	20
		54626.897	0.2387	0.741(20)	—	14.3	90	20
		54626.909	0.2409	—	-4.982(20)	13.8	135	20
	2007 Jun 10	54627.903	0.4182	0.522(25)	—	13.8	0	20
		54627.915	0.4204	—	-4.969(17)	13.7	45	20
		54627.927	0.4226	0.519(25)	—	14.5	90	20
54627.939		0.4247	—	-4.958(18)	14.2	135	20	
2007 Jun 11	54628.905	0.5973	0.617(24)	—	14.3	0	20	
	54628.917	0.5994	—	-4.961(23)	14.3	45	20	
	54628.929	0.6016	0.591(20)	—	14.8	90	20	
	54628.941	0.6037	—	-4.947(29)	14.6	135	20	
2007 Jun 12	54629.865	0.7687	0.643(20)	—	12.0	0	16	
	54629.875	0.7705	—	-5.000(16)	12.2	45	16	
	54629.885	0.7722	0.623(21)	—	12.4	90	16	
	54629.895	0.7740	—	-4.985(18)	12.3	135	16	
2007 Jun 13	54630.876	0.9491	0.541(28)	—	12.8	0	20	
	54630.888	0.9513	—	-4.94(23)	12.9	45	20	
	54630.900	0.9534	0.515(19)	—	13.0	90	20	
	54630.912	0.9556	—	-4.902(21)	12.7	135	20	
2007 Jun 14	54631.862	0.1252	—	-4.908(21)	13.4	135	20	
	54631.874	0.1274	0.655(17)	—	13.5	90	20	
	54631.886	0.1295	—	-4.913(24)	13.6	45	20	
	54631.898	0.1317	0.675(27)	—	13.7	0	20	

Table 4.2: BME Fit Parameters

Data Set	W08	W07	W _{mean}	K80	DT89	All	
Fit Orders	0.1,2	0.2	0.1,2	0.1,2,3	0.1,2	0.1,2	
Period (days)	5.599829	5.599829	5.599829	5.599829	5.600	5.599829	
Epoch (MJD)	51729.949	51729.949	51729.949	51729.949	41000.6	41868.610	
q_0 (%)	+0.6044	+0.5807	+0.6102	+0.6143	+0.6073	+0.6539	+1.1010
q_1 (%)	+0.0051	—	-0.0734	-0.0794	-0.0342	-0.0066	-0.0965
q_2 (%)	+0.0312	—	-0.0225	-0.0182	+0.0044	-0.0155	-0.0182
q_3 (%)	-0.0894	-0.0835	-0.0612	-0.0705	-0.0753	+0.0002	-0.0624
q_4 (%)	+0.0378	+0.0284	+0.0152	+0.0147	+0.0265	+0.0778	+0.1121
q_5 (%)	—	—	—	-0.0246	—	—	—
q_6 (%)	—	—	—	+0.0271	—	—	—
q_I (%)	0.0316	—	0.0767	0.0815	0.0344	0.0168	0.0982
q_{II} (%)	0.0971	0.0882	0.0631	0.0720	0.0798	0.0778	0.1283
q_{III} (%)	—	—	—	0.0366	—	—	—
$\frac{1}{2}(q_{\max} - q_{\min})$ (%)	0.1140	0.0882	0.1187	0.1491	0.0986	0.0890	0.2016
χ^2_Q	11.9	25.4	1.3	1.3	—	—	—
n_Q	14	18	18	18	—	—	—
α_Q	0.615	0.115	1.000	1.000	—	—	—
u_0 (%)	-4.9510	-4.7052	-4.6653	-4.5972	-4.8082	-4.8603	-4.6000
u_1 (%)	+0.0347	—	-0.1023	-0.2095	-0.0338	+0.0075	-0.0572
u_2 (%)	+0.0081	—	+0.0015	+0.0837	+0.0048	+0.0165	+0.0789
u_3 (%)	+0.0489	+0.0728	+0.1071	+0.1292	+0.0780	+0.0594	+0.0722
u_4 (%)	+0.0285	+0.0908	+0.0572	-0.1047	+0.0429	+0.0335	+0.0792
u_5 (%)	—	—	—	+0.0795	—	—	—
u_6 (%)	—	—	—	+0.0526	—	—	—
u_I (%)	0.0356	—	0.1023	0.2256	0.0341	0.0181	0.0975
u_{II} (%)	0.0566	0.1163	0.1214	0.1664	0.0890	0.0682	0.1072
u_{III} (%)	—	—	—	0.0953	—	—	—
$\frac{1}{2}(u_{\max} - u_{\min})$ (%)	0.0764	0.1163	0.1890	0.3510	0.1120	0.0812	0.1702
χ^2_U	22.9	86.6	25.8	23.6	—	—	—
n_U	14	19	19	19	—	—	—
α_U	0.061	1×10^{-10}	0.135	0.211	—	—	—
p_I (%)	0.0476	—	0.1279	0.2399	0.0485	0.0247	0.1383
p_{II} (%)	0.1124	0.1460	0.1368	0.1813	0.1196	0.1035	0.1672
p_{III} (%)	—	—	—	0.1021	—	—	—
p_I/p_{II}	0.42	—	0.93	1.32	0.41	0.24	0.83
ϵ_I	0.298	—	0.483	0.458	0.289	0.193	0.453
ϵ_{II}	0.702	1	0.517	0.346	0.711	0.807	0.547
ϵ_{III}	—	—	—	0.195	—	—	—
A (%)	0.0952	0.1022	0.1539	0.2500	0.1053	0.0851	0.1859
γ	297	163	369	974	666	—	287
$i_I, 1\sigma$ (°)	49⁺⁶₋₄₉	—	81 ± 1	85 ± 1	89 ± 1	89	51 ⁺⁵ ₋₅₁
$i_I, 90\%$ (°)	49⁺⁸₋₄₉	—	81 ± 2	85 ± 2	89 ± 2	89	51 ⁺⁷ ₋₅₁
$i_I, 2\sigma$ (°)	49⁺¹⁰₋₄₉	—	81 ± 3	85 ± 2	89 ± 2	89	51 ⁺⁹ ₋₅₁
$i_{II}, 1\sigma$ (°)	78 ± 1	68 ⁺⁴ ₋₆	81 ± 1	79 ± 1	76 ± 2	72	67 ⁺² ₋₄
$i_{II}, 90\%$ (°)	78⁺²₋₃	68 ⁺⁵ ₋₂₆	81 ± 2	79 ± 2	76 ± 3	72	67 ⁺³ ₋₁₃
$i_{II}, 2\sigma$ (°)	78⁺²₋₄	68 ⁺⁶ ₋₄₅	81 ± 3	79 ± 2	76 ± 3	72	67 ⁺⁴ ₋₂₂
$\Omega_a, 1\sigma$ (°)	148 ± 3	147 ± 8	125 ± 3	112 ± 3	136 ± 2	100	128 ± 8
$\Omega_a, 2\sigma$ (°)	148 ± 7	147 ± 16	125 ± 6	112 ± 7	136 ± 4	100	128 ± 14
$\Omega_b, 1\sigma$ (°)	48 ± 3	63 ± 8	58 ± 3	112 ± 3	51 ± 2	17	37 ± 8
$\Omega_b, 2\sigma$ (°)	48 ± 7	63 ± 16	58 ± 6	112 ± 7	51 ± 4	17	37 ± 14
$\Theta_{\text{quad,a}}, 1\sigma$ (°)	164 ± 2	164 ± 8	153 ± 2	146 ± 3	158 ± 2	140	154 ± 4
$\Theta_{\text{quad,a}}, 2\sigma$ (°)	164 ± 4	164 ± 16	153 ± 3	146 ± 7	158 ± 4	140	154 ± 7
$\Theta_{\text{quad,b}}, 1\sigma$ (°)	114 ± 2	121 ± 8	119 ± 2	146 ± 3	116 ± 2	98	109 ± 4
$\Theta_{\text{quad,b}}, 2\sigma$ (°)	114 ± 4	121 ± 16	119 ± 3	146 ± 7	116 ± 4	98	109 ± 7

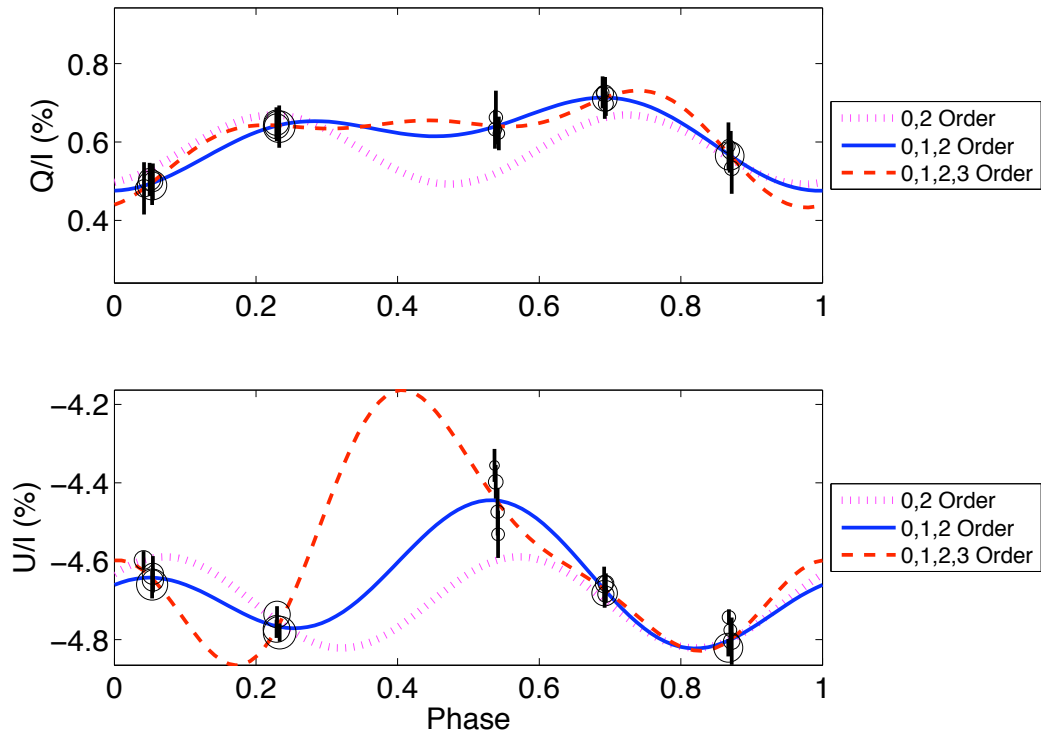


Figure 4.1: Binned observations of Cygnus X-1, August 2007 data. Area of each open circle is proportional to number of detected photons.

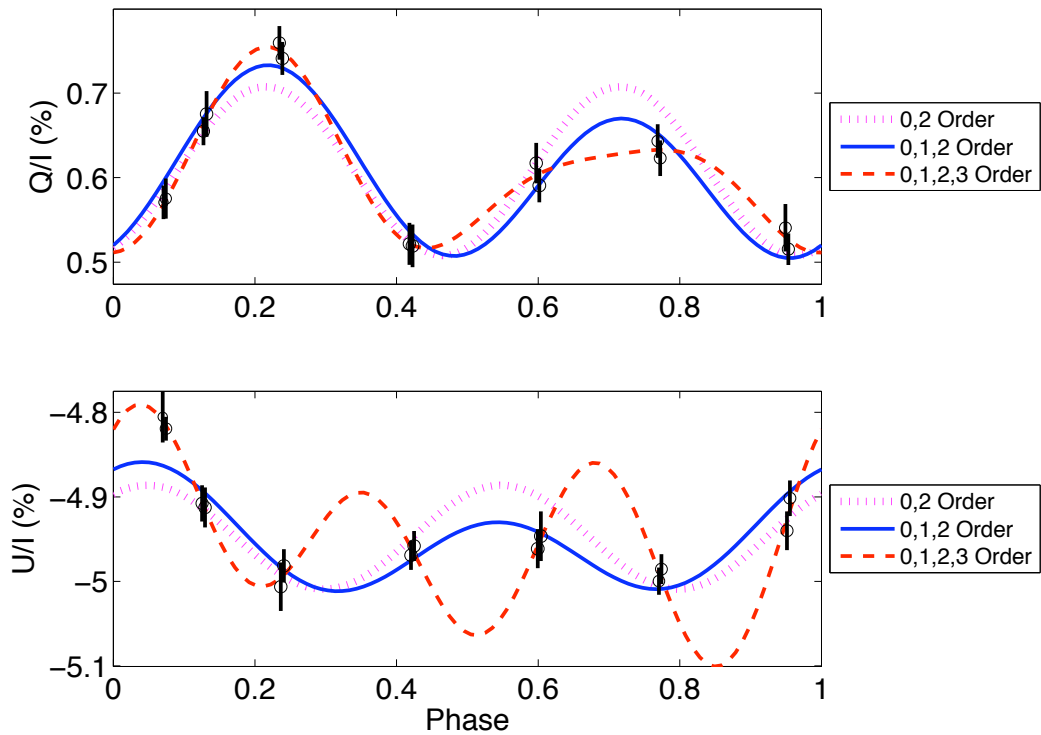


Figure 4.2: Binned observations of Cygnus X-1, June 2008 data. Observations at phase 0.13 correspond to the next orbit.

The fractional power in the first, second, and third harmonics for each fit are given as ϵ_I , ϵ_{II} , and ϵ_{III} , respectively, where $\epsilon_I + \epsilon_{II} + \epsilon_{III} = 1$. We require that $\alpha > 0.01$ in order to assume the fit is valid. It should be noted that values higher than $\alpha = 0.01$ do not imply that the model is a correct physical description of the scattering process. Indeed, it is expected that the fits to the Aug 2007 data involving zeroth through second and zeroth through third order in orbital frequency will have favorable values of α , regardless of whether the model is actually correct. This is because these fits have five and seven parameters, respectively, while the data essentially consist of five points (one per night). The zeroth through third order fit to the Jun 2008 data is also expected to fit the data well, because seven nights of data were taken.

Values lower than $\alpha = 0.01$, however, imply that either (1) the model does not accurately describe high-frequency modulation in the data, or (2) the model does not correctly describe the scattering process. Since the scatter in observations during each night is low, we can assert that high-frequency fluctuations in the polarization from Cygnus X-1 are not observed. For the Aug 2007 run, the 0th/2nd harmonic model is the only one tested for which data overconstrain the fit, so α for this fit is the probability that the model accurately describes the physical processes involved. Thus, the discrepancy between the 0th/2nd harmonic model and both Stokes parameters observed at phase 0.55 is significant: the first harmonic is essential in describing the polarimetric modulation in Cygnus X-1 to a confidence level $1 - \alpha_Q \alpha_U \approx 1 - 10^{-11}$. The data from the Jun 2008 run overconstrain the zeroth through second order fit, which is the standard fit for the BME technique. The BME model can be rejected for this run at the $1 - \alpha_Q = 0.38$ and $1 - \alpha_U = 0.94$ confidence levels for the Stokes Q and U data, respectively. The inadequacy of the BME model is evidenced by the poor Stokes U fit seen in Figure 4.2.

The large contribution of the third harmonic is seen most strongly in the Stokes U data, and it is most likely spurious. Indeed, the fit using the zeroth through third harmonics is radically different between the Aug 2007 and Jun 2008 runs, which can be seen in Figures 4.1 and 4.2. A rapid increase in U occurs between observations near phase 0.4 during the Aug 2007 run, which is a strong indicator that it is an artifact of the fit. To test this, we generated random data sets consisting of five points each, where the phase of the data points correspond to the phases in Figure 4.1. While the Q and U value for each point was chosen randomly, mean Q and U as well as the amplitudes were set to the observed values. Each synthetic data set was fit to Equations 4.4a and 4.4b. An example of a random data set is given as Figure 4.3. The amplitudes A_{fit} and A_{data} are shown as dashed and dotted lines, respectively.

Both a histogram of the ratio of amplitudes $A_{\text{fit}}/A_{\text{data}}$ and their cumulative distribution function (CDF) are plotted in Figure 4.4 for the randomly generated data sets. Ratios must be larger than unity, because the five-parameter fit will always pass through each five-point data set. Large ratios of amplitudes indicate that the fits have large fluctuations for phases between data points. For the 0th/1st/2nd order fit to the observations in Figure 4.1, the measured values of $A_{\text{fit}}/A_{\text{data}}$ are 1.08 and 1.10 for Q and U , respectively. The probabilities of random data having higher amplitude ratios are $1 - \text{CDF}_Q = 88\%$ and $1 - \text{CDF}_U = 87\%$, indicating the high probability that the 0th/1st/2nd order fit accurately represents the polarization during phases in which the system was not observed. However, $A_{\text{fit}}/A_{\text{data}}$ increases to 1.36 and 2.03 for the fit including the third harmonic. These ratios are lower than 43% and 5% of random data. Thus, the fits including the third harmonic have low probability of accurately describing the system, especially for the U fit. Since the third harmonic is generated by orbital eccentricity, the fact that the third harmonic is not necessary to fit the observed data agrees with the observation that orbital eccentricity is consistent with zero. Thus, we agree with the community's use of the 0th/1st/2nd order fit as being the most appropriate for Cygnus X-1.

For the Aug 2007 data, inclination determined from the first-order coefficients in Equation 4.5a is $i_{\text{I}} = 81.2^\circ$, while the second-order coefficients give $i_{\text{II}} = 81.3^\circ$ from Equation 4.5b. Thus, inclinations derived from the first and second order coefficients are mutually consistent. However, inclinations derived from the Jun 2008 data are $i_{\text{I}} = 48.9^\circ$ and $i_{\text{II}} = 77.8^\circ$, which are mutually inconsistent. To estimate the confidence interval on these inclinations, we first determine the figure of merit γ (Equation 4.8b). Since each bin has a different uncertainty, we choose to rewrite Equation 4.8b as a summation over bins j :

$$\gamma = \frac{1}{2} \sum_{j=1}^N \left(\frac{A}{\sigma_j} \right)^2. \quad (4.10)$$

To estimate the confidence interval on our derived inclination estimate, we consult Figure 4 of WD94 for $\gamma = 300$, which is plotted in Figure 4.5. Interpolating between the confidence intervals for $\gamma = 300$ and $\gamma = 1.2 \times 10^5$ in the same figure shows that the difference between $\gamma = 300$ and $\gamma = 369$ reduces the confidence interval by less than one degree. Therefore, we estimate the confidence intervals on derived inclination to be $80^\circ \leq i \leq 82^\circ$ (1σ) and $78^\circ \leq i \leq 84^\circ$ (2σ) for the Aug 2007 data. The 90% confidence interval is therefore $79^\circ < i < 83^\circ$. For the Jun 2008 run, the confidence intervals on derived inclination are $77^\circ \leq i \leq 79^\circ$ (1σ), $75^\circ \leq i \leq 80^\circ$ (90% confidence), and $74^\circ \leq i \leq 80^\circ$

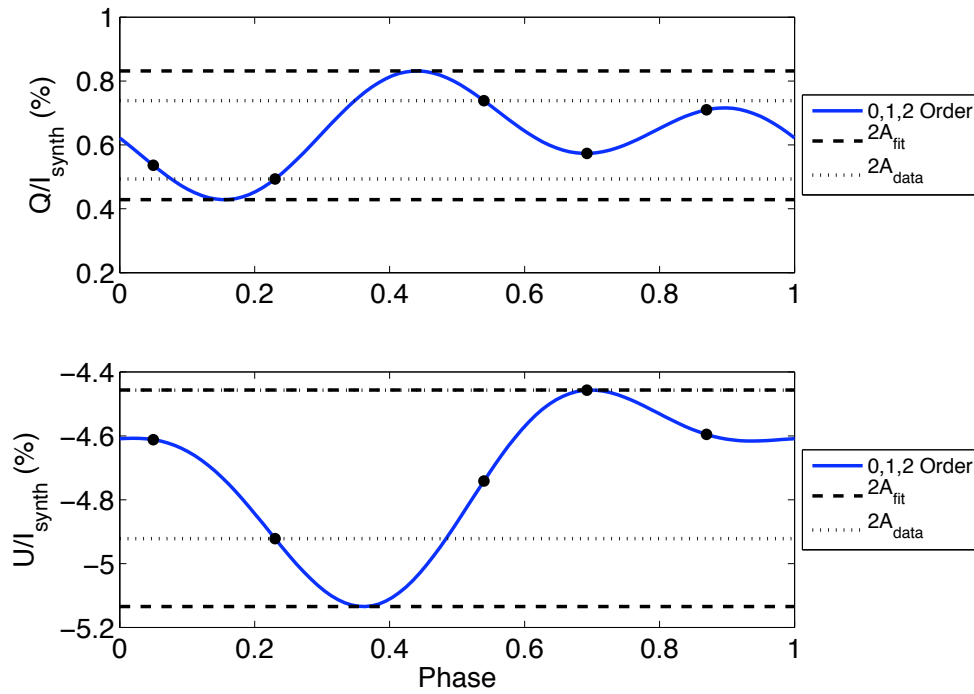


Figure 4.3: Examples of synthesized Q and U data sets. Extrema lying at phases between data points suggest that the fits do not accurately describe the system at all phases.

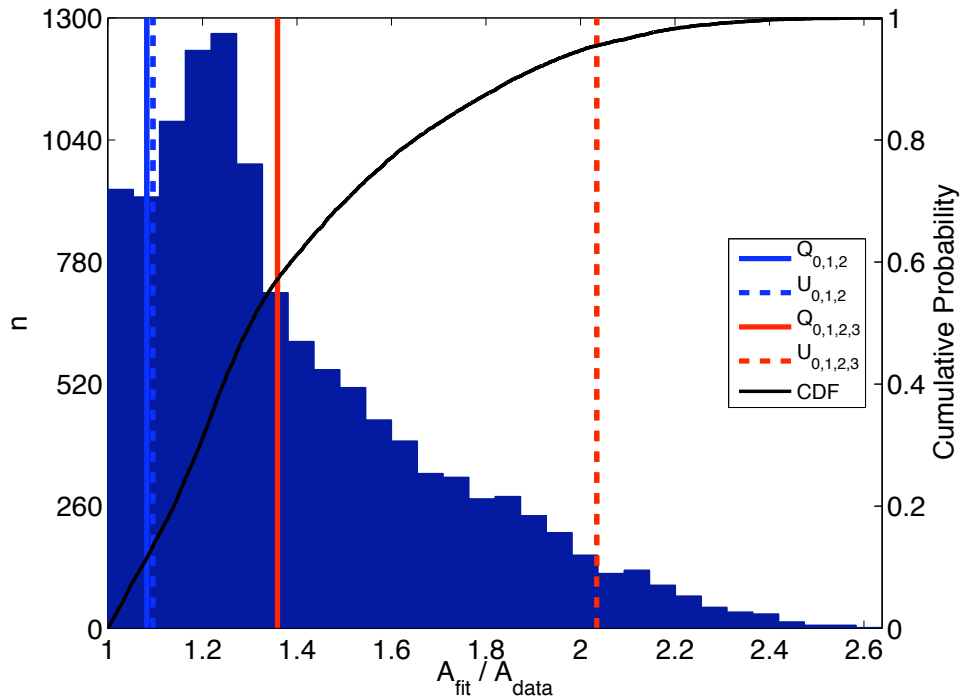


Figure 4.4: Histogram (left axis) and cumulative distribution function (right axis) of the ratios of amplitudes between BME fits and synthesized data. Large ratios indicate that the fit surpasses the range of the data.

(2σ). We find the values of Θ_{quad} from Equations 4.6b and 4.6c to be inconsistent for both the Aug 2007 and Jun 2008 runs.

4.5 Literature Estimates

Other groups have estimated the inclination of Cygnus X-1 as well as other binary systems (Table 4.3 and Figure 4.6). Uncertainties in parenthesis represent 1σ error, while ranges indicate 90% confidence intervals. An inclination of “?” indicates that the inclination inversion method failed to provide a fit at acceptable significance under the χ^2 test. Methods used generally fall into four categories: presence/lack of eclipses, radial velocity (mass function or tomography), ellipsoidal light modulation, and polarimetry.

4.5.1 Eclipses

Strong X-ray eclipses are not observed in Cygnus X-1, so the maximum allowable inclination is given by $\cos i_{\text{max}} = R/a$, where R is the radius of the supergiant and a is the semimajor axis of the orbit (Figure 4.7). These values are estimated at $a = 40.2 R_{\odot}$, $42 \pm 9 R_{\odot}$ (Herrero et al. 1995, Iorio 2007), $R = 18 R_{\odot}$, 17.0 to $22.9 R_{\odot}$, $22.77 \pm 2.3 R_{\odot}$ (Bochkarev et al. 1975, Herrero et al. 1995, Ziolkowski 2005), and $R/a = 0.4$ to 0.45 (Karitskaya & Bochkarev 1989). Thus, the maximum inclination is $i_{\text{max}} \approx 62 \pm 4^{\circ}$. This is inconsistent with the inclinations derived from individual runs at the $4\sigma - 5\sigma$ level. Thus, we can state with high confidence that the BME technique fails when determining the inclination of Cygnus X-1 from single-orbit observing runs. The maximum inclination is inconsistent at the 3σ level with the polarimetric modulation when co-adding both runs.

4.5.2 Radial Velocity Mass Function

Estimation of inclination from the radial velocity mass function proceeds from *a priori* knowledge of the masses of both binary components, which is usually estimated by stellar evolution modeling from observed spectral type (cf. Moffat et al. 1990a). Inclination is then derived from the definition of the mass function:

$$f(M_{\text{BH}}) = \frac{M_{\text{BH}} \sin^3 i}{(1 + M_{\text{star}}/M_{\text{BH}})^2}. \quad (4.11)$$

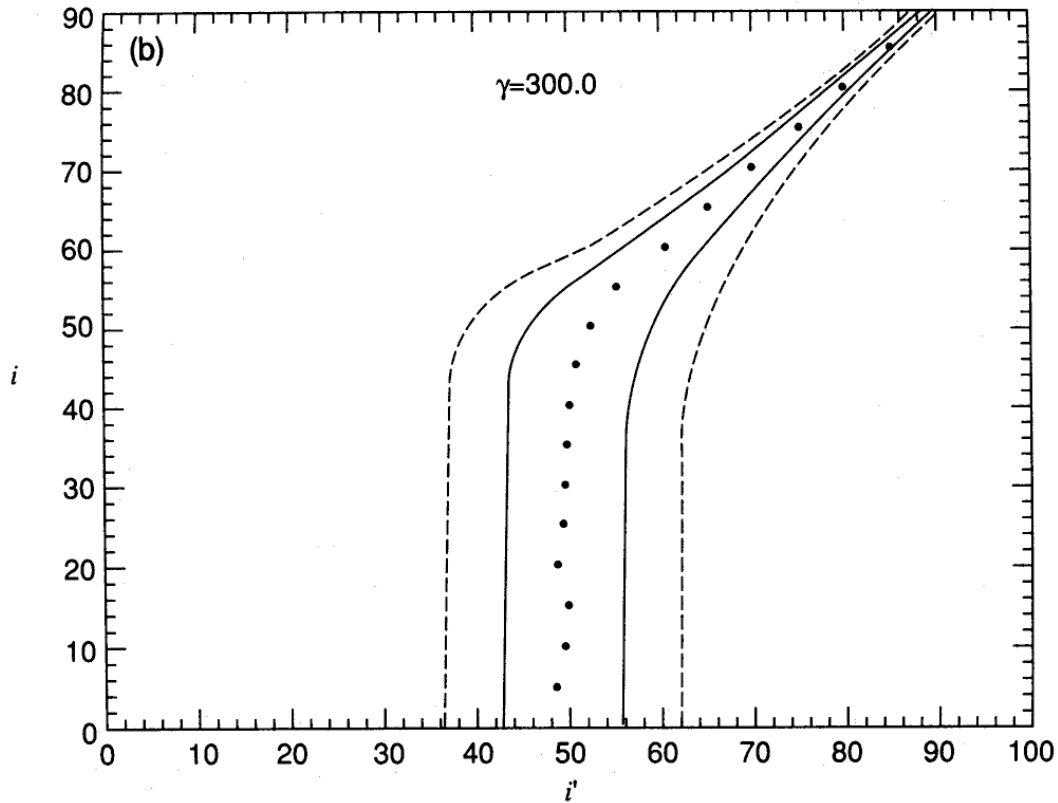


Figure 4.5: Confidence intervals for inclination estimates from the BME model, taken from Figure 4 of Wolinski & Dolan (1994). Derived inclination is i' and true inclination is i . The solid lines indicate the 1σ confidence interval, while the 2σ confidence interval is given by dashed lines. Therefore, derived inclination $i' \leq 56^\circ$ will have a 1σ confidence interval that extends down to $i = 0^\circ$.

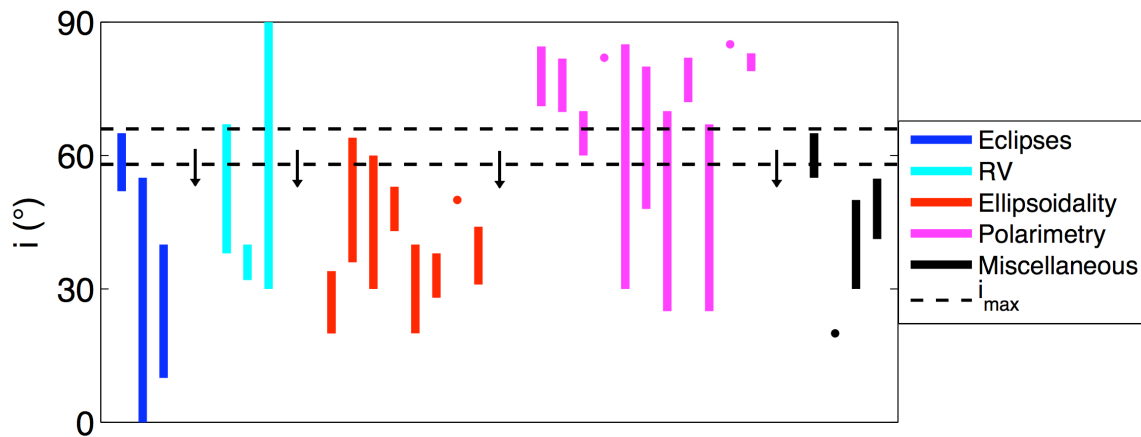


Figure 4.6: Cygnus X-1 inclination estimates from various methods. Note that many inclination estimates derived polarimetrically significantly exceed the maximum possible inclination, which is determined from the lack of observed X-ray eclipses.

Table 4.3: Comparison of Inclination Estimates

Binary	Reference	Method or Data	Band	i ($^\circ$)
Cygnus X-1 ¹	Bochkarev et al. (1979)	Minor eclipses	—	58(7)
	Sowers et al. (1998)	Wind non-eclipses	H α	< 55
	Wen et al. (1999)	Minor eclipses	X-rays	25(15)
	This work	Non-eclipses	X-rays	< 62 \pm 4
	Karitskaya & Bochkarev (1989)	Disk precession	V	60(5)
	Brocksopp et al. (1999a)	...	X-rays	20
	Miller et al. (2002)	Disk spectrum	X-rays	40(10)
	Shaposhnikov & Titarchuk (2007)	QPO scaling	—	8.7(8) M_\odot
	Iorio (2007)	S&T (2007)	—	48.0(6.8)
	Ninkov et al. (1987a)	Mass function	—	36(4)
	Davis & Hartmann (1983)	RV tomography	U	52(15)
	Gies et al. (2003)	...	H α	> 30(7)
	Hutchings et al. (1973)	Ellipsoidality	B	27(7)
	Bochkarev et al. (1975)	...	—	50(14)
	Hutchings (1978)	...	—	45(15)
	Guinan et al. (1979)	...	—	48(5)
	Brocksopp et al. (1999b)	...	UBV	50
	Gies & Bolton (1986a)	Ellip. + RV	—	33.5(5.5)
	Abubekerov et al. (2004)	...	—	37.5(6.5)
	Daniel (1981)	Ellip. + polarimetry	—	30(10)
	Kemp et al. (1978a)	Polarimetry	V	77.8(6.7)
	UV	75.8(6.0)
	Kemp et al. (1979)	...	—	65(5)
	Kemp (1980b)	...	—	82
	Simmons et al. (1980)	Kemp et al. (1979)	—	30 – 85
	...	Kemp (1980b)	—	48 – 80
	Long et al. (1980)	Polarimetry	X-rays	25 – 70
	Drissen et al. (1986a)	Kemp et al. (1978a)	—	77(5)
	Dolan & Tapia (1989)	Polarimetry	B	67
	V	55
	R	60
	BVR	25 – 67
Wolinski et al. (1996)	...	U	85	
This work (W07)	...	$\approx B$	79 – 83	
... (W08)	...	$\approx B$	75 – 80	
... (W _{mean})	...	$\approx B$	73 – 79	
Vela X-1 ^{1,2} (GP Vel) (HD 77581) (4U 0900 – 40)	Hutchings (1974)	Eclipses	—	80
	Hutchings (1978)	...	—	73
	Dolan & Tapia (1988)	Polarimetry	—	67 – 81
	Wolinski et al. (1996)	...	U	?
HD 153919 ^{1,2} (V884 Sco) (4U 1700-37)	Hutchings (1974)	Eclipses	—	90
	Hutchings (1978)	...	—	87(3)
	Dolan & Tapia (1984)	Polarimetry	—	85(3)
	Dolan & Tapia (1988)	...	U	53
	B	80
	R	84
	I	85
	UBRI	71 – 86
	Wolinski et al. (1996)	...	U	85
	—	83
HD 152667 (V861 Sco)	Dolan & Tapia (1988)	Polarimetry	U	83
	B	80
	G	85
	R	84
	I	86
	UBGRI	75 – 90
CX Dra	Horn et al. (1992)	Polarimetry	U	71
	Berdyugin & Piirola (2002)	Polarimetry	U	71
	U	75
	B	72
	B	70
	V	72
	V	66
	R	76
	R	81
	I	74
	I	86
	UBVRI	65 – 76 (2 σ)
	UBVRI	58 – 80 (2 σ)
	—	82
Algol ² (β Per) (HD 19356)	Batten (1967)	Eclipses	—	82
	Rudy & Kemp (1978)	Polarimetry	—	81(4)
	Aspin & Simmons (1982)	R&K (1978)	—	?

¹High mass X-ray binary²Eclipsing binary

Comparison of Inclination Estimates (continued)

Binary	Reference	Method or Data	Band	i ($^{\circ}$)
W Ser ²	Pirola et al. (2005)	Polarimetry	<i>U</i>	69.6
	<i>U</i>	64.3
	<i>B</i>	70.3
	<i>B</i>	56.3
	<i>B</i>	73.7
	<i>V</i>	78.3
	<i>V</i>	67.5
	<i>R</i>	74.1
	<i>R</i>	50.0
	<i>I</i>	79.0
	<i>I</i>	51.0
	...	Kruszewski (1972)	<i>B</i>	88.2
...	...	<i>G</i>	82.7	
AO Cas ² (HD 1337) (HR 65)	Batten (1967)	Eclipses	—	57
	Rudy & Kemp (1978)	Polarimetry	—	63(9)
	Aspin & Simmons (1982)	R&K (1978)	—	0 – 88
σ Ori E ² (HD 37479)	Kemp & Herman (1977)	Polarimetry	<i>B</i>	76(8)
	Aspin & Simmons (1982)	K&H (1977)	<i>B</i>	?
u Her ² (HD 156633) (68 Her) (HR 6431)	Merrill (1963)	Eclipses	—	77
	Batten (1967)	...	—	76
	Rudy & Kemp (1978)	Polarimetry	—	77(5)
	Aspin & Simmons (1982)	R&K (1978)	—	0 – 90
U Sge ² (HD 181182) (HR 7326)	Batten (1967)	Eclipses	—	90
	Rudy & Kemp (1978)	Polarimetry	—	87(3)
	Aspin & Simmons (1982)	R&K (1978)	—	0 – 90
MWC 1080 ² HD 47129 (Plaskett's Star)	Manset & Bastien (2001)	Polarimetry	—	43 – 81
	Rudy & Herman (1978) Aspin & Simmons (1982)	Polarimetry R&H (1978)	<i>B</i> —	71(9) 0 – 90
NTTS 162814 – 2427	Jensen & Mathieu (1997)	Mass function	—	71
	Manset & Bastien (2003)	Polarimetry	—	86.2(2.6)
WR 6 (EZ CMa) ³	McLean (1980)	Polarimetry	—	71.4(6.8)
WR 9 ^{2,3} (V443 Pup) (HD 63099)	Lamontagne et al. (1996)	Eclipses	—	56.8(2.0)
	Niemela et al. (1984)	Mass function	—	64
	...	Polarimetry	—	67.9(3.0)
WR 21 ^{2,3} (HD 90657)	Balona et al. (1989)	Eclipses	—	49.6(3.7)
	Massey (1981)	Mass function	—	45
	Niemela (1982)	...	—	48
	Lamontagne et al. (1996)	Polarimetry	—	62.4(2.2)
WR 31 ^{2,3} (V428 Car) (HD 94546)	Lamontagne & Moffat (1987)	Eclipses	—	61.6(1.7)
	Niemela et al. (1985)	Mass function	—	40
	Lamontagne et al. (1996)	Polarimetry	—	62.0(2.7)
WR 42 ^{2,3} (V431 Car) (HD 97152)	Balona et al. (1989)	Eclipses	—	40.3(2.9)
	Massey (1981)	Mass function	—	35
	Davis et al. (1981)	...	—	38
	St.-Louis et al. (1987)	Polarimetry	—	39 – 49
CD Cru ^{2,3} (WR 47) (HD 311884)	Moffat et al. (1990b)	Eclipses	—	63(7)
	Massey (1981)	Mass function	—	70
	Moffat et al. (1990b)	...	—	90
	Moffat & Seggewiss (1987)	Polarimetry	—	77
	St.-Louis et al. (1988)	...	—	76.9(1.7)
	Moffat et al. (1990b)	...	—	73(5)
WR 79 ^{2,3} (HD 152270) (HR 6265)	St.-Louis et al. (1987)	Eclipses	—	33.6(2.3)
	Massey (1981)	Mass function	—	25
	Seggewiss (1974)	...	—	34
	Luna (1982)	Polarimetry	—	42(10)
	St.-Louis et al. (1987)	...	—	40 – 50
WR 97 ^{2,3} (HD 320102)	Lamontagne et al. (1996)	Eclipses	—	?
	Niemela (1995)	Mass function	—	31
	Lamontagne et al. (1996)	Polarimetry	—	85.4(2.0)
CV Ser ^{2,3} (WR 113) (HD 168206)	Massey (1981)	Mass function	—	70
	Massey & Niemela (1981)	...	—	90
	Lipunova (1982)	Eclipses	—	70.4(2.3)
	Lamontagne et al. (1996)	Polarimetry	—	79.7(2.3)
QY Vul ^{2,3} (WR 127) (HD 186943)	Moffat & Shara (1986)	Eclipses	—	55.3(4.7)
	Massey (1981)	Mass function	—	70
	Massey et al. (1981)	...	—	90
	St.-Louis et al. (1988)	Polarimetry	—	0 – 90
V444 Cyg ^{2,3} (WR 139) (HD 193576)	Kron & Gordon (1950)	Eclipses	—	78.4
	Batten (1967)	...	—	80
	Cherepashchuk (1975)	...	—	78(1)
	Hiltner & Mook (1966)	Polarimetry	—	76(6)
	Rudy & Kemp (1978)	...	—	72(6)
	Aspin & Simmons (1982)	R&K (1978)	—	0 – 90
	Pirola & Linnaluoto (1988)	Polarimetry	—	82.8(0.9)
	Robert et al. (1990)	H&M (1966)	—	83.2(4.3)
	...	R&K (1978)	—	76.0(2.3)
...	Polarimetry	—	77 – 79	
WR 148 ³	Drissen et al. (1986a)	Polarimetry	—	66.6(4.0)
CX Cep ^{2,3} (WR 151)	Massey & Conti (1981a)	Eclipses	—	\geq 50
	Lipunova & Cherepashchuk (1982)	...	—	50

³Wolf-Rayet binary

Comparison of Inclination Estimates (continued)

Binary	Reference	Method or Data	Band	i ($^\circ$)
	De Greve et al. (1988)	...	—	51
	Schulte-Ladbeck & van der Hucht (1989)	Polarimetry	—	74(5)
	Villar-Sbaffi et al. (2006)	S-L&vdH (1989)	—	68(18)
	...	Kartasheva (2002b)	—	79(12)
	...	Polarimetry	—	70(2)
	U	89^{+1}_{-7}
	B	76(14)
	V	86^{+4}_{-9}
	R	81(8)
	I	87^{+3}_{-8}
GP Cep ^{2,3} (WR 153)	Moffat & Shara (1986)	Eclipses	—	74.0(0.7)
	St.-Louis et al. (1988)	Polarimetry	—	78(5)
CQ Cep ^{2,3} (WR 155) (HD 214419)	Leung et al. (1983)	Eclipses	—	68.0(0.4)
	Stickland et al. (1984)	...	—	70(4)
	Drissen et al. (1986b)	Polarimetry	—	78.0(1.0)
	Pirola & Linnaluoto (1988)	...	—	78.1(1.7)

Here, M_{BH} is the mass of the black hole and M_{star} is the mass of the visible binary component. Modeling of the mass of the optical component is highly error-prone because of uncertainties both in the distance to the system and in evolutionary modeling. Therefore, inclination determined from the radial velocity mass function should only serve as a rough guide when no other inclination estimates exist.

4.5.3 Radial Velocity Tomography

Radial velocity tomography is used on stars exhibiting P Cygni profiles, and therefore on stars exhibiting mass loss. It is generally assumed that outflow velocity from all stellar latitudes is isotropic, so the radial velocity of the blueshifted absorption should be equal in magnitude, but opposite in sign, to the radial velocity of the redshifted emission for a nearly edge-on orientation at phase 0.5 (a truly edge-on geometry would exhibit no redshifted emission due to occultation by the supergiant). At this phase, the black hole is in superior conjunction, so the radial velocity of the supergiant is zero in a frame comoving with the system center of mass.

For stars nearly filling their Roche lobes, the density enhancement in the focused stellar wind will cause most of the redshifted P Cygni emission to be from material in the plane of the orbit. Thus, emission radial velocity will be related to absorption radial velocity by $v_{\text{em}} = v_{\text{abs}} \sin i$ (Figure 4.7). G03 acknowledge that the assumption of isotropic wind velocity is most likely not correct. Friend & Castor (1982) suggest that the enhanced density in the plane of the orbit, due to the focused stellar wind, will slow the equatorial wind with respect to the wind flowing toward the observer. Since decreased wind velocity in the plane of the orbit will bias the derived inclination towards lower values, inclinations determined by radial velocity tomography represent lower limits.

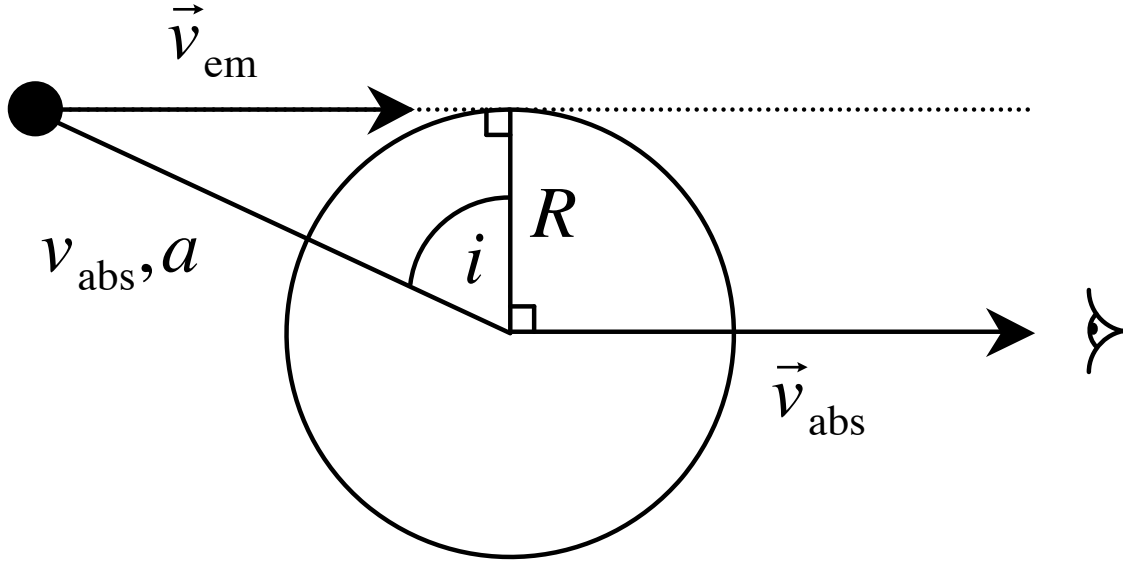


Figure 4.7: Geometry for eclipses and for radial velocity tomography. Arrows indicate P Cygni emission towards the observer. The magnitude of the absorption radial velocity v_{abs} has been scaled to the semimajor axis a ; however, the semimajor axis and supergiant radius R are not to scale.

4.5.4 Ellipsoidal Modulation

The cross-sectional area of the tidally distorted supergiant varies at twice the orbital frequency, generating a so-called “ellipsoidal” lightcurve. In analogy to the modulation of polarization degree throughout the orbit, the lightcurve is indicative of orbital inclination. However, this technique assumes that the only photometric variability in the system is due to the ellipsoidality of the star. The focused stellar wind contributes to the flux from the system, which complicates ellipsoidal fitting. Cygnus X-1 is known to have an inclined, precessing accretion disk (section 4.2.2), so flux reflected off the disk generates a periodic phase shift with ≈ 150 and/or 294 day period added to the total system flux. Therefore, inclination of Cygnus X-1 derived from ellipsoidal modulation may not be equal to the physical inclination of the system.

When flux from the visible binary component dominates the system lightcurve, however, inclinations inverted from the ellipsoidal modulation technique can be very precise. For example, the X-ray luminosity of the black hole binary GRO J1655 – 40 is low during quiescence; therefore, accretion is low during this state. The visible, F5IV component dominates the optical and near-IR flux from the system, so ellipsoidal lightcurve fitting can yield accurate inclination. Greene et al. (2001) find $i_{\text{J1655}} = 70.2 \pm 1.9$ (2σ) from *BVIJK* band photometry and a black hole mass of $M_{\text{J1655}} = 6.3 \pm 0.5 M_{\odot}$.

4.5.5 Polarimetry

The first Cygnus X-1 inclination estimate via polarimetry came from Kemp et al. (1978a, hereafter K78). From 180 nights of data taken over two years on a 61 cm telescope, they find strong second harmonic modulation in V band and weak modulation in U band. K78 phase-wrap the data onto an ephemeris generated by their own photometric data, and they bin the data at certain phase intervals to account for random fluctuations from orbit to orbit. K78 observe an ellipse in the (Q, U) plane, and they determine an inclination of $i = 77.8 \pm 6.7^\circ$ by fitting for the eccentricity of this ellipse (Equation 4.7). Uncertainty in inclination was calculated by formal error propagation from uncertainties in the amplitudes of the first and second Fourier harmonics (Equations 4.4a and 4.4b).

Kemp et al. (1979, hereafter K79) phase-wrap and bin 348 nights of data, including the data from K78. After smoothing third and higher harmonics, they show a (Q, U) locus that has significant departures from ellipticity. They state that this cannot be reconciled with the symmetric, canonical model of BME, which assumes symmetry in scatterers above and below the orbital plane. To explain their observed polarization, K79 suggest a model involving eclipses of a hot spot generated at the intersection of the supergiant's gas stream and the accretion disk. The model requires the hot spot to be eclipsed by a geometrically thick accretion disk when the black hole is at inferior conjunction (phase 0.5), which implies an inclination of $i = 65 \pm 5^\circ$. Milgrom (1978) and Kemp (1980a) propose that the accretion disk is flared due to irradiation by the X-ray source, and Kemp (1980a) model the inclination to be $i = 67.5 \pm 2.5^\circ$.

Simmons et al. (1980, hereafter S80) object to the dismissal by K79 of the applicability of the BME canonical model to Cygnus X-1, and they use both the symmetric and asymmetric canonical models to fit the data of K79. The asymmetric model allows the distribution of scatterers to be asymmetric about the orbital plane, which generates first harmonic periodicity in the polarization curves. S80 also criticize the small inclination uncertainties of K78 and K79 on the grounds that fits with a larger range of inclinations could acceptably represent the data in a χ^2 analysis. They argue that the 90% confidence interval on inclination from K79 should in fact be $i = 78_{-48}^{+7^\circ}$. The asymmetry in error bounds comes from the fact that a given increase in inclination causes a stronger change in the polarimetric signal than does a decrease in inclination by the same amount. In addition, S80 criticize the massive phase-binning of the K78 data to form mean polarization curves, because orbit-to-orbit changes of unknown cause are observed. S80 recommend observations with

larger telescopes to minimize uncertainty on each data point. This allows inclination inversion across data obtained over fewer orbits.

In the same volume as S80, Kemp (1980b, hereafter K80) reject the asymmetric canonical model of BME as an accurate representation of their phase-binned data, which now consist of 528 nights. While the asymmetric BME model predicts only first, second, and third harmonic modulation of polarization in a binary, K80 observe weak first harmonic and strong second through fifth harmonic modulations. They claim a probability of only 60% that the first harmonic is even present in their data, while the probability of the third through fifth being present is 85% as a group. Further, they observe the fifth harmonic at a significance of 99%.

K80 suggest that the physical reasoning for first harmonic modulation in the BME model, asymmetry in scatterers about the orbital plane, should also generate harmonics higher than the second. They state that any model that incorporates the first harmonic should be accepting of third and higher harmonics as well. Thus, they assume the only model of BME with any validity is the symmetric canonical model, which only assumes second harmonic modulation. K80 fit their data to the symmetric model to find an inclination of $i = 82^\circ$. Unfortunately, no uncertainty is provided on this inclination estimate, and K80 do not address the issue of underestimation of inclination uncertainty raised by S80.

K80 assume that orbit-to-orbit variations in polarization are random, because uncertainty in phase bins is observed to decrease as the inverse square root of the number of observations. K80 claim that their large, phase-binned data set is therefore a true representation of the mean state of Cygnus X-1. Since a true inclination of $i = 82^\circ$ would cause X-ray eclipses, K80 reconcile their inclination estimate with the lack of observed X-ray eclipses by claiming that shadowing or variable absorption are driving the polarimetrically-derived inclination toward higher values. Thus, K80 claim that the inclination of Cygnus X-1 is large but less than $i = 82^\circ$. Finally, K80 disagree that larger telescopes and shorter observing epochs are the best way to minimize observational uncertainty, because they claim the “intrinsic noise” of Cygnus X-1 can have timescales longer than one month.

In proof, S80 caution that the addition of higher harmonics in data fitting will always generate a better fit; however, a better fit does not necessarily imply a more accurate representation of the

physical processes involved. S80 find the asymmetric canonical model acceptably fits the data of K80 at 10% significance, and the 90% confidence interval on derived inclination is $i = 71_{-23}^{+9}$. They find the symmetric canonical model implies $i = 70 \pm 8^\circ$ with a fit acceptable at only 5% significance. S80 admit that the unknown cause of the orbit-to-orbit polarimetric variations in Cygnus X-1, and therefore the unknown statistical distribution of those variations, makes an optimum observing campaign difficult to plan. Thus, S80 suggest that a short observing run on a large telescope be performed to test the validity of massive phase-binning of data.

Long et al. (1980) observe significant polarization of Cygnus X-1 in X-rays which they attribute to scattering of the X-ray source off the accretion disk. For an optically thick disk, polarization is expected to be parallel to the major axis of the disk when projected onto the plane of the sky (Angel 1969, Sunyaev & Titarchuk 1985, Phillips & Mészáros 1986, Kartje & Königl 1991), which implies a disk inclination of $i_{\text{disk}} = 59.5 \pm 10.5^\circ$ (1σ). However, an optically thin disk is expected to be polarized perpendicular to the major axis (Shakhovskoi 1965, Pringle & Rees 1972, Shakura & Syunyaev 1973), which suggests $i_{\text{disk}} = 35 \pm 10^\circ$ (1σ). The disk is thought to be optically thick with $\tau \approx 1 - 2$ (Syunyaev & Trümper 1979; Zdziarski et al. 1996, 1997; Gierliński et al. 1997; Poutanen 1998; Di Salvo et al. 2001; Frontera et al. 2001; Miller et al. 2002; Zdziarski & Gierliński 2004; Ibragimov et al. 2005; Ibragimov et al. 2007), so the inclination estimate of $i_{\text{disk}} = 59.5 \pm 10.5^\circ$ (1σ) seems more likely. Since the disk is thought to be inclined, $i - \delta \leq i_{\text{disk}} \leq i + \delta$ depending on disk precession phase. Here, δ is disk obliquity, which is estimated to be $\delta = 15 \pm 7^\circ$ (Karitskaya & Bochkarev 1989, Ibragimov et al. 2007). Therefore, orbital inclination is $i_{\text{disk}} - \delta \leq i \leq i_{\text{disk}} + \delta$, which implies $i = 60 \pm 13^\circ$.

Daniel (1981, hereafter D81) criticize the interpretation of K79 of eclipsing of a scattering region at the rim of the accretion disk on its *ad hoc* nature. Since tidal distortion of the supergiant causes the ellipsoidal lightcurve, and that Daniel (1980) suggest prolate ellipsoids can be up to 5% polarized, D81 assume the variability in polarization of the system is dominated by the tidal distortion of the supergiant, which is modeled to be ellipsoidal in shape. By simultaneously fitting the lightcurve and the modulation of polarization degree from the data of K79, D81 arrive at an inclination of $i = 30 \pm 10^\circ$. However, D81 acknowledge that modeling the polarization degree, instead of Stokes Q and U separately, introduces additional uncertainty to their inclination estimate.

While Bochkarev et al. (1979) caution against the approximation of the shape of the photosphere by an ellipsoid, they support the hypothesis that the tidally distorted supergiant causes the polari-

metric variability of the system. These authors model the amplitude of polarimetric variability of Cygnus X-1 to be $\Delta P_{\text{star}} = 0.3\%$ from pure Thomson scattering by the Roche lobe-filling supergiant. However, Bochkarev et al. (1986) model the distribution of the single-scattering albedo as well as scatterers in the Roche lobe-filling photosphere and find the variability amplitude to be only $\Delta P_{\text{star}} = 0.023\%$, which is a full order of magnitude weaker than the observed variability (Table 4.2).

Dolan & Tapia (1984, 1988) observe changes in polarization curves on a ≈ 10 day timescale in HD 152667, HD 153919, and Vela X-1, which are also close binaries with OB supergiant primaries. Dolan & Tapia (1992, hereafter DT92) note that polarization curves of Cygnus X-1 taken 10 months apart on a 1.5m telescope are inconsistent at the $< 10^{-5}$ level of significance. Dolan & Tapia (1989, hereafter DT89) and DT92 therefore object to phase-binning, obtained over many orbital cycles, by K78, K79, and K80. DT89 and DT92 subscribe to the view of S80 that inclinations derived from single-orbit observations are more accurate in estimating the true orbital inclination of these binaries. Using the asymmetric canonical model of BME, as well as the method of S80, Aspin et al. (1981), and Simmons et al. (1982) for estimation of inclination uncertainty, DT89 determine the inclination of Cygnus X-1 to be $i = 62^{+5}_{-37}^{\circ}$ (90% confidence interval). This range is so large that it not only offers no additional constraint on the inclination of the system, but it also provides no confirmation of previous constraints.

DT89 and DT92 note that tidal distortion polarization (TDP) biases inclinations derived from the BME model toward higher values. In addition, it is not possible to subtract this component from the observed polarization curves before fitting to the BME model, because TDP is inclination-dependent. However, since TDP is expected to represent the equilibrium state of the supergiant, polarization modulation due to TDP should not change from orbit to orbit. Since mean polarization changed by only $< 0.05\%$ over their 10 month time interval, DT92 claim that the changes in polarization curves over this interval are due neither to changes in TDP nor interstellar polarization. They attribute this change to stochastic processes in the system and assert that TDP must therefore not be the dominant source of polarization. This agrees with the calculations of Bochkarev et al. (1986), above.

Wolinski et al. (1996, hereafter W96) observe Cygnus X-1 over one orbit in U band with the High Speed Photometer on the Hubble Space Telescope. They note that the polarization spectrum in the ultraviolet departs significantly from the interstellar relation of Serkowski et al. (1975), which indicates that polarization in this wavelength regime is intrinsic to the binary. Indeed, the amplitude

of polarimetric variability versus wavelength is well-approximated by the addition of wavelength-dependent Rayleigh scattering and wavelength-independent Thomson scattering. While Thomson scattering is explained by free electrons in the circumbinary envelope, Rayleigh scattering results from neutral material in the accretion stream. Such neutral material has been observed in Cygnus X-1 (Mason et al. 1974, Kitamoto et al. 1984), HD 153919 (White et al. 1983), and Vela X-1 (Kallman & White 1982).

Of their thirteen observations of Cygnus X-1, the last one was taken one full phase later than initial observations. This point differs insignificantly from the first observations in Stokes Q , but Stokes U decreases from $U \approx 5\%$ to $U \approx 3.75\%$ over the 5.6 day period. This stochastic variation is comparable to the amplitude of orbital modulation. In order to obtain a fit to the BME model acceptable at $> 5\%$ significance, W96 must reject the observation at the end of the run. This fit implies an inclination of $i = 85^\circ$ for Cygnus X-1 (no uncertainty is provided), which is unphysical. However, the amplitudes of variation in the Stokes Q and U data are $\Delta Q = 0.5\%$ and $\Delta U \approx 1\%$, while the amplitudes of the fits are $\Delta Q_{\text{fit}} \approx 1\%$ and $\Delta U_{\text{fit}} \approx 1.5\%$, respectively. Indeed, Cygnus X-1 is certainly not phase locked over even two orbits, which is one of the assumptions of the BME model. Thus, the observations of W96 cast doubt that the BME model is an accurate representation of the U band variability of the system.

W96 also observe the polarimetric variability of HD 153919 (eclipsing, O6f + neutron star binary) and Vela X-1 (eclipsing, B0.5Ib + neutron star X-ray binary) in U band. Data taken one full phase apart on Vela X-1, a nine-day time interval, differ by $\Delta Q, U \approx 4\%$ in both Stokes Q and U . However, the amplitude of variability is only $\Delta Q, U \approx 2\%$. Furthermore, both HD 153919 and Vela X-1 exhibit strong changes in polarization near phase 0.25 (first quadrature). This effect is twice the amplitude for HD 153919 in both Stokes Q and U ($\Delta Q = 2.5\%$ and $\Delta U = 1\%$), while it is equal to the Stokes Q amplitude and twice the Stokes U amplitude for Vela X-1 ($\Delta Q, U = 4\%$). The fact that this effect occurs at the same phase for both binaries with neutron star companions leads W96 to suggest an additional source of scattering in these systems.

Even after rejecting inconsistent observations on Vela X-1, W96 are unable to acceptably fit data in the F327M filter at $> 5\%$ significance. Therefore, the BME method fails for ultraviolet observations of Vela X-1. Rejecting inconsistent observations, W96 find an inclination of $i = 85^\circ$ for HD 153919, which is consistent with prior estimates (Table 4.3). However, we caution that both

biases inherent to the BME inclination inversion method, resulting from noise as well as from tidal distortion polarization of the visible companion, act to increase inclination estimates. We measure a similar, high inclination for the non-eclipsing Cygnus X-1 that other polarimetrists measure for eclipsing systems. Indeed, all polarimetrically derived inclinations in Table 4.3 are higher than those derived using other methods. Thus, we claim that high inclinations derived polarimetrically are not independent checks of orbital inclination for high-inclination systems.

4.5.6 Disk Precession

Karitskaya & Bochkarev (1989) fit the lightcurve of Kemp et al. (1987), collected on 1,912 nights over a 4,500 night span, in the context of an inclined, precessing accretion disk to obtain an orbital inclination of $i = 60 \pm 5^\circ$ and disk obliquity $i_{\text{disk}} = 17.5 \pm 2.5^\circ$. This value is consistent with the Ibragimov et al. (2007) determination of $i_{\text{disk}} = 15 \pm 7^\circ$ from the precessional modulation of radio and X-ray emission, although they assume $i = 37.5 \pm 7.5^\circ$. However, Brocksopp et al. (1999a) derive a value of $i_{\text{disk}} = 37^\circ$ from precessional modulation of X-rays, but they provide no estimate of uncertainty on this value.

Bruevich et al. (1978) suggest that the blackbody radiation from the disk in addition to reprocessing of X-rays brings the disk emission to $B_{\text{disk}} = 0.03$ and $V_{\text{disk}} = 0.04$ mag. Indeed, a sudden fading event of the system by $\Delta V = 0.04$ mag from the expected ellipsoidal lightcurve over one week has been interpreted as the disappearance and reappearance of the accretion disk (Karitskaya & Goranskij 1996). Delays in optical and X-ray flares have also been observed to span one to two weeks (Karitskaya et al. 2000, 2001). These results indicate the timescale between the deposition of material onto the disk (by the focused stellar wind) and accretion of that material by the black hole may be one to two weeks.

Disk loss is not uncommon in X-ray binaries, as the $\Delta V \approx 0.6$ mag decrease in flux from X Per from 1989 to 1990 is interpreted to be caused by disk loss (Norton et al. 1991, Fabregat et al. 1992). The correlation between decrease in flux and decrease in net polarization of the system during this period ($\Delta P \approx -0.5\%$) shows that the polarization from an accretion disk can be large indeed (Roche et al. 1997).

4.5.7 Quasi-Periodic Oscillation Scaling

Titarchuk & Fiorito (2004, hereafter TF04) show that an accretion disk revolving about the black hole at the Keplerian frequency will transition to sub-Keplerian rotation at a particular radius. This radius will be proportional to the Schwarzschild radius, which is proportional to the mass of the black hole. The normal mode oscillation of this bounded, sub-Keplerian region will be at a frequency inversely proportional to the radius of the sub-Keplerian region. Thus, TF04 suggest that the power spectrum of quasi-periodic oscillations of black holes will be related to black hole mass. They further suggest that the scaling of this power spectrum between two black holes is equal to the mass ratio of those objects.

Shaposhnikov & Titarchuk (2007, hereafter ST07) utilize this technique to verify the mass of the GRS 1915+105 black hole from the known mass of GRO J1655 – 40. Using the mass estimate of GRO J1655 – 40 of $M_{\text{J1655}} = 6.3 \pm 0.5 M_{\odot}$ from ellipsoidal modulation (Greene et al. 2001), ST07 determine the mass of GRS 1915+105 to be $M_{1915} = 15.6 \pm 1.5 M_{\odot}$. This value is consistent with the estimate of Greiner et al. (2001, hereafter G01), where $M_{1915} = 14 \pm 4 M_{\odot}$. G01 deduce an inclination of $i_{1915} = 70 \pm 2^{\circ}$ from the Doppler shifts of the jet and counterjet. Since this inclination has been observed to be stable for years, the precession period of the GRS 1915+105 accretion disk must be long. Therefore, the accretion disk must have obliquity $\delta_{1915,\text{disk}} \approx 0^{\circ}$, indicating $i_{1915} \approx i_{1915,\text{disk}}$.

Buoyed by the successful prediction of the mass of the GRS 1915+105 black hole, ST07 apply the QPO scaling technique to Cygnus X-1. They determine a mass of $M_{\text{CygX-1}} = 8.7 \pm 0.8 M_{\odot}$, which confirms its suspected black hole status. From the mass estimate of ST07, the radial velocity-derived mass ratio (G03), and a self-consistent analysis of the orbital dynamics of the binary, Iorio (2007, hereafter I07) derive an inclination of $i = 48.0 \pm 6.8^{\circ}$ for Cygnus X-1. They also determine the semimajor axis to be $a = 42 \pm 9 R_{\odot}$, the supergiant radius to be approximately equal to the Roche lobe radius $R_{\text{star}} = 21 \pm 6 R_{\odot}$, and the supergiant mass to be $M_{\text{star}} = 24 \pm 5 M_{\odot}$.

This mass is inconsistent with the estimate of $M_{\text{star}} = 17.8 M_{\odot}$ from Herrero et al. (1995), who assumed an inclination of $i = 35^{\circ}$ and a radius of $R_{\text{star}} = 17 R_{\odot}$. The supergiant mass estimate from I07 is also inconsistent with $M_{\text{star}} = 40 \pm 5 M_{\odot}$ from Ziłkowski (2005), whose result depended on the effective temperature of and distance to the supergiant. Since the QPO scaling technique is independent of such assumptions, and since it accurately reproduced the mass of GRS 1915+105,

I07 claim that the $M_{\text{CygX-1}} = 8.7 \pm 0.8 M_{\odot}$ estimate from ST07 and their own $i = 48.0 \pm 6.8^{\circ}$ estimate are correct.

4.6 Discussion

Our high signal to noise data remove any possibility that single-orbit inclination estimates derived using BME model fitting to polarimetric data of Cygnus X-1 can be reconciled with those from eclipse studies, ellipsoidal modulation, and radial velocity tomography. Furthermore, such single-orbit inclination estimates cannot represent the true inclination of the system, because the lack of strong X-ray eclipses provides an upper limit of $i < 65^{\circ}$. Our derived inclinations, from two orbits spaced ten months apart, are inconsistent with this upper limit at the $4\sigma - 5\sigma$ level.

To determine the efficacy of the BME model when data are phase-binned over many orbits, we construct mean polarization curves from K80, DT89, and our observations. The Stokes Q and U axes in DT89 are the same as in our observations; namely, Q points north-south on the sky, and U is oriented northeast-southwest. However, K80 define their Stokes Q axis at a position angle of 95° . Therefore, we rotate their Stokes curves (Q'_{K} and U'_{K}) by -95° :

$$Q_{\text{K}} = Q'_{\text{K}} \cos 190^{\circ} - U'_{\text{K}} \sin 190^{\circ} \quad (4.12a)$$

$$U_{\text{K}} = Q'_{\text{K}} \sin 190^{\circ} + U'_{\text{K}} \cos 190^{\circ}. \quad (4.12b)$$

Next, we re-wrap the curves of K80 and DT89 to the ephemeris used in our fits, which is from Gies et al. (2003: G03). From the ephemerides listed in Table 4.2, we derive the following conversions between the phases of K80 (ϕ_{K}), DT89 (ϕ_{DT}), and G03 (ϕ):

$$\phi = (1 + 3.05 \times 10^{-5})\phi_{\text{K}} - 0.137 \quad (4.13a)$$

$$\phi = (1 - 1.59 \times 10^{-5})\phi_{\text{DT}} - 7.17 \times 10^{-3}. \quad (4.13b)$$

We construct the mean polarization curves from both of our observing runs. This is equivalent to taking the mean for each q_i and u_i amplitude parameter in Table 4.2. Figure 4.8 shows the

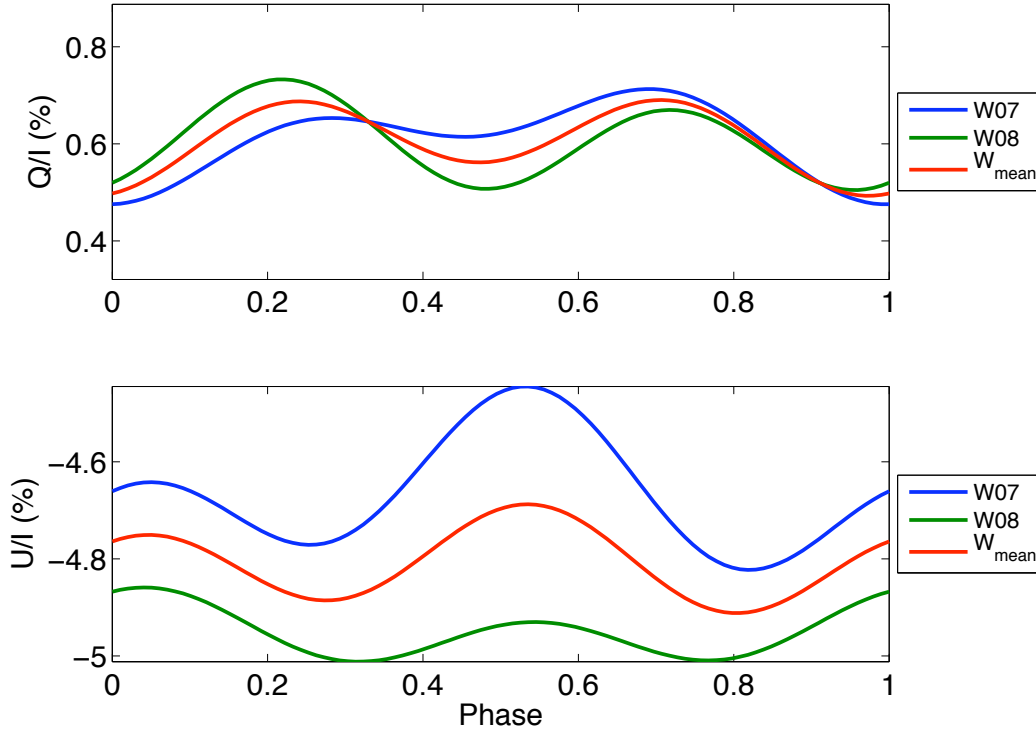


Figure 4.8: Polarimetric modulation observed in Aug 2007 and Jun 2008. The mean modulation from the two runs is also shown.

polarization curves from both runs as well as the curves obtained when taking their mean. We now take the mean Q, U versus phase across the data sets. Individual Q, U versus phase curves and their mean are shown in Figure 4.9. Plotting U versus Q throughout the orbit is used in the literature to get a sense of the distribution of scatterers as well as the presence of eclipses. While we do not use these curves to suggest the nature of the scattering, we nevertheless plot them in Figure 4.10. Our data show the strongest departure from ellipticity in the (Q, U) plane, which is explained by the fact that our data possess the largest ratio of the first to the second harmonic amplitudes of all three datasets ($p_{\text{I}}/p_{\text{II}}$ in Table 4.2). The K80 curves are re-wrapped to our ephemeris and rotated to our coordinate system, while the DT89 curves are re-wrapped to our ephemeris.

We then fit the mean curves according to Equations 4.4a and 4.4b, derive inclination from Equations 4.5a and 4.5b, and determine the position angle of the line of quadratures from Equations 4.6a through 4.6g. In addition, we re-derive these results from K80 and DT89 data (Table 4.2). With the addition of the K80 and DT89 data sets to our data (the “All” column in Table 4.2), we find that the inclination estimates decrease to the maximum allowable inclination set by the lack of observed X-ray eclipses. It is therefore tempting to speculate that the inclusion of all three data sets

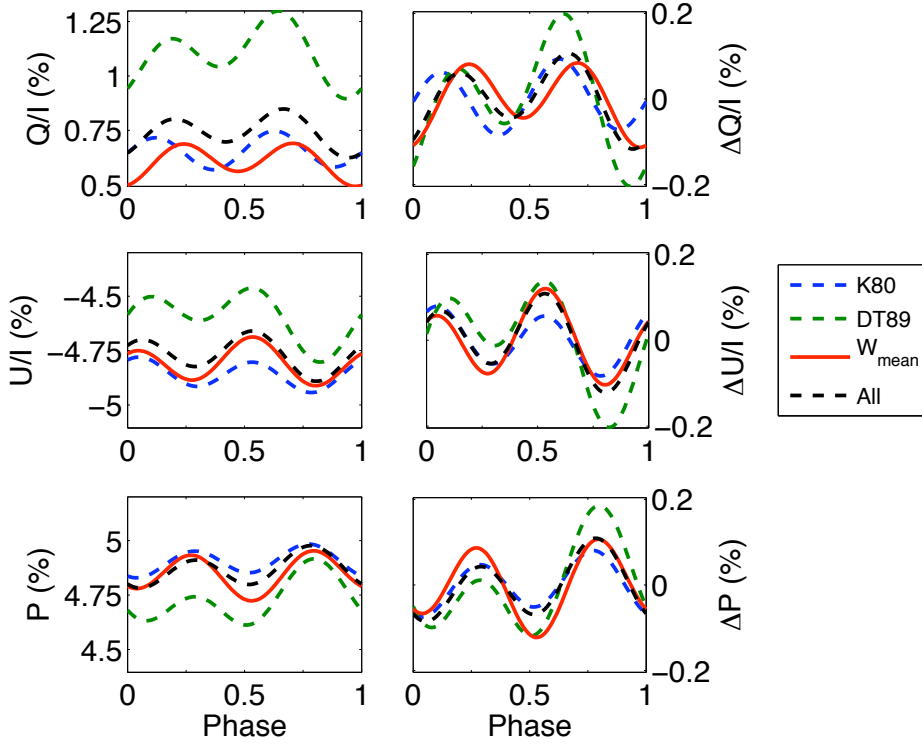


Figure 4.9: Cygnus X-1 polarimetric modulation from Kemp (1980: K80), Dolan & Tapia (1989: DT89), mean modulation from this work (W_{mean}), and mean modulation between all three data sets (“All”). Note the difference in scaling between absolute (Q, U, P) and relative $\Delta(Q, U, P)$ polarization.

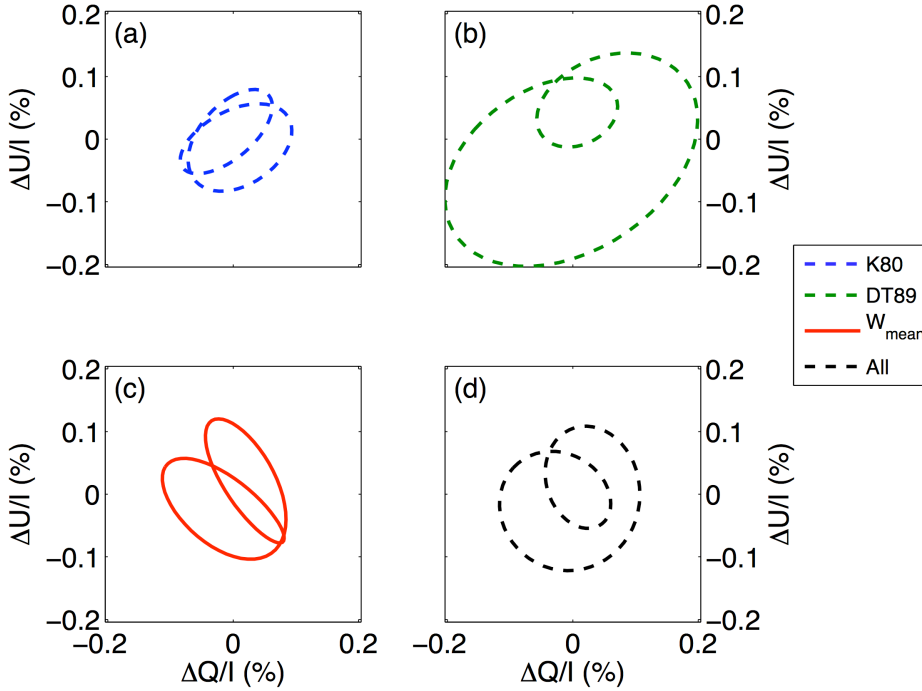


Figure 4.10: U versus Q for the data sets in Figure 4.9.

Table 4.4: Photometric, Precessional Modulation

Reference	MJD Range	ΔB_{orb} (mmag)	ΔB_{prec} (mmag)	$\Delta B_{\text{orb}}/\Delta B_{\text{prec}}$
Kemp et al. (1987)	42655 – 45318	48(3)	9.5(2.0)	5.1(1.1)
Brocksopp et al. (1999a)	50240 – 51100	28.60(78)	16.409(29)	1.733(47)

has averaged out stochastic changes in the polarization of Cygnus X-1 and produced the “mean” state of the system, which evidently lies near the maximum allowable inclination. However, it is unlikely that the addition of only three orbits to the ≈ 100 from K80 should unveil such a pristine mean state, regardless of the quality of those extra orbits. Since the overwhelming data set of K80 produces an unacceptably high inclination, due to lack of eclipses, we must conclude that the mean polarization curves from an arbitrary number of orbits cannot uncover a physically meaningful inclination estimate.

We are therefore left with the conclusion that the BME method fails in determining the inclination of Cygnus X-1, regardless of the combination of telescope aperture and observing duration. This is perhaps not surprising when the high degree of complexity of the system, with each part contributing to the total polarization signature, is considered:

- (1) The supergiant is tidally distorted
- (2) The circumbinary envelope is ionized
- (3) The focused stellar wind consists of ionized, Thomson scatterers and neutral, Rayleigh scatterers
- (4) The size of the accretion disk changes during the low/hard and high/soft states, and it may disappear altogether over an entire orbit
- (5) The strength of the focused stellar wind, the degree of ionization of all parts of the system, and the frequency of flaring change during the low/hard and high/soft states
- (6) The optical ellipsoidal modulation disappears (Brocksopp et al. 1999a) or becomes single-peaked (Voloshina et al. 1997) in the high/soft state
- (7) The accretion disk is inclined and precessing, and the dominant precession period is not stable on decadal timescales
- (8) The accretion disk rim likely contains a hot spot that is subject to flaring

Table 4.4 lists orbital and precessional modulation of the system photometry roughly 15 years

apart. There appears to be a significant increase in the amplitude of the precessional modulation compared to the orbital, ellipsoidal modulation between 1982 and 1996. This implies that either the accretion disk became brighter, the supergiant became fainter, or both occurred in this time interval. Karitskaya et al. (2006, hereafter K06) observe dimming of the system by $\Delta U = 65 \pm 3$, $\Delta B = 31 \pm 3$, and $\Delta V = 29 \pm 3$ mmag from 1997 to 2004. They also report cooling of the photosphere by $\Delta T_{\text{eff}} \approx 1,400$ K (from the HeI $\lambda 4713\text{\AA}$ line), from $T_{\text{eff}} = 31,800 \pm 500$ K to $T_{\text{eff}} = 30,400 \pm 500$ K, during this interval. Additionally, K06 show an increase in X-ray emission during the stellar dimming.

K06 interpret these observations in terms of a $\Delta R/R \approx 1 - 2\%$ increase in radius and resultant photospheric cooling. The increased radius increases accretion onto the black hole due to increased Roche lobe overflow. In addition, the lower photospheric temperature decreases the velocity of the radiatively-driven, focused stellar wind, which allows for more efficient accretion. A higher accretion rate is expected to increase the optical luminosity of the black hole due to increased X-ray reprocessing and inward migration of the inner radius of the accretion disk. Thus, the observations of Brocksopp et al. (1999a) were taken during a time when the supergiant was dimming and the accretion disk was brightening.

The accretion disk rotates by $\approx 360^\circ$ over one orbit about the angular momentum axis of the binary, since the precession period is much longer than the orbital period. Scattering of optical flux from the supergiant by the accretion disk therefore produces photometric and polarimetric modulation at the orbital frequency. Bochkarev & Karitskaya (1988a, hereafter BK88) model the amplitude of the polarimetric variability of the disk to be $\Delta P_{\text{disk}} \approx 0.25\%$, which is comparable to the observed variability of the system. However, Kemp et al. (1983, hereafter K83) observe the 294 day precessional period of the accretion disk in polarized light to only have amplitude $\Delta P_{\text{disk}} \approx 0.05\%$ from 1975 to 1983. This amplitude is 1/5 of that predicted by BK88.

BK88 further model that the second harmonic amplitude due to the disk should be $p_{\text{II,disk}} = 0.11\%$, and that the ratio of amplitudes of the first and second harmonics should be $(p_{\text{I}}/p_{\text{II}})_{\text{disk}} = 0.8$ for disk obliquity $i_{\text{disk}} < 20 - 30^\circ$. The observations of K80 exhibit $p_{\text{I}}/p_{\text{II}} = 0.24$ (Table 4.2), which is 1/3 of that calculated by BK88 for significant disk polarization. BK88 calculate the polarimetric variability of scattering by the accretion disk to therefore contribute $< 25 - 50\%$ of the observed variability. However, the observations of DT89 as well as our own (W07 and W08) show the strength

of the first harmonic to be $p_I/p_{II} > 0.8$ since June 1988, which is consistent with scattering by the accretion disk.

It should be noted that our W08 data set shows a first harmonic amplitude half of this value (Table 4.2), but the BME fit does not accurately model the large first harmonic modulation observed. That is, the zeroth through second order BME fit in Figure 4.2 underestimates the strength of the modulation near phase 0.05. Indeed, adding the $\Delta U \approx 0.05\%$ difference between model and data to u_I gives a ratio of $p_I/p_{II} = 0.81$. This suggests that the fractional polarization of the accretion disk increased during the 1980s and that it is currently significant. This is corroborated by the above result that the relative flux of the accretion disk has increased during that interval: the amplitude of photometric, precessional modulation is more than half the amplitude of photometric, orbital modulation. Since the dominant precessional period of the accretion disk also changed during this time (section 4.2.2), it appears the 1980s saw drastic changes in the accretion disk.

Cygnus X-1 is not the only high mass X-ray binary for which accretion disk polarization has been observed. Efimov et al. (1984) observe polarimetric modulation of the A7Ib supergiant/neutron star system SS 433 at both the 13 day orbital period as well as the 164 day precessional period of the inclined accretion disk. They observe the ratio of first to second harmonic amplitudes to be $p_I/p_{II} \approx 2.5$. This indicates that the contribution of the accretion disk polarization is significant.

We also observe an increase in mean polarization from $p_0 \equiv \sqrt{q_0^2 + u_0^2} = 4.71\%$ to $p_0 = 4.99\%$ (Table 4.2) in the ten months between the Aug 2007 and Jun 2008 runs. This $\Delta p_0 \approx 0.3\%$ increase is comparable to the amplitude of polarimetric orbital modulation. This is in contrast to the observations of K79, who observe a linear increase in mean system polarization of 1.8×10^{-6} per day, or an increase of only $\approx 0.06\%$ in ten months. Indeed, Dolan & Tapia (1992) also observe a change in mean polarization of only $\approx 0.05\%$ in the ten months between their observations (Sep 1987 to Jul 1988). However, they report that the amplitude of Stokes Q variability tripled in those ten months, while the amplitude in Stokes U was halved. Indeed, a χ^2 analysis of the two data sets shows them to be consistent at the $\alpha < 10^{-5}$ level of significance. Our Jun 2008 data are inconsistent with the polarization curves from the Aug 2007 observations: $\alpha_Q = 0$ ($\chi^2/n = 197/14$) and $\alpha_U = 0$ ($\chi^2/n = 2,721/14$). Thus, we confirm that the Cygnus X-1 system changes dramatically over a ten month time interval (≈ 50 orbits). It should be noted that the observations at phase 0.13 in Figure 4.2 correspond to the next orbit of the system, yet they appear to be consistent with the

observations from the first orbit. Therefore, we have weak evidence that the phase-locking of the system occurs over one to two orbits.

If the secular increase in system polarization seen by K79 is from variability in the ISM, one must conclude that the order of magnitude larger secular variability in our data is due to stochastic changes in the intrinsic polarization of the system. It is therefore likely that the degree of polarization of either the accretion stream, accretion disk, or both have increased in ten months. It is expected that ≈ 2.1 precessional periods, with 147 day period, have progressed in this time interval. The precessional phase of the accretion disk, and therefore the inclination of the disk to the line of sight, is expected to be similar between the two runs. Therefore, if the secular variability observed is due to the accretion disk, it must represent a change in the accretion disk as opposed to precession.

Given that the accretion disk represents a significant fraction of the polarimetric variability of Cygnus X-1, fluctuations in the disk are likely the cause of the stochastic noise seen by other polarimetrists. Bochkarev et al. (1998, hereafter B98) observe two large flares of $\Delta V_{\text{flare}} = 0.04$ mag of order one day duration coincident with dips in X-ray emission by 20%. Another flare exhibited a brightening in the *UBV* bands of $\Delta U_{\text{flare}} = 0.12$, $\Delta B_{\text{flare}} = 0.12$, and $\Delta V_{\text{flare}} = 0.02$. They assume this to be from optically thin hydrogen gas at $T = 20,000 \pm 10,000$ K, which indicates a hot spot in the accretion disk. The X-ray dips are thought to arise when the hot spot eclipses the X-ray source near the center of the disk (Karitskaya et al. 2000).

Poutanen et al. (2008, hereafter P08) observe the distribution of X-ray dips, of order one minute duration, versus disk precessional phase. Precessional phase $\Phi \equiv 0$ when the disk flux is at a minimum, and the precession period is now 151.43 days (Lachowicz et al. 2006). At precessional phase $\Phi = 0$, the disk is therefore closest to edge-on, and it is closest to face-on at $\Phi = 0.5$. P08 observe the X-ray dip distribution to peak at $\Phi \approx 0.05 - 0.1$, which is consistent with X-ray source occultation by a bulge located between the supergiant and black hole. The formation of the bulge at the disk rim results from the accretion stream impacting the disk, and P08 model the bulge location to lag behind the supergiant (as seen by the black hole), by $\phi_{\text{bulge}} \approx 25^\circ$. As the disk precesses, the bulge moves up and down, perpendicular to the orbital plane. This explains why dips are strong at precessional phase $\Phi \approx 0$ and weak at $\Phi \approx 0.5$. Occultation in the disk correlated with precessional phase is also suggested by optical polarimetric observations. Indeed, Kemp et al. (1983: K83) suggest that the non-sinusoidal modulation is caused by partial eclipsing of the polarized light from the disk at certain precessional phases.

Therefore, the perhaps *ad hoc* suggestion by Kemp et al. (1979: K79) of an occulted, scattering spot located at the intersection of disk and accretion stream (section 4.5.5) now seems to have some merit. However, it should be noted that this model was suggested on the basis of the non-elliptical locus in (Q, U) space from K79, which appears similar to our own data (Figure 4.10c). As noted before, Simmons et al. (1980: S80) successfully fit the data of K79 by the BME model without requiring the scattering spot of K79. However, the BME model does not accurately represent the physical state of Cygnus X-1, and the scattering spot model may still have some merit in light of the observations of DT89 as well as our own.

In addition to disk occultation on the precessional period, there is a wealth of evidence that X-ray dips also occur near orbital phase $\phi \approx 0$, when the black hole is in superior conjunction (Li & Clark 1974; Mason et al. 1974; Parsignault et al. 1976a, b; Pravdo et al. 1980; Remillard & Canizares 1984; Kitamoto et al. 1989; Balucinska-Church et al. 2000; Feng & Cui 2002; P08). The occulting material in this case is thought to be neutral material in the accretion stream. Kitamoto & Miyamoto (1984, hereafter KM84) observe the X-ray spectrum of the source during an X-ray dip in the low/hard state, and they see the K-absorption edge of iron at $E = 7.18 \pm 0.18$ keV (90% confidence interval). This is interpreted to arise from weakly ionized Fe VI or less, implying a temperature of $T < 30,000$ K. This suggests most elements present in the stream are effectively neutral. The decrease in orbital, polarimetric modulation with increasing wavelength observed by Wolinski et al. (1996: W96, see section 4.5.5) suggests that such neutral material in the accretion stream comprises a significant component to the polarimetric variability of the system.

Absence of the iron emission line implies a small occulting blob size, and KM84 estimate it to be of order $d_{\text{blob}} = 10^9$ cm in length. The presence of short X-ray dips, of $t \approx 2$ s duration, suggests an upper limit to the size of the X-ray source of $d_{\text{X-ray}} < 4 \times 10^8$ cm. Ibragimov et al. (2005) fit the X-ray spectrum for column density and find that it increases near orbital phase $\phi = 0$. This result adds weight to the theory that X-ray dips at superior conjunction of the black hole are due to occultation of the X-ray source by the focused stellar wind. Therefore, Brocksopp et al. (1999a, hereafter B99) suggest that the observed orbital modulation of radio and X-ray emission is due to absorption by the focused stellar wind, while the ultraviolet, optical, and near-IR modulation is due to the ellipsoidal modulation of the supergiant (section 4.2.2).

The complexity in the Cygnus X-1 system is very high, even during the fiducial low/hard state.

During the high/soft state, additional events are introduced. Natali et al. (1978) observe photometric flickering of $\Delta V = 0.06 - 0.10$ mag over ≈ 30 min timescales during this state, which is one to two times the strength of the orbital, ellipsoidal modulation. One might therefore expect the polarimetric flickering during the high/soft state to be dramatic.

The disappearance of observed orbital modulation in the radio and X-rays during this state (B99), as well as the single-peaked (Voloshina et al. 1997) or nonexistent (B99) optical lightcurve, suggest that dramatic changes in Cygnus X-1 occur in the high/soft state. On the grounds that the photometric contribution of the accretion disk is only $\approx 3\%$ during the low/hard state (Bruevich et al. 1978, see section 4.5.6) B99 claim that the increased optical output in the high/soft state is not completely due to a brighter accretion disk. They suggest that the hemisphere of the supergiant facing the black hole as well as the accretion stream become brighter due to increased irradiation by the X-ray source. The absence of orbital modulation in the radio is attributed to the disappearance of jets, while increased X-ray flaring overwhelms the orbital modulation in X-rays.

4.7 Conclusion

The enhanced sensitivity to asymmetry in a system from polarimetry over photometry provides geometric information that is difficult to determine with any other method. However, the exorbitant number of free parameters, and the large number of significant and variable polarization sources in Cygnus X-1, causes difficulty in polarimetric modeling of the system. Others have claimed that the scattering model of Brown et al. (1978: BME) can accurately determine the inclination of binary systems from polarimetry. These claims generally result from the agreement of BME-derived inclinations with inclinations derived from eclipses. However, we note that inclinations derived by this model are systematically higher (towards edge-on geometries) than those determined by other methods. Therefore, the true inclination of eclipsing binaries will be derived from the BME model simply from biases in the model.

Cygnus X-1 inclinations determined both by monitoring of order 100 orbits with a small telescope and large telescope monitoring of individual orbits are consistently higher than allowed by the lack of X-ray eclipses. Therefore, the scattering model of BME is not applicable to the Cygnus X-1 system, and it may not be applicable to most binary systems as well. Previous authors have attributed the

failure of the BME model to produce physically plausible inclinations to low signal-to-noise data. However, our high precision observations (night-to-night polarimetric precision of one part in 10^4) refute this hypothesis: the BME model cannot produce the true inclination of the system, regardless of the number of nights and telescope aperture.

The critical assumptions of the BME model are single scattering in a phase-locked system. Our observations spaced ten months apart confirm the finding by Wolinski et al. (1996) that the polarization of the Cygnus X-1 system varies on orbital timescales. Indeed, phase-locking of similar systems is also known to occur over one to ten orbits (Dolan & Tapia 1984, 1988). The cause of this stochastic variability is unknown, but variable accretion rate and flaring in the Cygnus X-1 disk contribute significantly. Scattering of the flux from the supergiant by the optically thick accretion disk, which is inclined and precessing with a 147 day period, must also contribute to the long-term variability of the system. Indeed, the precession period and brightness of the accretion disk also seem to be variable on decadal timescales.

It is unlikely that polarimetry will meaningfully constrain the mass of the black hole in Cygnus X-1. A more promising method is the scaling of quasi-period oscillation (QPO) frequency between this black hole and others of known mass (Titarchuk & Fiorito 2004). Indeed, Shaposhnikov & Titarchuk (2007) have successfully predicted the mass of the GRS 1915+105 black hole with this technique, and they estimate the black hole in Cygnus X-1 to be $M_{\text{BH}} = 8.7 \pm 0.8 M_{\odot}$. However, the failure of polarimetry in determining the mass of black holes in high mass X-ray binaries results from the fact that they are too sensitive to asymmetry in the system. When applied to extrasolar planets, polarimetric monitoring provides geometric information that cannot be determined from other methods. The future of polarimetry in this field looks bright indeed. In an attempt to describe the atmospheres of extrasolar planets, the next chapter investigates the stability of liquid water oceans in so-called “hot Neptunes”.

References

- Abubekerov, M. K., Antokhina, E. A., & Cherepashchuk, A. M. 2004, *Astron. Rep.* 48, 550.
- Albert, J., Aliu, E., Anderhub, H., Antoranz, P., Armada, A., Baixeras, C., Barrio, J. A., Bartko,

- H., Bastieri, D., Becker, J. K., Bednarek, W., Berger, K., Bigongiari, C., Biland, A., Bock, R. K., & 125 coauthors. 2007, *ApJ* 665, L51.
- Angel, J. R. P. 1969, *ApJ* 158, 219.
- Aspin, C. & Simmons, J. F. L. 1982, *MNRAS* 199, 601.
- Aspin, C., Simmons, J. F. L., & Brown, J. C. 1981, *MNRAS* 194, 283.
- Avery, R. W., Stokes, R. A., Michalsky, J. J., & Ekstrom, P. A. 1975, *AJ* 80, 1026.
- Balog, N. I., Goncharkii, A. V., & Cherepashchuk, A. M. 1981, *SvA* 25, 38.
- Balona, L. A., Egan, J., & Marang, F. 1989, *MNRAS* 240, 103.
- Balucinska-Church, M., Belloni, T., Church, M. J., & Hasinger, G. 1995, *A&A* 302, L5.
- Balucinska-Church, M., Church, M. J., Charles, P. A., Nagase, F., LaSala, J. & Barnard, R. 2000, *MNRAS* 311, 861.
- Barrett, P. 1996, *PASP* 108, 412.
- Batten, A. H. 1967, *Pub. Dom. Ap. Obs.* 13, 8.
- Berdyugin, A. & Piirola, V. 2002, *A&A* 394, 181.
- Bochkarev, N. G. & Karitskaya, E. A. 1988a, *Adv Sp Res* 8, 205 (BK88).
- Bochkarev, N. G., Karitskaya, E. A., & Shakura, N. I. 1975, *SvAL* 1, 118.
- Bochkarev, N. G., Karitskaya, E. A., Syunyaev, R. A., & Shakura, N. I. 1979, *SvAL* 5, 99.
- Bochkarëv, N. G., Karitskaya, E. A., Loskutov, V. M. & Sokolov, V. V. 1986, *SvA* 30, 43.
- Bochkarev, N. G., Karitskaya, E. A., & Lyuty, V. M. 1998, *IAU Symp.* 188, 384 (B98).
- Bolton, C. T. 1972, *Nature* 235, 271.
- Bolton, C. T. 1975, *ApJ* 200, 269.
- Bondi, H. & Hoyle, F. 1944, *MNRAS* 104, 273.
- Brockopp, C., Fender, R. P., Larionov, V., Lyuty, V. M., Tarasov, A. E., Pooley, G. G., Paciesas, W. S., & Roche, P. 1999a, *MNRAS* 309, 1063 (B99).
- Brockopp, C., Tarasov, A. E., Lyuty, V. M., & Roche, P. 1999b, *A&A* 343, 861.
- Brown, J. C., McLean, I. S., & Emslie, A. G. 1978, *A&A* 68, 415 (BME).

- Bruevich, V. V., Kilyachkov, N. N., Syunyaev, R. A., & Shevchenko, V. S. 1978, SvAL 4, 292.
- Castor, J. I., Abbott, D. C., & Klein, R. I. 1975, ApJ 195, 157.
- Cherepashchuk, A. M. 1975, SvA 19, 47.
- Daniel, J. Y. 1980, A&A 86, 198.
- Daniel, J.-Y. 1981, A&A 94, 121 (D81).
- Davis, A. B., Moffat, A. F. J., & Niemela, V. S. 1981, ApJ 244, 528.
- Davis, R., & Hartmann, L. 1983, ApJ 270, 671.
- De Greve, J. P., Hellings, P., & van den Heuvel, E. P. J. 1988, A&A 189, 74.
- Di Salvo, T., Done, C., Zycki, P. T., Burderi, L., & Robba, N. R. 2001, ApJ 547, 1024.
- Dolan, J. F. 1984, A&A 138, 1.
- Dolan, J. F. & Tapia, S. 1984, A&A 139, 249.
- Dolan, J. F. & Tapia, S. 1988, A&A 202, 124.
- Dolan, J. F. & Tapia, S. 1989, ApJ 344, 830 (DT89).
- Dolan, J. F. & Tapia, S. 1992, ApJ 384, 249 (DT92).
- Dolan, J. F., Coe, M. J., Crannell, C. J., Dennis, B. R., Frost, K. J., Orwig, L. E., & Caraveo, P. 1979, Nature 280, 126.
- Drissen, L., Lamontagne, R., Moffat, A. F. J., Bastien, P. & Seguin, M. 1986a, ApJ 304, 188.
- Drissen, L., Moffat, A. F. J., Bastien, P., Lamontagne, R., & Tapia, S. 1986b, ApJ 306, 215.
- Efimov, Y. S., Piirola, V., & Shakhovskoy, N. M. 1984, A&A 138, 62.
- Esin, A. A., Narayan, R., Cui, W., Grove, J. E., & Zhang, S.-N. 1998, ApJ 505, 854.
- Fabregat, J., Reglero, V., Coe, M. J., Clement, R., Gorrod, M. J., Norton, A. J., Roche, P. D., Suso, J., & Unger, S. J. 1992, A&A 259, 522.
- Fender, R. P., Stirling, A. M., Spencer, R. E., Brown, I., Pooley, G. G., Muxlow, T. W. B., & Miller-Jones, J. C. A. 2006, MNRAS 369, 603.
- Feng, Y. X. & Cui, W. 2002, ApJ 564, 953.
- Fosalba, P., Lazarian, A., Prunet, S., & Tauber, J. A. 2002, ApJ 564, 762.

- Friend, D. B. & Castor, J. I. 1982, *ApJ* 261, 293.
- Frontera, F., Palazzi, E., Zdziarski, A. A., Haardt, F., Perola, G. C., Chiappetti, L., Cusumano, G., Dal Fiume, D., Del Sordo, S., Orlandini, M., Parmar, A. N., Piro, L., Santangelo, A., Segreto, A., Treves, A., & Trifoglio, M. 2001, *ApJ* 546, 1027.
- Gallo, E., Fender, R., Kaiser, C., Russell, D., Morganti, R., Oosterloo, T., & Heinz, S. 2005, *Nature* 436, 819.
- Gehrels, T. 1972, *ApJ* 173, L23.
- Gierliński, M., Zdziarski, A. A., Done, C., Johnson, W. N., Ebisawa, K., Ueda, Y., Haardt, F., & Philips, B. F. 1997, *MNRAS* 288, 958.
- Gies, D. R. & Bolton, C. T. 1982, *ApJ* 260, 240.
- Gies, D. R. & Bolton, C. T. 1986a, *ApJ* 304, 371.
- Gies, D. R. & Bolton, C. T. 1986b, *ApJ* 304, 389.
- Gies, D. R., Bolton, C. T., Thomson, J. R., Huang, W., McSwain, M. V., Riddle, R. L., Wang, Z., Wiita, P. J., Wingert, D. W., Csák, B., & Kiss, L. L. 2003, *ApJ* 583, 424 (G03).
- Gnedin, Y. N. & Silant'ev, N. A. 1980, *SvAL* 6, 344.
- Gnedin, Y. N., Borisov, N. V., Natsvlshvili, T. M., Piotrovich, M. Y., & Silant'ev, N. A. 2003, arXiv:0304158v1 (Gn 03).
- Greene, J., Bailyn, C. D., & Orosz, J. A. 2001, *ApJ* 554, 1290.
- Greiner, J. Cuby, J. G. & McCaughrean, M. J. 2001, *Nature* 414, 522 (G01).
- Guinan, E. F., Dorren, J. D., Siah, M. J., & Koch, R. H. 1979, *ApJ* 299, 296.
- Herrero, A. Kudritzki, R. P., Gabler, R., Vilchez, J. M., & Gabler, A. 1995, *A&A* 297, 556.
- Hiltner, W. A. & Mook, D. E. 1966, *ApJ* 143, 1008.
- Ho, C. & Arons, J. 1987, *ApJ* 316, 283.
- Holt, S. S., Kaluzienski, L. J., Boldt, E. A., & Serlemitsos, P. J. 1976, *Nature* 261, 215.
- Holt, S. S., Kaluzienski, L. J., Boldt, E. A., & Serlemitsos, P. J. 1979, *ApJ* 233, 344.
- Horn, J., Hubert, A. M., Hubert, H., Koubsky, P., & Bailloux, N. 1992, *A&A* 259, L5.
- Hutchings, J. B. 1974, *ApJ* 188, 341.

- Hutchings, J. B. 1978, *ApJ* 226, 264.
- Hutchings, J. B., Crampton, D., Glaspey, J., & Walker, G. A. H. 1973, *ApJ* 182, 549.
- Ibragimov, A., Poutanen, J., Gilfanov, M., Zdziarski, A. A., & Shrader, C. R. 2005, *MNRAS* 362, 1435.
- Ibragimov, A., Zdziarski, A. A., & Poutanen, J. 2007, *MNRAS* 381, 723.
- Iorio, L. 2007, arXiv: 0707.3525 (I07).
- Jensen, E. L. N. & Mathieu, R. D. 1997, *AJ* 114, 301.
- Kallman, T. R. & White, N. E. 1982, *ApJ* 261, L35.
- Karitskaya, E. A. 1979, *Astron. Tsirk. No.* 1088, 1.
- Karitskaya, E. A. & Bochkarev, N. G. 1989, in *Variable Phenomena in Close Binary Stars*, Communications from the Konkoly Observatory of the Hungarian Academy of Sciences 10, No. 93, ed. L. Patkós (Budapest), p. 255.
- Karitskaya, E. A. & Goranskij, V. P. 1996, *IAU* 4404, 1.
- Karitskaya, E. A. & Goranskii, V. P., Grankin, K. N., & Mel'nikov, S. Y. 2000, *Astron Lett* 26, 22.
- Karitskaya, E. A., Voloshina, I. B., Goranskii, V. P., Grankin, K. N., Dzhaniashvili, É. B., Ezhkova, O. V., Kochiashvili, N. T., Kumsiashvili, M. I., Kusakin, A. V., Lyutyi, V. M., Mel'nikov, S. Y., Metlova, N. V. 2001, *Astron Rep* 45, 350.
- Karitskaya, E. A., Lyuty, V. M., Bochkarev, N. G., Shimanskii, V. V., Tarasov, A. E., Bondar, A. V., Galazutdinov, G. A., Lee, B.-C., & Metlova, N. V. 2006, *IAU* 5678, 1 (K06).
- Kartasheva, T. A. 2002b, *Bull. Spec. Astrophys. Obs.* 54, 56.
- Kartje, J. F. & Königl, A. 1991, *ApJ* 375, 69.
- Kemp, J. C. 1980a, *ApJ* 235, 595.
- Kemp, J. C. 1980b, *A&A* 91, 108 (K80).
- Kemp, J. C. 1983, *IAU Circ.* 3780.
- Kemp, J. C. & Herman, L. C. 1977, *ApJ* 218, 770.
- Kemp, J. C., Southwick, R. G., & Rudy, R. J. 1976, *ApJ* 210, 239.
- Kemp, J. C., Barbour, M. S., Herman, L. C. & Rudy, R. J. 1978a, *ApJ* 220, L123 (K78).

- Kemp, J. C., Herman, L. C., & Barbour, M. S. 1978b, *AJ* 83, 962.
- Kemp, J. C., Barbour, M. S., Parker, T. E., & Herman, L. C. 1979, *ApJ* 228, 23 (K79).
- Kemp, J. C., Barbour, M. S., Henson, G. D., Kraus, D. J., Nolt, I. G., Radostitz, J. V., Priedhorsky, W. C., Terrell, J., & Walker, E. N. 1983, *ApJ* 271, 65 (K83).
- Kemp, J. C., Karitskaya, E. A., Kumsiashvili, M. I., Lyutyi, V. M., Khruzina, T. S., & Cherepashchuk, A. M. 1987, *SvA* 31, 170.
- Khaliullina, A. I. & Khaliullin, K. F. 1981, *SvA* 25, 593.
- Kitamoto, S. & Miyamoto, S. 1984, *PASJ* 36, 731 (KM84).
- Kitamoto, S., Miyamoto, S., & Yamamoto, T. 1989, *PASJ* 41, 81.
- Kitamoto, S., Egoshi, W., Miyamoto, S., Tsunemi, H., Ling, J. C., Wheaton, W. A., & Paul, B. 2000, *ApJ* 531, 546.
- Kron, G. E. & Gordon, K. C. 1950, *ApJ* 111, 454.
- Kruszewski, A. 1972, *Acta Astron.* 22, 405.
- Lachowicz, P., Zdziarski, A. A., Schwarzenberg-Czerny, A., Pooley, G. G., & Kitamoto, S. 2006, *MNRAS* 368, 1025 (L06).
- Lamontagne, R. & Moffat, A. F. J. 1987, *AJ* 94, 1008.
- Lamontagne, R., Moffat, A. F. J., Drissen, L., Robert, C., & Matthews, J. M. 1996, *AJ* 112, 2227.
- Leahy, D. A. & Ananth, A. G. 1992, *MNRAS* 256, 39.
- Lester, D. F., Nolt, I. G., & Radostitz, J. V. 1973, *Nature Phys. Sci.* 214, 125.
- Leung, K.-C., Moffat, A. F. J., & Seggewiss, W. 1983, *ApJ* 265, 961.
- Li, F. K. & Clark, G. W. 1974, *ApJ* 191, L27.
- Lipunova, N. A. 1982, *SvAL* 8, 128.
- Lipunova, N. A. & Cherepashchuk, A. M. 1982, *AZh* 59, 73.
- Long, K. S., Chanan, G. A., & Novick, R. 1980, *ApJ* 238, 710.
- Luna, H. C. 1982, *PASP* 94, 695.
- Lyutyi, V. M. 1985, *SvA* 29, 429.

- Lyutyj, V. M., Sunyaev, R. A., & Cherepashchuk, A. M. 1973, SvA 17, 1.
- Manchanda, R. K. 1983, *Astrophys. Space Sci.* 91, 455.
- Manchanda, R. K. 2001, *J. Astrophys. Astr.* 22, 9.
- Manset, N. & Bastien, P. 2001, *AJ* 122, 3453.
- Manset, N. & Bastien, P. 2003, *AJ* 125, 3274.
- Martin, P. G. 1974, *ApJ* 187, 461.
- Mason, K. O., Hawkins, F. J., Sanford, P. W., Murdin, P., & Savage, A. 1974, *ApJ* 192, L65.
- Massey, P. 1981, *ApJ* 244, 157.
- Massey, P., & Conti, P. S. 1981a, *ApJ* 244, 169.
- Massey, P. & Niemela, V. S. 1981, *ApJ* 245, 195.
- Massey, P., Conti, P. S., & Niemela, V. S. 1981, *ApJ* 246, 145.
- Mathewson, D. S. & Ford, V. L. 1970, *Mem. RAS* 74, 139.
- McLean, I. S. 1980, *ApJ* 236, 149.
- Merril, J. E. 1963, in *Photoelectric Astronomy for Amateurs*, ed. F. B. Wood. Macmillan, New York, p. 176.
- Metzger, A. E. & Dolan, J. F. 1968, *AJ* 73, 107.
- Michalsky, J. J. & Swedlund, J. B. 1977, *ApJ* 212, 221.
- Michalsky, J. J., Swedlund, J. B., & Avery, R. W. 1975a, *Nature* 254, 39.
- Michalsky, J. J., Swedlund, J. B., & Stokes, R. A. 1975b, *ApJ* 198, L101.
- Milgrom, M. 1978, *A&A* 65, L1.
- Miller, J. M., Fabian, A. C., Wijnands, R., Remillard, R. A., Wojdowski, P., Schulz, N. S., Di Matteo, T., Marshall, H. L., Canizares, C. R., Pooley, D. & Lewin, W. H. G. 2002, *ApJ* 578, 348.
- Miller, J. M., Wojdowski, P., Schulz, N. S., Marshall, H. L., Fabian, A. C., Remillard, R. A., Wijnands, R., & Lewin, W. H. G. 2005, *ApJ* 620, 398.
- Moffat, A. F. J. & Seggewiss, E. 1987, *ESO Messenger* No. 49, 26.

- Moffat, A. F. J. & Shara, M. M. 1986, AJ 92, 952.
- Moffat, A. F. J., Niemela, V. S., & Marraco, H. 1990a, ApJ 348, 232.
- Moffat, A. F. J., Drissen, L., Robert, C., Lamontagne, R., Coziol, R., Mousseau, N., Niemela, V. S., Cerruti, M. A., Seggewiss, W., & van Weeren, N. 1990b, ApJ 350, 767.
- Nadzhip, A. E., Khruzina, T. S., Cherepashchuk, A. M., & Shenavrin, V. I. 1996, Astron. Rep. 40, 338.
- Nagae, O., Kawabata, K. S., Fukazawa, Y., Okazaki, A., & Isogai, M. 2008, AIPC 968, 328.
- Natali, G., Fabrianesi, R. & Messi, R. 1978, 62, L1.
- Niemela, V. S. 1982, IAU Symp 99, 299.
- Niemela, V. S. 1995, IAU Symp 163, 223.
- Niemela, V. S., Massey, P., & Conti, P. S. 1984, PASP 96, 549.
- Niemela, V. S., Mandrini, C. H., & Méndez, R. H. 1985, Rev Mex Astron Astr 11, 143.
- Ninkov, Z., Walker, G. A. H., & Yang, S. 1987a, ApJ 321, 425.
- Ninkov, Z., Walker, G. A. H., & Yang, S. 1987b, ApJ 321, 438.
- Nolt, I. G., Kemp, J. C., Rudy, R. J., Southwick, R. G., Radostitz, J. V., & Caroff, L. J. 1975, ApJ 199, L27.
- Norton, A. J., Coe, M. J., Estela, A., Fabregat, J., Gorrod, M. J., Kastner, J., Payne, B. J., Reglero, V., Roche, P., & Unger, S. J. 1991, MNRAS 253, 579.
- Özdemir, S. & Demircan, O. 2001, Astron. Space Sci 278, 319.
- Paciesas, W. S., Robinson, C. R., McCollough, M. L., Zhang, S. N., Harmon, B. A., & Wilson, C. A. 1997, AIPC 410, 834.
- Parsignault, D. R., Epstein, A., Grindlay, J., Schreier, E., Schnopper, H., Gursky, H., Brinkman, A. C., Heise, J., Schrijver, J., & Tanaka, Y. 1976a, Ap&SS 42, 175.
- Parsignault, D. R., Grindlay, J. E., Schnopper, H., Schreier, E. J., & Gursky, H. 1976b, in *X-ray Binaries*, eds. E. Boldt & Y. Kondo. National Technical Information Service, Springfield, p. 429.
- Phillips, K. C. & Mészáros, P. 1986, ApJ 310, 284.

- Pirola, V. & Linnaluoto, S. 1988, in *Polarized Radiation of Circumstellar Origin*, ed. G. V. Coyne et al. Vatican Observatory, Vatican, p. 655.
- Pirola, V., Berdyugin, A., Mikkola, S., & Coyne, G. V. 2005, *ApJ* 632, 576.
- Pooley, G. G., Fender, R. P., & Brocksopp, C. 1999, *MNRAS* 302, L1.
- Poutanen, J. 1998, in *Theory of Black Hole Accretion Discs*, eds. Abramowicz, M., Björnsson, G., Pringle, J. Cambridge Univ. Press, Cambridge, p. 100.
- Poutanen, J., Zdziarski, A. A., & Ibragimov, A. 2008 arXiv:0802.1391v1 (P08).
- Pravdo, S. H., White, N. E., Becker, R. H., Kondo, Y., Boldt, E. A., Holt, S. S., Serlemitsos, P. J., & McCluskey, G. E. 1980, *ApJ* 327, L71.
- Priedhorsky, W. C., & Terrell, J. 1982, *BAAS* 14, 618.
- Priedhorsky, W. C., Terrell, J., & Holt, S. S. 1983, *ApJ* 270, 233.
- Priedhorsky, W. C., Brandt, S., & Lund, N. 1995, *A&A* 300, 415.
- Pringle, J. E., & Rees, M. J. 1972, *A&A* 21, 1.
- Remillard, R. A. & Canizares, C. R. 1984, *ApJ* 278, 761.
- Robert, C., Moffat, A. F. J., Bastien, P., St.-Louis, N., & Drissen, L. 1990, *ApJ* 359, 211.
- Roche, P., Larionov, V., Tarasov, A. E., Fabregat, J., Clark, J. S., Coe, M. J., Kalv, P., Larionova, L., Negueruela, I., Norton, A. J., & Reig, P. 1997, *A&A* 322, 139.
- Rudy, R. J. & Herman, L. C. 1978, *PASP* 90, 163.
- Rudy, R. J. & Kemp, J. C. 1978, *ApJ* 221, 200.
- Russell, D. M., Fender, R. P., Gallo, E., & Kaiser, C. R. 2007, *MNRAS* 376, 1341.
- Sculte-Ladbeck, R. E. & van der Hucht, K. A. 1989, *ApJ* 337, 872.
- Seggewiss, W. 1974, *A&A* 31, 211.
- Serkowski, K., Mathewson, D. S., & Ford, V. L. 1975, *ApJ* 196, 261.
- Severny, A. B. & Kuvshinov, V. M. 1975, *ApJ* 200, L13.
- Shakhovskoi, N. M. 1965, *SvA* 8, 833.
- Shakura, N. I. & Syunyaev, R. A. 1973, *A&A* 24, 337.

- Shapiro, S. L., Lightman, A. P., & Eardley, D. M. 1976, ApJ 204, 187.
- Shaposhnikov, N. & Titarchuk, L. 2007, ApJ 663, 445 (ST07).
- Simmons, J. F. L., Aspin, C., & Brown, J. C. 1980, A&A 91, 97 (S80).
- Simmons, J. F. L., Aspin, C., & Brown, J. C. 1982, MNRAS 198, 45.
- Sowers, J. W., Gies, D. R., Bagnuolo, W. G., Jr., Shafter, A. W., Wiemker, R., & Wiggs, M. S. 1998, ApJ 506, 424.
- St.-Louis, N., Drissen, L., Moffat, A. F. J., & Bastien, P. 1987, ApJ 322, 870.
- St.-Louis, N., Moffat, A. F. J., Drissen, L., Bastien, P., & Robert, C. 1988, ApJ 330, 286.
- Stevens, I. R. 1991, ApJ 379, 310.
- Stickland, D. J., Bromage, G. E., Budding, E., Burton, W. M., Howarth, I. D., Jameson, R., Sherrington, M. R., & Willis, A. J. 1984, A&A 134, 45.
- Stirling, A. M., Spencer, R. E., de la Force, C. J., Garrett, M. A., Fender, R. P., & Ogle, R. N. 2001, MNRAS 327, 1273.
- Sunyaev, R. A. & Titarchuk, L. G. 1985, A&A 143, 374.
- Syunyaev, R. A. & Trümper, J. 1979, Nature 279, 506.
- Titarchuk, L. & Fiorito, R. 2004, ApJ 612, 988 (TF04).
- Villar-Sbaffi, A., St-Louis, N., Moffat, A. F. J., & Piirola, V. 2006, ApJ 640, 995.
- Voloshina, I. B., Lyuty, V. M., & Tarasov, A. E. 1997, SvA 23, 3.
- Walborn, N. R. 1973, ApJ 179, L123.
- Walker, E. N. 1972, MNRAS 160, 9P.
- Webster, B. L. & Murdin, P. 1972, Nature 235, 37.
- Wen, L., Cui, W., Levine, A. M. & Bradt, H. V. 1999, ApJ 525, 968.
- White, N. E., Kallman, T. R., & Swank, J. H. 1983, ApJ 269, 264.
- Wilking, B. A., Lebofsky, M. J., Kemp, J. C., Martin, P. G., & Rieke, G. H. 1980, ApJ 235, 905.
- Wolinski, K. G. & Dolan, J. F. 1994, MNRAS 267, 5 (WD94).
- Wolinski, K. G., Dolan, J. F., Boyd, P. T., Biggs, J. D., Nelson, M. J., Percival, J. W., Taylor, M., & van Citters, G. W. 1996, ApJ 457, 859 (W96).

- Zdziarski, A. A. & Gierliński, M. 2004, *Prog. Theor. Phys. Suppl.* 155, 99.
- Zdziarski, A. A., Gierliński, M., Gondek, D., & Magdziarz, P. 1996, *A&AS* 120, 553.
- Zdziarski, A. A., Johnson, W. N., Poutanen, J., Magdziarz, P., & Gierliński, 1997, in *The Transparent Universe, Proc. 2nd INTEGRAL Workshop*, eds. C. Winkler, T. J.-L. Courvoisier, & P. Durouchoux. ESA Publications Division, Noordwijk, p. 373.
- Zhang, S. N., Robinson, C. R., & Cui, W. 1996, *IAU Circ.* 6510.
- Ziólkowski, J. 2005, *MNRAS* 358, 851.

Chapter 5

Liquid Water Oceans in Ice Giants

5.1 Introduction

Water is spectroscopically undetectable in both Uranus and Neptune; its saturated mixing ratio in their cold photospheres is less than 10^{-25} . However, the compressed, deep interior density of these planets is strikingly close to that of pure water (Hubbard 1999). Additionally, successful density models require an ice to rock mass ratio greater than unity (Hubbard et al. 1995) and gas comprising less than 18% of the planet’s mass (Podolak et al. 2000). When addressing planetary mass, we take “gas” to mean hydrogen and helium, and we assume “ice” consists of water ice as well as methane, ammonia, and hydrogen sulfide. There is evidence based on CO observations that the enhancement of oxygen in Neptune’s atmosphere with respect to the solar value is larger than that for carbon, nitrogen, and sulfur (Lodders & Fegley 1994). Since oxygen is the most abundant element in the solar system next to hydrogen and helium, water is thought to be the dominant component of ice in the outer solar system. Thus, there must be a significant water reservoir in Uranus and Neptune. Indeed, there has been speculation about oceans” in their deep interiors (Atreya 1986, p. 64; Hubbard et al. 1995), but these oceans” describe ionic phase transitions at thousands of degrees Kelvin.

We explore the necessary conditions for bona fide liquid water-hydrogen oceans to exist in the upper interior of Neptune, where pressure is less than about 20 kbar and temperature is less than about 800 K. We define the word “ocean” to mean a body with an interface between a hydrogen-rich, saturated vapor and a water-rich, liquid ocean. We set up favorable conditions for an extant Neptunian water ocean to show that its existence is unlikely: water, hydrogen, and helium are assumed to be well mixed in the interior of the planet, and we assume a saturated (moist) water adiabat

¹This chapter has been published as Wiktorowicz, S. J. & Ingersoll, A. P. 2007, *Icarus* 186, 436.

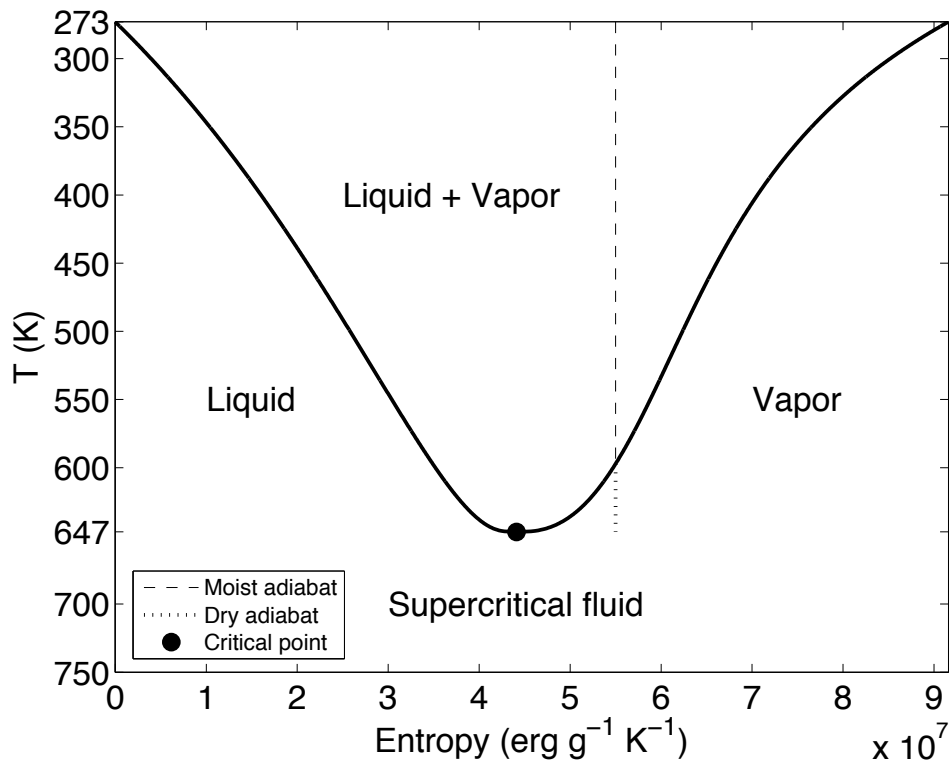


Figure 5.1: Temperature-entropy curve for pure water. Note that an adiabat is a vertical line in this diagram and that temperature is shown increasing downward.

descends from the photosphere. The photospheric adiabat and the interior adiabat join at a phase boundary that is either a cloud base or an ocean surface. The temperature-entropy diagram for pure water (Figure 5.1) provides a qualitative illustration of how this works. We show temperature decreasing upward in this figure, so an adiabat from the deep interior is a vertical line from below. If it approaches the phase boundary on the right (the high-entropy side of the critical point), then liquid droplets will form in the vapor. If the interior adiabat approaches the phase boundary on the left (the low-entropy side of the critical point), then vapor bubbles will form in the liquid. The former is analogous to a cloud base and the latter is analogous to an ocean surface. The critical adiabat is the one that intersects the phase boundary at the critical point, which is also the warmest point (647 K) on the phase boundary.

Since hydrogen is present in ice giants in addition to water vapor, the critical point at each pressure level will depend on its composition. To describe these mixtures, Figure 5.1 should be three-dimensional with composition as the third axis. The critical point from Figure 5.1 then becomes a critical curve. The locations of phase boundaries will be strongly affected by mixture composition. Seward & Franck (1981), hereafter referred to as SF, experimentally identify the criti-

cal curve. They also investigate the phase boundaries of water-hydrogen mixtures for temperatures, pressures, and compositions below 654 K, 2.5 kbar, and 60 mol-% hydrogen to (water + hydrogen).

In an ice giant with a moist adiabat connecting the photosphere to a phase transition, the existence of a cloud base or an ocean surface depends on two input parameters: the water to total gas mixing ratio of the deep interior and the photospheric temperature. The moist adiabat extending down from the photosphere contains two phases, a gas phase and a condensed phase. A cloud base will result if the gas phase reaches the deep interior mixing ratio before the condensed phase does. Conversely, an ocean surface will result if the condensed phase reaches the deep interior mixing ratio before the gas phase does.

To understand liquid water oceans on Neptune, it is helpful to consider an idealized model of the Earth’s ocean/atmosphere system. In equilibrium, the concentration of dry air (mostly nitrogen, oxygen, and argon) in the ocean is set by its solubility and is denoted by X_{dry} . Under present conditions, X_{dry} is $\approx 2 \times 10^{-5}$ by mass. We define the photospheric temperature T_{phot} as the atmospheric temperature at the 0.4 bar level. The atmospheric temperature and pressure follow a pseudo-adiabat – a moist adiabatic expansion in which the condensed water is removed from the system as soon as it forms (e.g., Emanuel 1994, Salby 1996). Although the condensate is removed, the atmosphere is saturated at every pressure level, which means that a liquid water droplet suspended in the atmosphere just above the surface has the same X_{dry} as the ocean itself. With these assumptions, the values of X_{dry} and T_{phot} determine everything about the system, including the ocean temperature T_{ocean} and the partial pressures of water and dry air at the ocean interface. If T_{phot} were to increase, the mixing ratio of water on the moist adiabat would increase. Then, for X_{dry} fixed, T_{ocean} would have to increase in order to match the increased mixing ratio of water in the atmosphere (the Henry’s Law constant for air is a weaker function of temperature than the vapor pressure of water is). Increasing T_{ocean} is like moving toward the critical point from the left (low temperature) side of Figure 5.1. Alternately, for T_{ocean} fixed, X_{dry} would have to decrease. This lowers the equilibrium partial pressure of dry air relative to water and again matches the increased mixing ratio of water in the atmosphere.

In temperature-composition space, the boundary between the region of cloud base solutions and the region of ocean surface solutions will be a line. We refer to this boundary as the critical ocean, and it lies at the critical temperature for its composition. At the critical ocean, both the water

mixing ratios and densities will be equal between the gas and condensed phases. As in Figure 5.1, no phase transitions are possible for temperatures higher than the critical temperature.

For a suite of ice giants with different photospheric temperatures, different deep interior water mixing ratios, and different atmospheric gas masses, the qualitative effects on the existence of oceans are as follows. A cooler photosphere results in a photospheric adiabat with decreased water mixing ratio in the gas phase (and therefore increased water mixing ratio in the condensed phase) at each pressure level. Since the condensed phase mixing ratio will reach the deep interior value before the gas phase ratio does, the photospheric adiabat will terminate in an ocean surface. For an ice giant with a large water mixing ratio in the interior, the condensed phase ratio will again reach the interior value before the gas phase ratio does. This ice giant will also contain an ocean surface. As in Figure 5.1, higher-entropy photospheric adiabats terminate in cloud bases. Entropy can be increased either by increasing the photospheric temperature or by decreasing the pressure at a given temperature. The latter is similar to decreasing the atmospheric gas mass.

Even though we complicate the Neptune calculations by assuming van der Waals gases as well as condensation of methane, ammonia, and hydrogen sulfide, the qualitative aspects derived above still apply. We pin the moist adiabat at 59 K and 0.4 bar (Figure 8 in Burgdorf et al. 2003), and we extend it downward until a phase transition is reached. We determine which of these transitions is likely by following the photospheric adiabat until it intersects the phase transition curves of SF. Published models of Neptune’s density structure are then compared to our density estimates.

5.2 Photospheric Adiabat

5.2.1 Construction

Because gas at the temperature and pressure of a phase transition is non-ideal, the van der Waals relation is the basis of our model:

$$P = \frac{RT}{V - b_{\text{H}_2}} - \frac{a_{\text{H}_2}}{V^2}, \quad (5.1)$$

where a_{H_2} and b_{H_2} are the molar van der Waals coefficients for hydrogen (2.45×10^{11} erg cm³ mol⁻²

and $26.61 \text{ cm}^3 \text{ mol}^{-1}$, respectively; see Fishbane et al. (2005)), T is the temperature, and V is the molar volume of the water-hydrogen mixture. Quantities without subscripts, other than P , R , T , or V , denote water vapor.

We assume that internal heat is convected up from the deep interior of ice giants to the photosphere, at about 0.4 bar, and then radiated to space. Thus, it is reasonable to assume their pressure-temperature profiles follow adiabats. Hydrogen and helium affect molecular mass and heat capacity along the photospheric adiabat. Carbon, nitrogen, and sulfur are assumed to exist as methane, ammonia, and hydrogen sulfide. We include their effect on molecular mass and heat capacity in addition to allowing their condensation. Thus, we assume that these species are also saturated along the photospheric adiabat. Since we do not take into account the heat capacity or volume of the condensed phases, the photospheric, moist adiabat is similar to a pseudoadiabat.

The temperature versus molar volume profile is calculated from the following equation, which is derived in Appendix E:

$$\frac{dV}{dT} = - \left[\frac{C_v + \sum_i \left(\frac{L_i}{1 + q_i} \right) \left(\frac{\partial q_i}{\partial T} \right)_V}{\frac{RT}{V - b_{\text{H}_2}} + \sum_i \left(\frac{L_i}{1 + q_i} \right) \left(\frac{\partial q_i}{\partial V} \right)_T} \right]. \quad (5.2)$$

The summations occur over each species i (hydrogen, helium, water vapor, methane, ammonia, and hydrogen sulfide). Since hydrogen and helium are not condensing, their latent heats are set to zero. R is the molar gas constant and q_i is the molar mixing ratio of the condensing species to the other five species, given by the following:

$$q_i = \frac{f_i}{1 - f_i}, \quad (5.3)$$

where f_i is the molar mixing ratio of species i to total gas and L_i is the species' latent heat (by mole) of sublimation or condensation. The mixture's molar heat capacity at constant volume is given by C_v , which is derived in Appendix E:

$$C_v = \sum_i \left(C_{p_i} - \frac{R}{1 - \frac{2a_{\text{H}_2}(V - b_{\text{H}_2})^2}{RTV^3}} \right) f_i \quad (5.4)$$

for a van der Waals gas. Here, C_p is the mixture's molar heat capacity at constant pressure (the weighted mean, by mole, of the heat capacities of all six species).

For each species, the C_p values and latent heats of sublimation are taken from Atreya (1986). The latent heats of vaporization for methane and ammonia are 8.519×10^{10} erg mol⁻¹ for $T \geq 90.6$ K (National Institute of Standards and Technology) and 2.5×10^{11} erg mol⁻¹ for $T \geq 194.95$ K (Osborne & van Dusen 1918), respectively. The temperature dependences of L and the saturation vapor pressure e for pure water, are taken from Wagner & Pruss (1993). Saturation vapor pressures versus temperature for methane (Ziegler 1959), hydrogen sulfide (Giaque & Blue 1936, Vorholz et al. 2002), and ammonia (Karwat 1924, International Critical Tables 1928) are compiled in Atreya (1986). Latent heat and saturation vapor pressure of pure water are used because we do not have an adequate description of how these quantities vary, as a function of water vapor mixing ratio, in a water-hydrogen mixture. Limited data on saturation vapor pressure are indeed given in SF, so an interpolation is required to integrate the photospheric adiabat. The accuracy of this interpolation will be addressed later (Figure 5.2). As will be seen in section 5.4.1, the fact that latent heat goes to zero at 647 K (the critical point for pure water) causes unphysical behavior at higher temperatures. We attempt to remedy this by extrapolating data from $T < 600$ K to predict high temperature behavior.

Temperature and volume along the photospheric adiabat translate to pressure according to the van der Waals relation (Equation 5.1). In order to determine f , the mixing ratio of water to total gas, we modify Equation 5.1 to describe water vapor in the gas phase: P becomes e , a_{H_2} and b_{H_2} become the coefficients for water (a and b), and V becomes V/f . This is because the volume per mole of water is the volume per mole of the mixture (V) times the moles of mixture per mole of water ($1/f$). Therefore,

$$e = \frac{RTf}{V - bf} - \frac{af^2}{V^2}. \quad (5.5)$$

Here, $a = 5.507 \times 10^{12}$ erg cm³ mol⁻² and $b = 30.4$ cm³ mol⁻¹ (Fishbane et al. 2005). Using Equation 5.5, we find

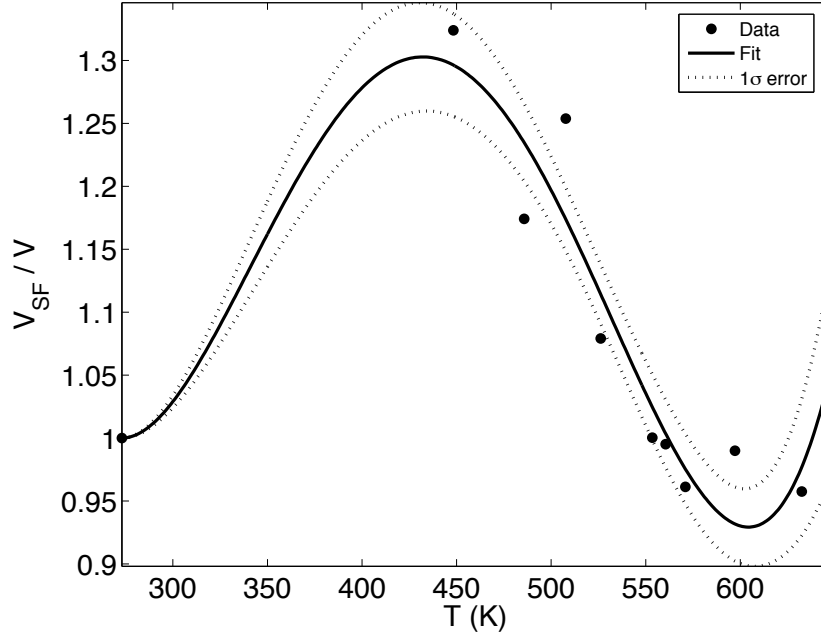


Figure 5.2: Photospheric adiabat uncertainty. We sample nine (T, P, f) points along two experimentally determined phase boundaries ($f = 10$ mol-% and 40 mol-%) of SF. Using T and f for each point, we calculate the volume from the photospheric adiabat using Equation 5.5. We then calculate the volume from experiment using Equation 5.1. The ratio of these volumes gives a correction factor which is then applied to the photospheric adiabats slope. We assume that ideal gas conditions at 273 K imply the uncertainty here to be zero.

$$\left(\frac{\partial f}{\partial T}\right)_V = \frac{V^2 (V - bf)^2 \frac{de}{dT} - RV^2 f (V - bf)}{RTV^3 - 2af (V - bf)^2} \quad (5.6a)$$

$$\left(\frac{\partial f}{\partial V}\right)_T = \frac{RTV^3 f - 2af^2 (V - bf)^2}{RTV^4 - 2Vaf (V - bf)^2}. \quad (5.6b)$$

From the definition of q in Equation 5.3, we can determine the quantities $\left(\frac{\partial q}{\partial T}\right)_V$ and $\left(\frac{\partial q}{\partial V}\right)_T$, which are necessary for Equation 5.2.

In ice giants, the other condensable species form cloud bases above the level of significant water condensation, and their main effect is to lower the temperature of the photospheric adiabat within the water cloud. To make the calculations simpler, we use the ideal gas approximation for the other condensable gases. The van der Waals constants in Equation 5.5 can be set to zero, and

$$e_j = \frac{RTf_j}{V}. \quad (5.7)$$

Here, the summation index j is taken to mean methane, ammonia, and hydrogen sulfide. For numerical integration, it is useful to formulate $\left(\frac{\partial f_j}{\partial T}\right)_V$ and $\left(\frac{\partial f_j}{\partial V}\right)_T$ in terms of f_j :

$$\left(\frac{\partial f_j}{\partial T}\right)_V = \left(\frac{1}{e_j} \frac{de_j}{dT} - \frac{1}{T}\right) f_j, \quad (5.8a)$$

$$\left(\frac{\partial f_j}{\partial V}\right)_T = \frac{f_j}{V}. \quad (5.8b)$$

5.2.2 Application to Neptune

Neptune itself might not be fully mixed from photosphere to rocky core. It is possible that there exists stable stratification in the deep interior. However, the maximum water mixing ratio along the photospheric adiabat cannot exceed the deep interior value, because density must increase with depth. Thus, the true water mixing ratio at the phase transition must be less than or equal to the deep interior value. To provide our Neptune model with the most optimistic parameters for the existence of oceans, we assume the phase transition occurs when the water mixing ratio equals the deep interior ratio.

We tie the van der Waals, photospheric adiabat to a pressure-temperature estimate (59 K at 0.4 bar) obtained by a combination of Voyager radio occultation experiments (Lindal 1992) and Infrared Space Observatory observations (Burgdorf et al. 2003). We hold Neptune's helium to hydrogen gas mole fraction at 19/81 along the photospheric adiabat and also in the deep interior (Lindal 1992). Baines et al. (1995) find a constant methane mixing ratio below the methane cloud base of $f_{\text{CH}_4} = 2.2^{+0.5}_{-0.6}$ mol-%. We estimate the mixing ratio of the other condensables at their cloud bases by assuming solar values of [C]:[N]:[S] along the photospheric adiabat. Given $\frac{[\text{C}]}{[\text{H}_2]} = 7.96 \times 10^{-4}$, $\frac{[\text{N}]}{[\text{H}_2]} = 2.24 \times 10^{-4}$, and $\frac{[\text{S}]}{[\text{H}_2]} = 3.7 \times 10^{-5}$ in the Sun (Gautier et al. 1995), the ammonia and hydrogen sulfide cloud bases occur when $f_{\text{NH}_3} = 0.6^{+0.1}_{-0.2}$ mol-% and $f_{\text{H}_2\text{S}} = 0.10^{+0.02}_{-0.03}$ mol-%.

We overlay the photospheric adiabat on the phase transition curves from Figure 2 of SF, and we present them as Figure 5.3. The thick line is the photospheric adiabat, and the thin lines are the curves from SF. Each pressure-temperature point between 450 K and 650 K has two phase transition curves passing through it. Each curve is labeled with its corresponding percentage hydrogen to (wa-

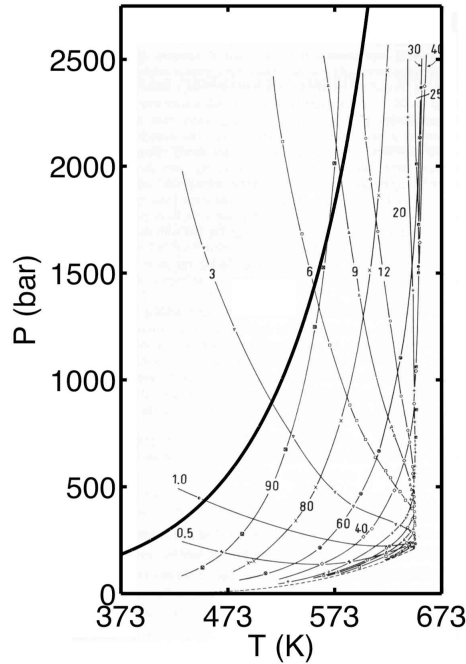


Figure 5.3: Photospheric adiabat overlying SF phase boundaries. Phase boundaries are thin lines, and numbers on each boundary denote hydrogen to (water + hydrogen) mixing ratio. The photospheric adiabat is given as the thick line and follows, for the most part, the 90 mol-% phase boundary. However, it can be seen that the water mixing ratio in the gas phase *increases* along the photospheric adiabat as temperature is increased (hydrogen mixing ratio *decreases*).

ter + hydrogen) molar mixing ratio, X_{H_2} . The curves with high values of X_{H_2} give the composition of the vapor, and the curves with low values of X_{H_2} give the composition of the liquid when the two phases are in equilibrium. A critical point occurs when the liquid and vapor have the same composition, i.e., where the curve for a given composition has infinite dP/dT . It is important to note that liquid water infused with more than about 1 mol-% hydrogen is in equilibrium with vapor only at a higher pressure than the critical pressure for that mixture. For a given composition, then, an ocean surface must lie at supercritical pressure.

To estimate the uncertainty in the photospheric adiabat, dV/dT from Equation 5.2, we compare experimentally determined (P, T, f) data to those predicted along the photospheric adiabat. We follow two saturated vapor to dry vapor phase boundaries of SF which correspond to $f = 10$ mol-% and 40 mol-% ($X_{\text{H}_2} = 90$ mol-% and 60 mol-%, respectively). Note that $f = X = 100$ mol-% $- X_{\text{H}_2}$ for SF data because their system only contains water and hydrogen. Also note that their phase boundaries are only printed for $T > 450$ K. Since we know T and f from SF (f is either 10 mol-% or 40 mol-%), we predict the volume along the photospheric adiabat by solving for V in

Equation 5.5 (saturation vapor pressure, e , is only a function of T). Using P and T from SF, we calculate the volume along their phase boundaries, V_{SF} , by solving for V in Equation 5.1. The quantity V_{SF}/V is a measure of the discrepancy between the photospheric adiabat and experimental data.

Figure 5.2 shows V_{SF}/V for nine pressure-temperature points in the temperature range 450 K $< T < 630$ K. The conditions for $T \leq 273$ K along the photospheric adiabat are ideal: $\left| \frac{PV}{RT} - 1 \right| = 7.1\%$ at 273 K. Since the van der Waals equation of state tends towards the ideal gas formulation at low temperatures and pressures, we assume that $V_{\text{SF}}/V = 1$ for $T \leq 273$ along the photospheric adiabat. By multiplying V_{SF}/V by the calculated dV/dT from Equation 5.2, we can correct the photospheric adiabat to agree with SF.

$$\frac{dV}{dT_{\text{true}}} = \frac{V_{\text{SF}}}{V} \frac{dV}{dT} \quad (5.9)$$

Therefore, we fit a fourth-order polynomial to V_{SF}/V versus temperature from the nine pressure-temperature points to provide a correction factor at each temperature. We force the value and slope of this factor at $T = 273$ K to be one and zero, respectively. The dotted lines in Figure 5.2 represent the 1σ error bounds on the fourth-order fit. The corrected, photospheric adiabat, extending from 59 K to the critical temperature of pure water (647 K), is shown as the middle, thick curve in Figure 5.4. The 1σ upper and lower bounds to the fourth-order fit are multiplied by dV/dT from Equation 5.2 to determine the 1σ upper and lower bounds to the photospheric adiabat. These error bounds are given as the thin curves in Figure 5.4.

5.3 Phase Transition

5.3.1 Cloud Base

By assuming values for both Neptune’s photospheric temperature and its deep interior water mixing ratio, we determine which phase transition exists. Therefore, as we integrate downward from the 59 K photosphere, the target is the deep interior mixing ratio. We estimate this value by assuming Neptune has a deep interior ice to rock mass ratio of $3.0_{-2.0}^{+0.5}:1$ (Podolak & Reynolds 1984, Podolak et al. 1991) and a gas mass of $2.0_{-0.5}^{+1.2} M_{\oplus}$ (Gudkova et al. 1988, Hubbard et al. 1995, Podolak et

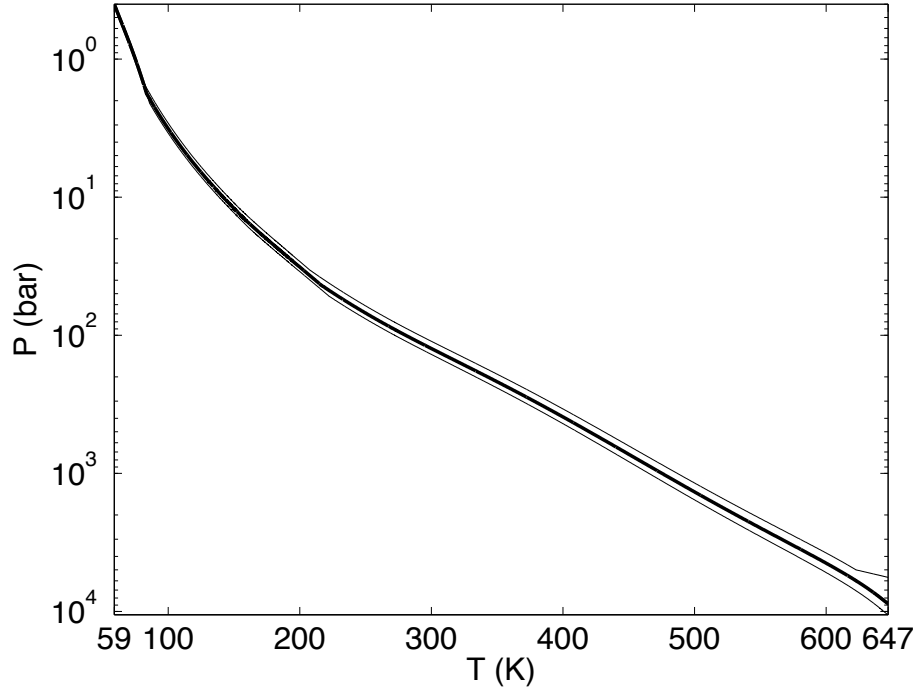


Figure 5.4: Pressure-temperature profile along the photospheric adiabat. The van der Waals, photospheric adiabat containing H_2 , He, water vapor, CH_4 , NH_3 , and H_2S is pinned at 59 K, 0.4 bar and extends to the critical temperature for pure water (647 K). The photospheric adiabat reaches this temperature at $8.8^{+1.8}_{-3.1}$ kbar.

al. 2000). The above authors obtained these values by fitting density models to Neptune’s gravitational harmonics which were measured during the Voyager flyby. We assume that the deep interior $[\text{H}_2]:[\text{He}]$ value is the same as the value in the atmosphere (19/81). This will comprise the deep interior gas mass given above. The mass and mole fraction makeup of Neptune’s deep interior gas is shown in Table 5.1.

Since the total planetary mass is $17.14 M_\oplus$ (Hubbard et al. 1995), the corresponding deep interior ice mass is $11.4^{+0.6}_{-2.1} M_\oplus$. Since the makeup of this ice is unknown, we assume that the ratios $[\text{C}]:[\text{N}]:[\text{O}]:[\text{S}]$ are solar in the deep interior. The corresponding mass and mole fraction components of Neptune’s deep interior ice are given in Table 5.1.

As can be seen from the bold value in Table 5.1, the deep interior water vapor to total gas mixing ratio (hydrogen, helium, water, methane, ammonia, hydrogen sulfide) is $f_{\text{interior}} = 26.9^{+5.2}_{-9.5}$ mol-%. This means that a water vapor cloud base will be reached if the water vapor mixing ratio f reaches f_{interior} along the photospheric adiabat before the critical temperature is reached (see section 5.1).

Table 5.1: Deep Interior Mixing Ratios

Species	Ice and gas separate		Ice and gas combined	
	By mole	By mass	By mole	By mass
H ₂	81.0%	68.1%	45.8%	10.2%
He	19.0%	31.9%	10.8%	4.8%
H ₂ O	61.7%	63.3%	26.9%	53.8%
CH ₄	28.8%	26.3%	12.5%	22.3%
NH ₃	8.1%	7.9%	3.5%	6.7%
H ₂ S	1.3%	2.6%	0.6%	2.2%

We have a nominal, deep interior water mixing ratio and its associated upper and lower bounds, and we also have a nominal, photospheric adiabat with upper and lower bounds (Figure 5.4). The combination that favors a cloud base is the low-pressure, photospheric adiabat bound paired with the lower mixing ratio bound ($f_{\text{interior}} = 17.4$ mol-%), and it reaches cloud base at 623 K and 5.0 kbar. The combination that favors a liquid ocean is the high-pressure, photospheric adiabat bound paired with the upper mixing ratio bound ($f_{\text{interior}} = 32.1$ mol-%), and a cloud base is reached at 705 K and 19.5 kbar. The nominal, photospheric adiabat paired with the nominal interior mixing ratio ($f_{\text{interior}} = 26.9$ mol-%) is our best estimate, and it reaches cloud base at 663 K and 10.7 kbar. Therefore, the water vapor cloud base is reached at $T = 663^{+42}_{-41}$ K and $P = 10.7^{+8.8}_{-5.7}$ kbar. These temperatures are above 647 K, which is the critical temperature for pure water, because the mixture consists of water and hydrogen. This will be discussed in section 5.4.1.

5.3.2 Supercritical Fluid

Below the cloud base, the atmosphere conforms to a dry (non-condensing), adiabatic gas with about 27 mol-% water vapor to total gas. The pressure-temperature profile of this dry adiabat can be found by setting $L = 0$ in Equation 5.2, keeping $df/dT = 0$, and solving for pressure in Equation 5.1. Eventually, as one descends further, the gas will slowly transition into a supercritical fluid whose density equals that of a liquid of the same composition. This supercritical fluid is not a true ocean with a saturated vapor to liquid interface. Hot, ionic “oceans” have been predicted in Neptune’s deep interior (Atreya 1986, p. 64; Hubbard et al. 1995), and they would lie at $\approx 2,000$ K (Atreya et al. 2005).

5.4 Ocean Requirements

5.4.1 Deep Interior Mixing Ratio

By assuming a value for Neptune’s photospheric temperature and by leaving the deep interior water mixing ratio as a free parameter, we find the minimum deep interior water mixing ratio that will allow an ocean to exist. This particular ocean will be a critical ocean. A critical ocean will occur if the photospheric adiabat (in temperature-composition space) intersects the critical curve, and if the pressure at that intersection is higher than the critical pressure for that composition (Figure 5.3 and the text in section 5.2.2 describing it). The composition at this intersection is the minimum deep interior mixing ratio that allows an ocean to exist. Since we only aim to examine the requirements for a critical ocean, it is unnecessary to calculate the water mixing ratio in the condensed phase. To determine the location of a cool ocean, however, the water mixing ratio in the condensed phase must be calculated. This will require the mixing ratios of the other condensables to be determined in the water-hydrogen condensate. Currently, experimental data are not sufficient for this to be done accurately.

We extrapolate the data in Table 1 of SF (and the additional data point on page 3, column 2 of their paper) to construct the critical curve over a large temperature range, and thus to allow the photospheric adiabat to intersect at high temperature oceans. This table lists critical temperature and pressure for a variety of compositions. Because the photospheric adiabat utilizes f (mixing ratio of water to total gas), we employ composition as the water to (water + hydrogen) mixing ratio, defined as X . Thus, $X + X_{\text{H}_2} = 100$ mol-%. We fit the data with piecewise cubic Hermite polynomials because a spline fit appears unphysical. The critical curve in temperature- X space is given as Figure 5.5, and the critical curve in pressure- X space is given as Figure 5.6.

We extrapolate the photospheric adiabat, with a spline in temperature- X space, to temperatures higher than 647 K. This is because water-hydrogen phase transitions can occur at higher temperatures. Unfortunately, using all $T < 647$ K in this fit gives a multivalued profile. This unphysical behavior occurs because we are forced to approximate the mixture’s latent heat and saturation vapor pressure with the expressions given for pure water: this is invalid near 647 K. However, including only $T < 600$ K in the extrapolation eliminates this problem. It is a reasonable approximation because latent heat is fairly constant with temperature until it very quickly goes to zero near the critical temperature. In Figure 5.7, the photospheric adiabat is given as the thick, solid curve, and

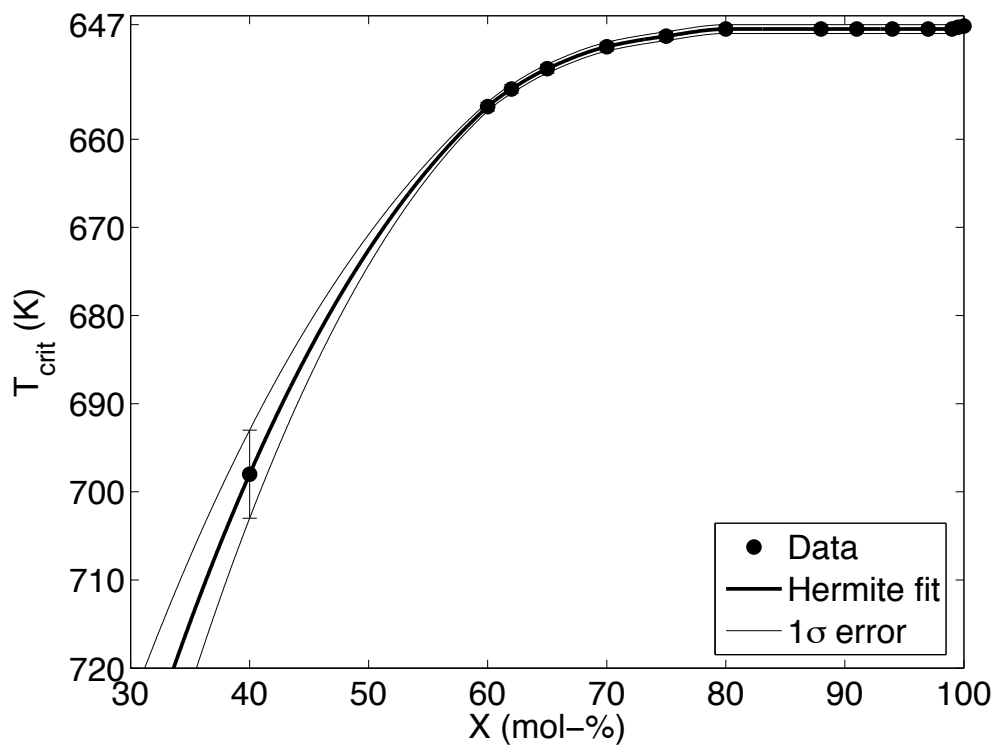


Figure 5.5: Critical curve: temperature vs. X . Data from SF are fit by a piecewise cubic interpolating Hermite polynomial.

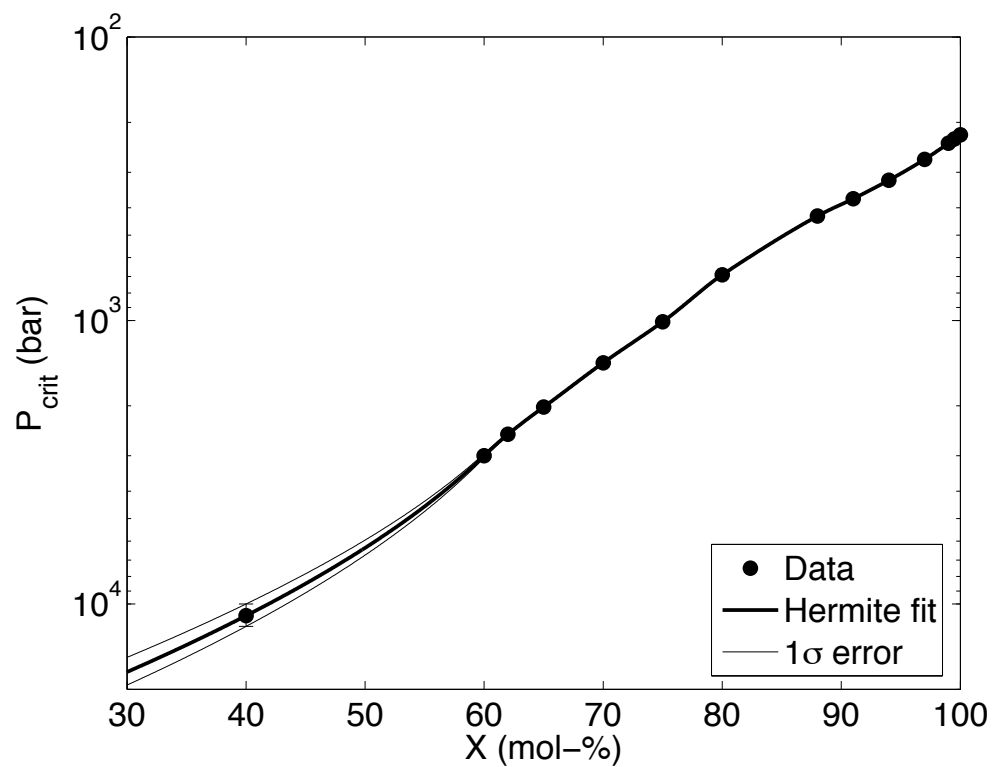


Figure 5.6: Critical curve: pressure vs. X . Data from SF are fit by a piecewise cubic interpolating Hermite polynomial.

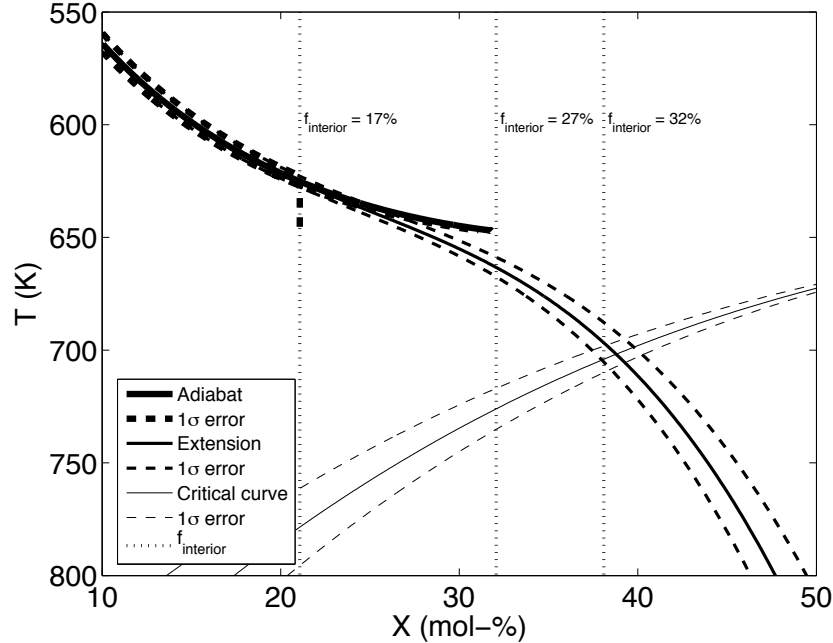


Figure 5.7: Minimum water mixing ratio for an ocean. The photospheric adiabat, extrapolated for $T > 647$ K, and the critical curve are shown. Dashed curves indicate 1σ errors on each profile. The two curves intersect at $X = 38.8 \pm 1.4$ mol-%. This represents the minimum water to (water + hydrogen) mixing ratio necessary to support an ocean under the current, 59 K Neptunian photosphere. Since the deep interior f corresponds to $X = 32_{-11}^{+6}$ mol-% at an ocean, Neptune is too dry to harbor oceans.

its extension to $T > 647$ K is given as the solid curve. The critical curve is shown as the thin, solid curve. Dashed curves indicate the associated 1σ errors on each curve. Finally, the vertical, dotted lines show the range of deep interior mixing ratios assumed for Neptune.

We attempt to place upper and lower limits on the shape of the extended, photospheric adiabat, and we acknowledge that it is a crude extrapolation. The extended, photospheric adiabat intersects the critical curve, and therefore terminates in a critical ocean, at $T = 702.1_{-7.3}^{+6.1}$ K and $X = 38.8 \pm 1.4$ mol-%. When factoring in the mixing ratios of the other species, we find $f = 33.0 \pm 1.3$ mol-%. By extending the photospheric adiabat in pressure-temperature space, we determine the pressure of this critical ocean to be $P = 18.7_{-5.3}^{+6.6}$ kbar. Since the critical pressure for this composition is lower than the pressure of the critical ocean ($P = 11.65_{-0.42}^{+0.21}$ kbar, Figure 5.6), we verify that the critical ocean is indeed liquid. An extant ocean in Neptune thus requires a deep interior water mixing ratio of at least $f = 33.0 \pm 1.3$ mol-%, but we estimate its current value to be $f_{\text{interior}} = 26.9_{-9.5}^{+5.2}$ mol-%. Neptune is therefore slightly too dry to harbor oceans.

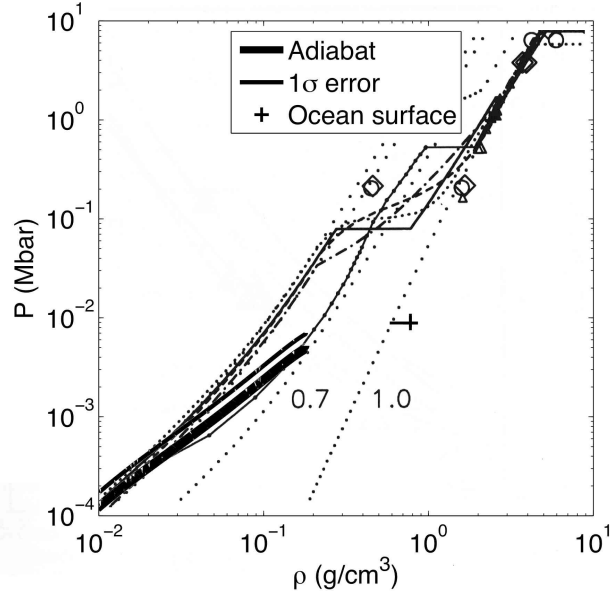


Figure 5.8: Density along the photospheric adiabat overlying density models. The thick, linear feature in the lower left (from 10^{-4} to 10^{-2} Mbar) represents pressure versus density along the photospheric adiabat. 1σ error bounds are roughly the thickness of the line. The cross at about 10^{-2} Mbar and about 1 g/cm^3 shows the location of the critical ocean, under a 59 K photosphere, in pressure-density space. This figure is modified from Figure 5 of Hubbard et al. (1995), and thin curves (solid, dashed, and dot-dashed) are different density models in that paper. Numbered, dotted curves represent adiabats from that paper labeled with varying ice mass fractions. These adiabats lie in ice giants composed only of hydrogen, helium, and ice. Note that the photospheric adiabat lies within the range of density models while the ocean surface is far outside them. Thus, we conclude not only that Neptune has no extant liquid water-hydrogen ocean, but also that the photospheric adiabat is consistent with Voyager data.

5.4.2 Gravitational Signature

We investigate whether the photospheric adiabat is consistent with density models of Neptune's interior. At each pressure level, we calculate the density by dividing molar mass by molar volume, V . We treat molar mass as simply a mean, weighted by mixing ratio, of the molar masses of the constituent species. We plot pressure against density along the photospheric adiabat as Figure 5.8, and we overlay these results on Figure 5.5 from Hubbard et al. (1995). As can be seen, the photospheric adiabat is consistent with density models from photosphere to cloud base. We find the 5 to 20 kbar cloud base from section 5.3.1 has a density of $0.221^{+0.048}_{-0.076} \text{ g/cm}^3$, while density models predict 0.09 to 0.30 g/cm^3 . The location of the cloud base is above the density discontinuity at ≈ 100 kbar, as expected.

We now determine whether the critical ocean is consistent with density models. To estimate the density of the critical ocean, we ignore the contribution of all species except water and hydrogen.

This is because water and hydrogen dominate the vapor, and the dissolved mole fraction of the other species should be even lower in the liquid. We use the following law of additive volumes (Hubbard 1972):

$$\frac{1}{\rho_{\text{mix}}} = \sum_{i=1}^n \frac{M_i}{\rho_i}, \quad (5.10)$$

where M_i and ρ_i are the mass mixing ratio and density, respectively, of species i . To calculate the densities of hydrogen and water at the surface of the 19 kbar critical ocean, we use equation of state fits compiled by Hubbard et al. (1995) from various sources. Plugging in the densities for these two species, we find the critical ocean has a density of $0.772_{-0.059}^{+0.061}$ g/cm³. Based on planetary density models calculated from Voyager gravitational constraints, the density between 13 and 25 kbar (range of pressures at the critical ocean) lies between 0.14 g/cm³ and 0.34 g/cm³ (Figure 5.8), which is inconsistent with an ocean; the required water mixing ratio is too high. Again, Neptune is too dry to harbor oceans.

5.4.3 Photospheric Temperature

By assuming a value for Neptune’s deep interior water mixing ratio and by leaving the photospheric temperature as a free parameter, we aim to find the maximum photospheric temperature that will allow an ocean to exist. Neptune is not in thermal equilibrium with the Sun’s radiation; since its thermal emission is 2.6 times as strong as its solar heating (Hubbard et al. 1995), Neptune is slowly cooling. As an adiabatic atmosphere cools, its entropy decreases, which moves the phase boundary to the left in Figure 5.1. As an ice giant with a high-entropy, low-temperature cloud base cools, its cloud base will migrate to high temperature. After further cooling of the ice giant, the cloud base will pass through the critical point to become a liquid ocean at high temperature. Finally, the cloud base will transition to a liquid ocean at low temperature. Thus, it is worthwhile to ask whether Neptune will eventually cool enough to permit the existence of liquid water oceans. Since the critical point for hydrogen gas is 33.2 K, 13.0 bar (National Institute of Standards and Technology), hydrogen gas will begin to condense at cooler temperatures. Since we do not take hydrogen condensation into account, we do not attempt to model ice giants cooler than 30 K at 0.4 bar. We investigate the probability of an ocean’s existence by considering a suite of ice giants with photospheric temperatures higher than 30 K.

We assume f in the ocean will equal the deep interior mole fraction, $f_{\text{interior}} = 26.9_{-9.5}^{+5.2}$ mol-% (see section 5.3.1). Given the atmospheric mixing ratios of the other species (see section 5.2.2), $X = 32_{-11}^{+6}$ mol-% in the ocean. Since the cloud base mixing ratios of the other condensables are much lower than their assumed mixing ratios in the deep interior, X in the ocean will not equal X_{interior} . From Figures 6 and 7, we find the critical point to be at 726_{-28}^{+69} K and 16_{-5}^{+12} kbar for $X = 32_{-11}^{+6}$ mol-%. We set the 0.4 bar temperature to 30 K and integrate the photospheric adiabat, as well as its upper and lower bounds, down to 647 K. We then fit a spline to the temperature- X profile for $T < 600$ K and extrapolate to higher temperatures. We find the lower, photospheric adiabat bound reaches the lower value of $X = 21$ mol-% at 636 K. Since this pressure level is much cooler than its 796 K critical temperature, the lower, photospheric adiabat bound terminates in a cloud base. The nominal, photospheric adiabat reaches the nominal $X = 32$ mol-% at 707 K, which is cooler than that pressure level's 726 K critical temperature. Thus, the nominal, photospheric adiabat also intersects a cloud base.

However, the upper, photospheric adiabat bound does not reach the upper value of $X = 38$ mol-% before its 698 K critical temperature. In fact, the upper bound to the photospheric adiabat intersects the critical curve at $720.9_{-5.9}^{+6.3}$ K and $X = 33.26_{-0.53}^{+0.54}$ mol-%, which implies that it reaches a critical ocean. The uncertainties in temperature and composition of this critical ocean are solely due to the uncertainties of SF in measuring the critical curve. Extending the upper, photospheric adiabat bound with a spline fit in pressure-temperature space, we find this critical ocean to lie at 155_{-12}^{+14} kbar. These calculations are probably unqualified to accurately predict a pressure this high. However, this critical ocean certainly lies at a higher-than-critical pressure of $15.1_{-1.9}^{+2.0}$ kbar. Therefore, we verify that the upper, photospheric adiabat bound (pinned to a 30 K photosphere) intersects a critical ocean.

The existence of a critical ocean under a 30 K photosphere can only occur if the actual profile intersects the critical curve before reaching the deep interior water mixing ratio. Thus the probability of an ocean's existence is related to the probability that Neptune's deep interior water mixing ratio is higher than the nominal value. The minimum value of X necessary for an ocean is the composition at the intersection between the nominal, photospheric adiabat and the critical curve. Assuming Gaussian statistics, this occurs at $X = 33.37_{-0.64}^{+0.65}$ mol-%, which is $0.22 \pm 0.11\sigma$ away from the ocean's $X = 32_{-11}^{+6}$ mol-%. Therefore, the probability of such a high water mixing ratio, and thus the probability of a 30 K photosphere terminating in an ocean surface, is $41.5 \pm 4.2\%$. It should

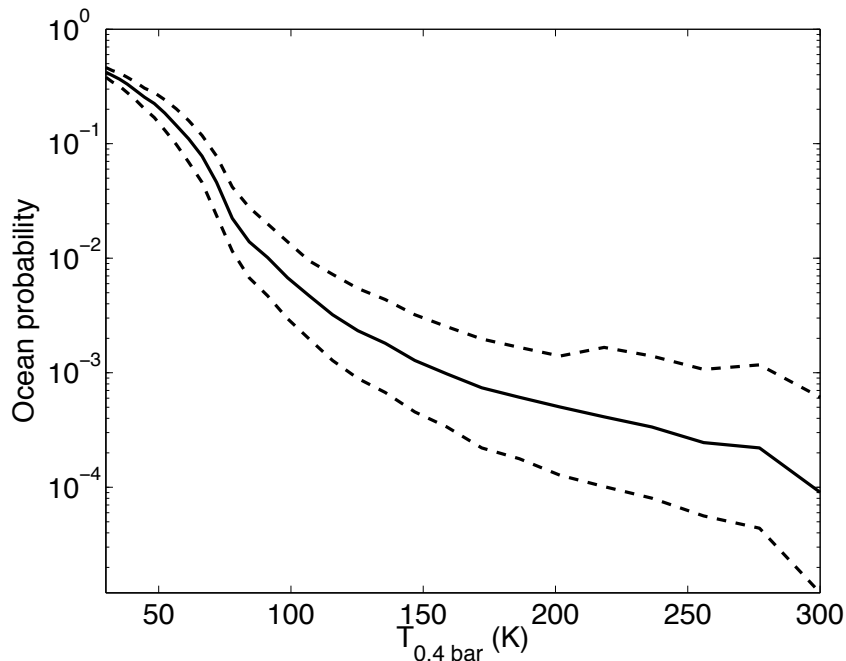


Figure 5.9: Ocean probability. With a 30 K photosphere, Neptune would have a $41.5 \pm 4.2\%$ probability of having an ocean, while its current 59 K photosphere only has a probability of $13.1^{+5.4}_{-4.3}\%$ of overlying an ocean. This is because liquid water preferentially exists at low entropy and thus low atmospheric temperature.

be emphasized that the probabilistic nature of an ocean's existence is due to uncertainty both in the thermodynamics of the photospheric adiabat and in the value of Neptune's deep interior water mixing ratio.

This approach can also be applied to a suite of photospheres with higher temperatures, but the probability of an ocean will decrease with increasing photospheric temperature (Figure 5.9). Note that Neptune's current 59 K photosphere has only a $13.1^{+5.4}_{-4.3}\%$ probability of terminating in an ocean. While a 13% probability is not insignificant, Voyager gravitational data verify that Neptune has no oceans (see section 5.4.2). Thus, Neptune is too warm to harbor oceans.

Will Neptune ever cool down to 30 K? Simply finding the temperature at which Neptune's thermal emission is in equilibrium with solar buffering provides a very rough estimate of the extent to which it can cool:

$$4\pi R^2 \sigma T_e^4 = (1 - \Lambda) \pi R^2 (\pi F_\odot). \quad (5.11)$$

Here R is planetary radius, σ is the Stefan-Boltzmann constant, T_e (effective temperature) is assumed to be the temperature at 0.4 bars, Λ is Bond albedo, and πF_\odot is solar insolation. Keeping solar luminosity and Neptune's albedo fixed, Neptune's 0.4 bar level cannot cool below 47 K. Moreover, the Sun will brighten continuously for about 6 billion years (reaching $1.1 L_\odot$ in 1.1 Gyr and $1.4 L_\odot$ in 3.5 Gyr; Sackmann et al. 1993). Thus, the maximum probability of forming oceans in Neptune, while the Sun is on the main sequence, is the present probability (only $13.1^{+5.4}_{-4.3}\%$).

As the Sun slowly (compared to Neptune's orbital period) loses about half its mass through the red giant and AGB phases, Neptune's orbit will gradually expand. Neptune will either collide with Uranus, be ejected from the Solar System, or assume a stable orbit with roughly twice its current semimajor axis (Debes & Sigurdsson 2002). This comes from angular momentum conservation:

$$L_{\text{Neptune}} = M_{\text{Neptune}} \sqrt{GM_\odot a_{\text{Neptune}} (1 - e_{\text{Neptune}}^2)}, \quad (5.12)$$

where L is angular momentum, M is mass of each body, a is semimajor axis and e is eccentricity. As a very young white dwarf, the Sun's luminosity will be large. However, as it rapidly cools, the Sun's luminosity will decrease dramatically.

A collision would certainly mix Neptune's interior water ice into its atmosphere, and the essentially absent solar irradiance would allow the surviving planet to cool quickly. Significant cooling will also occur if Neptune is ejected from the Solar System. Thus, regardless of Neptune's eventual state, it may be free to cool down below 30 K, where its water clouds have a $41.5 \pm 4.2\%$ probability of condensing and forming oceans. Billions of years from now, after the Sun has gone, Neptune may therefore become the only object in the Solar System with liquid water oceans.

5.5 The Water-Hydrogen-Helium System

We integrate the photospheric adiabat without methane, ammonia, and hydrogen sulfide to show that the conclusions above are unchanged. We set the heat capacity and latent heat due to these species to zero; therefore, this model atmosphere only contains hydrogen gas, helium, and water vapor. In Figure 5.10, the bold, solid curve indicates the photospheric adiabat pinned at 59 K and

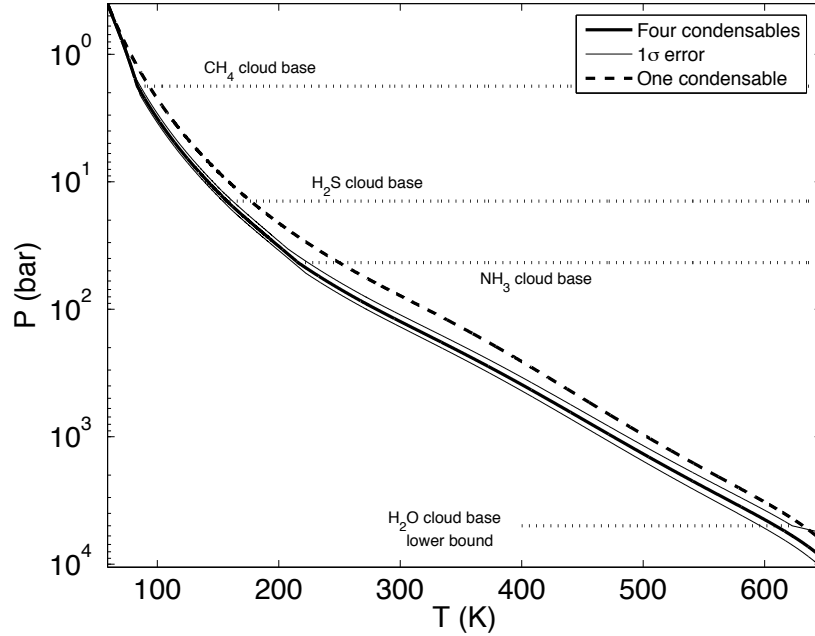


Figure 5.10: Pressure-temperature profiles along photospheric adiabats with different condensable species. The solid curves represent the photospheric adiabat (and error bounds) with all species condensing (water, CH_4 , H_2S , and NH_3), whereas the dashed curve is a photospheric adiabat with only water condensing. For clarity, error bounds are only shown for the adiabat with all species condensing. All photospheric adiabats are pinned at 59 K. Note that more condensation causes a photospheric adiabat to run colder at depth, thus increasing the probability of an oceans existence.

Table 5.2: Cloud Bases

Species	One condensable	Four condensables
CH_4	—	$83.6_{-3.1}^{+2.2}$ K, $1.78_{-0.34}^{+0.31}$ bar
H_2S	—	$157.3_{-4.4}^{+3.2}$ K, $14.2_{-2.4}^{+2.2}$ bar
NH_3	—	$215.8_{-8.4}^{+6.2}$ K, $43.0_{-9.5}^{+8.9}$ bar
H_2O	645_{-28}^{+43} K, $6.3_{-2.6}^{+5.2}$ kbar	663_{-41}^{+42} K, $10.7_{-5.7}^{+8.8}$ kbar

containing all six species. The error bounds are given as the thin, solid curves. The 59 K photospheric adiabat containing only three species is shown as the bold, dashed curve. The error bounds are left off of the three-species adiabat for clarity. Table 5.2 presents the locations of all cloud bases.

The calculation with water as the only condensable still predicts a water cloud base, as opposed to an ocean surface, though the cloud base is now at lower temperature and pressure (from 663_{-41}^{+42} K, $10.7_{-5.7}^{+8.8}$ kbar to 645_{-28}^{+43} K, $6.3_{-2.6}^{+5.2}$ kbar). This effect is primarily due to the lack of a methane cloud near the photosphere, as can be seen in Figure 5.10. Clouds act to steepen dP/dT , so eliminating clouds of methane and the other condensables should indeed cause the pressure at the phase

transition to be lower. Since a critical ocean requires the temperature to be critical and the pressure to be supercritical, clouds of other species therefore make conditions slightly more favorable for the existence of liquid water. Indeed, a critical ocean requires less water when clouds of many species are present ($X = 38.8 \pm 1.4$ mol-% and $f = 33.0 \pm 1.3$ mol-%, see section 5.4.1) than when only water clouds are present ($X = 40.4 \pm 1.3$ mol-% and $f = 35.4_{-1.2}^{+1.3}$ mol-%).

5.6 Extrasolar Hot Neptunes

Most extrasolar planets discovered are of order one Jupiter mass and reside less than about 1 AU from their parent stars (<http://exoplanets.org>); they presumably migrated many AU inward from their sites of formation (Lin et al. 1996, Boss 1996). Neptune-mass planets that have also migrated inward (“hot Neptunes”) are beginning to be found around other stars (Santos et al. 2004, Bonfils et al. 2005, Udry et al. 2006, Lovis et al. 2006). It is reasonable to expect that many more will soon be found as technological accuracy increases. We show above that while the temperature in Neptune rapidly approaches the critical temperature with depth, the water mixing ratio reaches the deep interior value before the critical curve is reached. This is why a cloud base is reached in Neptune as opposed to an ocean surface. Thus, if Neptune at 30 AU is too hot to allow liquid water oceans to exist in its interior, then hot Neptunes at less than 1 AU must be far too hot.

We present a simplified assessment of how migration affects the possibility of liquid water oceans. We consider a family of extrasolar ice giants that have Neptune’s deep interior composition and Bond albedo of 0.29, have saturated upper atmospheres, orbit stars of solar luminosity, have semimajor axes between 1 AU to 50 AU, and have photospheres that are in thermal equilibrium with their parent stars. We also assume that the atmospheres are convecting all the way down to the critical temperature and that they equilibrate to moist adiabatic states throughout the inward migration. We ignore any effects due to radiative zones in the ice giants. These assumptions may not stand up to rigorous numerical calculation; however, our goal is to present an idealized description of the effect of planetary migration on the existence of oceans. We calculate the effective planetary temperature by balancing solar heating with thermal emission (Equation 5.11). The inner semimajor axis limit, 1 AU, is chosen because the cloud base occurs at 0.4 bars: for closer semimajor axes, no cloud base would exist below a 0.4 bar photosphere. The outer choice of 50 AU is arbitrary.

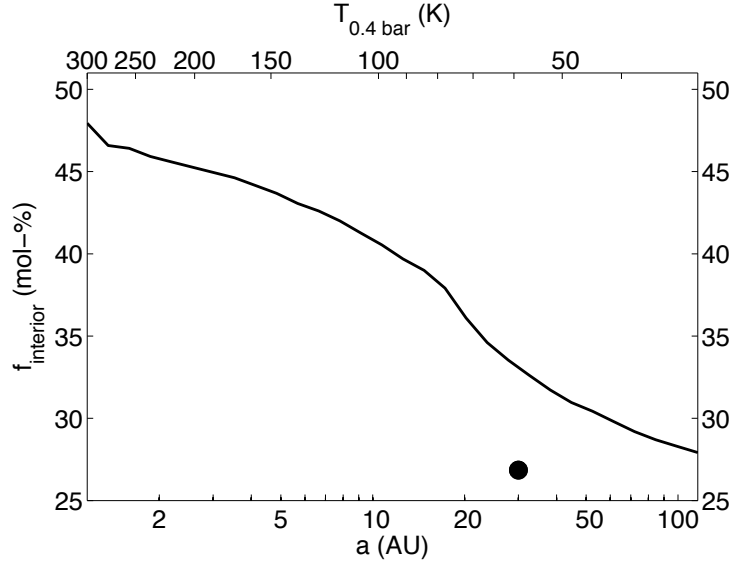


Figure 5.11: Minimum deep interior water mixing ratio necessary for ocean existence. As Neptune-like planets migrate inward, and planetary effective temperature increases, oceans that once existed may boil away. The solid curve represents the minimum planetary f necessary for an ocean to exist in an ice giant at a given semimajor axis a . The effective temperature T_e assumes a Neptune-like Bond albedo of 0.29. The large, required f at effective temperatures higher than 200 K casts serious doubt on the idea that hot Neptunes ($a < 1$ AU) can harbor liquid water oceans. Neptune itself lies at the filled circle in the lower right of the diagram, and it is too dry ($f_{\text{interior}} \approx 27$ mol-%) to permit the existence of oceans.

As can be seen in Figure 5.11, closer-in, hotter ice giants require a larger deep interior water fraction in order to have liquid water in their interiors. Thus, as Neptune-mass planets migrate inward, any ocean surface they have may evaporate into a cloud base, assuming stellar insolation is able to propagate down to this level. A Neptune-like planet with a 273 K photosphere, and therefore with liquid water droplets present in its photosphere, would need a deep interior water mixing ratio of almost 50% in order to harbor an ocean. Therefore, Neptune-like planets are very unlikely to have liquid water oceans in their interiors if water vapor is detected in their atmospheres. Conversely, the non-detection of water vapor in Neptune-like planets is actually favorable towards the existence of interior oceans. Even though photospheric water vapor should cause albedo to be different from that of Neptune, effective temperature only varies as the fourth root of albedo.

By inverting the process in section 5.3.1, we calculate deep interior gas mass as a function of deep interior water mixing ratio. From section 5.4.1, Neptune’s minimum deep interior water mixing ratio for an ocean is $f = 33.0 \pm 1.3$ mol-%. This corresponds to a maximum deep interior gas mass of $1.40_{-0.10}^{+0.11} M_{\oplus}$. We assume Neptune’s gas mass to be $2.0_{-0.5}^{+1.2} M_{\oplus}$ (see section 5.3.1), which is just slightly higher than the maximum value for an ocean.

If the “ocean planets” of Leger et al. (2004) have deep enough atmospheres, liquid water oceans can exist inside them provided the deep interior has very little gas. For example, a $6 M_{\oplus}$ planet with $3 M_{\oplus}$ of interior ice and a 300 K photosphere can only have an ocean if the deep interior has less than $0.117_{-0.030}^{+0.036} M_{\oplus}$ of gas ($f \geq 47.9_{-3.1}^{+2.9}$ mol-%).

5.7 Future Work

We have used the van der Waals equation of state in this work, and we have shown it to be accurate to only 30% in describing temperature, pressure, and composition simultaneously for $T \approx 450$ K (Figure 5.2). The next step is to continue this work using, for example, the modified Redlich-Kwong equation of state (Redlich & Kwong 1949), which is more consistent with the phase transition curves of SF. We would also like to see whether an ocean of density 0.8 g/cm^3 descending from 19 kbar can successfully be incorporated into models of Neptune’s density structure. To determine the conditions appropriate for cool oceans, the mixing ratio along the photospheric adiabat of water in the condensed phase must be obtained. This avenue would be useful when describing water-rich planets with less massive atmospheres. Finally, it would be beneficial to have an accurate treatment of Neptune’s true photosphere with age, which will of course depend on composition. This will better address (1) whether it is possible for Neptune to cool down enough to permit liquid oceans to rain out, and (2) the length of time before this may happen.

5.8 Conclusion

Neptune’s significant water content raises the interesting possibility that liquid water-hydrogen oceans, with a saturated vapor to liquid interface, exist in its interior. This liquid would be infused with over 60% hydrogen to (hydrogen + water) by mole. To be a true liquid, this ocean would have to lie at a temperature lower than the critical temperature, and a pressure higher than the critical pressure, for this composition (about 700 K and 12 kbar). There is a minimum deep interior water mixing ratio in Neptune that allows an ocean to exist. Neptune’s deep interior ice mass based on density models in the literature, $f_{\text{interior}} = 26.9_{-9.5}^{+5.2}$ mol-%, is less than the minimum required value of $f = 33.0 \pm 1.3$ mol-% for a critical ocean. Indeed, we find that Neptune currently has less than a 15% probability of harboring an ocean. The gravitational constraints confirm this

low probability, because an extant liquid water-hydrogen ocean would be denser than measured (0.8 g/cm^3 instead of 0.1 to 0.3 g/cm^3 at the ≈ 15 kbar level). Thus, Neptune is both too warm and too dry for an ocean to exist at present. If the photosphere were to cool from its current 59 K to 30 K , as hydrogen gas itself begins to condense out of the atmosphere, the probability of the water clouds raining out would increase to 40% .

As the Sun ages and becomes a cool white dwarf, its buffering of Neptune's atmosphere will decrease significantly. Neptune may be allowed to cool sufficiently in the ensuing billions of years for its existing water clouds to rain out. Thus, it is possible that Neptune may form liquid water oceans many billions of years from now. While terrestrial extrasolar planets with semimajor axes near 1 AU may have liquid water oceans on their surfaces, those oceans would freeze out for more distant semimajor axes. However, the inner reaches of extrasolar systems are apparently too hot for the existence of liquid water oceans in the interiors of Neptune-mass ice giants. Only the frigid conditions at many tens of AU are suitable, if the planet is watery enough, for hydrogen-rich oceans to lie at thousands of atmospheres of pressure.

References

- Atreya, S. K., 1986, *Atmospheres and Ionospheres of the Outer Planets and their Satellites*. Springer-Verlag, New York.
- Atreya, S. K., Egeler, P. A., & Wong, A. S. 2005, Amer. Geophys. Union, Fall Meeting, P11A-0088 (abstract).
- Bonfils, X., Forveille, T., Delfosse, X., Udry, S., Mayor, M., Perrier, C., Bouchy, F., Pepe, F., Queloz, D., & Bertaux, J.-L. 2005, *A&A* 443, L15.
- Boss, A. P. 1996, *Lunar. Planet. Sci.* XXVII, 139 (abstract).
- Burgdorf, M., Orton, G. S., Davis, G. R., Sidher, S. D., Feuchtgruber, H., Griffin, M. J., & Swinyard, B. M. 2003, *Icarus* 164, 244.
- Debes, J. H. & Sigurdsson, S. 2002, *ApJ* 572, 556.
- Emanuel, K. A. 1994, *Atmospheric Convection*. Oxford University Press, New York.

- Fishbane, P. M., Gasiorowicz, S. G., & Thornton, S. T., 2005, *Physics for Scientists and Engineers*. Prentice-Hall, Upper Saddle River.
- Gautier, D., Conrath, B. J., Owen, T., de Pater, I., & Atreya, S. K. 1995, in *Neptune and Triton*, ed. D. P. Cruikshank. University of Arizona Press, Tucson, p. 547.
- Giauque, W. F., & Blue, R. W. 1936, *J. Am. Chem. Soc.* 58, 831.
- Hubbard, W. B. 1972, *ApJ* 176, 525.
- Hubbard, W. B., Podolak, M., & Stevenson, D. J. 1995, in *Neptune and Triton*, ed. D. P. Cruikshank. University of Arizona Press, Tucson, p. 109.
- Hubbard, W. B. 1999, in *The New Solar System*, eds. J. K. Beatty, C. C. Petersen, & A. Chaikin. Sky Publishing Co., Cambridge, MA, p. 193.
- International Critical Tables. 1928. McGraw-Hill Book, New York.
- Karwat, E. 1924. *Z. Phys. Chem. Stöchiomet. Verwandtschaftsr.* 112, 486.
- Léger, A., Selsis, F., Sotin, C., Guillot, T., Despois, D., Mawet, D., Ollivier, M., Labéque, A., Valette, C., Brachet, F., Chazelas, B., & Lammer, H. 2004, *Icarus* 169, 499.
- Lin, D. N. C., Bodenheimer, P., & Richardson, D. C. 1996, *Nature* 380, 606.
- Lindal, G. F. 1992, *AJ*, 103, 967.
- Lodders, K. & Fegley, B., Jr. 1994, *Icarus* 112, 368.
- Lovis, C., Mayor, M., Francesco, P., Yann, A., Benz, W., Bouchy, F., Correia, A. C. M., Laskar, J., Mordasini, C., Queloz, D., Santos, N. C., Udry, S., Bertaux, J.-L., & Sivan, J.-P. 2006, *Nature* 441, 305.
- Marley, M. S., Gómez, P., & Podolak, M. 1995, *J. Geophys. Res.* 100, 23349.
- National Institute of Standards and Technology: <http://webbook.nist.gov/chemistry/name-ser.html>
- Osborne, N. S. & van Dusen, M. S. 1918, *J. Am. Chem. Soc.* 40, A14.
- Podolak, M. & Reynolds, R. T. 1984, *Icarus* 57, 102.
- Podolak, M., Hubbard, W. B., & Stevenson, D. J. 1991, in *Uranus*, eds. J. Bergstrahl, E. Minor, & M. S. Matthews. University of Arizona Press, Tucson, p. 29.
- Podolak, M., Podolak, J. I., & Marley, M. S. 2000, *Planet. Space Sci.* 48, 143.

- Redlich, O. & Kwong, J. N. S. 1949, *Chem. Rev.* 44, 233.
- Sackmann, I.-J., Boothroyd, A. I., & Kraemer, K. E. 1993, *ApJ* 418, 457.
- Salby, M. L. 1996, *Atmospheric Physics*. Academic Press, San Diego.
- Santos, N. C., Bouchy, F., Mayor, M., Pepe, F., Queloz, D., Udry, S., Lovis, C., Bazot, M., Benz, W., Bertaux, J.-L., Lo Curto, G., Delfosse, X., Mordasini, C., Naef, D., Sivan, J.-P., & Vauclair, S. 2004, *A&A* 426, L19.
- Seward, T. M. & Franck, E. U. 1981, *Ber. Bunsen Phys. Chem.* 85, 2 (SF).
- Stanley, S. & Bloxham, J. 2004, *Nature* 428, 151.
- Udry, S., Mayor, M., Benz, W., Bertaux, J.-L., Bouchy, F., Lovis, C., Mordasini, C., Pepe, F., Queloz, D., & Sivan, J.-P. 2006, *A&A* 447, 361.
- Vorholz, J., Rumpf, B., & Maurer, G. 2002, *Phys. Chem. Chem. Phys.* 4, 4449.
- Wagner, W. & Pruss, A. 1993, *J. Phys. Chem. Ref. Data* 22, 783.
- Zemansky, M. W. 1957, *Heat and Thermodynamics*. McGraw-Hill Book Company, Inc., New York.
- Ziegler, W. T. 1959, *Natl. Bur. Stand. Tech. Notes* 6038, Washington, DC.

5.9 Appendix E: Moist Adiabats

To derive the equation for dV/dT , we note the following thermodynamic equations:

$$TdS = C_v dT + T \left(\frac{\partial P}{\partial T} \right)_V dV \quad (\text{Zemansky 1957, p. 245}), \text{ and} \quad (\text{E1})$$

$$TdS = C_p dT - T \left(\frac{\partial V}{\partial T} \right)_P dP \quad (\text{Zemansky 1957, p. 246}). \quad (\text{E2})$$

Therefore,

$$C_p - C_v = -T \left(\frac{\partial V}{\partial T} \right)_P^2 \left(\frac{\partial P}{\partial V} \right)_T \quad (\text{Zemansky 1957, p. 251}). \quad (\text{E3})$$

Evaluate Equation E3 for the van der Waals equation of state (with a and b coefficients for hydrogen gas) by taking the partial derivative of Equation 5.1 with respect to V at constant P :

$$\left(\frac{\partial V}{\partial T} \right)_P^{-1} \frac{R}{V - b_{\text{H}_2}} - \frac{RT}{(V - b_{\text{H}_2})^2} + \frac{2a_{\text{H}_2}}{V^3} = 0 \quad (\text{E4})$$

$$\left(\frac{\partial V}{\partial T} \right)_P = \frac{\frac{R}{V - b_{\text{H}_2}}}{\frac{RT}{(V - b_{\text{H}_2})^2} - \frac{2a_{\text{H}_2}}{V^3}} \quad (\text{E5})$$

$$\left(\frac{\partial P}{\partial V} \right)_T = -\frac{RT}{(V - b_{\text{H}_2})^2} + \frac{2a_{\text{H}_2}}{V^3}, \text{ so} \quad (\text{E6})$$

$$C_p - C_v = \frac{R^2 T^2}{T (V - b_{\text{H}_2})^2} \left(\frac{1}{\frac{RT}{(V - b_{\text{H}_2})^2} - \frac{2a_{\text{H}_2}}{V^3}} \right). \text{ Thus,} \quad (\text{E7})$$

$$C_p - C_v = \frac{R}{1 - \frac{2a_{\text{H}_2}(V - b_{\text{H}_2})^2}{RTV^3}}, \quad (\text{E8})$$

which is the same as Equation 5.4 for one species. Adding latent heat to Equation E1, we find

$$TdS = C_v dT + T \left(\frac{\partial P}{\partial T} \right)_V dV + \sum_i (1 - f_i) L_i dq_i = 0, \quad (\text{E9})$$

where the factor $(1 - f_i)$ converts to “per moles of mixture”. From the definition of q_i in Equation 5.3, we see that

$$1 - f_i = \frac{1}{1 + q_i}. \quad (\text{E10})$$

Rearranging terms,

$$\left[C_v + \sum_i \left(\frac{L_i}{1 + q_i} \right) \left(\frac{\partial q_i}{\partial T} \right)_V \right] dT + \left[T \left(\frac{\partial P}{\partial T} \right)_V + \sum_i \left(\frac{L_i}{1 + q_i} \right) \left(\frac{\partial q_i}{\partial V} \right)_T \right] dV = 0, \text{ but} \quad (\text{E11})$$

$$T \left(\frac{\partial P}{\partial T} \right)_V = \frac{RT}{V - b_{\text{H2}}} \quad (\text{E12})$$

for a van der Waals equation of state. Thus,

$$\left(\frac{dV}{dT} \right)_S = - \left[\frac{C_v + \sum_i \left(\frac{L_i}{1 + q_i} \right) \left(\frac{\partial q_i}{\partial T} \right)_V}{\frac{RT}{V - b_{\text{H2}}} + \sum_i \left(\frac{L_i}{1 + q_i} \right) \left(\frac{\partial q_i}{\partial V} \right)_T} \right]. \quad (\text{E13})$$